Computational Studies of Massively Separated Wake Flows of Transport Aircraft

A thesis accepted by the Faculty of Aerospace Engineering and Geodesy of the University of Stuttgart in fulfilment of the requirements for the degree of Doctor of Engineering Sciences (Dr.-Ing.)

by

Andreas Waldmann

born in Vorkuta

Main referee: Prof. Dr. Ewald Krämer
Co-referee: Prof. Dr. Ralf Rudnik

Day of defense: April 22, 2021

Institute of Aerodynamics and Gas Dynamics
University of Stuttgart

2021

Acknowledgments

Altough my name is on the cover, this work could not have existed without the contribution of many. Prof. Ewald Krämer and Dr. Thorsten Lutz have my gratitude for offering me the opportunity to conduct research on complex aerodynamics and to compile this thesis. They deserve plaudits for keeping faith with the project even when the funding was initially declined, deeming this particular research area important enough to continue. I appreciate the funding contribution by the Deutsche Forschungsgemeinschaft, which helped make this work possible. Further, I thank Prof. Rudnik for taking on the role of co-referee and for his constructive feedback.

The work that culminated in this thesis would not have been possible without input from various peers. The many fruitful discussions with my colleagues at the Institute of Aerodynamics and Gas Dynamics helped me understand the phenomena that I was studying. We spent a lot of time together, both at work and outside of it. Over the years, many of these professional relationships turned to friendships that I cherish.

Apart from this, I received scientific support in various ways. Dr. Werner Würz and Jonas Romblad enabled us to conduct our own validation experiments in their wind tunnel, which enormously expanded our horizons as fluid dynamicists. My time as a visiting scholar with Dr. Oriol Lehmkuhl and Daniel Pastrana at the Barcelona Supercomputing Center helped me gain a different perspective on the phenomena I was researching. Matthias Schulz with his colleagues from the European Transonic Windtunnel, and Dr. Robert Konrath from DLR each patiently explained the intricacies of the experimental validation data they provided. Many others, be it collaborators or conference acquaintances, contributed their insights and helped make this work better.

Of course, none of this would have been possible without my family and their support. My beloved Vanessa bore the brunt of the highs and the lows that come with such an academic endeavor. Despite this, she still agreed to become my wife along the way and to make me the happiest I can be.

Contents

Acknowledgments i

List of Figures vii

List of Tables xiii

Nomenclature xv

List of Abbreviations xviii

Abstract xxi

Kurzfassung xxiii

1. Introduction 1
- 1.1. Motivation for Flight Envelope Boundary Research . . . 3
- 1.2. State of the Art . . . 4
  - 1.2.1. Aircraft Stall Research . . . 5
  - 1.2.2. Computational Methods in Edge of Envelope Research . . . 8
- 1.3. Objectives . . . 10
- 1.4. Outline . . . 10

2. Theory and Physics 13
- 2.1. Stall and its Consequences for Airliners . . . 13
- 2.2. Airfoil Stall, Separation and Wake . . . 16
  - 2.2.1. Stall Types . . . 16
  - 2.2.2. The Shear Layer and Kelvin-Helmholtz Instability . . . 19
  - 2.2.3. The Wake . . . 20
- 2.3. Three-Dimensional Swept Wing Flows and Their Post-Stall Characteristics . . . 23

3. Methodology **27**
3.1. Computational Methods . . . 27
3.1.1. Governing Equations . . . 27
3.1.2. Resolution of Unsteady Turbulent Motion . . . 29
3.2. Practical Simulation . . . 33
3.2.1. Flow Solver . . . 33
3.2.2. Artificial Dissipation . . . 33
3.3. Postprocessing . . . 34

4. Aircraft Configuration and Experimental Background **39**
4.1. The Common Research Model . . . 39
4.2. Experimental Background . . . 41
4.2.1. Measurements . . . 41
4.2.2. PIV . . . 42
4.3. Wind Tunnel Effects and Model Configurations . . . 43

5. Simulation and Validation in Subsonic Post Stall Conditions **47**
5.1. Simulation Approach . . . 48
5.2. Method Choice and Validation . . . 51
5.2.1. General Flow Field Topology . . . 52
5.2.2. Inboard Wake in CFD . . . 57
5.2.3. Dissipation of Resolved Turbulence . . . 60
5.2.4. Spatial and Temporal Resolution . . . 66
5.3. Sensitivity to Model Configuration . . . 68
5.4. Sensitivity to Reynolds Number . . . 70
5.5. Analysis of Uncertainty due to Temporal Sampling . . . 71
5.6. Concluding Remarks . . . 74

6. Wake Flow in Low Speed Stall **75**
6.1. Separation and Flow Topology in Post Stall . . . 76
6.1.1. Three-Dimensional Separation and Flow Topology . . . 76
6.1.2. Forces and Load Distributions . . . 78
6.1.3. Shape of Near and Far Wake . . . 80
6.1.4. Concluding Remarks . . . 89
6.2. Dynamics of Separation and Wake . . . 90
6.2.1. Proper Orthogonal Decomposition Analysis of Longitudinal Wake Slices 90
6.2.2. Phase Assignment using POD . . . 101
6.2.3. Changes in Dynamics due to Angle of Attack . . . 104
6.2.4. Concluding Remarks . . . 106
6.3. Quantitative Characteristics of Wake Turbulence . . . 106
6.3.1. Turbulent Stresses in Separated Flow . . . 106
6.3.2. Turbulence Statistics and Signal Analysis . . . 111
6.3.3. Scales and Correlations of Turbulence . . . 129
6.3.4. Concluding Remarks . . . 133
6.4. Wake Propagation and Tailplane Loads . . . 134
6.4.1. Wake Meandering . . . 134
6.4.2. Propagation Speed . . . 136
6.4.3. Tailplane Interaction . . . 138
6.4.4. Concluding Remarks . . . 140

7. Conclusion **141**

A. RANS Turbulence Models **145**

B. Experimental Settings **147**

C. Solver Parameters **149**

D. Wake Quantities in Low Speed Stall **151**

Bibliography **153**

List of Figures

1.1. Maneuvering envelope according to FAR25, title 14, §25.333. Dashed line: representative buffet boundary, adapted from Abbas-Bayoumi and Becker [14]. 2
1.2. Schematic sketch of generic flight envelope boundaries of a transonic civil transport aircraft. Solid line: upper limit of linear lift region, dashed line: upper limit of nonlinear region and beginning of full stall. 2
1.3. Commercial aviation fatalities per million departures since 1970, with data from [3]. 4

2.1. Top view of an A350−900, from [1]. 14
2.2. Section through a wing and tail configuration at high α. 14
2.3. Stalled aircraft wake at two angles of attack and the corresponding pitching moment, adapted from Teng. [150]. Red lines represent wake edges. Point 1 is at pitch break, point 2 is in post stall. 15
2.4. The classification of airfoil separation, from Polhamus [105]. 17
2.5. Mean streamlines around a bluff body, adapted from Hucho [59]. Dashed line denotes the mean boundary of the backflow region. S1 denotes the separation points. 18
2.6. Flow topology around a stalled airfoil without reattachment. Dashed line denotes the mean boundary of the backflow region, the black circular dot is the position of the rear stagnation point. 18
2.7. Shear layer with parallel flows U_1 and U_2. 19
2.8. Turbulent plane wake with time-averaged velocity profile, adapted from Tennekes and Lumley [151]. 21
2.9. Representative stall mode signals, analogous to hotwire signal representation from Huang and Lee [57]. 22
2.10. Top view of a finite wing flow. Photograph on the left from van Dyke [158]. Red lines show flow direction above the wing, blue dashed lines below the wing. 24
2.11. Evolution of the leading edge vortex on a swept wing, adapted from Zhang et al. [180]. Angle of attack from left to right: 7°, 8°, 9°, 14°. 25

3.1. Turbulence energy spectrum, double logarithmic representation. 30

3.2. POD mode shapes of a von Kármán vortex street behind a NACA0012 airfoil. 36

4.1. CRM in the ETW test section. 40
4.2. Coordinate system origins and directions. 40
4.3. Positions of the nine pressure measurement rows on the wing suction side. . . 42
4.4. PIV setup in the ETW with CRM installed, from Konrath [70]. 43
4.5. Effect of the sting on the pressure coefficient distribution in the symmetry plane at $\alpha = 5°$, $\mathrm{Re}_\infty = 11.6 \cdot 10^6$. Δc_p is the difference between the results obtained with and without sting. Image from Waldmann et al. [167]. 44
4.6. Effect of the sting on the Mach number distribution in the symmetry plane at $\alpha = 5°$, $\mathrm{Re}_\infty = 11.6 \cdot 10^6$. Image from Waldmann et al. [167]. 45
4.7. Support system of the CRM in the ETW. 45
4.8. Wing bend and twist increments at $M_\infty = 0.25$ relative to $1g$ shape for a series of angles of attack, scaled to $Re_\infty = 11.6 \cdot 10^6$. 46

5.1. Experimental force and moment polars from the European Transonic Windtunnel (ETW) at run 316 ($Re_\infty = 11.6 \cdot 10^6$, $M_\infty = 0.25$). 48
5.2. Position of the wake block relative to the CRM, grids A and B. 49
5.3. Isosurfaces of instantaneous $\lambda_2 = -10^5 \mathrm{s}^{-2}$ colored by streamwise velocity u. Near-surface values and outboard data $y > 0.5\,\mathrm{m}$ are not shown for clarity. . . 53
5.4. Forces and moments at $\alpha = 18°$. Vertical bars indicate the confidence bounds based on the signals's standard error where applicable. 55
5.5. Wing pressure distributions at $\alpha = 18°$ for various modelling approaches. $M_\infty = 0.25$, $Re_\infty = 11.6 \cdot 10^6$, $\alpha = 18°$. 55
5.6. Location of the PIV window relative to the CRM. Inset contours: mean velocity $\overline{u}/u_\infty$ in WT coordinates. Inflow direction in the insets from the right. . 56
5.7. PIV and CFD results in the wake at $\alpha = 18°$ in wind tunnel coordinates. . . . 57
5.8. Inboard mean streamwise velocity distributions $\overline{u}/u_\infty$ at $\eta = 20.1\,\%$ and $\eta = 28.3\,\%$. 58
5.9. Inboard resolved k_t distributions at $\eta = 20.1\,\%$ and $\eta = 28.3\,\%$. 59
5.10. Time-averaged eddy viscosity and hybrid model functions at $\eta = 28.3\,\%$ for low-dissipation URANS (U4) and DDES (D4). 61
5.11. Contour lines of $\overline{u}/u_\infty$ in the $\eta = 28.3\%$ plane. Contour lines at $\overline{u}/u_\infty = \{0, 0.4, 0.8\}$. 62
5.12. Streamwise evolution of inboard wake properties at $\eta = 20.1\,\%$ and $\eta = 28.3\,\%$ for 3 dissipation settings. x axis coordinate originates at the trailing edge position. 63
5.13. Resolved turbulence kinetic energy k_t in plane perpendicular to the inflow at $x/c_{ref} = 5.7$. Vertical lines represent positions $\eta = 20.1\,\%$ and $\eta = 28.3\,\%$. . . . 64
5.14. Power spectral densities of streamwise velocity u for U1, U4, D4 and D5. Dashed line represents a -5/3 slope. 65
5.15. Convective CFL number at 28.3% semispan. Dashed line denotes CFL = 1. . . 66
5.16. Wing pressure distributions at $\alpha = 18°$ for different grids and Δt. 67
5.17. Power spectral densities of u for different resolutions. Dashed line represents $-5/3$ slope indicating inertial range. 68
5.18. Configuration differences: Grey surface is baseline CRM WBT0. WBT0d deformed wing shown in yellow, WBT0ssd support system in red. 69
5.19. Configuration effects. 69
5.20. Spanwise distribution of wing and tailplane loads at different Re_∞. 70

5.21. Isoline $\overline{u} = 0$ at $\alpha = 18°$ at inboard wing for three different Reynolds numbers. 71
5.22. Running statistics of the aircraft lift coefficient. Dashed lines represent confidence boundaries for each statistic according to Eq. 3.27. 72
5.23. Autocorrelation function (ACF) of lift coefficient signals at $Re_\infty = 11.6 \cdot 10^6$, $\alpha = 18°$, DDES, grid B. 73
5.24. Distribution of N_{eff} for the streamwise velocity u at $\eta = 28.3\,\%$ for three different runtimes. 73
5.25. Uncertainty due to sampling error of first and second order velocity statistics in the wake at 5 streamwise positions ($x = \{1, 2, 3\}c_{ref}$ from the trailing edge in WT system) at $\eta = 28.3\,\%$, $\alpha = 18°$. Dashed lines indicate the range of the appropriate 95 % confidence interval at each location, orange for $N = 2200$, gray for $N = 500$. 74

6.1. Instantaneous spanwise vorticity ω_y inboard and outboard at $\alpha = 18°$. 76
6.2. Time-averaged streamlines at inboard wing and instantaneous spanwise vorticity component ω_y in two slices inboard and outboard at $\alpha = 18°$. Streamlines are colored by mean spanwise velocity $\overline{v}$. ω_y is mirrored to the left wing for clarity, with $|\omega_y| < 500$ omitted. 77
6.3. $\overline{\omega_y} c_{ref}/u_\infty$ (top row) and $\overline{u'w'}/u_\infty^2$ (bottom row) at $\alpha = 18°$. Mean in-plane streamlines are superimposed on the mean vorticity. 78
6.4. Wing pressure distributions for three angles of attack at $M_\infty = 0.25$, $Re_\infty = 11.6 \cdot 10^6$. 78
6.5. Spanwise distributions of c_L and circulation characteristics. 79
6.6. Contours of time-averaged spanwise velocity $\overline{v}/u_\infty$ in a slice parallel to the outboard trailing edge and contours of time-averaged streamwise vorticity in multiple slices in the wake at $\alpha = 18°$. Red and black contour lines represent $\overline{u'w'}/u_\infty^2 = \{0.05, 0.1\}$. Wing-aligned slice position shown on top right. 80
6.7. Time-averaged surface streamlines derived from intergration of the local wall friction coefficient vector. 81
6.8. Mean spanwise and transverse velocities in the wake at $\alpha = 18°$. Dashed contour lines in the bottom row represent negative values. 82
6.9. Top views of $\overline{u}/u_\infty = 0.5$ isosurface colored by mean spanwise velocity $\overline{v}$. . . . 82
6.10. Time-averaged extent of the recirculation area delimited by contours of $\overline{u} = 0$ at three spanwise positions for three angles of attack. Colored dashed lines mark the streamwise location of the rear stagnation point. 83
6.11. Turbulence kinetic energy k_t/u_∞^2 at $Re_\infty = 11.6 \cdot 10^6$. Dashed blue line represents $\overline{u} = 0$. 84
6.12. Production of resolved turbulence kinetic energy for the three flow topology types. Data in parentheses denotes the specific solution shown as example. . . 85
6.13. Magnitude of wake velocity deficit $|\overline{u_d}|$ for three angles of attack, plotted over distance from the trailing edge. 86
6.14. Magnitude of momentum thickness Θ for three angles of attack. 86
6.15. Wake half-width l_s for three angles of attack. 87
6.16. Downwash angle ξ averaged over time and over the vertical extent of the wake between $z = -0.05\,\text{m}$ and $z = 0.25\,\text{m}$. 88
6.17. Time averaged mean streamwise velocity and superimposed locations of wake center based on $\overline{u}$ at $\eta = 28.3\,\%$. 88

6.18. Time-averaged position of the velocity minimum at each streamwise position, dashed lines showing ξ_{lin}. 89
6.19. POD mode eigenvalues in wake slices at $\alpha = 18°$. 91
6.20. First four POD modes at $\eta = 28.3\%$ and $\alpha = 18°$, coupled POD. 92
6.21. POD coefficient signal characteristics at $\eta = 28.3\,\%$, $\alpha = 18°$. 93
6.22. POD spectra for first eight modes at different longitudinal planes for $\alpha = 18°$, $Re_\infty = 11.6 \cdot 10^6$. Shaded region denotes range of Strouhal numbers $Sr_d = 0.09...0.22$ based on the local value of d. The vertical arrangement of spectra and the coloring are the same as in Fig. 6.21a. 94
6.23. u and w components of the first POD mode at $\eta = 20.1\,\%, 39.7\,\%, 60.3\,\%$ at $\alpha = 18°$. 94
6.24. Lift coefficient fluctuation $c_l(\eta)$ at $\alpha = 18°$. 95
6.25. Low order POD modes of surface c_p. 96
6.26. Instantaneous spanwise velocities at $\alpha = 18°$. Contours in a longitudinal slice at $\eta = 39.7\,\%$ (A) and a slice parallel to the wing leading edge (B). Slice positions are indicated in the inset view. Dashed black line indicates intersection between the two slices. 96
6.27. Power spectral density of wall c_p along the local chord, $\alpha = 18°$. 98
6.28. Temporal evolution of local flow features at $\eta = 39.7\,\%$ during a lift increase period from t_a to t_b. 99
6.29. Local flow features at $\eta = 39.7\,\%$ during a lift increase period from t_a to t_b. . . 99
6.30. Streamwise velocities reconstructed using 2 modes at t_a and t_b. 101
6.31. Instantaneous u at $\eta = 28.3\,\%$ overlaid with contours of the $\phi_{u,1}$ mode from Fig. 6.20, displayed here using lines only for positive (solid) and negative (dashed) regions. 101
6.32. Phase relationship between POD modes a_1 and a_2 at $\eta = 28.3\,\%$. Red vertical line and ■ indicate t_c, blue vertical line and ● denote t_d. 102
6.33. Phase average of original (top row) and reconstructed (bottom row) streamwise velocity at $\eta = 28.3\,\%$ at two different phase angles. Dashed orange line denotes $\overline{u} = 0$. 103
6.34. Spectral maps of section lift coefficients $c_l(\eta)$ at $Re_\infty = 11.6 \cdot 10^6$. 104
6.35. Power spectral densities of POD coefficients at $\alpha = 16°$, $Re_\infty = 11.6 \cdot 10^6$, linear scales. 105
6.36. Power spectral densities of POD coefficients at $\alpha = 20°$, $Re_\infty = 11.6 \cdot 10^6$, linear scales. 105
6.37. Resolved Reynolds stress components at $\alpha = 18°$ and $\eta = 28.3\,\%$. 107
6.38. Anisotropy map showing fluctuations along the time averaged wake centerline (ξ_{lin} shown in Fig. 6.18) at $\eta = 28.3\,\%$. Point colors represent distance along the wake centerline. Color coding is shown in Fig. 6.38a,. 109
6.39. Anisotropy map showing fluctuations along the time averaged wake centerline. Point colors represent distance along the wake centerline. The locations $1c$, $2c$ and $3c$ denote one-component, two-component and three-component turbulence, respectively. 110
6.40. Anisotropy componentiality contours at $\eta = 28.3\,\%$. Color coding given in Fig. 6.40a with magenta: one-component, yellow: axisymmetric two-component, cyan: isotropic three-component. 111

6.41. Shear layer point positions at $\eta = 28.3\,\%$. Red symbols represent points SL1, SL2, SL3. Velocity contour colors are cut off above $0.9u_\infty$, overlaid orange lines indicate $\overline{u}/u_\infty = 0$ (solid) and $\overline{u}/u_\infty = 0.4$ (dashed).. Green vertical lines represent extraction locations. 112
6.42. Profiles of shear layer quantities at $\eta = 28.3\,\%$, WT coordinate system. Vertical profiles are extracted at positions shown via green lines in Fig. 6.41, with plots horizontally offset by a constant amount for clarity. Grey dotted lines represent zero value at each of the five position. The scale is given in each figure using a double arrow. 113
6.43. Shear layer quantities along the shear layer length. 114
6.44. Reynolds stresses in the shear layer for three angles of attack and $\eta = 28.3\,\%$. Lines are at 20%, 40%, 60%, 80%, 100% of local chord. 115
6.45. Profiles of skewness and kurtosis of the three velocity components in the shear layer at $\alpha = 18°$ and $\eta = 28.3\,\%$. Lines are at 20%, 40%, 60%, 80%, 100% of local chord. 116
6.46. Skewness and kurtosis of streamwise velocity in the shear layer at $\eta = 28.3\%$ at three angles of attack. Line legend as in Fig. 6.42. Lines are at 20%, 40%, 60%, 80%, 100% of local chord. 117
6.47. Velocity signals at the positions SL1 (top), SL2 (middle), SL3 (bottom) in the upper shear layer at $\alpha = 18°$. Red line indicates zero in all panels. 118
6.48. Premultiplied power spectral densities of velocity at the positions SL1, SL2 and SL3 in the upper shear layer at $\alpha = 18°$. 118
6.49. Wavelet coherence $|W^{uw}|$ between u and w at SL1, SL2 and SL3 at $\alpha = 18°$. Dashed horizontal line indicates $Sr_{c_{\text{ref}}} = 0.22$. Arrow direction indicates phase angle, right-facing arrows represent 0 and phase increasing in counter-clockwise direction. Arrows are drawn on evey 100th point of the grid. 119
6.50. Fluctuation spectrum along the shear layer. Solid line shows most amplified f_{KH,δ_ω}, dashed line shows f_{KH,δ_Θ}. 120
6.51. Contours of joint probability density functions with the associated u and w histograms at SL1, SL2, SL3. u histogram shown on top and w to the right, with common scaling. The range of u'/u_∞ and w'/u_∞ is from -1 to 1 in all panels. 121
6.52. Quadrant analysis in the shear layer at $\alpha = 18°$. Dashed green line in **(b)** denotes total shear stress $\overline{u'w'}$. 123
6.53. Point positions at $\eta = 28.3\,\%$. Instantaneous velocity contour colors are cut off above $0.9u_\infty$. Green vertical lines represent extraction locations. 124
6.54. Skewness and kurtosis of streamwise velocity in the wake at $\eta = 28.3\,\%$ at three angles of attack. Three streamwise positions shown, at $(x - x_{TE})/c_{\text{local}} = \{1, 2, 3\}$ as indicated in Fig. 6.53. Dashed horizontal lines represent position of the wake centerline. Coordinates in WC system. 124
6.55. Premultiplied power spectral densities of velocity at the positions WC1, WC2, WC3 along the wake centerline at $\alpha = 18°$. 125
6.56. Premultiplied power spectral densities of velocity at the far wake position points FW1-FW3 at $\alpha = 18°$. 126
6.57. Power spectral density of streamwise velocity u along vertical lines at $\eta = 28.3\,\%$, $\alpha = 18°$. Data extraction lines located at $(x - x_{TE})/c_{\text{ref}} = \{1, 2, 3\}$ in WC coordinates. 127

6.58. Contours of joint probability density functions with the associated u and w histograms at WC1-3 and FW1-3. u histogram shown on top and w to the right of the contour plots, with common scaling. 127
6.59. Quadrant analysis in the wake at $\alpha = 18°$. Lines are at $(x - x_{TE})/c_{\text{ref}} = \{1, 2, 3\}$. Dashed green line in **(b)** denotes total shear stress $\overline{u'w'}$. Coordinates in WC system. 128
6.60. Two-point correlations at point SL2 in the upper shear layer at $\eta = 28.3\,\%$, $\alpha = 18°$, WT coordinates. 129
6.61. Two-point correlations in the wake at $\eta = 28.3\,\%$ and $\alpha = 18°$, WC coordinates. Colors show R_{uu} ranging from -1 to 1, grey lines show distribution of k_t. 130
6.62. Correlation functions R_{uu} with x_0 at WC1, WC2 and WC3, $\eta = 28.3\,\%$. 131
6.63. Integral length scale L_{uu} at three positions downstream of the trailing edge, WC system. The distortion at the lower edge is caused by integration approaching the tailplane. 132
6.64. Integral length scales $L_{uu,Taylor}/c_{\text{ref}}$ using Taylor's hypothesis, $\alpha = 18°$, WC system. Contours cut off above $L_{uu}/c_{\text{ref}} = 1$. 133
6.65. Wake meandering at $\alpha = 18°$, $\eta = 28.3\%$. 135
6.66. Wake maximum extent via extrema of A over streamwise distance. Only every 10th sample is shown for clarity. WC system. 136
6.67. Space-time plot of low-pass filtered meander function over time at $\eta = 28.3\,\%$. Dashed green line in Fig. 6.67a indicates typical slope of a ridge. 136
6.68. Cross-correlation of the local wing lift at $\eta = 28.3\,\%$ and the corresponding spanwise position on the tailplane. Vertical dashed line indicates lag of highest absolute correlation coefficient. 137
6.69. Time series of tailplane forces. 138
6.70. Tailplane loads at three angles of attack. 139
6.71. k_t/u_∞^2 at $x/c_{\text{ref}} = 8.5$. Volume slice is fixed in WT system. 139
6.72. Resolved k_t/u_∞^2 at $\eta = 28.3\,\%$ near the tailplane and time-averaged in-plane streamlines. Purple isoline denotes $k_t/u_\infty^2 = 0.01$. 140

D.1. Mean streamwise velocity $\overline{u}/u_\infty$ at $Re_\infty = 11.6 \cdot 10^6$. Dashed orange line represents $\overline{u} = 0$. 151

List of Tables

4.1. CRM wing and tailplane geometry data 40
4.2. Reference coordinate positions in the CRM coordinate system at model scale. . 41

5.1. Grids used in the study. 50
5.2. Validation runs. 52
5.3. Time-averaged forces and moments for different computational model approaches. Only runs pertinent to artificial dissipation discussion are shown. . . 61
5.4. Time step and grid variation. 66
5.5. Time-averaged forces and moments for different CRM configurations. 69

6.1. Low speed stall flow conditions. 75
6.2. Time-averaged forces and moments at three different angles of attack. 79
6.3. Streamwise location of the rear stagnation point at different angles of attack and spanwise locations. Data in absolute WT coordinates. 83
6.4. Wake centerline slope angles of the linear wake portion ξ_{lin} at different angles of attack and positions. 89
6.5. Positions of the wake analysis points at $\alpha = 18°$. 124

B.1. Overview of experimental conditions. 147

C.1. TAU computational parameters for CRM simulations. 149

Nomenclature

Greek Symbols

α	[°]	Angle of attack
Γ	[$\mathrm{m^2\,s^{-1}}$]	Circulation
γ	[$\mathrm{m\,s^{-1}}$]	Spanwise gradient of circulation
γ	[-]	Ratio of specific heats
δ_{ij}	[-]	Kronecker symbol
δ_ω	[m]	Vorticity thickness
ε	[$\mathrm{Pa\,s\,m^{-1}}$]	Destruction of turbulent viscosity in the SA model
η	[-]	Dimensionless spanwise position
θ	[rad]	Wing twist
θ	[m]	Momentum thickness
Λ	[m]	Wake meander wavelength
λ_2	[$\mathrm{s^{-2}}$]	Value of λ_2 criterion, eigenvalue of $S_{ij}^2 - \Omega_{ij}^2$
λ_i	[-]	i-th eigenvalue of the anisotropy tensor a_{ij}
λ_j	[-]	j-th POD eigenvalue
μ	[Pa s]	Dynamic viscosity of the fluid, laminar viscosity
μ_t	[Pa s]	Eddy viscosity
ν	[$\mathrm{m^2\,s^{-1}}$]	Kinematic viscosity of the fluid
ξ	[°]	Local downwash angle
ξ_{lin}	[°]	Inclination angle of the wake centerline
Φ_{uu}	[$\mathrm{m^2\,s^{-2}}$]	Power spectral density of velocity u
ϕ_i	[-]	i-th POD mode
ψ	[rad]	Phase angle
ρ	[$\mathrm{kg\,m^{-3}}$]	Density
$\rho(x)$	[-]	Autocorrelation function
σ	[-]	Standard deviation
τ	[s]	Time scale
τ_{ij}	[$\mathrm{N\,m^{-2}}$]	Stress tensor

τ_{ij}^{EVM}	[N m^{-2}]	Eddy viscosity model based Reynolds stress tensor
Ω	[m^3]	Volume of the control volume
Ω_{ij}	[s^{-1}]	Rotation rate tensor
ω	[s^{-1}]	Vorticity

Latin Symbols

A	[m]	Wake meander amplitude
a_i	[-]	POD time coefficient i
a_{ij}	[-]	Anisotropy tensor
b	[m]	Wing span
C_{DES}	[-]	DES constant
C_{ic}	[-]	Barycentric metrics of anisotropy, $i = \{1, 2, 3\}$
C_D	[-]	Drag coefficient
C_L	[-]	Lift coefficient
C_M	[-]	Pitching moment coefficient
C_i	[-]	Stress contribution in quadrant i
c	[m]	Local chord
c_μ	[-]	Turbulence model constant
c_{ref}	[m]	Mean aerodynamic chord
c_l	[-]	Lift coefficient of a section
c_p	[-]	Pressure coefficient
$\tilde{d}$	[m]	DES length scale
D_i	[-]	Duration fraction in quadrant i
d	[m]	Projected height
d_w	[m]	Wall distance
E	[J kg^{-1}]	Energy per unit mass
f	[Hz]	Frequency
f_d	[-]	DDES delay function
f_s	[Hz]	Sampling rate
II_a, III_a	[-]	Second and third invariants of the anisotropy tensor
i_{HTP}	[rad]	Incidence angle of the horizontal tailplane
K	[-]	Kurtosis
$k^{(2)}, k^{(4)}$	[-]	Central scheme artificial dissipation coefficients
k_{cut}	[m]	Cut-off wave number for wake meandering analysis
k_t	[J]	Turbulence kinetic energy
L_{ij}	[m]	Tensor of integral length scales
L_{Taylor}	[m]	Length scale based on Taylor's hypothesis
l_s	[m]	Half-width of a wake
M	[-]	Mach number
$\mathcal{O}(n)$	[-]	Order of magnitude in big-O notation
P_k	[J s^{-1}]	Production of turbulence kinetic energy k_t
p	[Pa]	Pressure
q	[Pa]	Dynamic pressure
Re	[-]	Reynolds number
S	[K]	Sutherland model constant
S	[-]	Skewness

S_i	[-]	Stress fraction
S_{ij}	[s^{-1}]	Shear rate tensor
Sr	[-]	Strouhal number
T	[K]	Temperature
R	[$J\,kg^{-1}\,K^{-1}$]	Specific gas constant
R	[-]	Shear layer velocity ratio
u, v, w	[$m\,s^{-1}$]	Streamwise, spanwise and vertical velocity component
W^{ij}	[-]	Wavelet coherence between two signals
x, y, z	[m]	Streamwise, spanwise and vertical coordinate
x_B,y_B	[-]	Barycentric anisotropy map coordinates
y^+	[-]	Nondimensional wall-normal distance

Superscripts

$\langle\rangle$	Conditionally averaged quantity
$\overline{\ }$	Averaged quantity
$'$	Fluctuating (mean subtracted) quantity

Subscripts

AC	Quantity in aircraft coordinate system
HTP	Quantity or coefficient pertaining to the horizontal tailplane
∞	Bulk inflow quantity
eff	Effective value
local	Quantity referenced to local chord projected length
ref	Reference value
SL	Quantity or coefficient pertaining to a shear layer
WC	Quantity in coordinate system oriented with wake centerline
WT	Quantity in wind tunnel coordinate system oriented with inflow

List of Abbreviations

ACF Autocorrelation Function

AIM Anisotropy Invariant Map

ATRA Advanced Technology Research Aircraft

CAST Commercial Aviation Safety Team

CFD Computational Fluid Dynamics

CICTT CAST/ICAO Common Taxonomy Team

CMY Cyan-magenta-yellow color model

CRM Common Research Model

CWT Continuous Wavelet Transformation

DDES Delayed Detached Eddy Simulation

DES Detached Eddy Simulation

DLR Deutsches Zentrum für Luft- und Raumfahrt

DMD Dynamic Mode Decomposition

DNS Direct Numerical Simulation

DPW Drag Prediction Workshop

DR Departure Region

EASA European Aviation Safety Agency

ETW European Transonic Windtunnel

FAA Federal Aviation Administration

FR Focus Region

FTLE Finite Time Lyapunov Exponent

FFT Fast Fourier Transform

HTP horizontal tailplane

ICAO International Commercial Aviation Organization

IDDES Improved Delayed Detached Eddy Simulation

LES Large Eddy Simulation

NASA National Aeronautics and Space Administration

MAC Mean Aerodynamic Chord

MSC Magnitude Squared Coherence

PIV Particle Image Velocimetry

POD Proper Orthogonal Decomposition

PSD Power Spectral Density

RANS Reynolds Averaged Navier Stokes

RPK Revenue Passenger Kilometers

SAS Scale Adaptive Simulation

SL Shear Layer

SPT Stereo Pattern Tracking

SST Shear Stress Transport

URANS Unsteady Reynolds Averaged Navier Stokes

UPRT Upset Recovery and Prevention Training

VR Viscous Region

Abstract

This work focuses on the investigation of flow phenomena associated with low speed stall on a representative commercial transport aircraft configuration. Subsonic stall at high Reynolds number involves a highly complex turbulent flow field, which is difficult to analyze in its entirety via experimental approaches. Various computational approaches based on URANS and hybrid RANS/LES were evaluated, utilizing a validation data set accumulated during the ESWI^{RP} experimental campaign in the European Transonic Windtunnel. Scale resolving computational approaches were leveraged to gain deeper insight into the processes occurring in such a wake. Compared with validation data from the wind tunnel, DDES-based methods were found to be able to resolve the flow features occurring at the separation location and in the wake. URANS is considered to be unable to properly resolve local flow features which are fundamental to the entire wake flow. An extensive study on the impact of solver settings, computational grids, model geometry and inflow Reynolds number was carried out in order to permit specific validation of the chosen approach.

Using these findings, the massively separated wake flow was studied at three angles of attack in post stall conditions: 16°, 18° and 20°. These computational results show that the wake is strongly three-dimensional in nature, associated with separation near the wing leading edge nearly over the entire span. The strong spanwise circulation gradient induces longitudinal vorticity in the wake, which propagates downstream. Nevertheless, planar longitudinal volume slices at fixed spanwise positions were found to exhibit remarkably clear characteristics of plane wake flows. Spanwise flow and its fluctuations tend to become less significant with downstream distance in the wake. Study of wake turbulence and dynamics in such planar slices helps shed light on the structure of the wake, which consists of a center region of mostly isotropic turbulence and boundary regions interacting with the outer flow above and below. Three different regimes of formation of the separated wake were identified via the main locations where turbulence kinetic energy k_t is produced. Analysis of anisotropy, turbulence length scales and signal characteristics provided insight into the propagation of the wake and the mixing processes.

The dynamics of the separation and wake fluctuations were studied via Proper Orthogonal Decomposition (POD) of the wake velocity time series, showing how the recirculation

dynamics and the wake fluctuations occur at different frequencies. The downstream wake mode has the shape of a von Kármán vortex street. The POD results combined with spectral analysis of point signals enable the analysis of propagation of the wake features, and of their role in the momentum exchange between the smooth outer flow and the turbulent wake. The recirculation dynamics originating at the wing propagate through the wake and can be detected in local fluctuation spectra downstream. Propagation velocities of the large scale structures were computed using both velocity field analysis and correlation of wing and tailplane forces. Finally, the knowledge of large scale wake dynamics and propagation characteristics enables the association of tailplane lift coefficient spectra with the flow structures arriving from upstream. The computed tailplane load fluctuations show that they are affected both by structures originating from the near-wing recirculation region and by the pure wake vortex street phenomenon.

Kurzfassung

Diese Arbeit hat die Analyse von massiv abgelösten Flügelnachlaufströmungen am Verkehrsflugzeug zum Gegenstand. Die turbulente Strömung bei niedriger Machzahl, hoher Reynoldszahl und hohem Anstellwinkel ist von hoher Komplexität gekennzeichnet, die hohe Anforderungen an experimentelle und numerische Verfahren stellt. Ein Beitrag zum Verständnis der physikalischen Prozesse kann von skalenauflösenden numerischen Simulationsmethoden geleistet werden, die spezifische Validierung erfordern. Hierfür wurden im Rahmen des europäischen Projektes ESWI^{RP} gesammelte Messergebnisse herangezogen. Diese Daten aus dem Europäischen Transsonischen Windkanal wurden verwendet, um mehrere Simulationsansätze basierend auf URANS sowie auf skalenauflösenden hybriden RANS/LES-Verfahren auf ihre Eignung zur plausiblen Wiedergabe der gemessenen Größen zu untersuchen. Es wurde beobachtet, dass URANS-Ansätze nicht in der Lage sind, die Gesamtheit der Nachlauffluktuationen korrekt abzubilden. Die korrekte Simulation neuralgischer Punkte der Strömung, wie der ablösenden Vorderkantenscherschicht, ist für die physikalisch plausible Entstehung des Nachlaufs entscheidend. Die vorliegende Untersuchung hat gezeigt, dass hierzu nur hybride Methoden in Verbindung mit geeigneten Lösereinstellungen und Rechengittern in der Lage sind.

Neben der Methodenauswahl wurde eine umfassende Parameterstudie zu zeitlicher und räumlicher Auflösung, sowie zu den Einflüssen der Modellgeometrie, ihrer Deformation und der Anström-Reynoldszahl durchgeführt. Ausgehend vom ausgewählten und validierten Rechenansatz unter Anwendung von DDES wurden Simulationen des Nachlaufs bei drei verschiedenen Anstellwinkeln α durchgeführt, welche im *post stall* Bereich der Polare liegen: 16°, 18° sowie 20°. Die Ergebnisse zeigen eine komplexe dreidimensionale Struktur des Nachlaufs, welche von Ablösung nahe der Vorderkante über die gesamte Flügelspannweite beherrscht wird. Der spannweitige Zirkulationsgradient am Flügel erreicht im Bereich des Hinterkantenknicks besonders hohe Werte. An dieser Stelle befindet sich eine große longitudinale Wirbelstruktur die sich in Abströmrichtung ausrichtet. Trotz dieser Dreidimensionalität weisen longitudinale Volumenschnitte an konstanten spannweitigen Positionen Eigenschaften einer ebenen Nachlaufströmung auf. Geschwindigkeitsfluktuationen in spannweitiger Richtung nehmen mit zunehmender Stromabdistanz relativ zu denjenigen in den anderen beiden Raumrichtungen ab. Untersuchungen der Nachlaufturbulenz ermöglichen die Identifikation

einer Struktur bestehend aus einem annähernd isotrop turbulenten Nachlaufkern sowie aus Interaktionsgebieten zwischen Nachlauf und ungestörter Außenströmung. Die hauptsächlichen Orte der Produktion von turbulenter kinetischer Energie k_t hängen vom Anstellwinkel und der spannweitigen Position ab. Analysen der Turbulenzanisotropie, der turbulenten Längenskalen sowie der Signaleigenschaften der Geschwindigkeitsfluktuationen geben Aufschluss über die Ausbreitung des Nachlaufs und die Mischungsprozesse zwischen Nachlaufströmung und Außenströmung.

Die Analyse der Dynamik der turbulenten Fluktuationen sowie die Identifikation der wichtigsten Fluktuationsmoden geschah mittels Proper Orthogonal Decomposition (POD). Die Nachlauffluktuation wird im wesentlichen von zwei Moden niederer Ordnung bestimmt, wobei die Oszillation des flügelnahen Rezirkulationsgebietes bei niedrigerer charakteristischer Frequenz zu beobachten ist als die der sich stromab ausbildenden Kármánschen Wirbelstraße. Dabei sind die beiden Phänomene im Nachlauf überlagert und in den Geschwindigkeitsspektren detektierbar. Die kombinierten Untersuchungen der POD, der Signalspektren und -statistiken, sowie der Quadrantanalyse der Scherspannung ermöglichen einen Überblick über das Verhalten des Nachlaufs und die Propagation der Strömungsstrukturen. Die Ausbreitungsgeschwindigkeit der großskaligen Strukturen wurde mittels Analyse des Geschwindigkeitsfeldes sowie mittels Korrelation zwischen Flügel- und Leitwerkslasten bestimmt. Schlussendlich konnte gezeigt werden, wie Leitwerkslasten sowie Lastspektren sich in Abhängigkeit vom Anstellwinkel verhalten. Es wurde beobachtet, dass sowohl die Fluktuation des Flügelrückströmgebietes als auch die Wirbelstraße sich im Lastspektrum des Leitwerks niederschlagen.

CHAPTER 1

Introduction

> It's easy to explain how a rocket works, but explaining how a wing works takes a rocket scientist.
>
> —P. R. Spalart, via D. McLean: *Understanding Aerodynamics: Arguing from the Real Physics, 2012*

The unrelenting growth and commoditization of air travel over the recent decades have resulted in an unprecedented volume of global air traffic. It grew by an average of 5.4 % in terms of Revenue Passenger Kilometers (RPK) each year between 2006 and 2017 [10], and industry forecasts agree on a sustained annual growth of commercial passenger numbers by 3.4 %-4.6 % on average over the following two decades [2][4][5]. Even slowdowns of the global economy such as the 2008 subprime mortgage crisis resulted in only minor setbacks in the growth curve. Increased competition between aircraft operators, both due to deregulation and to the appearance of emerging economies, spurred the development of more efficient aircraft. More recently, the recognition of environmental issues associated with carbon-based economies, and with air travel in particular, contributed further to the desire for increased fuel efficiency. These factors have brought significant improvements of fuel consumption and cost of operation [75].

Coincident with the increase in traffic, large strides have been undertaken to increase the safety of this mode of travel. The ever higher volume of air traffic in terms of trips taken per capita strengthens the desire to keep commercial passenger flight as safe as possible by reducing all types of accidents.

In this context, precise understanding of the aerodynamic behavior of a given aircraft configuration in all phases of flight is important. Knowledge of aerodynamic loads is crucial for proper dimensioning of every component, as excessive structural weight is detrimental to fuel consumption and thereby to the airline's operating costs. Science and engineering made large advances toward better prediction and modeling of aerodynamics. However, significant

knowledge gaps remain in areas of aircraft aerodynamics that involve unsteady, large scale complex flow dynamics. These gaps exist mainly due to the effort and expense associated with tackling them.

Aircraft Aerodynamics and Flight Envelope

From the introduction of powered flight until the end of the 20th century, civil airliners have continuously increased their flight velocity and size. After some iterative configuration changes, modern airliner design based on turbofan propulsion has converged to tube-and-wing layouts with horizontal and vertical tailplanes and large underwing engine nacelles. Such configurations are highly optimized in terms of performance and operational efficiency. As such, their aerodynamic characteristics are well understood when the aircraft is operated within its envelope boundaries. The flight conditions permitting safe operation of an aircraft define its flight envelope. A typical representation of the boundaries in terms of airspeed and load factor is shown in Fig. 1.1.

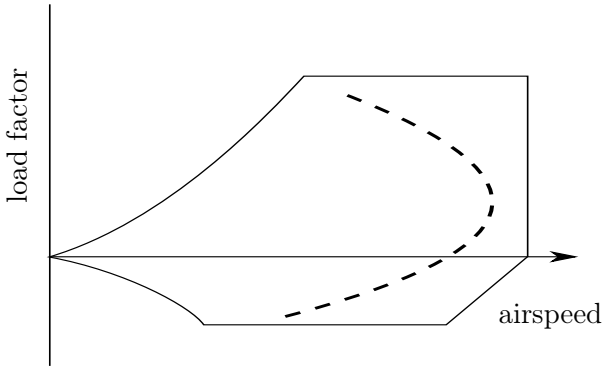

Fig. 1.1.: Maneuvering envelope according to FAR25, title 14, §25.333. Dashed line: representative buffet boundary, adapted from Abbas-Bayoumi and Becker [14].

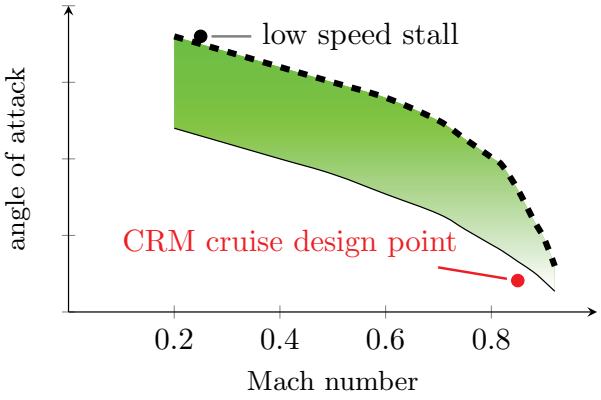

Fig. 1.2.: Schematic sketch of generic flight envelope boundaries of a transonic civil transport aircraft. Solid line: upper limit of linear lift region, dashed line: upper limit of nonlinear region and beginning of full stall.

Certification of transport aircraft requires the strength requirements to be met for each combination of airspeed and load factor within this envelope. A *design condition* can be defined for a given configuration, representing typical cruise flight. Far from the boundaries, and especially near this design condition, the flow around the aircraft can be largely assumed to be steady and attached. Transport aircraft spend the majority of the time during flight near the design condition, which is why significant resources are typically devoted to optimizing this regime. Conventional Computational Fluid Dynamics (CFD) methods are well adapted to flows of this type and are often able to predict aircraft performance with satisfactory precision [14]. The state of the art in computational analysis has achieved a high degree of accuracy and reliability in this context.

While the maneuvering envelope in Fig. 1.1 is useful from a flight mechanics and requirements perspective, the representation in terms of angle of attack α over Mach number M_∞ in Fig. 1.2

reflects the wide range of aerodynamic flow conditions the aircraft may encounter in flight.[1] The conditions contemporary long range airliners are designed for have converged to transonic Mach numbers around $M_\infty = 0.85$, which represents a compromise between sufficiently fast travel while avoiding cost penalties due to excessive drag. This transonic design point drives the aerodynamic characteristics of passenger aircraft configurations, such as the wing sweep and airfoil shape. A design point is indicated in Fig. 1.2 along with the line representing the approximate boundary of linear lift.

The complexity of the flow physics increases dramatically at off-design conditions toward the edges of the flight envelope, which is mainly associated with local flow separation phenomena. Excessive angles of attack due to maneuvering or speed increase can shift the flight condition into the shaded region, where flow separation occurs and the lift is no longer a linear function of the angle of attack. The flow is strongly separated above the dashed line, which is an inherently unsteady and highly turbulent multiscale phenomenon. In the presence of separation, the flow velocity fluctuations affect the forces acting on the wing and propagate downstream where they may interact with the tailplane. These interactions may impose unsteady loads on the tailplane, which has the potential to cause controllability issues for the aircraft or to lead to structural limits exceedance.

1.1. Motivation for Flight Envelope Boundary Research

It is a natural desire for an aircraft designer or operator to understand the physics at off-design conditions and in more extreme situations encountered at the edges of the envelope. Understanding the behavior helps to optimize the operation of current aircraft and enables potentially improved future designs. Improved knowledge of the loads and increased confidence in their predictions even outside the envelope may help design structures that are resilient without having to add excessive structural weight. Apart from these considerations, there is the aspect of safety. Despite the aforementioned growth of global air traffic, the engineering advances of the recent decades have led to record lows in accident numbers. This development is shown in Fig. 1.3 in terms of fatality rate per flight and asymptotically approaches a low level without reaching zero.

Mishaps do continue to occur and result in human or property damage. Delving into accident causes in more detail, Belcastro et al. [20] observe that one incident category stands out disproportionately: loss of control in flight (LOC-I) as defined by the CAST/ICAO Common Taxonomy Team (CICTT). Despite the decrease in overall accident rates seen in Fig. 1.3, LOC-I events have persisted and stagnated over time. Although such events can typically be traced back to a variety of reasons and combinations thereof, crew errors in the form of inappropriate reaction to aerodynamic stall is a common factor for a significant number of them according to Grant et al. [46]. Well-publicized accidents such as Air France flight 447 [8] or Colgan Air flight 3407 [7] provide examples of complex chains of events that involve stall conditions.

Barring structural damage, stall is typically associated with operation of an aircraft at the edge of its flight envelope. Although safeguards like modern fly-by-wire flight control systems have been introduced in order to avoid approaching envelope boundaries, such situations

[1] The shown envelope does not represent any specific aircraft, rather a sketch based on values obtained for the Common Research Model (CRM) configuration used in the present work.

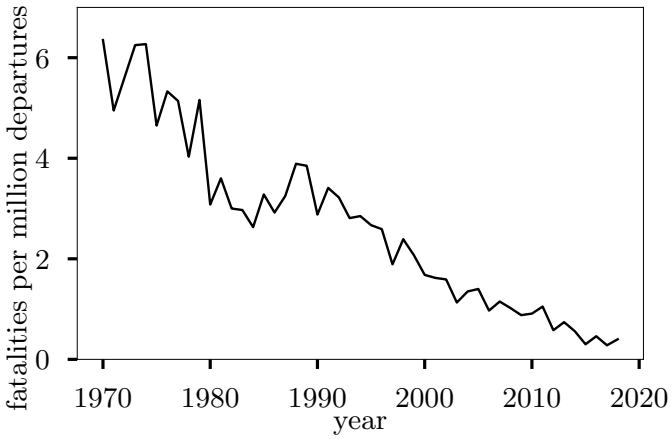

Fig. 1.3.: Commercial aviation fatalities per million departures since 1970, with data from [3].

cannot be ruled out. Fundamentally, Belcastro et al. [20] recognize that the current state of the art is ill-equipped to ensure prevention and recovery from LOC-I. Aircraft design and analysis practices have not been able to fully explore the entire range of possible flight conditions. Therefore, research is directed at increasing modeling and simulation capabilities that are able to characterize flow phenomena at off-nominal conditions.

One benefit arising from better understanding of physics is improved training of flight crew and increased ability to handle non-nominal flight conditions. Improved simulator training may result in better chances to rectify such situations. Recent efforts by the International Commercial Aviation Organization (ICAO) recognize that:

> "Pilots must be or become situationally aware before they are able to take appropriate actions." [9]

The need for Upset Recovery and Prevention Training (UPRT) is a consequence of this insight, and is as such being mandated by European Aviation Safety Agency (EASA) within their regulatory framework [12] and also by the Federal Aviation Administration (FAA). This poses a challenge for the present approach to flightcrew training, which relies on Flight Simulation Training Devices (FSTD). They can be suitable for prevention training [16], but significant expense may be required in order to make them capable of reproducing recovery maneuvers. The new URPT regulations require simulators that are able to model full stall situations and appropriate recovery [46] [150]. This motivates research on full stall behavior of commercial aircraft.

1.2. State of the Art

Historically, critical behavior of aircraft at the edges of the flight envelope was recognized early as a challenging problem that requires in-depth physical study. Approaching the flight envelope edge was associated with buffeting, a structural vibration occurring due to aerodynamic loads.

Early works, e.g. by Abdrashitov [15], described conditions such as tail buffet, a vibration due to unsteady aerodynamic loads imposed on the tail, and observed undesirable and unintended motion and vibration. Mabey [85] provided an overview over various unsteady flow phenom-

ena arising from separation at off-design conditions, and described the associated dangers. He described buffeting as structural vibration of airframe parts in response to aerodynamic excitation, which may have catastrophic consequences.

National Aeronautics and Space Administration (NASA)'s Aviation Safety and Security Program [134] recognized the lack of aerodynamic data for aircraft behavior outside the envelope and undertook computational and wind tunnel studies aiming at reducing the accident rate in civilian air traffic.

1.2.1. Aircraft Stall Research

Aside from the aforementioned safety and efficiency considerations in the civil world, military aircraft designers have long focused on stall research due to their inherent demands on manouevrability. Combat aircraft spend a larger proportion of their times in conditions far from straight and level cruise, with high angles of attack or sideslip encountered on a regular basis. Woodson et al. [175] investigated the abrupt wing stall phenomenon observed on several fighter aircraft such as F/A-18E during its development, highlighting the necessity for time-accurate numerical simulations capable of resolving the relevant turbulence scales. The reliance of many modern combat aircraft on vortex-induced lift places great importance on the behavior of the longitudinal vortices generated at the wing leading edge. Morton et al. [98] analyzed the breakdown of such vortices and the loads generated by that process. As an example tackling specific flight mechanical phenomena, Forsythe et al. [39] undertook scale-resolved computations to gain insight into the spin characteristics of an F-15E at angles of attack up to $\alpha = 65°$.

High angle of attack flight research for civil applications has mostly focused on high lift applications, i.e. aircraft in landing configurations with deployed high lift devices. Such configurations are geometrically complex and difficult to replicate in CFD, but efficiency goals made research in this direction worthwhile. However, high lift system design focuses on maximum performance and efficiency, aiming to keep the extent of separation from becoming excessive. The complexity of such flows still presents a significant challenge for contemporary CFD, as underlined by the results of large scale collaborative undertakings such as the AIAA High Lift Prediction Workshop [123]. Recent research projects like High lift INflight VAlidation (HINVA) [121] aimed at understanding the flow physics in stall using both cruise and high lift versions of actual aircraft, in that case the Advanced Technology Research Aircraft (ATRA).

Wake Interaction and Tail Buffet

The latter project involved studies of the interaction between the wake and tail of an airliner [121]. Abdrashitov's [15] definition of tail buffet as a "vibration of the tailplane under the aerodynamic action of the wake" succinctly describes the early researchers' recognition of the dangers associated with aircraft stall and wake/tail interaction.

Havas and Jenaro Rabadan [50] describe how aircraft manufacturers concern themselves with tailplane buffet, as regulations [13] require the demonstration of aircraft behavior above $C_{L,max}$. They expressed the desire of obtaining models for global forces and moments based on unsteady pressure measurements. In a similar vein, Whitney et al. [172] employed unsteady CFD to estimate asymmetric tailplane loads that had been encountered in flight tests.

Farokhi et al. [38] researched ways to use measured dynamic pressure data from wind tunnel tests as inputs to finite element models in order to study structure dynamics.

As above, published research on tail loads often focuses on military applications due to specific features involved in high angle of attack flows on highly swept wings. Off-body vortical flow structures emanating from geometry elements such as leading edge root extensions may impinge on vertical tails, or impart stochastic loads if they burst upstream. In contrast with civil applications, this has been an area of active research for a longer time due to higher probability of occurrence of such interactions and the necessity to alleviate problems arising associated with structural loads. Zimmerman et al. [181] provided an account of such issues during the development of the F-18C aircraft and other instances of incidents related to tail buffet. Lee [74] surveyed the efforts undertaken to understand the interplay between leading edge vortices and structural loads on the vertical tails common on contemporary combat aircraft.

Subsonic Stall

Stall can be characterized according to the Mach number region it occurs at, as it drastically influences the mechanism causing the flow separation. Subsonic stall on an airfoil or wing typically occurs at high angles of attack, when the wing's ability to generate lift is suddenly or gradually impaired. These processes and the types of separation have been extensively researched, with e.g. McCullough and Gault [89] providing overviews over the types of separation on an airfoil. Smith [139] provided a comprehensive survey over the conditions leading to separation. In the context of a wing, local variation of inflow and geometry can cause separation to occur on different sections of the wing. The location of flow separation, and the flight conditions it occurs at, determine the stall characteristics of an aircraft. McVeigh and Kisielowski [90] described how straight wing aircraft approach stall, concluding that it is largely possible to design this type of aircraft with sufficiently benign stall characteristics. With the increase in speed from early subsonic aircraft to transonic airliners, wing sweep has increased as well. Mabey [85] noted that stall behavior strongly depends on wing sweep, assigning a "difficulty" to the prediction of the phenomena as a function of sweep. Harper and Maki [48] described the efforts undertaken to understand swept wing aircraft stall characteristics and the challenges posed by such configurations, such as their relatively low maximum lift and nonlinear pitching moment behavior. They also provided a general overview of swept wing stall characteristics. Polhamus [105] presented a comprehensive study of the effects of leading edge radius and sweep on flow separation and the wing's behavior in terms of post stall loads. More recently, Luckring [80] showed which factors influence leading edge separation from swept wings.

In accordance with Mabey's concept of difficulty of analysis associated with different wing sweeps, much of the past reseach focuses on the two comparatively benign extremes of the wing sweep range, i.e. straight wings and highly swept slender delta-type planforms. Much of the more detailed flow dynamics research on post-stall and the wake has largely taken place in the context of extruded airfoils, partly due to difficulty of conducting experiments on full scale aircraft. Compared to the military high angle of attack research mentioned above, published simulation studies of civil-type geometries in cruise configuration at such conditions have been far fewer in number. High angle of attack flows around commercial configurations with deployed flaps have garnered some research interest, as underlined by large undertakings such as the aforementioned series of High Lift Prediction Workshops. Escobar et al. [36]

investigated the DLR F-11 high lift aircraft configuration using hybrid RANS/LES methods, highlighting the general difficulty associated with accurate prediction of flow quantities. In recent editions, high lift aircraft configurations such as JAXA's Standard Model (JSM) or the High Lift Common Research Model were studied [123], with the TAU solver used in the present work being employed by Rudnik et al. [122] for these cases. More recently, Yang et al. [177] published a comparable study involving the same Common Research Model cruise configuration that the present work is based on, similarly concluding the necessity of appropriate resolution of turbulent separation for robust force and moment prediction in post stall. Studies specifically focussing on computational analysis of both three-dimensional separation and wake propagation are not known at the time of writing.

Transonic Stall

Although the present work exclusively focuses on the phenomena associated with subsonic flows, the corresponding phenomenon in the transonic Mach number range is relevant for a complete picture. As in the subsonic regime, transonic airfoils experience separation at excessive angles of attack. However, the associated α values are typically significantly lower than for the corresponding subsonic condition. Transonic flow over a wing or airfoil typically involves the presence of a shock on the suction side, which grows in strength at higher speeds or during maneuvering. This can cause separation and excite oscillation of the shock itself, a phenomenon known as transonic buffet whose physics were described by Lee [73].

The complexity of the flow phenomena increases when practical transonic aircraft geometries are involved, i.e. including a sweep angle and spanwise variations of incidence, chord and airfoil shape. Several recent publications highlight the profoundly different nature of three-dimensional buffet in comparison to the two-dimensional airfoil flows described above. Iovnovich et al. [62] investigated the isolated influence of the sweep angle on the buffet behavior and established that the buffet mechanism switches from a mainly chordwise motion to a spanwise one when a certain sweep angle is exceeded. Dandois [31] performed an experimental study of a wing-fuselage configuration with an elastic wing. He suggested that buffet on a swept wing is connected to a spanwise movement of spatially limited buffet cells toward the wingtip. Koike [67] and Sugioka et al. [148] experimentally confirmed the existence of such buffet cells using JAXA's small-scale CRM wind tunnel model and investigated the behavior of the phenomena over a wider angle of attack range. Crouch et al. [30] performed a global stability analysis based on URANS simulations of swept and unswept wings and suggested that buffet on swept wings is associated with a global flow instability, but with a different primary instability mode than on two-dimensional or unswept wings.

In terms of computational studies of representative geometries, Sartor et al. [125] investigated transonic aircraft configurations with shock-induced separation using CFD. Ohmichi et al. [101] characterized the shock fluctuation on the wing using modal decomposition. Illi [61] [128] carried out computational analysis of buffet-induced wake flows using novel hybrid RANS/LES methods. He determined turbulence characteristics and spectral properties in the separated flow, and demonstrated the TAU solver's capability for aircraft wake propagation simulation.

High Reynolds Number Research

Although the growth of flight velocity and aircraft size stagnated in recent decades, the combination of high transonic speeds and large physical dimensions of modern long-range aircraft translates to a high Reynolds number $Re = u_\infty L/\nu$, with a flight velocity u_∞, a characteristic dimension L and the kinematic viscosity of the fluid ν. This dimensionless number represents the ratio of inertial and viscous forces in a fluid flow. For a given geometry and inflow Mach number, Re determines the boundary layer state and the transition location. It has an effect on the occurrence and the characteristics of separation, making it an important parameter for this type of research.

Much of the basic research on stall exists for low Reynolds numbers, as these are much more easily achievable in experimental facilities. The necessity to conduct research at appropriately elevated Reynolds numbers on the order of 10^7 and above spawned the construction of cryogenic, pressurized wind tunnels. While generating a high Reynolds number flow is possible via increasing flow velocity at atmospheric conditions, this simultaneously increases the Mach number and the aerodynamic loads on the model due to the increased dynamic pressure q. Replicating high speed atmospheric flight at realistic conditions requires decoupling of Re and M, which is accomplished via separate control of wind tunnel pressure and temperature. Such decoupling enables control of Re, M and q as wind tunnel operating parameters. Fixing one of them permits an operating envelope where the other two parameters can be varied independently from each other. Effects of Reynolds number, Mach number and aerodynamic loads can be isolated. For instance, Reynolds number effects can be studied without the aerodynamic loads altering the model shape, as the ratio of dynamic pressure and the model's elasticity modulus E can be kept constant.

Testing at flight Reynolds numbers permits obtaining high fidelity results for representative configurations. The aerodynamics community established cooperative and comparative studies such as the Drag Prediction Workshop (DPW) [77] working on generic aircraft configurations such as the DLR F6 [120] or the CRM developed by Vassberg et al. [160]. This approach enabled the research community to hone the predictive capabilities of CFD using representative configurations for steady flows. The DPW series focused on near-design conditions and showed that a reasonable degree of quantititative accuracy can be achieved in the linear lift region. However, these studies using representative geometries typically do not focus upon unsteady and separated flow regimes. One of the few such cases was the ESWI$^{\mathrm{RP}}$ project [84] which focussed on improving wind tunnel capabilities and high Reynolds number research using representative aircraft configurations. Parts of the associated wind tunnel campaigns were dedicated to stall studies at high Re.

1.2.2. Computational Methods in Edge of Envelope Research

Sophisticated wind tunnels can provide precise data at realistic flight conditions, but they are associated with considerable expense. Similarly, flight testing of actual aircraft at potentially dangerous conditions at the edges of the flight envelope poses a high risk. These considerations drive efforts to enable computational analysis of off-design conditions.

Flow dynamics at stall are often characterized by high levels of turbulent fluctuations and are inherently unsteady. Hence, conventional steady-state RANS approaches are typically unable to replicate these processes. While Direct Numerical Simulation (DNS) can provide

useful insights into the precise mechanics of flow separation in simple cases such as airfoil flows [117], the required extreme computational effort precludes their use for all but the simplest cases. Similarly, the high Reynolds numbers also pose problems for wall-resolved Large Eddy Simulation (LES) methods due to near-body resolution requirements. Spalart [140] estimated that LES computations of full wings would not be feasible in an engineering context until 2045. Choi and Moin [28] provided estimates for the expense of such calculations in terms of required grid points N, estimating $N \sim Re^{13/7}$ for LES and $N \sim Re^{37/14}$ for DNS.

Hybrid methods such as Scale Adaptive Simulation (SAS) [92] and Detached Eddy Simulation (DES) [143] emerged as feasible computational approaches for cases involving high Reynolds numbers and large scale off-body unsteadiness. DES combines the application of Reynolds Averaged Navier Stokes (RANS) in attached boundary layer regions where the LES resolution requirements would make its use expensive, while retaining the latter's ability to resolve turbulent fluctuations away from the near-wall regions involving small scale turbulence. This has enabled studies of unsteady wake flows [147] and the method has remained popular since, being used for cases like rocket afterbodies [102], engine nozzle jet flows [162] or wingtip wakes [114]. Concurrently, Unsteady RANS (URANS) has been used with partial success for unsteady wake flows and post stall cases [41]. The hybrid methods' capability to resolve more of the turbulent flow has resulted in their popularity in this type of research, underlined by the fact that many of the computational studies referred to earlier in this section relied on DES [39] [166] [84] [125].

The popularity of DES-type hybrid methods has remained high in recent years, and much effort is ongoing with the aim to improve their physical accuracy and reliability. International research efforts like Go4Hybrid [95] are examples of these efforts. The idea of DES has been incorporated into various models aiming to counter specific weaknesses of the original approach, such as erroneous prediction of smooth surface separation or delayed appearance of resolved turbulence. For example, Improved Delayed Detached Eddy Simulation (IDDES) by Shur et al. [135] may enable more rapid generation of turbulence than in the original formulation, while methods described by Probst et al. [111] involve locally targeted introduction of resolved fluctuations. Probst et al. [110] also presented an approach involving algebraic sensors for boundary layer state detection. Deck [32] described a zonal approach, enabling the user to prescribe the boundaries between RANS and LES regions.

Concerning application of hybrid methods to wing and airfoil stall, there is significant overlap with the dynamic stall community studying intermittent high angle of attack stall phenomena occurring on the retreating blade of a helicopter rotor. Stall phenomena and large scale separation require accurate spatial and temporal resolution of the unsteady turbulent flow around a blade section, necessitating high fidelity modeling. Hybrid approaches and the mitigation of their inherent issues have received attention in that field. Recent publications by authors such as Jain et al. [63], Letzgus et al. [76] or Visbal and Garmann [163] provide an overview of the level of detail involved in such studies. Despite some parallels in the flow mechanisms, the varying angle of attack associated with dynamic stall conditions introduces fundamental differences like hysteresis compared to static stall phenomena. Comparison of such effects is out of the scope of the present work, which focuses exclusively on static aircraft stall.

Despite the progress, full aircraft simulation has remained expensive and cumbersome, restricting these applications to the research domain. Such simulations often have the character of flagship projects which sometimes yield good results for specific problems with single point validation. The provision of validation data for complex cases is difficult and expensive. Re-

cent research efforts, e.g. the ComFliTe [71] project, aimed specifically at improving the predictive capabilities of computational methods with a view to computational flight testing. That work involved concerted measurement and simulation efforts in order to understand the physics, and by extension, the strength and weaknesses of different computational methods. Similarly, HINVA [121] aimed to improve the prediction performance of CFD for high lift configurations, which involved taking into account the wake of the ATRA research aircraft. Works associated with the ESWI^{RP} project [166] [84] also aimed at better understanding and specific validation of hybrid methods for airliner stall conditions.

1.3. Objectives

The discussion of the state of the art above leads to the conclusion that gaps exist in the understanding of massively separated flows of swept wing airliners at the flight envelope boundaries and at flight-representative Reynolds numbers. Appropriate computational methods do exist, but few systematic studies on their relative merits and drawbacks in the context of such flows are known to date. This thesis shall attempt to close some of these gaps in knowledge. The associated questions and goals are:

- Identification of appropriate CFD methods and settings that yield accurate results for low speed stall conditions. Determination of when and why Unsteady Reynolds Averaged Navier Stokes (URANS) methods can be used and in which areas they fall short, necessitating hybrid methods.
- Specific validation of the different approaches via the available experimental data and identification of the main influencing factors for the comparability of experimental and computational results.
- General characterization of the flow physics in the massively separated wake of a transport aircraft at low speed stall.
- Improved understanding of the propagation and transport of turbulence in such separated wake flows.
- Characterization of the interaction of the wake with the tailplane and the dependence of such phenomena on inflow conditions, i.e. α and Re.
- Characterization of the aerodynamic loads acting on the wing and tailplane, and improved understanding of their relationship with the turbulent wake flow phenomena.

1.4. Outline

The following chapters provide an overview over the flow physics encountered at the conditions focused on in this work. Chapter 2 describes the different canonical phenomena contributing to the formation and propagation of the wake. Chapter 3 includes the description of the employed methodology, the solver and computational models as well as the analysis methods used for the interpretation of the wake phenomena.

Background information on the origin of the validation data, as well as on the choice of flow conditions, are given in Chapter 4. The simulation approach and model choice, and specific validation of aircraft wake flow in low speed stall are shown in Chapter 5. Chapter 6 forms

the bulk of the thesis, including the results of low speed stall simulations.

CHAPTER 2

Theory and Physics

This chapter provides an overview over the fluid dynamics phenomena encountered by aircraft in post stall. The physics are discussed using simplified canonical flow configurations at appropriately representative conditions. The origin of several of these phenomena are described, along with their implications for the resulting wake flow.

2.1. Stall and its Consequences for Airliners

Steady inflow at moderate angle of attack α involves a linear relationship between α and the coefficient of lift C_L. Wing or airfoil stall is a condition at which a lifting surface suffers a partial loss of lift, i.e. a situation in which C_L ceases to increase after having reached its maximum value $C_{L,max}$. This typically occurs at values of α which are excessive for a given flight Mach number M_∞. The deviation of the C_L-α polar from the linear shape begins well below this angle of attack $\alpha(C_{L,max})$ due to incipient flow separation.

Stall

Subsonic, or *low speed stall*, is usually associated with high angles of attack at low flight Mach numbers. The separation mechanism is termed pressure-induced, as the airfoil pressure distribution and the involved pressure gradients at increasing α cause the flow to separate from the surface. Transonic, or *high speed stall*, occurs at higher flight Mach numbers when parts of the flow are locally supersonic. The supersonic region ends with a normal shock, which creates a strong adverse local pressure gradient. Further increasing shock strength at higher α causes this pressure gradient to grow on the suction side surface, which may also lead to separation. This phenomenon is therefore described as shock-induced separation. While subsonic stall occurs at relatively high values of α, transonic flow requires comparatively small α increases to separate.

The modeling of such flight conditions for an aircraft is difficult due to the nonlinear relation between α and the aerodynamic forces, and to the coupling between the force and moment components described by Teng et al. [150]. The strong nonlinearity means that such conditions are not necessarily stable. Asymmetry between the two wings, be it caused by random turbulence, environmental effects or flight conditions at stall entry, may lead to additional rolling moments. The interplay between these effects is difficult to model, and flight test data is scarce due to the inherent danger of such testing. Furthermore, the nonlinear effects can be strongly influenced by configuration details such as engine position or high lift devices, which restricts the applicability of data obtained for a given configuration. This lack of data precludes the creation of more advanced post stall flight models caused by limited validation possibilities.

Geometry and Pitch Behavior

The aforementioned contemporary airliner configurations are typically based on a backward swept wing and vertical and horizontal tailplanes (VTP and HTP) mounted at the aft end of the fuselage. Depending on flight condition and center of gravity (CG) location, the horizontal tailplane provides a balancing positive or negative force in order to counteract the pitching moment caused by the wing. What is more, the elevator responsible for pitch control is mounted to the horizontal stabilizer. The stabilizer is itself a backward swept wing. Its lift is therefore a function of its shape, the inflow velocity vector and the resulting angle of attack. The view from above in Fig. 2.1 demonstrates how the wing is positioned upstream from the tailplane.

Fig. 2.1.: Top view of an A350−900, from [1].

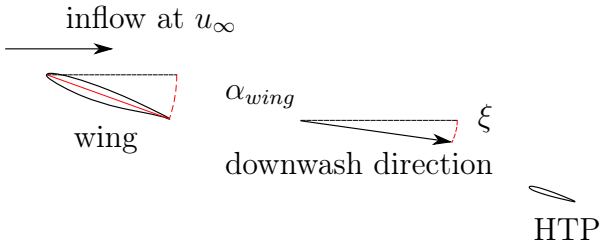

Fig. 2.2.: Section through a wing and tail configuration at high α.

Conceptually, the aircraft can be treated as a tandem wing system in the inboard region. The angle of attack α of the aircraft is defined as the angle between the freestream inflow velocity and the aircraft coordinate system, which is typically aligned with the fuselage axis. The wing experiences largely undisturbed inflow, with its angle of attack α_{wing} roughly equal to the aircraft's α. In accordance with Newton's third law, the wing generates upward lift force by imparting downward momentum on the surrounding flow, creating downwash. Generally, the magnitude of downwash is a function of the lift generated by the corresponding local wing section. This flow deflection caused by the wing with respect to the aircraft inflow is termed ξ and visualized in Fig. 2.2. The tailplane is positioned at a given indicence i_{HTP} in relation to the fuselage. Its effective angle of attack is diminished by ξ, i.e.

$$\alpha_{HTP,eff} = \alpha + \xi + i_{HTP} \qquad \xi = tan^{-1}(w/u) \tag{2.1}$$

As ξ is negative when the wing lift is positive, this leads to $\alpha_{HTP,eff} < \alpha$. Both $\alpha_{HTP,eff}$ and ξ vary with spanwise position. The decreased HTP angle of attack helps the tailplane to remain effective as a stabilizer surface and to provide sufficient pitch control authority to the pilot. Typical airliner tail designs ensure that the wing wake passes well below the tailplane in normal operation, avoiding direct impingement of turbulent flow on the tailplane.

Massive flow separation causes an unsteady wake flow that may interact with the tailplane and impart unsteady aerodynamic loads on its structure, as described by Havas and Jenaro Rabadan [50]. These unsteady interactions may cause exceedance of dynamic or fatigue loads on the aircraft tail. In terms of flight mechanics, Teng et al. [150] described the interaction between wing wake and the horizontal tail for different configurations. Fig. 2.3 shows the longitudinal stability characteristics of aircraft conventional tail, i.e. the HTP mounted to the fuselage. The position of the wing wake relative to the tail strongly influences the amount of stabilizing pitching moment C_M the tail contributes. Normal operation takes place in the linear region of the $C_M(\alpha)$ polar, at angles of attack lower than at point 1. Typical airliner configurations involve a center of pressure of the wing aft of the center of gravity, which necessitates downforce at the tailplane. The pitch break, i.e. the angle of attack at which C_M departs from a linear shape, coincides with the angle of attack at which the tail becomes immersed in the wing wake denoted by the red lines.

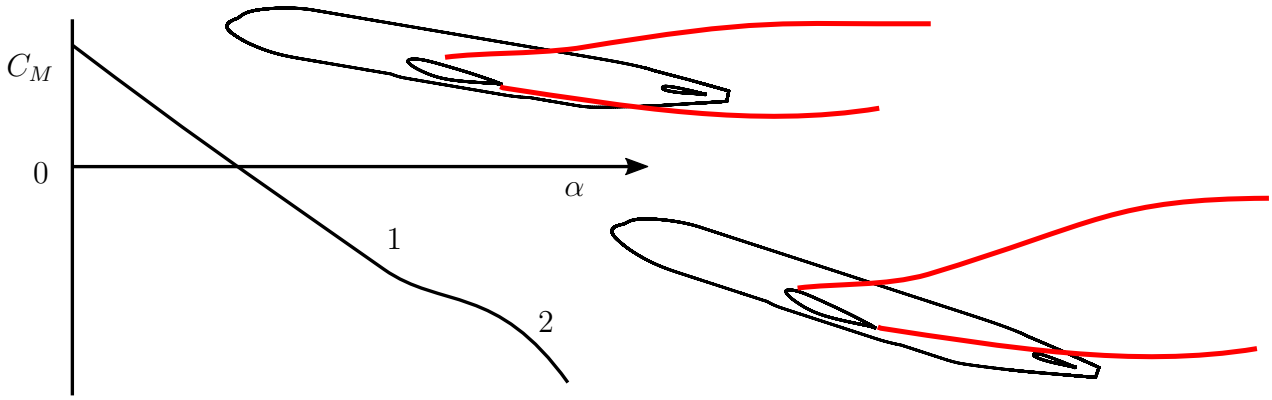

Fig. 2.3.: Stalled aircraft wake at two angles of attack and the corresponding pitching moment, adapted from Teng. [150]. Red lines represent wake edges. Point 1 is at pitch break, point 2 is in post stall.

The aircraft's design is intended to ensure longitudinal stability, with the positive lift at the tailplane providing sufficient nose-down pitching moment, i.e. negative C_M. The tailplane's ability to provide lift and thereby contribute to nose-down pitching moment is impeded if it is immersed in the wing wake. The tailplane can re-emerge from the wake into undisturbed flow at still higher α, as shown at point 2.

The configuration in Fig. 2.3 is hypothetical, and the situation depends on the actual aircraft geometry and flight conditions. In effect, the pitching moment is the result of a complex interrelation between angle of wing downwash, the degree to which the tail is immersed in the wing wake, and the tailplane aerodynamics. Havas and Jenaro Rabadan [50] described conditions in which the tailplane itself may reach such a significant angle of attack $\alpha_{HTP,eff}$

that it exceeds its stall and experiences flow separation. Such effects are inherently nonlinear and possibly unsteady. Therefore, the relevant questions to be answered in a stall situation are:

- What is the downwash angle of the wing and the effective angle of attack of the HTP?
- What is the size and extent of the separated wing wake?
- Is the tailplane immersed in the wake or does it experience smooth inflow?
- Is the tailplane flow separated, even if the inflow is smooth?
- If the tailplane is immersed in the wake, what are the characteristics of the imparted unsteady loads?

The understanding and prediction of the interactions between flow separation, wake flow and tail loads are the main focus of the present work.

2.2. Airfoil Stall, Separation and Wake

Although swept wing aircraft involve significant three-dimensional flow effects, many of the subsonic stall phenomena can be understood by study of two-dimensional flow phenomena. A large body of research on airfoil aerodynamics exists for this reason. While classical thin airfoil theory permits analytical analysis of attached flow conditions at low to moderate angles of attack employing vortex sheet representations from potential theory [17], the airfoil behavior in presence of separation is more complex in nature. Airfoil geometry features such as thickness, camber and leading edge radius determine its aerodynamic characteristics. An airfoil of a given shape can experience a multitude of flow conditions depending on M_∞, Re_∞ and α, potentially causing different types of stall. Chapter 2.2 provides an overview of stall phenomena under the assumption of incompressible, i.e. subsonic, flows.

2.2.1. Stall Types

Much of the historical research was carried out at Reynolds numbers below those of modern airliner configurations. Low Reynolds number boundary layers are initially laminar and the transition to turbulence is a significant part of their analysis. The transition behavior also influences the separation characteristics, involving phenomena such as laminar separation bubbles. While these phenomena are of lesser importance in high Reynolds number flows that constitute the focus of this work, the fundamental background is nevertheless a useful starting point. Stall behavior is the study of the phenomena taking place when the angle of attack reaches levels when first local separation phenomena occur, and how they develop when α is increased further. Typical classifications of the stall phenomenon focus on the location of separation. McCullough and Gault [89] identified three distinct types, depending on flow condition and geometric airfoil properties:

- **thin airfoil stall** (left in Fig. 2.4a) with a laminar separation bubble near the leading edge with subsequent reattachment. The bubble expands rearward at increasing α.
- **leading edge stall** (center in Fig. 2.4a) occurring at the leading edge. This state may or may not involve subsequent reattachment.

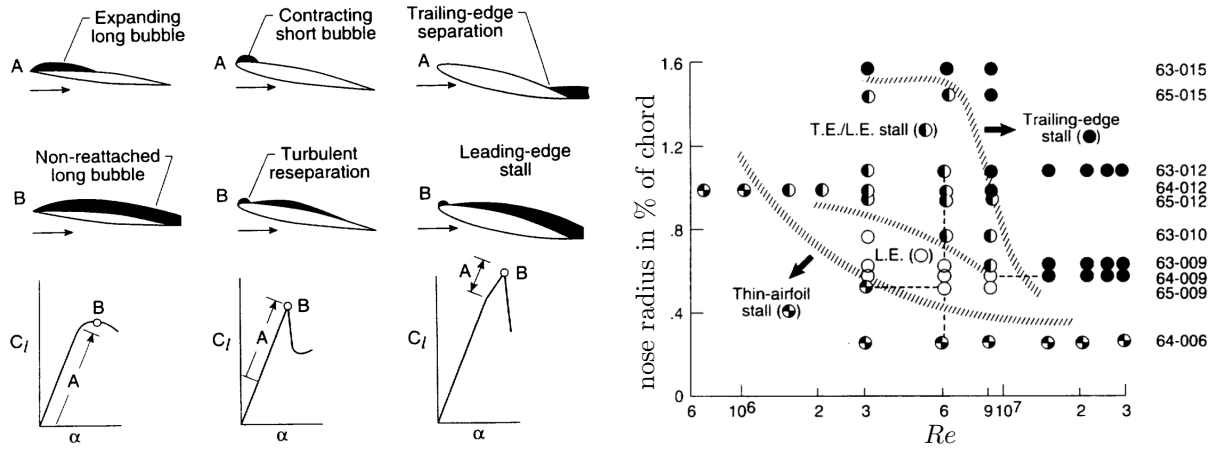

(a) Stall topologies

(b) Effect of nose radius r/c and Re for a set of NACA 6-digit airfoil series. Airfoil numbers shown on the right.

Fig. 2.4.: The classification of airfoil separation, from Polhamus [105].

- **trailing edge stall** (right in Fig. 2.4a) with the initially attached suction side flow unable to overcome a pressure gradient and separating near the rear part of the airfoil. The separation point moves forward at increasing α.

They concede that these types are not necessarily mutually exclusive and may occur in combination, for instance the trailing-edge/leading-edge stall. The different types of stall topology ultimately determine the shape of the polar, as shown in the lower part of Fig. 2.4a. These polars indicate that the location of incipient separation and the nature of the expansion of the separated area plays a large role for the stall behavior of an airfoil or wing at a given flow condition. For instance, sudden expansion of the separation bubble in the case of leading edge stall causes a sudden loss of lift (center in Fig. 2.4a), whereas a decreased lift gradient as in the region denoted with A in the polar denoting trailing edge stall (right in Fig. 2.4a) may be considered more benign.

High Reynolds number airfoil flows typically do not involve separation bubbles like in the left and middle cases in Fig. 2.4a. Due to earlier transition at high Reynolds numbers, any laminar separation bubble may become very short or disappear altogether. Polhamus [105] argues in his summary of airfoil stall research that the middle regime of Fig. 2.4a, leading edge stall, possibly disappears at very high Re. Fig. 2.4b provides an overview of the effect of Reynods number on the separation characteristics within a single airfoil family. The preference for trailing edge stall is a consequence of the ability of a turbulent boundary layer to withstand higher adverse pressure gradients than a laminar one. If a sufficiently high Reynolds number moves the transition point upstream and causes it to occur ahead of the theoretical laminar separation location, leading edge separation is less likely to take place. At extreme angles of attack, separation can move upstream by such a distance that flow separates over the entire surface, at which point the distinction becomes irrelevant.

Massive Separation and Bluff Body Flow Topology

The separated wake of a fully stalled airfoil is in many respects akin to a bluff body wake. A bluff body type flow can be generated by various types of bodies at appropriate flow conditions. Craze [29] and Roshko [119] described the concept of *bluffness*, which is a body's

property to diverge the incoming streamlines, to create a wake, and to generate significant drag. The divergence of the mean streamlines around a body of arbitrary shape is indicated in Fig. 2.5. Such topology is typical for symmetric flows, i.e. around a cylinder. With the exception of very low flow velocities and Reynolds numbers, the sketched streamlines can usually only be observed as a time average. At meaningful flow velocities this flow topology becomes unstable and unsteady. Turbulence and unsteadiness may be significant at larger Re and need to be taken into account.

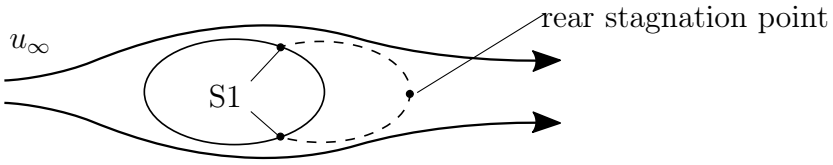

Fig. 2.5.: Mean streamlines around a bluff body, adapted from Hucho [59]. Dashed line denotes the mean boundary of the backflow region. S1 denotes the separation points.

In Fig. 2.5, the mean streamlines do not follow the the body contour and separate from the surface at the points S1. These time averaged outer streamlines follow a different contour and converge downstream of the body in a rear mean stagnation point [29].

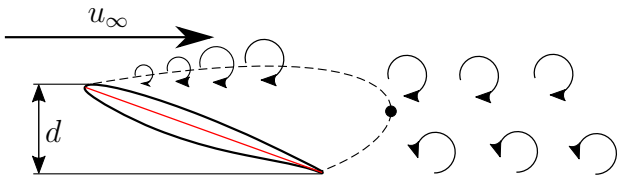

Fig. 2.6.: Flow topology around a stalled airfoil without reattachment. Dashed line denotes the mean boundary of the backflow region, the black circular dot is the position of the rear stagnation point.

Any shape can exhibit bluff body behavior at appropriate inflow conditions. For instance, Yarusevych and Boutilier [178] and Huang and Lin [58] observed that wake flows of stalled airfoils without reattachment behave similarly to bluff body wakes as described by Roshko [119]. The topology of a massively separated flow around an airfoil in post stall is sketched in Fig. 2.6. The dashed line indicating the region of zero streamwise velocity corresponds to the line departing from the surface at S1 in Fig. 2.5. The inflow streamlines initially diverge upward and away from the surface, before converging toward a rear stagnation point at the downstream end of the recirculation area. An airfoil at nonzero incidence does not have a symmetry axis parallel to the inflow, which results in an asymmetric flow topology.

The salient features of such a flow are shear layers emanating from the separation location and at the boundaries of the wake, as well as the general wake unsteadiness. The latter may occur as a random turbulent fluctuation or a quasi-periodic large scale motion, or any combination thereof. The periodic motion is of particular interest and occurs in the shape of alternating vortex shedding, as indicated in Fig. 2.6. The shear layer is a phenomenon associated with

local instabilities, while the vortex shedding has been described as a feature resulting from global instability [176]. All these mechanisms introduce their own characteristic frequencies, and it is their interplay that determines the behavior of the resulting wake. Proper simulation of stalled airfoil flow requires appropriate resolution all of these phenomena.

2.2.2. The Shear Layer and Kelvin-Helmholtz Instability

The canonical shear layer[1] is a ubiquitous flow configuration present in many engineering flows, which has resulted in a very large body of literature focused on its characteristics. In its simplest form, a mixing layer occurs at the location of contact between two initially separated, parallel flows with different velocities U_1 and U_2. For a stalled airfoil, the leading edge shear layer occurs at the dashed line separating the outer flow and the recirculation downstream of the leading edge in Fig. 2.6, with the outer fluid moving at U_1 and the recirculating flow at U_2. A seminal work, exhaustively describing the behavior of this type of flows, was provided by Huerre and Rossi [60].

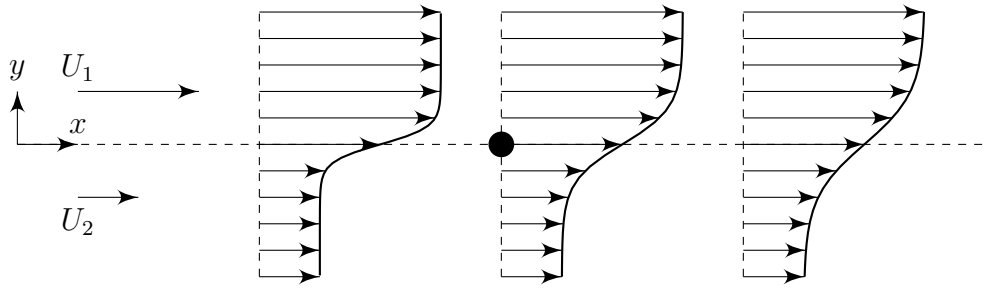

Fig. 2.7.: Shear layer with parallel flows U_1 and U_2.

Fig. 2.7 is a sketch of a shear layer with parallel streams in x direction and $U_1 > U_2$. In the present work, only differences of velocity will be taken into account, without considering density, temperature or concentration gradients. Beginning at the point of initial contact, transverse velocity gradients of streamwise velocity $\partial u/\partial y$ occur due to viscous diffusion of the fluid. The flow is therefore dominated by spanwise vorticity ω_z, whose maximum at each streamwise position occurs at the inflection point of the transverse velocity profile. The shear layer can be characterized by the shear magnitude $\Delta U = U_1 - U_2$ or the velocity ratio R:

$$R = \frac{U_1 - U_2}{U_1 + U_2} \tag{2.2}$$

R in Eq. 2.2 remains between 0 and 1 if both flow velocities are positive. The recirculation regions encountered in massive separation situations result in counterflow mixing layer with a negative value of U_2.

Linear stability theory predicts that the presence of an inflection point in the vertical profile of the mean velocity is a necessary condition for instability in inviscid flows [55, 60]. According to Huerre and Rossi, a shear layer initially undergoes viscous diffusion processes before the appearance of vortex roll-up, with the latter being an essentially inviscid phenomenon. The roll-up concentrates the initially distributed vorticity into eddy structures.

[1]The terms "mixing layer" and "shear layer" are used interchangeably in this work.

These Kelvin-Helmholtz vortices merge and undergo pairing processes while increasing in size proportionally to ΔU [60], becoming a nonlinear instability phenomenon. The vortex merging causes a spreading of the shear layer and a decrease of the velocity gradient, as visualized in Fig. 2.7. The spreading is quantified using the shear layer thickness, which can be defined as a vorticity thickness

$$\delta_\omega = \frac{U_1 - U_2}{\max\left(\partial U \partial / y\right)} \tag{2.3}$$

at each streamwise location using the local maximum of the velocity gradient.

A turbulent shear layer grows approximately linearly. The spreading rate of a shear layer, i.e. the increase of the thickness with streamwise distance x, typically increases with R [55]. In a turbulent shear layer, the spreading rate becomes linear over x due to the randomness of the vortex pairing locations [26, 55]. Monkewitz and Huerre [97] described characteristic frequencies of the vortex roll-up processes using linear stability theory and deduced a "most amplified frequency", which is characteristic for a given shear layer and depends on its thickness. Similarly, Ho and Huang [54] determined that the mixing layer dynamics are governed by a frequency which represents the passage frequency of the coherent structures. Based on the vorticity thickness definition, the most amplified Strouhal number of these Kelvin-Helmholtz instabilities is about $Sr_{\delta_\omega} \approx 0.135$, based on vorticity thickness and mean velocity $\overline{U} = 0.5(U_1 + U_2)$. Ho and Huerre [55] give a similar Strouhal number based on another quantity, the momentum thickness δ_Θ. According to them, the most amplified frequency occurs at $Sr_{\delta_\Theta} = 0.032$, or higher if the shear layer is turbulent from the beginning.

Strictly speaking, these quantities have been derived for simple shear layers and parallel flows. There is some evidence of this Strouhal number being reproducible in computational studies of cylinder base flows [102] or airfoils [114]. However, Dong et al. [126] observed for a circular cylinder that the large scale fluctuations downstream influence the shear layer instability, causing a variation of the most unstable frequency. Wu et al. [176] confirmed that an unforced airfoil leading edge shear layer has a variable most unstable frequency as well. In accordance with the inviscid nature of the phenomenon, the Reynolds number does not affect the dynamics in a significant way according to Ho and Huang [54]. Prasad and Williamson [109] cautioned that more complex configurations such as the shear layer bounding a bluff body wake do not necessarily scale in the same manner due to geometric constraints.

2.2.3. The Wake

Plane Wake Model

Independently of the precise mechanism of separation, the wake behind a body is a free shear flow which contains turbulent flow in its interior. Intermittency surfaces separate it from the surrounding ambient flow at any instant [156]. Fig. 2.8 provides an impression of this plane wake model with the mean flow confined to the x-y plane. By definition, plane wakes evolve slowly in streamwise direction compared to transverse direction [151]. The upper and lower boundaries, or intermittency surfaces, experience high shear and enhanced mixing. The similarity of the velocity profile in Fig. 2.8 to the shear layers discussed above shows that the wake boundaries can be expected to exhibit characteristics similar to shear layers. As

opposed to a pure shear layer, wakes contain vorticity of both signs. In a symmetrical wake like the pure plane wake in Fig. 2.8, the mean vorticity over the vertical extent is zero.

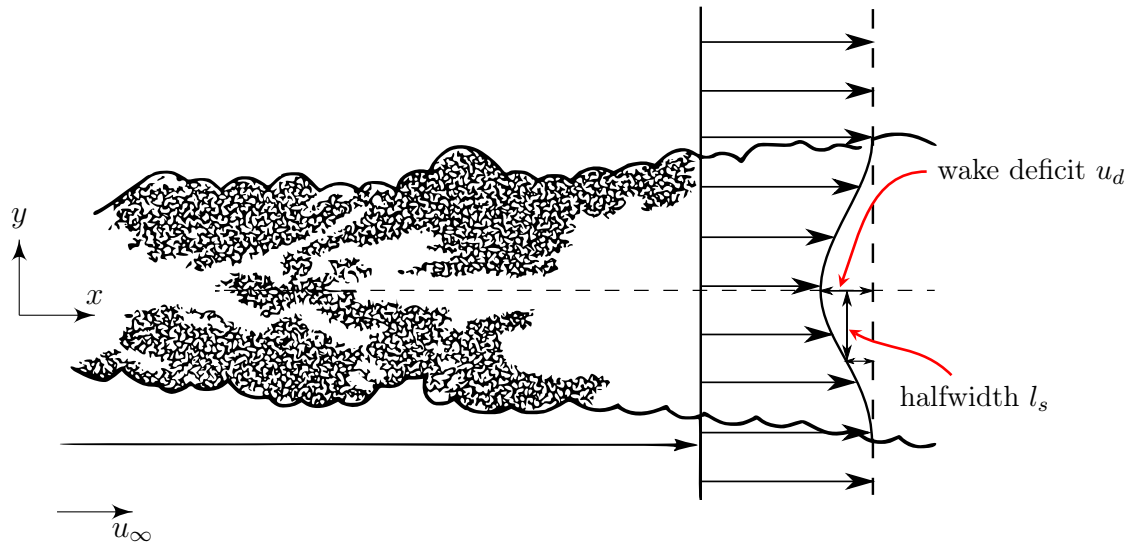

Fig. 2.8.: Turbulent plane wake with time-averaged velocity profile, adapted from Tennekes and Lumley [151].

Much of the theory on plane wakes focuses on circular cylinder wakes. This is a useful configuration and exhibit natural symmetry in transverse direction. According to Brown and Roshko [26] a plane wake can be decomposed in four characteristic zones at different streamwise distances, with the zone boundaries dependent on Re_∞:

- Near wake: direct interaction between flow and cylinder surface
- Mid wake: vortex shedding, but little influence of the wake on the cylinder surface
- Far wake and asymptotic wake: approximately self-similar behavior of the mean flow variables with varying degrees of universality

While this is conceptually a useful decomposition, distinguishing the vary far wake is of less significance for the direct interaction between the an aircraft's wing and tail surfaces due to the typically short distances between them. The wake vortices which persist over large distances in the wake of an aircraft are out of the scope of the present work.. Hucho [59] breaks down the wake into a near wake which encompasses the backflow region, and a far wake downstream of the rear stagnation point. This is a useful concept for the present case, as the very far downstream distances described by Brown and Roshko are not relevant in the context of aircraft tailplane interaction.

The plane wake model enables the definition of several quantities for wake analysis. Fig. 2.8 shows the wake deficit $u_d(x) = min_y(u(x)) - u_\infty$, describing the loss of momentum via the maximum loss of velocity at a coordinate x. The wake halfwidth $l_s(x)$ is a characteristic length scale, computed as the vertical distance between the centerline and the point where the velocity is $u_d/2$.

Stalled Airfoil Wake

The separated flow around a fully stalled airfoil is a combination of a leading edge shear layer and a separated wake downstream, as sketched in Fig. 2.6. In Huerre and Rossi's terminology, the shedding phenomenon is a prototypical hydrodynamic oscillator. Yarusevych et al. [178, 179] and Huang and Lin [58] discussed the behavior of airfoil separation characteristics at chord-based Reynolds numbers on the order of $\mathcal{O}(10^5)$. They likened the vortex shedding characteristics behind an airfoil to those of the von Kármán vortex street behind a circular cylinder, with the associated laminar, subcritical, transitional, and supercritical regimes established by Lienhard [6]. The vortex street phenomenon, consisting of alternating discrete vortices shed from the body and convected downstream, was observed by von Kármán [164]. He described the spatial arrangements of vortices that lead to stable propagation.

Most published research in the field focuses on low Reynolds numbers. At these conditions, the suction side boundary layer undergoes laminar separation, and the reattachment behavior is determined by the transition of the separated shear layer. At the flight-like Reynolds numbers this work is aimed at, the transition is expected to occur early along the body surface. At sufficiently high Reynolds number, separation nevertheless occurs. The reattachment of the flow, or the lack thereof, constitutes an important feature of the flow. High Reynolds numbers and airfoil angles of attack are indicative of turbulent boundary layer separation, placing the flow in the supercritical bluff body flow regime described by Huang and Lin [58] and Huang and Lee [57]. The representative velocity spectra from Huang and Lee in Fig. 2.9 show these fluctuation characteristics. They observe a large scale fluctuation in the wake due to action of the vortex street superimposed by significant broadband turbulent fluctuations. This is in contrast to high frequency narrowband fluctuation discovered in the laminar regime, as visualized in Fig. 2.9a. The overall fluctuation level of the spectrum is relatively low. The supercritical phenomenon is much more broadband, with a comparatively low frequency, high amplitude oscillation superimposed on top of the small scale turbulent motion. This frequency is typically associated with vortex shedding.

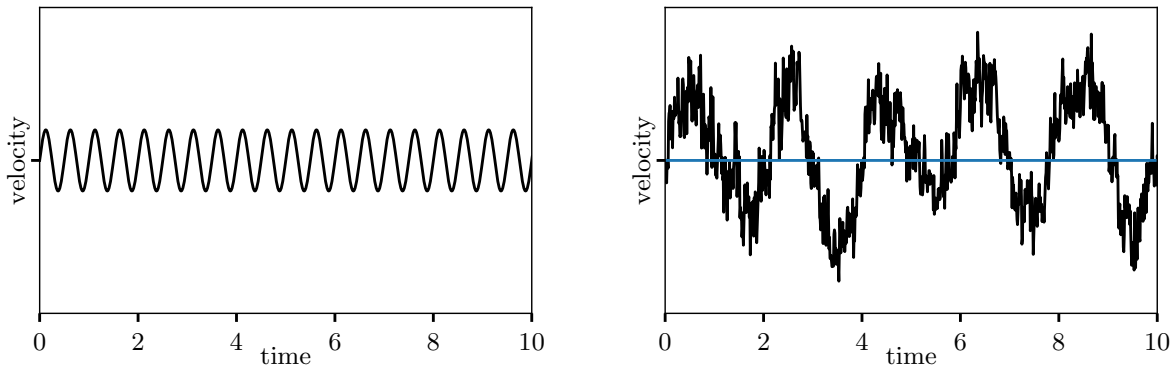

(a) Subcritical mode **(b)** Supercritical mode

Fig. 2.9.: Representative stall mode signals, analogous to hotwire signal representation from Huang and Lee [57].

The frequency of the alternating vortex shedding is typically nondimensionalized by the projection of the wake-generating body to a plane normal to the flow. This projected quantity d is indicated in Fig. 2.6. Vortex shedding occurs at a Strouhal number on the order of $\mathcal{O}(10^{-1})$. For cases where no reattachment occurs, Yarusevych and Boutilier [178] observed

only a weak variation of the Strouhal number with the Reynolds number Re_d, with multiple bluff body shapes and airfoils converging to a Strouhal number of $Sr_d \approx 0.2$. Schlichting and Gersten give a relation $Sr_d = 0.198\,(1 - 19.7/Re_d)$, which only weakly depends on Re_d at high values. According to Roshko [119], this behavior and the Strouhal number range is typical of bluff-body wakes, and was observed by other authors for similar configurations [100].

Despite these observations, the particular type and topology of vortex shedding are not necessarily the same in all situations. Meena et al. [44] provided a classification of vortex alternation and merging patterns at different flow conditions, and more studies of this type exist. However, Wu et al. [176] described the difficulties inherent in such classification attempts. For instance, a circular cylinder wake may have a well-defined Reynolds number range in which periodic vortex shedding with a vortex street occurs in the wake, permitting a dominant fluctuation frequency to be observed. An airfoil at stall is a more complex, multi-frequency system with characteristic frequencies that are not mutual integer multiples of each other, resulting in random behavior [176]. The coupling between the shear layers and modulation of the different fluctuation phenomena may result in broadband fluctuations centered around the aforementioned dominant frequencies [179].

Bluff body flows involving recirculation may involve not only vortex shedding, but also other types of motion. For instance, Berger et al. [22] described recirculation area oscillation behind circular disks at frequencies around $Sr_D = 0.05$ based on disk diameter D. In a more complex geometry, Depres et al. [33] similarly observed a pumping motion of the recirculation behind a launcher afterbody at a low frequency of $Sr_D < 0.1$ with D being the launcher diameter. According to Wolf [174], such motion is a general characteristic of recirculating flows.

2.3. Three-Dimensional Swept Wing Flows and Their Post-Stall Characteristics

Prandtl's lifting line theory [108] predicts varying lift over the span of a finite wing. The two-dimensional airfoil separation mechanisms discussed in Section 2.2 can be found on finite wings, but even simple rectangular wings with constant cross section exhibit three-dimensional effects like spanwise variation of effective angle of attack. The characteristics are determined by the wing section shape, local chord variation due to taper, and the spanwise twist distribution. The pressure differential and equilibration between the upper and lower wing surfaces near the tip causes inward flow on the upper surface and outward flow on the lower surfaces, as indicated in the sketch on the right-hand side of Fig. 2.10.

The smoke visualization of the same effect in the photograph shows concentrated longitudinal vortices near the tips and spanwise curvature of the wake streamlines which entrain them into these vortices. The lifting line theory associates a spanwise distribution of circulation $\Gamma(y)$ and its gradient $\gamma(y)$ with this flow configuration. The roll-up motion of the longitudinal vorticity sheet downstream leads to the formation of two concentrated tip vortices after some distance downstream of the trailing edge. These phenomena are inviscid.

Wing sweep causes S-shaped curvature of the inviscid streamlines when viewed from the top, due to the fact that the wing surface isobars are locally aligned with the leading and trailing edges [165]. The viscous flow in the boundary layer does not have sufficient momentum to follow the inviscid streamline curvature, which results in outward spanwise flow near the surface. This shear inside the boundary layer contributes to the longitudinal vorticity

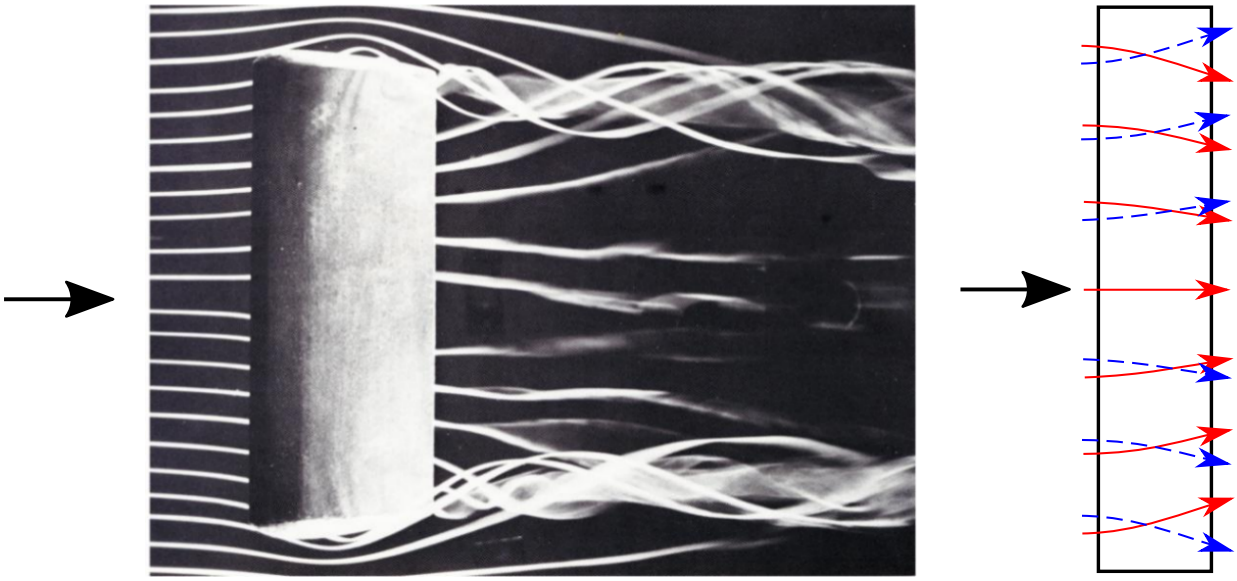

Fig. 2.10.: Top view of a finite wing flow. Photograph on the left from van Dyke [158]. Red lines show flow direction above the wing, blue dashed lines below the wing.

downstream of the trailing edge.

If no countermeasures such as twist are taken, the flow along tapered or swept wings tends to separate outboard due to the maximum of the spanwise c_l distribution being located there. This is a result from inviscid considerations, and in the case of swept wing this is further exacerbated by the viscous effects associated with spanwise boundary layer flow. The spanwise flow results in a thicker boundary layer on the outboard wing, and the tapered planform of a typical wing causes a lower local Reynolds number near the tip. Both of these factors promote separation near the wing tip.

The danger of tip stall in terms of flight mechanics is that it may be asymmetric and abrupt. As turbulent separation is a nonlinear process, tip stall may occur only on one side and potentially cause a large rolling moment. Even ideally symmetric stall is undesirable, as the wing tips are typically behind the aircraft center of gravity. Onset of tip stall therefore lowers lift acting behind the aircraft center of gravity, creating a nose-up pitching moment that drives the aircraft further into stalled conditions [165]. These properties tend to be counteracted by careful wing design, by optimizing the taper and the effective angle of attack via spanwise washout.

Of the airfoil separation regimes described in Section 2.2 and presented in Fig. 2.4, the leading edge separation becomes most prevalent in presence of significant sweep according to Harper and Maki [48]. The same authors describe the mechanism of leading edge separation near the tip causing a vortex aligned with the leading edge. The extreme case of a highly swept wing is represented by a delta wing common in combat aircraft, with large stable vortices emanating from the highly swept leading edge and generating nonlinear lift. On the contrary, in a transonic civil aircraft context with a moderate sweep angle, such vortical structures do not occur by design within the standard flight envelope.

Nevertheless, a vortex aligned with the leading edge occurs at significant angle of attack and expands toward the trailing edge with increasing α. At the same time, it grows inward in spanwise direction. According to Polhamus [105], this vortical structure is due to the relative

strength of the spanwise pressure gradient that occurs due to wing sweep. He showed that this vortex is highly stable and may increase inboard lift due to additional mass entrainment and downward deflection of flow. The vortex can curve back, leave the wing [48] as visualized in Fig. 2.11, or burst at some point. At higher α, the vortex grows inward, and the position where it departs from the wing moves in the same direction. Zhang et al. [180] conducted measurements on a wing with 40° at high angles of attack, observing the vortex development as shown in Fig. 2.11.

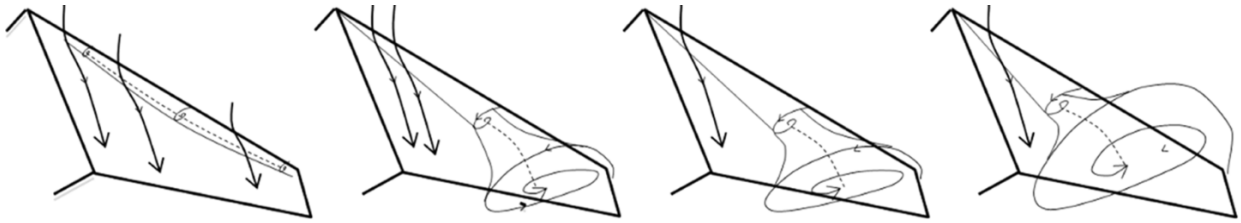

Fig. 2.11.: Evolution of the leading edge vortex on a swept wing, adapted from Zhang et al. [180]. Angle of attack from left to right: 7°, 8°, 9°, 14°.

According to Vos and Farokhi [165], the presence of a leading edge vortex depends on the geometry, especially on the nose radius. The nose radius of typical supercritical airliner airfoils tends to be relatively large, which increases the critical angle of attack above which a leading edge vortex can appear [106]. Schütte [130] recently published an exhaustive study of parameters influencing separation on a strongly swept wing. Like Zhang et al. [180], he was able to detect outward orientation of the surface streamlines and a leading edge vortex departing the surface with increasing angle of attack.

CHAPTER 3

Methodology

3.1. Computational Methods

3.1.1. Governing Equations

The dynamics of a Newtonian fluid behaving as a continuum can be described using the Navier-Stokes equations. This system of equations represents the conservation of mass, momentum and energy in a control volume. Following the derivation by Blazek [23], the conservative integral form is used. This is an intuitive representation for a transport equation of this kind, and is essentially a conservation law for the vector of conservative variables $\vec{W}$

$$\vec{W} = \begin{pmatrix} \rho \\ \rho u \\ \rho v \\ \rho w \\ \rho E \end{pmatrix}, \tag{3.1}$$

which represents the density ρ, the three spatial components of momentum and the total energy per unit mass E. The conservation law for $\vec{W}$ then reads:

$$\underbrace{\frac{\partial}{\partial t}\int_{\Omega} \vec{W} d\Omega}_{\text{temporal}} + \oint_{\partial\Omega} \left(\underbrace{\vec{F_C}}_{\text{convective flux}} - \underbrace{\vec{F_V}}_{\text{viscous flux}} \right) dS = \underbrace{\int_{\Omega} \vec{Q} d\Omega}_{\text{source}} \tag{3.2}$$

with the convective fluxes $\vec{F_C}$ representing convective transport in the flow and viscous fluxes $\vec{F_V}$ for viscous stresses. $\vec{Q}$ is a source term representing body forces. The latter is typically of lesser importance in external aerodynamics, and is consequently neglected by the computational solver used in this work. The integral form can be converted to differential form by

applying Gauss' theorem to the surface integral on the left hand side. For the momentum equation, this results in:

$$\frac{\partial \rho u_i}{\partial t} + \frac{\partial \rho u_j u_i}{\partial x_j} = -\frac{\partial p}{\partial x_i} + \frac{\partial \tau_{ij}}{\partial x_j} \tag{3.3}$$

This employs Einstein's summation convention, where multiple occurrence of an index in a single term implies summation over all values of this index. Independent of the representation, the five conservative variables in $\vec{W}$ in these equations cannot fully define the physical system without a gas model. Aerodynamics problems involving non-reacting air flows justify the use of the perfect gas model, i.e. associating the state variables with each other via the specific gas constant R:

$$p = \rho R T = (\gamma - 1)\rho \left[E - \frac{u^2 + v^2 + w^2}{2} \right] \tag{3.4}$$

The second part of the equation is valid for a calorically perfect gas, with the ratio of specific heats γ and the total energy per unit mass E. The dependence of the viscosity on the temperature is provided by Sutherland's equation

$$\mu = \mu_0 \left(\frac{T}{T_0} \right)^{3/2} \frac{T_0 + S}{T + S}, \tag{3.5}$$

which uses the constants $T_0 = 273.15K$, $S = 110.4\,\mathrm{K}$ and $\mu_0 = 1.716 \cdot 10^{-5}\,\mathrm{N\,s\,m^{-2}}$ for atmospheric air flows.

Reynolds Averaging

The fundamental equations described above can be employed to predict the entirety of the fluid motion across all spatial and temporal scales with a finite volume discretization approach. This can be accomplished computationally using DNS, which has the associated prohibitive cost at higher Re described in Chapter 2. Turbulence fluctuations can occur at many different scales, not all of which need to be necessarily known. The idea that mean quantities and other low order statistics may be sufficient for the description of an engineering flow gave rise to averaging approaches, making the equations more conducive to numerical simulation via statistical turbulence modeling methods. The spatially and temporally resolved governing equations can be simplified by decomposing the variables u into a mean part $\overline{u}$ and a fluctuating part u':

$$u = \overline{u} + u' \tag{3.6}$$

Reynolds averaging can involve time, space or ensemble averaging. Usage of this approach, or the density-weighted averaging according to Favre, results in the Reynolds-Averaged Navier-Stokes (RANS) equations. Their incompressible differential form often found in literature is as follows:

$$\frac{\partial \overline{u_i}}{\partial t} = -\frac{1}{\rho}\frac{\partial p}{\partial x_i} + \frac{1}{\rho}\frac{\partial \overline{\tau_{ij}}}{\partial x_j} - \frac{\partial \overline{u_i' u_j'}}{\partial x_j} \tag{3.7}$$

This approach introduces additional independent variables which make up the Reynolds stress tensor $-\rho\overline{u_i' u_j'}$. These quantities represent the additional effect of momentum transfer by turbulent motion acting on the mean flow. Since they are unknown, the resulting system of equations requires closure in order to be solvable. The most well-known closure approach is the linear eddy viscosity ansatz based on the Boussinesq assumption [24]. This implies a linear relationship between the velocity gradient and the Reynolds stress tensor. For incompressible flows with zero divergence of the velocity field, this is written as follows:

$$-\rho\overline{u_i' u_j'} = 2\mu_t \overline{S_{ij}} - \frac{2}{3}\rho\delta_{ij}k \tag{3.8}$$

As such, they focus on providing a value for the scalar $\mu_t = \rho\nu_t$, which is the eddy viscosity. This scalar has the same unit as molecular viscosity and models the effect of turbulence on the mean flow in a similar manner, in that it drains energy from the flow and dampens fluctuations. It is meant to replace fully resolved simulation of small scale turbulent fluctuations by a viscosity-like local term representing the effect of turbulence.

These approaches give rise to a large variety of turbulence models, most of which employ one or two additional transport equations. The Spalart-Allmaras (SA) one-equation model [142] is in widespread use in external aerodynamics applications. Its formulation is based on a single transport equation for the SA eddy viscosity $\tilde{\nu} = \mu_t/(\rho f_{v1})$:

$$\frac{\partial\tilde{\nu}}{\partial t} + \frac{\partial\rho u_i\tilde{\nu}}{\partial x_i} = P - \varepsilon + \frac{1}{\sigma}\left[\frac{\partial}{\partial x_i}\left((\mu+\mu_t)\frac{\partial\tilde{\nu}}{\partial x_i}\right)\right], \tag{3.9}$$

where P is the production term modeling generation of $\tilde{\nu}$ due to shear and ε is the destruction of the same variable:

$$P = c_{b1}\hat{S}\tilde{\nu} \qquad \varepsilon = c_{w1}f_w\rho\left(\frac{\tilde{\nu}}{d_w}\right) \tag{3.10}$$

The constants f_{v1}, c_{w1}, f_w, and several others used in the model equation are empirical values derived by Spalart and Allmaras and can be found in their original work [142]. Various models using one or more equations exist. In addition to SA, the present work employs Menter's [91] Shear Stress Transport (SST) two-equation eddy viscosity model. Apart from this, a Reynolds stress model (RSM) will be used for comparison. The implementation of this model (SSG/LRR-g) in the solver was described by Togiti [154]. Additional details on the transport equations and model background can be found in Appendix A.

3.1.2. Resolution of Unsteady Turbulent Motion

Turbulence Spectrum

The turbulent energy cascade is a result of the concept that turbulence consists of three-dimensional eddies, the largest of which draw energy from the mean flow and pass it on to smaller scales via vortex stretching processes. Most of the fluctuation energy is contained in the large eddies. This typical idealized energy distribution is sketched in Fig. 3.1 for homogeneous isotropic turbulence.

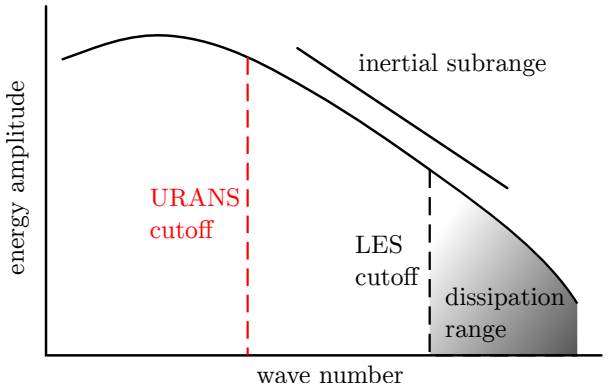

Fig. 3.1.: Turbulence energy spectrum, double logarithmic representation.

The energy is high at low wave numbers, representing large spatial scales. The shear occurring in the flow drains energy from the mean and generates turbulence energy, the shear magnitude of the large eddies is comparable to that of the mean flow [151]. The vortex stretching transfers this energy to ever smaller scales. Kolmogorov [68] observed local isotropy at small scales for sufficiently large Reynolds numbers, which is to say that the processes occuring at small scales have short timescales and tend to respond quickly to any changes imposed by the mean flow. Statistics of the small scales are largely independent from orientation effects of the mean flow and the large scales. The small eddies are at approximate equilibrium with the local mean conditions, giving rise to the term *equilibrium range* of the turbulence spectrum. The equilibrium range contains the *dissipation range* at high wavenumbers, which includes viscous effects, and the *inertial subrange* at medium wavenumbers. The latter's wavenumber range increases with flow Reynolds number and was shown to have a slope of $-5/3$ in double logarithmic coordinates. The inertial subrange occurs in energy spectra and in one-dimensional velocity spectra [151], making it an often-used tool for rough validation of time-resolved computations.

Turbulence Motion Resolution

It follows from Kolmogorov's [68] work that, at sufficiently high Reynolds number, the small scales are statistically isotropic and possess a universal character in the sense that their temporal and spatial statistics are determined only by the kinematic viscosity and the dissipation rate. The RANS-based methods shown above use this observation and model the entire spectrum of turbulent fluctuation energy. This has proven to be a valid approach especially for steady state high Reynolds numbers flows with attached boundary layers. RANS models are being successfully used in virtually every engineering fluid mechanics discipline, both for internal and external flows. They can be formulated in a time-independent form as unsteady RANS (URANS) equations in order to resolve large scale unsteadiness in the flow field. The application of such methods implies the reliance on the existence of a spectral gap, resolving the low wave number features and modelling the more universal high wavenumber region as shown in Fig. 3.1. The spectral gap is required to ensure that the time and length scales of the turbulent motion are sufficiently separated from the resolved motion. This is justifiable in cases such as moving geometry or shock motion [94], which are essentially "non-turbulent" processes. According to Mockett [94], bluff body wake flows can also be resolved by URANS approaches. While these methods are attractive due to their potential ability to resolve

complex flows with reasonable computational cost, ensuring the spectral gap a priori is not trivial. The dissipative nature of RANS models causes an unphysical drain of fluctuation energy if the spectral gap is not sufficient. The feasibility of URANS needs to be evaluated on a by-case basis.

Scale Resolving Simulation and Hybrid Methods

The universality of small scale eddies drove the development of methods which resolve large motion scales with their associated complex characteristics, while leaving the universal small scales to a simple model. Large Eddy Simulation (LES) applies a spatial filter depending on the local grid size Δ, enabling the resolution of turbulent length scales of the same order of magnitude. Smaller scales are typically treated using a subgrid scale model (SGS) such as Smagorinsky's [138], which bases its subgrid scale quantities on the local grid resolution and the resolved shear stress tensor. LES methods aim to resolve a large part of the turbulent motion, while using the simple SGS for isotropic small-scale turbulence only. This reduces computational effort compared to a DNS, but the required resolution is still prohibitive in near-surface regions and especially at high Reynolds numbers as described in Section 1.2.2. One approach aiming to rectify this is the use of wall models in conjunction with LES in order to further reduce resolution requirements in the near-wall region. Such wall-modeled LES (WMLES) employ a wall stress model in the lower part of the boundary layer where the turbulence scales are very small, while the upper part remains in regular LES mode.

Hybrid methods such as DES by Spalart [143] and its descendants approach this issue by treating attached boundary layer regions in RANS mode and switching to LES-like behavior in separated flow regions. DES implements this by employing the SA RANS model and modifying ε, the destruction of SA eddy viscosity $\tilde{\nu}$, in accordance with the local grid resolution. This is accomplished by replacing the wall distance that is used as the turbulence length scale in Eq. 3.10 with the local grid size Δ scaled by a constant C_{DES} where appropriate, i.e. where the value of ΔC_{DES} is smaller than d_w:

$$\tilde{d} = \min(d_w, \Delta C_{DES}) \tag{3.11}$$

The constant C_{DES} is usually set to 0.65. The definition of Δ in the context of DES is:

$$\Delta = \max(\Delta x, \Delta y, \Delta z) \tag{3.12}$$

In effect, this decreases the eddy viscosity away from the wall to the amount that is appropriate for the local grid size Δ. The lower eddy viscosity enables the direct resolution of turbulent fluctuations instead of modelling via a scalar quantity. Eq. 3.11 places a lower bound on $\tilde{d}$, ensuring that eddy viscosity is not excessively decreased close to the wall where $d < \Delta C_{DES}$, forcing RANS behavior in that region. This has the advantage of LES-like behavior away from the wall, while ensuring robust modeling of attached boundary layers using RANS.

A disadvantage arises from the fact that the switching between RANS and LES is based on a fixed metric dependent on the local Δ. Spalart et al. [144] described this shortcoming and its effects, which can contribute to premature separation due to high grid resolution (i.e., low Δ) near the wall. This tendency to grid-induced separation is caused by decreased $\tilde{d}$ via Eq. 3.11 leading to excessive and destabilizing decrease of ν_t. This modeled stress depletion (MSD) is

a consequence of switching to LES within the boundary layer without the necessary increase in turbulent stresses. It is partly rectified by the Delayed Detached Eddy Simulation [144] (DDES), which introduces a delay function f_d and a boundary layer sensor r_d in order to shield attached boundary layer regions from this effect. The delay function

$$f_d = 1 - \tanh\left[(8r_d)^3\right] \tag{3.13}$$

is based on a boundary layer detector function r_d

$$r_d = \frac{\nu_t + \nu}{\sqrt{S_{ij}}\kappa d}. \tag{3.14}$$

These definitions lead to an additional modification of the length scale:

$$\hat{d} = f_d \max(0, d - C_{DES}\Delta) \tag{3.15}$$

Delayed Detached Eddy Simulation (DDES) tends to be better able to shield attached boundary layers from the incursion of resolved turbulence.

A common issue of DES-type methods is the generation of resolved turbulence, which needs to take place near the separation location. Modeled turbulent stresses transported from upstream need to be translated to resolved turbulence. This so-called grey area problem is a focus of ongoing research, with a recent overview over the state of mitigation strategies given by Probst et al. [111] with a focus on the results of Go4Hybrid [95]. These issues are of special importance in the context of smooth surface separation, where the local shear strength may be insufficient to generate resolved turbulent fluctuations.

Further DES varieties have been proposed, mostly centering on improved detection of those regions where resolution of turbulent fluctuations is appropriate. One such example is Improved Delayed Detached Eddy Simulation (IDDES) described by Travin et al. [157] and Shur et al. [135], employing a more sophisticated definition of Δ and adding the ability to act as a Wall-Modeled LES (WMLES) model on top of the DDES-based behavior. Manual zonal selection is in use as well, as in the Zonal DES (ZDES) approach by Deck [32]. DES and its variants are not strictly bound to a specific turbulence model. While the original version employed SA, which is computationally efficient by virtue of being a one-equation model, Travin et al. [157] combined the method with the two-equation SST model. Further, Illi [128] and Probst [110] employed Reynolds stress models for specific tasks.

The present work can be expected to be a well-posed problem for DES-type approaches, with separation occurring at a largely fixed location close to the leading edge. The pressure gradients are of such magnitude that boundary layer shielding does need to not play a significant role. Conversely, the rapid generation of resolved fluctuations immediately after the separation location is an important aspect. The ability of URANS and DES methods to resolve appropriate physics in these areas is scrutinized in Chapters 5 and 6. Apart from URANS, DDES is the only hybrid method used in this work, as IDDES has not shown any appreciable difference compared to DDES in the flow regimes encountered here.

3.2. Practical Simulation

3.2.1. Flow Solver

The simulations forming the bulk of the present work were carried out using DLR's TAU CFD solver [131]. TAU is an unstructured, compressible second-order finite volume solver capable of handling hybrid grids constructed using various geometrical element types. It employs a cell-vertex scheme on a dual grid, i.e. on approximate Voronoi volumes [93] generated around the nodes of a primary grid. Spatial discretization is implemented using a central difference scheme. This involves the computation of inviscid and viscous fluxes, for which TAU implements various types of schemes. Essentially, TAU solves the Navier-Stokes equations in the form

$$\frac{\partial \vec{W}}{\partial t} + \frac{\partial \vec{F}(\vec{W})}{\partial x} = 0, \tag{3.16}$$

with the vector of conservative variables $\vec{W}$ and the flux $\vec{F}(\vec{W})$ a nonlinear function of $\vec{W}$. The finite volume approach computes constant values of $\vec{W}$ in each control volume of the grid and fluxes $\vec{F}(\vec{W})$ across the control volume surfaces. The sum of fluxes and sources is the residual $\vec{R}(\vec{W})$, the minimization of which is the solver's objective. The right hand side is zero due to discarding of the source terms in the mean flow equations. This does not generally apply to the turbulence equations, which do involve source terms.

Local time stepping is employed for steady state computations, whereas dual time stepping is used for unsteady runs. The linear system is solved using a lower-upper symmetric Gauss-Seidel (LU-SGS) scheme. The convective fluxes of the turbulence equations are computed using a first order Roe scheme [118]. Various parameters are involved in the solution of unsteady flows, most of which are selected according to best practice settings documented in cited works. The specific settings and methods applied in these computations were previously validated by contributors from the author's working group [128, 166, 168] for the types of flows encountered in this thesis.

The implicit backward Euler scheme for time discretization is second order accurate and involves inner iterations at every time step, for which appropriate values need to be chosen. Solution convergence is monitored using global residuals and force coefficients. Apart from proper convergence, accurate representation of small scale turbulence is essential in flow situations of the type encountered in this thesis.

3.2.2. Artificial Dissipation

Spatial discretization using central differences is unstable due to the shape of the computational stencil [93]. The addition of artificial dissipation is therefore necessary to stabilize the computation of convective fluxes. Increased dissipation tends to smooth the solution, increasing stability. This has a tendency to smear spatial gradients and to reduce accuracy. On the other hand, decreased dissipation may lead to odd-even decoupling and spatial oscillations in the solution [34]. The particulars of this dissipation show a large influence on the results in massively separated flows, which merits a deeper discussion.

The representation of small scale turbulent fluctuation and the corresponding portion of the energy spectrum is handled by the turbulence model in URANS. This has the effect of dampening small scale fluctuation. Scale resolving simulation methods such as DES decrease this

effect by intentionally lowering the eddy viscosity. In order to avoid unnecessary dissipation, artificial dissipation needs to be tightly controlled.

TAU employs an unstructured version of the Jameson-Schmidt-Turkel [64] scheme involving second and fourth order differences. The 4th order term is active in most of the field except near discontinuities such as shocks, which are detected via a pressure gradient sensor and are treated using the second order term [93]. The default mode is scalar dissipation, with two parameters $k^{(2)}$ and $k^{(4)}$ controlling the amount of second- and fourth-derivative dissipation added to the flux [34]. These parameters are user-accessible, with the specific setting a compromise between accuracy and computational stability or convergence rate. According to Dwight [34], increasing the dissipation smooths the solution, thereby increasing its error. An obvious remedy is to decrease the dissipation. However, at a certain point, the errors due to oscillations in the solutions mount to such a degree that they dominate. A matrix-valued dissipation scheme by Swanson et al. [149] enables more fine grained artificial dissipation. Instead of using the spectral radius of the flux Jacobian for dissipation scaling, the matrix dissipation approach uses all eigenvalues and scales each equation appropriately. Matrix dissipation in TAU is considered to be the superior of the two schemes, and is recommended for use when low dissipation is desired [11].

3.3. Postprocessing

Processing of unsteady datasets requires a large amount of data manipulation. First and second order statistics can be accumulated at runtime in TAU itself, while further processing involved programs using the Python programming language, Matlab and Tecplot. The processing methods employed in this work will be briefly introduced in the following.

Spectral Analysis

Apart from the computation of statistical quantities, spectral characteristics were computed via Fourier analysis and other methods. Most of this processing was carried out using two dimensional data sampled at regular intervals during the simulation process. Fourier spectra were obtained using standard Fast Fourier Transform (FFT) calculation and spectral estimation approaches such as Welch's method [171], which involves segmenting a time series and averaging the resulting spectra in order to reduce variance.

Proper Orthogonal Decomposition

Proper Orthogonal Decomposition (POD) is a statistical decomposition method, which involves obtaining an orthogonal basis for a given dataset. This is a common approach used by data reduction and analysis methods in various fields such as machine learning and statistics, where it is typically referred to as principal component analysis (PCA). These methods have gained popularity in recent years, as technological advances enabled use of computationally intensive processing methods. The method derivation is widely available in literature, e.g. [174], and is shown only briefly in the following.

POD decomposes a given dataset consisting of spatial samples collected at regular temporal intervals over time. The dataset $X(x,t)$ then consists of N temporal snapshots at times

$t_1 \dots t_N$ and M spatial data points. The method provides a decomposition of the fluctuating part of these temporally evolving snapshots, expressed as a linear combination of spatial eigenmodes $\phi_i(x)$ and temporal coefficients $a_i(t)$, i.e.:

$$X(x,t) = \overline{u(x)} + u(x,t)' = \overline{u(x)} + \sum_{i=1}^{N} a_i(t)\phi_i(x) \tag{3.17}$$

In this context, x denotes a general spatial coordinate and not a particular direction. The procedure yields N eigenmodes with corresponding coefficients. The computation of eigenmodes is based on manipulation of the entire dataset. The snapshot matrix of size $M \times N$ is constructed as follows:

$$A = \begin{pmatrix} u(x_1,t_1)' & u(x_1,t_2)' & \dots & u(x_1,t_N)' \\ u(x_2,t_1)' & u(x_2,t_2)' & \dots & u(x_2,t_N)' \\ \vdots & \ddots & & \vdots \\ u(x_M,t_1)' & u(x_M,t_2)' & \dots & u(x_M,t_N)' \end{pmatrix} \tag{3.18}$$

Each temporal and spatial sample may consist of P different variables (e.g. velocity components), in which case the matrix A is simply extended by stacking and then consists of $M \cdot P$ rows. In CFD datasets, typically $M \gg N$, which is why the snapshot POD method by Sirovich [137] based on the temporal correlation is usually favored. It involves the solution of the eigenvalue problem for the correlation matrix C constructed from the data:

$$C = (A^T \cdot A)/N, C \in \Re^{N \times N} \qquad Cv = \lambda v \tag{3.19}$$

Each eigenvalue λ_i represents the modal energy of mode i, with a relative share $\lambda_i / \sum_j \lambda_j$ often used to express the fraction of the total variance contributed by mode i, i.e.:

$$\sum_{j=1}^{N} \lambda_j = \frac{1}{N} \sum_{i=1}^{M} \sum_{j=1}^{N} u(x_i,t_j)' u(x_i,t_j)' \tag{3.20}$$

The right hand side represents a variance, which is equivalent to the definition of turbulence kinetic energy in the context of fluctuating velocity fields. Each column of the eigenvector matrix v is a temporal POD coefficient a_i, representing the temporal evolution of mode i. The mode shapes ϕ_i are obtained from the eigenvectors via:

$$\phi_i = \frac{A \cdot v}{\sqrt{\lambda_i N}} \tag{3.21}$$

The eigenmodes are pairwise orthogonal. The decomposition can be used for spatiotemporal reconstruction via:

$$u_{rec}(x,t) = \sum_{k=1}^{N_{rec}} a_k(t) \cdot \phi_k(x) + \overline{u(x)} \tag{3.22}$$

The modes are sorted by energy, permitting the identification of the most significant POD contributors. This implies the possibility of low order modeling, by discarding higher order

modes that contribute negligible amounts to the fluctuation. Such partial low order reconstruction amounts to a spatial low pass filter [174] by using modes only up to $N_{rec} < N$. Zimmermann et al. [182] investigated the differences between Fourier transformed flow fields and POD modes in the aircraft wake.

In order to provide an example, representative POD modes obtained from a DDES computation of a NACA0012 airfoil at high angle of attack in post stall conditions are shown in Fig. 3.2[1]. The flow topology corresponds to the sketch in Fig. 2.6. This comparatively simple flow configuration involves periodic boundary conditions, i.e. a 2.5D computation with essentially infinite span and little spanwise flow. The u and w component of the first and second mode shapes are shown. High magnitudes of the spatial POD mode distribution occur mainly downstream from the trailing edge, with little fluctuating content upstream from it. The fluctuation downstream is cleanly ordered in space and constitutes alternating upward and downward velocity components which match high and low velocities above and below them. These features are indicative of a vortex street.

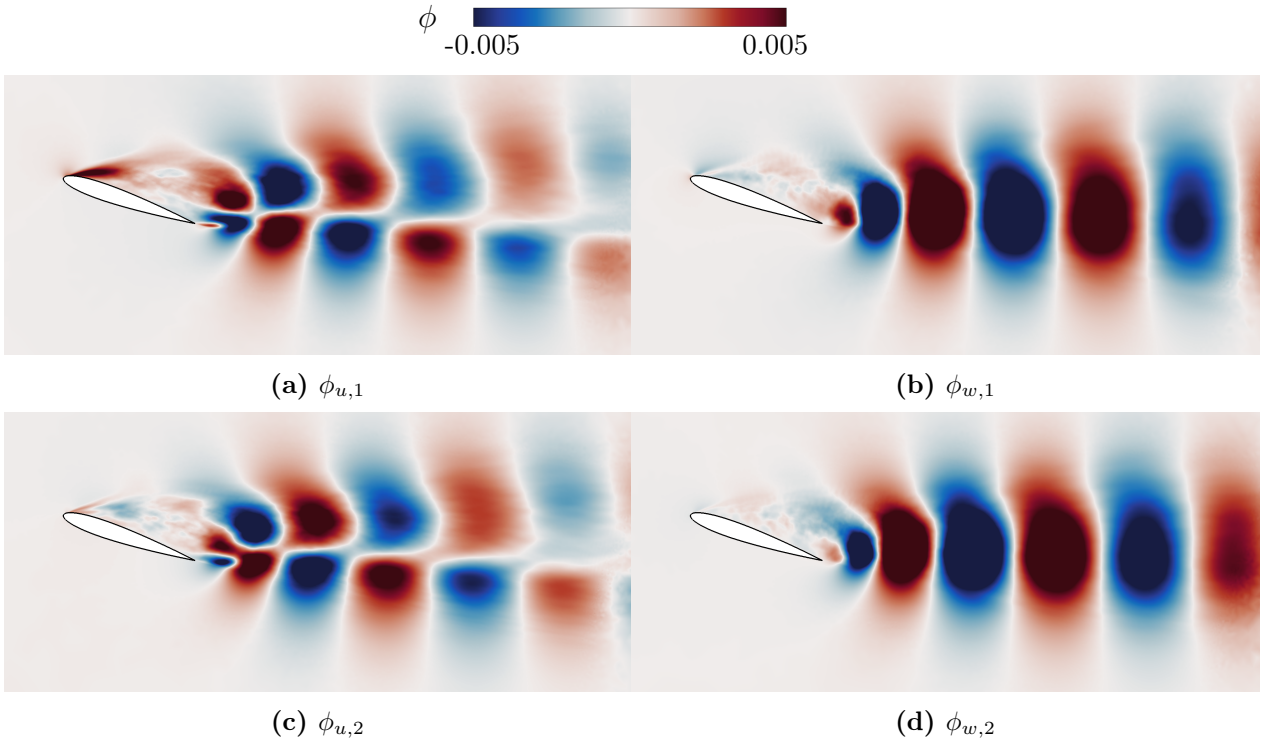

(a) $\phi_{u,1}$ **(b)** $\phi_{w,1}$

(c) $\phi_{u,2}$ **(d)** $\phi_{w,2}$

Fig. 3.2.: POD mode shapes of a von Kármán vortex street behind a NACA0012 airfoil.

The question what constitutes an appropriate low order model is the subject of some debate. An energy threshold requiring, for instance, 90 % of the total variance to be represented may be overly demanding and calls for a large number of modes. Liberzon et al. [78] addressed this by evaluating the error associated with dropping modes, and concluded that a choice of N_{rec} based purely on energy is not sufficient. Therefore, the reconstruction parameters need to be selected on a by-case basis.

[1]This case was computed using DDES at $Re_\infty = 3 \cdot 10^6$, $M_\infty = 0.3$ and $\alpha = 19°$.

Statistical Analysis and Error Estimation

Running and interpreting unsteady time-resolved simulations essentially amounts to a statistics problem, in the sense that a large number of samples is collected in order to obtain information on the observed process.While some point-based experimental techniques, such as hotwire measurements, permit very long measurement times limited only by storage infrastructure, the computational effort and associated expense required for complex and unsteady flow simulations may mean that the available time series length is insufficient for reliable statistical analysis. A quantification of uncertainty and the sampling error associated with given simulation results is therefore essential.

Performing an unsteady simulation or conducting a measurement is akin to recording one realization of an otherwise unknown process. That is, the recorded signal is a sample from a population representing the underlying process, and the sample statistics are estimates of the unknown true population statistics. In keeping with the central limit theorem, a sufficiently large number N of random samples x_i drawn from the population will be approximately normally distributed as N becomes large. The variance $\sigma^2 = \sum_{i=1}^{N}(x_i - \overline{x})^2$ of this sample distribution contains information on the sampling uncertainty. A common uncertainty measure is the standard error σ_{mean} of the mean, i.e. the standard deviation of the sample mean:

$$\sigma_{mean} = \frac{\sigma}{\sqrt{N}} \tag{3.23}$$

This holds true for the sampling mean, which is normally distributed if a sufficiently large number of random samples N is drawn. The underlying mental model is that repeatedly taking the mean of a sample of N will yield a distribution of sample means. σ^2_{mean} is the variance of this distribution and enables an estimate of the uncertainty. Garcia et al. [42] refer to it as *error variance*. This variance gives rise to the definition of a confidence interval for the given statistic, denoting the range of values which will contain the true value of the statistic with a given frequency after repeated realizations of the sampling process. A typical value of 5 % is employed in this work, which is equivalent to confidence interval boundaries of $\pm 1.96\sigma_{mean}$ around the calculated value of the statistic [42] such as the mean. Such boundaries can be computed for different statistics with varying degrees of difficulty. Benedict and Gould [21] derived formulations for the estimation of further quantities of interest in turbulent flows, both with and without the assumption of normality.

Highly resolved unsteady CFD simulations are able to yield a large number of samples N, which enables low values of σ_{mean} as computed by Eq. 3.23. However, the high sampling rate does not necessarily imply a large degree of information content in the signal. This is caused by the interdependence and correlation of the samples making up the signal. In other words, an increase in sampling frequency does not imply greater information content about the process. The correlation between samples in fact invalidates the assumptions in the central limit theorem. Eq. 3.23 remains applicable only if the correlation structure of the process is taken into account. This is acccomplished by introducing an effective number of independent samples N_{eff} in place of N. According to George et al. [65], the number of independent samples when estimating the mean of a signal is

$$N_{\text{eff}} = \frac{t_{total}}{2\tau}, \tag{3.24}$$

where t_{total} is the total recorded time and τ is the integral time scale. The latter is obtained via integration of the autocorrelation function $\rho(t')$ of the quantity x:

$$\rho(t') = \frac{\overline{x(t)\ x(t+t')}}{\overline{x(t)x(t)}} \tag{3.25}$$

t' represents the temporal lag. The autocorrelation function describes the degree to which the process is correlated with itself and retains a memory. Integrating the autocorrelation function over possible lags yields the integral time scale

$$\tau = \int_0^\infty \rho(t')dt' \tag{3.26}$$

which provides an estimate of the time required for the process to lose the memory of past events. Using N_{eff}, the uncertainty of the first and second order statistics estimates can be estimated as follows, as described by Benedict and Gould [21] and Garcia et al. [42]:

$$\sigma_{mean} = \frac{\sigma}{\sqrt{N_{\text{eff}}}} \qquad \sigma_{var} = \sqrt{\frac{2(\sigma^2)^2}{N_{\text{eff}}}} \tag{3.27}$$

In this, σ is termed the *uncorrelated* standard deviation, as it is obtained using the total sample size N without regard to autocorrelation via $\sigma = \sum_{i=1}^{N}(x_i - \overline{x})$.

CHAPTER 4

Aircraft Configuration and Experimental Background

With the difficulty of conducting flight tests in stall conditions, computational and wind tunnel studies are the only feasible ways of obtaining data in this type of flow. The convergence of long range passenger aircraft configurations toward a low-wing monoplane layout with a fuselage-mounted horizontal tailplane and moderately swept wing and tail surfaces has resulted in a wide range of commercial models with similar shapes and different dimensions. Collaborative research efforts such as AIAA's Drag Prediction Workshop series required an open and accessible geometry, which is nevertheless representative of contemporary aircraft. This led to the emergence of generic designs such as DLR's F6 or NASA's CRM. These representative aircraft models provide researchers with opportunities to carry out validation and quantitative comparison without infringing any manufacturer's intellectual property.

Parts of this section are reproduced from Waldmann et al. [166] and Waldmann et al. [167].

4.1. The Common Research Model

A working group in the Subsonic Fixed Wing project conducted at NASA created the design of the CRM, which is described in detail by Vassberg et al. [160]. The result is an aircraft designed for a cruise Mach number of $M_\infty = 0.85$ and a Reynolds number of $\mathrm{Re} = 40 \cdot 10^6$ based on its mean aerodynamic chord at an altitude of 37,000 ft with a design lift coefficient of $C_L = 0.5$. With a wing span of $b = 58.8\,\mathrm{m}$ and a reference chord of $c_{\mathrm{ref}} = 7\,\mathrm{m}$, the design is similar to the Boeing 777 long range widebody aircraft ($b = 60.93\,\mathrm{m}$ and $c_{\mathrm{ref}} = 7.07\,\mathrm{m}$, respectively).

It has been widely used in this capacity for various studies in different fields of aerodynamics research. The Drag Prediction Workshops 4 [161], 5 [77] and 6 [153] made use of it. Various

other publications using the CRM have appeared in the past several years, including fluid-structure simulation (Keye et al. [66]), combined wind tunnel and CFD studies (Rivers et al. [115], Lutz et al. [84], Waldmann et al. [166]) and many more.

Wind Tunnel Model

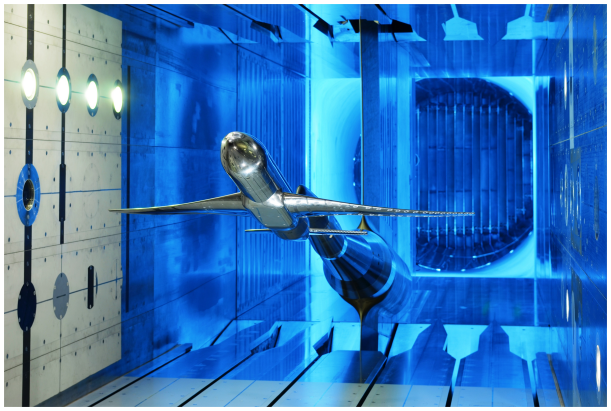

Fig. 4.1.: CRM in the ETW test section.

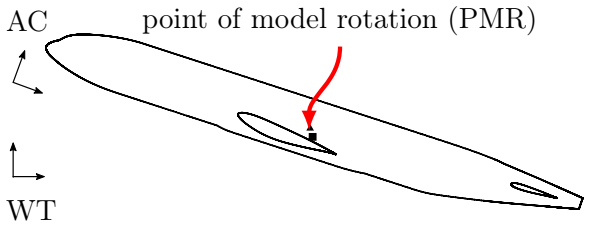

Fig. 4.2.: Coordinate system origins and directions.

A 2.7 % scale model exists for the wind tunnel studies, resulting in the dimensions shown in Table 4.1. Its basic configuration is WBT0, with a horizontal tailplane at zero incidence angle and no engine nacelles. The horizontal tailplane (HTP) is removable and can be set to incidence angles of $i_{HTP} = -2°, 0°, 2°$. The wing can be equipped with removeable flow-through nacelles representing engine installation, which was not done in the present investigation. There is no vertical tailplane, its space in the tailcone being used as the interface for the wind tunnel mounting system (see Fig. 4.1).

Tab. 4.1.: CRM wing and tailplane geometry data

Feature		full scale	model scale
Aspect ratio	Λ	9	9
Span	b	58.76 m	1.586 m
Wing sweep angle at quarter chord	$\varphi_{c/4}$	35°	35°
Wing reference chord length	c_{ref}	7 m	0.189 m
Wing reference area	S	383.7 m^2	0.280 m^2
Wing taper ratio	λ	0.275	0.275
HTP sweep angle at quarter chord	$\varphi_{c/4,\text{HTP}}$	37°	37°
HTP reference chord length	$c_{\text{ref,HTP}}$	4.69 m	0.127 m
HTP span	b_{HTP}	21.34 m	0.577 m
HTP reference area	S_{HTP}	92.9 m^2	0.067 m^2
HTP taper ratio	λ_{HTP}	0.35	0.35

The CRM geometry is defined in a coordinate system aligned with the aircraft fuselage, whose origin is situated upstream of the aircraft nose (cf. Fig. 4.2). This original CRM coordinate system aligned with the aircraft is referred to as AC in this work. Moment coefficients are

defined relative to the model reference point (MRP), whose position in this coordinate system is shown in Table 4.2. This is a point defined by the CRM design in [160]. It does not coincide with the point of model rotation (PMR) in the wind tunnel, which is defined by the model and support system kinematics.

Tab. 4.2.: Reference coordinate positions in the CRM coordinate system at model scale.

coordinate	PMR	MRP
x [m]	0.90249	0.90932
z [m]	0.14926	0.12192

In those instances in this work where absolute values are given, they refer to model scale quantities. Most of the flow analysis in this work employs a CRM-derived coordinate system aligned with the wind tunnel inflow, abbreviated as WT. It is obtained by rotating the AC system by α about the PMR, ensuring horizontal inflow. The WT and AC systems coincide at $\alpha = 0°$. The WT coordinate system is stationary with respect to the wind tunnel measurement section, while the AC system is not and rotates depending on α. Other coordinate systems used in this work are obtained in the same manner by rotating AC about PMR by a given angle.

4.2. Experimental Background

The European Strategic Wind Tunnels Improved Research Potential (ESWI$^{\mathrm{RP}}$) project aimed to enhance the capabilities of several European wind tunnels and to enable the international research community to access large scale measurement facilities. In February 2014, the experimental campaign was conducted using CRM in the ETW in Cologne [84]. The ETW is a closed-circuit, pressurised, cryogenic facility able to achieve transonic and low supersonic Mach numbers across a range of 0.15 to 1.35 [51]. It permits independent control of Re_∞ and M_∞ via adjustment of pressure and temperature, enabling high Reynolds number testing at transonic Mach numbers. The ESWI$^{\mathrm{RP}}$ campaign encompassed a range of Reynolds and Mach numbers, both in the transonic and subsonic regions. An overview of the measurement campaign and related computational studies is given by Lutz et al. [84].

4.2.1. Measurements

The force and moment measurements were conducted using an internal model balance. Wing static pressures are measured in rows of pressure taps at 9 spanwise stations ($\eta = 0.131$, 0.201, 0.283, 0.397, 0.502, 0.603, 0.727, 0.846, 0.950), where $\eta = 0$ represents the model symmetry plane. Their positions are indicated in Fig. 4.3. Wind tunnel wall pressure was also recorded for the purpose of wall interference correction. An optical Stereo Pattern Tracking (SPT) system [87] measured the static aeroelastic deformation of the wing and tailplane. The subsonic and transonic measurements under consideration were conducted at $\mathrm{M}_\infty = 0.25$ and $\mathrm{M}_\infty = 0.85$, respectively. Polar measurements were carried out as a continuous pitch traversal, providing data for steady state CFD validation in the linear regime. The subsonic stall wake measurement runs were carried out at two different wind tunnel operating points: $\mathrm{Re}_\infty = 11.6 \cdot 10^6$ (run 313) and $\mathrm{Re}_\infty = 16.85 \cdot 10^6$ (run 256). The wind tunnel environmental

conditions are listed in Appendix B. No transition fixing was employed in the experiment, since fully turbulent flow was assumed due to the large Reynolds number.

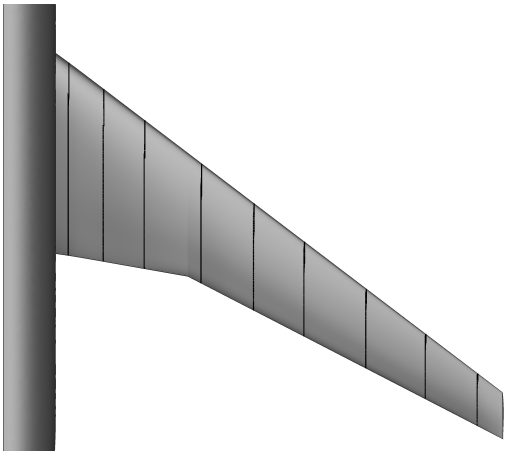

Fig. 4.3.: Positions of the nine pressure measurement rows on the wing suction side.

ESWI^{RP}'s outcome consists of several datasets with various levels of corrections applied. The present investigation employs data that was corrected for wall interference, flow curvature and Mach number effects, i.e. a correction that adjusts the Mach number at the model reference point [129]. The support system effect on the computational results is taken into account separately.

4.2.2. PIV

This subsection is a reproduction of the Particle Image Velocimetry (PIV) system's discussion in Waldmann et al. [166]. A PIV measurement system capable of obtaining time-resolved planar flow field data in the wake was employed in the ESWI^{RP} campaign. Its goal was the resolution and analysis of resolved turbulence fluctuation data in the separated wake. The measurement and data processing were carried out by Deutsches Zentrum für Luft- und Raumfahrt (DLR), with more detailed specifics of the measurement system published by Konrath et al. [70]. The description below is a synopsis of information relevant for the present study.

The installation and operation of time-resolved PIV systems in a pressurized cryogenic environment proved a challenge in its own right. The laser beam requires a complex guiding system with multiple deflections, as shown in Fig. 4.4. The laser beam enters the test section below the model centerline. The figure illustrates the oblique angle of the PIV laser sheet. The cameras were positioned inside the wind tunnel pressure vessel in heated enclosures, shielded from the cryogenic atmosphere. The system is capable of a sampling rate of 2000 Hz, which was deemed sufficient for the resolution of relevant turbulent scales in the wake after preliminary investigations [83].

The PIV laser sheet is a rectangle inclined by 21.6° with respect to the wind tunnel vertical walls, with a useable size of about 65 mm width by 135 mm height. It is positioned at approximately $\eta = 54\%$ behind the wing, aiming to capture the center of the wake. In contrast to the original data set used for validation in [166], the PIV data accuracy was subsequently improved by using the correlation method described by Hart [49] as described

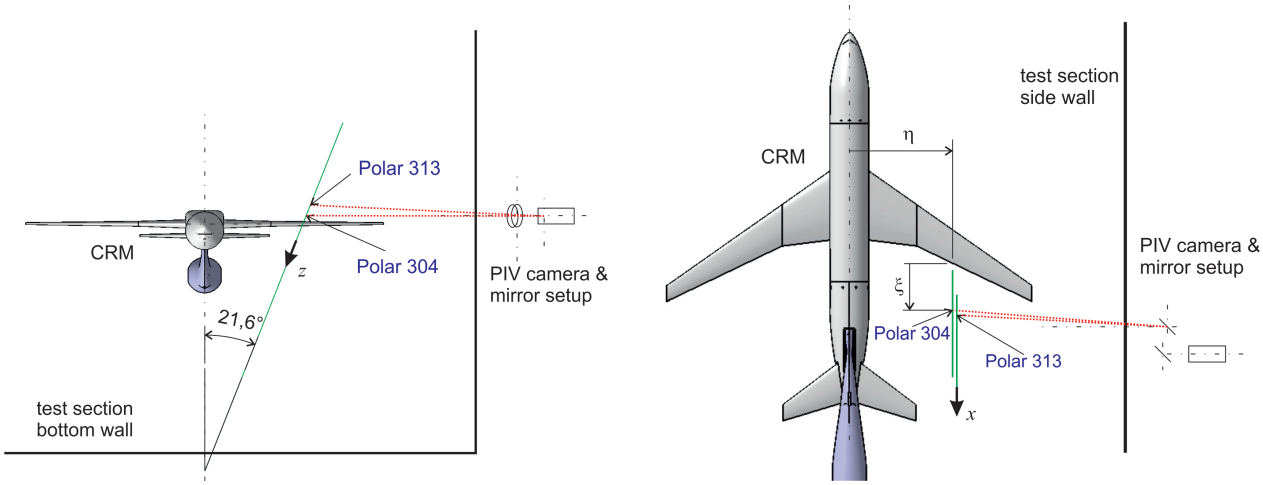

(a) Front view **(b)** Bottom view

Fig. 4.4.: PIV setup in the ETW with CRM installed, from Konrath [70].

by Konrath et al. [70].

The PIV measurement plane is positioned near mid-wing, outside of the wake/tailplane interaction area. Nonetheless, the velocity statistics enable some insight into the characteristics of the results. Due to the challenges encountered with the cryogenic conditions the data quality does not lend itself to in-depth comparisons of time-resolved fluctuation characteristics.

4.3. Wind Tunnel Effects and Model Configurations

This section is partly reproduced from Waldmann et al. [167].

Wind tunnel measurements and CFD simulations typically do not replicate identical inflow conditions. In most cases, CFD users seek to obtain data at free flight conditions without the additional complication and expense of simulating the surrounding wind tunnel infrastructure. However, wind tunnel walls and the support system impact the results, which gives rise to various correction methods in order to achieve comparability of data. A large body of literature addressing the various error sources and corrections has emerged over the past decades, with examples provided by compendia such as AGARDograph 109 [43] or AGARDograph 336 [37].

Wall Effects

The wind tunnel walls and their developing boundary layers introduce blockage effects by reducing the mass flow relative to an inviscid flow. This causes a Mach number in the test section that is different from a free flight condition. What is more, the walls enforce locally parallel flow and thereby constrain the streamline curvature around the model. Porous walls or slotted walls like those in the ETW serve to mitigate the wall influence by reducing the constriction, and the corresponding correction methods are well proven. Mokry [96] summarized the wall influence as "low perturbation effects", accessible via linearized potential methods. Gorbushin et al. [45] investigated these particular phenomena in the context of the ESWI^{RP} campaign in more detail. The wall effects will not be considered separately

in this work. The significant expense associated with taking slotted walls into account in the simulation outmatches the possible benefits, as the wall effects are considered of lesser magnitude.

Support System Effects

According to Stojanowski et al. [146], the support system's effect may be broken down into a near field and a far field contribution. Britcher et al. [25] described a similar classification based on three contributing components: an overall effect, a local flow disturbance and a geometrical distortion of the model. A previous study by Waldmann et al. [167] in steady state flows at moderate angle of attack showed this local effect for the CRM, as visualized in Fig. 4.5.

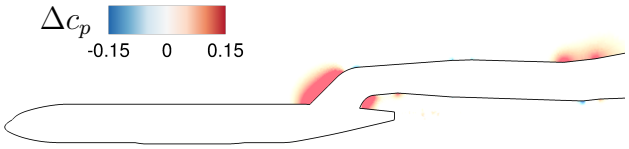

Fig. 4.5.: Effect of the sting on the pressure coefficient distribution in the symmetry plane at $\alpha = 5°$, $\mathrm{Re}_\infty = 11.6 \cdot 10^6$. Δc_p is the difference between the results obtained with and without sting. Image from Waldmann et al. [167].

The overall, or far field, effect largely stems from the streamwise pressure gradient that is introduced by the presence of the support in the test section, altering the pressure distribution around the model as well as the resulting forces. It alters the Mach number by slowing down the flow upstream of the support system, necessitating the Mach number correction mentioned above. This is sketched in Fig. 4.6, which shows the increment of Mach number caused by the isolated support system. This was obtained from an inviscid computation and provides a qualitative impression of the effect. While usual wind tunnel corrections typically assume a scalar increment to M_∞, the actual far field effect changes the local Mach number across the wind tunnel cross section. The effect is strongest near the centerline of the support system, with a fall-off toward the walls. This may change the spanwise lift distribution along the wing, in particular in transonic flow by shifting the shock position due to altering the local effective M and α.

The geometrical distortion effect arising from the model modification is due to e.g. missing surfaces at the location of the interface between model and support system. It is difficult to decouple from the local effect described above and is rarely explicitly determined [86].

The support system employed in the ETW campaign can be seen behind the CRM in Fig. 4.1. A fin sting was used, which enters the model fuselage in place of a vertical tail. As shown in Fig. 4.7, the support diameter increases downstream until it reaches its maximum diameter. Fig. 4.7b gives an impression of the relative diameters of the CRM and the sting as represented in CFD. König et al. [69] published an investigation of the wind tunnel effects for the transonic portion of the ESWI$^{\mathrm{RP}}$ campaign and at steady state conditions. The present author contributed a similar study for the subsonic regime in Waldmann et al. [167]. In this work, these considerations will be expanded into the post-stall regime.

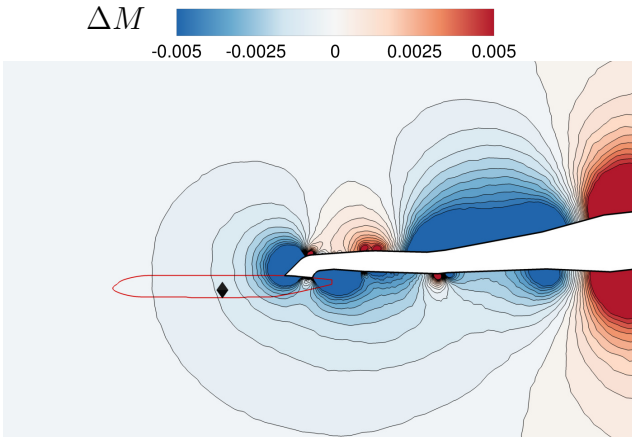

Fig. 4.6.: Effect of the sting on the Mach number distribution in the symmetry plane at $\alpha = 5°$, $\mathrm{Re}_\infty = 11.6 \cdot 10^6$. Image from Waldmann et al. [167].

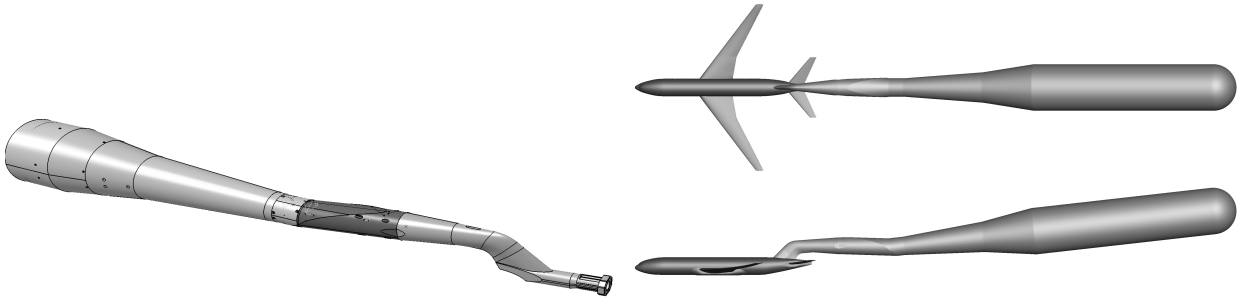

(a) CAD **(b)** CFD

Fig. 4.7.: Support system of the CRM in the ETW.

Aeroelastic Wing Deformation Effects

The flow in a pressurised cryogenic wind tunnel imposes significant aerodynamic loads on the model, causing non-negligible deformation. This mainly affects the wing and the tailplane. A swept wing bends upwards and twists when generating lift, with the twist increment $\Delta\Theta$ increasing the washout and thereby unloading the outboard part. As established by Rivers et al. [115], the shape of the CRM wind tunnel model as manufactured corresponds to an aeroelastic deformation at $1g$ load condition. This shape further deforms when subjected to loads in the wind tunnel. These bend and twist increments with respect to the wind-off shape, Δz and $\Delta\Theta$ at the quarter-chord line, were measured in the ETW, providing deformation data at discrete spanwise stations.

Low speed stall validation in the present work uses data from run 313 at $Re_\infty = 11.6 \cdot 10^6$, although the deformation measurement system was not active at these conditions. Deformation data obtained during run 256 (at $Re_\infty = 16.85 \cdot 10^6$) is used instead. The difference in dynamic pressure q/E between these operating points affects the loads and model deformation magnitude. This effect is taken into account by proportionally scaling the Δz and $\Delta\Theta$ distributions using q/E, as shown by Schulte am Hülse [128]. The HTP deforms under load as well, the magnitude is however very small. This deformation was neglected in the present investigation. The scaled deformation shape distributions are shown in Fig. 4.8.

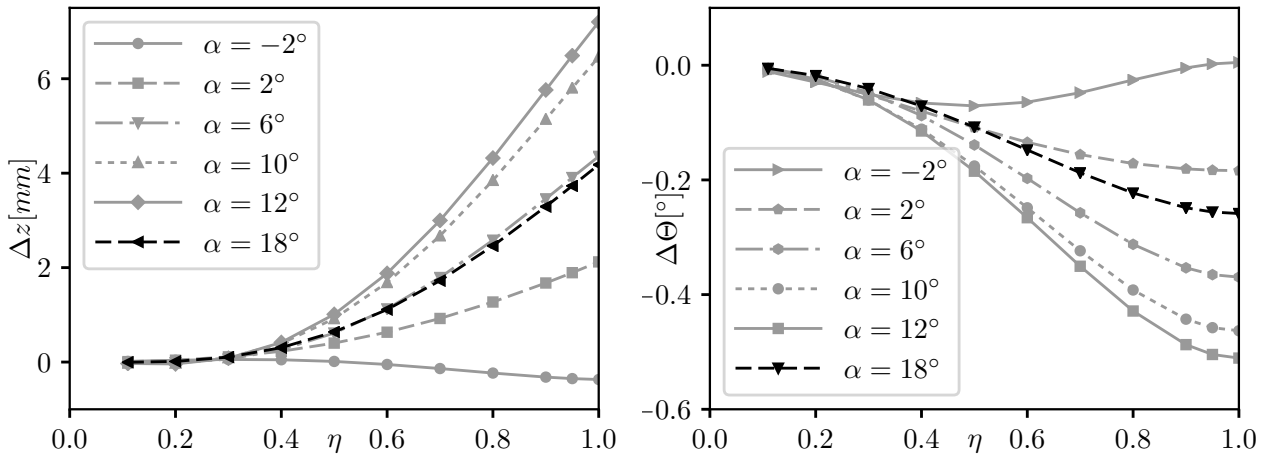

(a) Bend **(b)** Twist

Fig. 4.8.: Wing bend and twist increments at $M_\infty = 0.25$ relative to $1g$ shape for a series of angles of attack, scaled to $Re_\infty = 11.6 \cdot 10^6$.

CHAPTER 5

Simulation and Validation in Subsonic Post Stall Conditions

This chapter focuses on subsonic stall and provides justification for the choice of methods used in later wake studies. The low speed stall data set from the ESWI^{RP} campaign is used for this purpose, with $Re_\infty = 11.6 \cdot 10^6$, $M_\infty = 0.25$ and $\alpha = 18°$. Run 316 is a polar measurement dataset over an angle of attack range between $\alpha = 0°$ and $\alpha = 18°$, whereas run 313 was specifically performed to carry out PIV measurements at a single angle of attack of $\alpha = 18°$.

The subsonic ESWI^{RP} polars from run 316 in Fig. 5.1 show the range of angles of attack traversed by the CRM model. Fig. 5.1a shows the expected linear lift region from $\alpha = 0°$ until approximately $\alpha = 10°$. Prior to the initial departure from the linear lift region, the pitch break occurs and the pitching moment in Fig. 5.1c deviates from its linear shape. At $\alpha \approx 12.4°$, a drop in lift occurs which is associated with an increase in drag and a decrease in nose-down pitching moment. The post stall condition of $\alpha = 18°$ is at the high end of the angle of attack range, past a second drop in lift. The second discontinuity occurs at about $\alpha = 15.5°$, above which the lift coefficient increases only slightly. This fulfills the definition of stall described earlier. The wing experiences massively separated flow past this α value, which is accompanied by a strong increase of the drag coefficient values. The pitching moment decreases linearly with α.

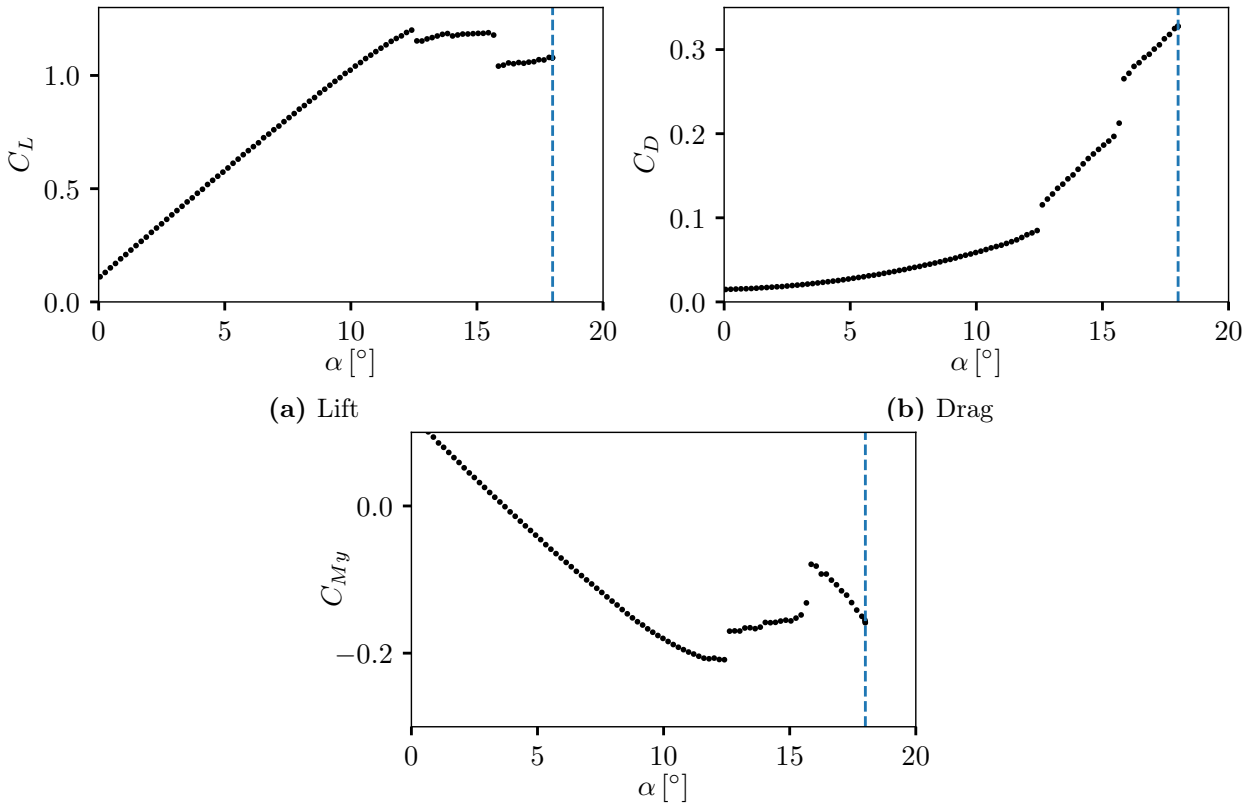

(a) Lift **(b)** Drag

(c) Pitching moment

Fig. 5.1.: Experimental force and moment polars from the ETW at run 316 ($Re_\infty = 11.6 \cdot 10^6$, $M_\infty = 0.25$).

5.1. Simulation Approach

The first validation step of any aircraft flow simulation is to obtain steady state overall forces and moments across the α range of the polars. This was done exhaustively by Gansel et al. [41] for subsonic cases. Waldmann et al. [167] provide a discussion of the appropriate simulation approach for this region of the polar and the sensitivity of the results to the model configuration. This shall not be discussed further, and the following descriptions focus on information pertinent to post stall simulation specifically.

After constructing the grid, the wing grid is deformed by imposing the deflection measured at the target flow conditions of $M_\infty = 0.25$, $Re_\infty = 11.6 \cdot 10^6$, $\alpha = 18°$ in the wind tunnel as shown in Fig. 4.8. Fully turbulent flow is assumed, without any prescribed transition location. A series of steady state RANS simulations was performed across a range of angles of attack in order to obtain appropriate starting conditions for stall runs. While providing force and moment data for the α range, these results are not acceptable as validation data due to being obtained with a deformed model shape appropriate for $\alpha = 18°$. The results are used for initialization of high angle of attack unsteady simulations. This is an approach that has been proven to be reliable and to save computational effort. After reaching the desired $\alpha = 18°$ in steady state mode, the solver is switched to time-resolving mode by enabling dual time stepping at a relatively coarse time step setting. All time steps and durations are given in relation to the convective time $t_\infty = c_{\text{ref}}/u_\infty$, representing the time required for the bulk inflow to pass over one mean aerodynamic chord. Prior experience with TAU has shown that a computational time step Δt of $0.1t_\infty$ is a reasonable starting point in order to establish an unsteady baseline, although it is too large to properly resolve the flow physics.

After achieving an approximately stationary state, the simulation is switched to the target set of parameters in terms of time step size, artificial dissipation settings, et cetera. A list of relevant solver settings is given in Appendix C. After reaching statistical stationarity, statistics are collected over at least $50t_\infty$.

Meshing Strategy and Grid Resolution

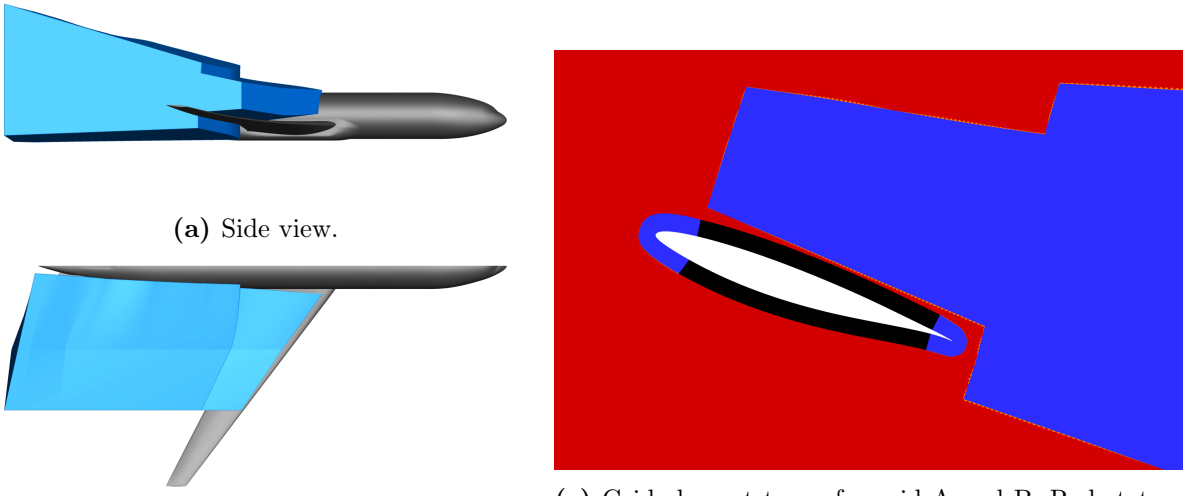

(a) Side view.

(b) Top view.

(c) Grid element types for grid A and B. Red: tetrahedra, blue: hexahedra, black: prisms.

Fig. 5.2.: Position of the wake block relative to the CRM, grids A and B.

The starting point for the meshes is the hybrid grid representing the aircraft and the boundary layer intended for steady state simulation. This baseline grid presented by Gansel et al. [41] consists of grid blocks extruded from the surface designed to fully contain the attached physical boundary layer. These structured regions comprise 50 to 70 layers and ensure a y^+ value below 1. A more thorough description of the CRM stall grid topology can be found in Waldmann et al. [166]. Computational grids aimed at wake simulation need to have appropriate resolution in the areas of interest. The approach described in Spalart's guidelines [141] for DES meshing involves several regions, most notably a Viscous Region (VR), a Focus Region (FR) and a Departure Region (DR). The VR includes the resolved boundary layer and is the same as in a steady state RANS computation. This grid region is constructed with size requirements appropriate for boundary layers in RANS simulations. For RANS, the remainder of the flow field is typically filled by comparatively coarse grid cells, as no resolved turbulence needs to be transported there. In order to ensure appropriate resolution of turbulent structures in scale-resolving simulations, a focus region (FR) with the required spatial resolution and grid quality is used in the region of interest. In the present case, the size of this region needs to encompass the extent of the separated wake flow and its expected propagation toward the tailplane. Its size is limited by the fact that high resolution outside of relevant areas requires unnecessarily high usage of computational resources. As the commonly used length scale in scale-resolving methods is based on $\Delta = \max(\Delta_x, \Delta_y, \Delta_z)$, Spalart [141] argues for cubic cells in such regions. The grid was created with this goal in mind, allowing the compromises necessitated by the three-dimensional shape of the wake block. Outside of the FR, the DR is responsible for smooth transition between the highly

resolved grid in the FR to the much coarser outer region without introducing excessive changes in volume between neighboring cells.

For stall simulations, a wake block consisting of near-isotropic hexahedral elements is added where large-scale unsteady turbulent wake flow is expected, forming the FR. The wing boundary layer grid includes both quadrilateral and prismatic elements. The hexahedral wake block therefore does not have a direct connection to the boundary layer grid, as shown in Fig. 5.2c. The space between the two is filled by tetrahedra.. Its position relative to the CRM is shown in Fig. 5.2. Grids A and B share this topology, with the difference between them being only the grid resolution inside the blue block in Figs 5.2a and 5.2b. The extruded boundary layer grid is in this case the VR and the wake block forms the focus region, with appropriate maximum size requirements. All grids are half spheres, with a far field boundary condition representing the flight conditions imposed on the outer shell. The latter is at a distance of about $25b$ from the aircraft, which corresponds to approximately $220c_{\mathrm{ref}}$. This distance is aimed at eliminating any boundary condition effects. Symmetry is enforced at the aircraft centerline.

Tab. 5.1.: Grids used in the study.

Name	Grid A	Grid B	Grid C
No. of domains	2048	1248	4128
No. of points, 10^6	51	20	110
Nominal wake cell size	$1\,\%c_{\mathrm{ref}}$	$2\,\%c_{\mathrm{ref}}$	$1\,\%c_{\mathrm{ref}}$

The high resolution wake block (FR) extends from the fuselage to about $\eta = 65\,\%$. This is motivated by the focus on the wake-tailplane interaction, which occurs within the span of the tailplane whose tip is at approximately $\eta = 30\,\%$. Care has been taken to ensure as high a degree of isotropy as practically possible. The characteristic wake grid resolution in grid A is approximately 1%-1.5% c_{ref}, while in grid B the grid spacing is halved. This results in the grid sizes listed in Table 5.1. There is some variation in cell size owed to wing sweep and the widening of the wake, therefore the characteristic size is intended as a representative quantity.

Apart from limiting the overall spanwise extent of the wake block, the approach involving decoupled VR and FR grid topologies in grids A and B results in moderate grid point counts. This is in large part due to the anisotropy in the wing surface and boundary layer grid inherited from the baseline steady state grid, which involves a larger spacing in spanwise than in chordwise direction and reduces the number of points. Eliminating the sliver of tetrahedra between the near-isotropic wake block grid and the boundary layer elements in Fig. 5.2c, and thereby coupling these latter two directly, increases the number of grid points in the boundary layer substantially. Nevertheless, a third grid C including this connection was used for validation in order to ensure that the above meshing strategy does not introduce unnecessary error. The wake block of grid C is fully connected to the wing surface grid, which consists entirely of structured hexahedra. Using the same typical cell size in the wake as grid A, this increases the grid point number by a significant amount. In addition, the wake FR in grid C extends to the wing tip and covers the full wing span. Overall, this results in a grid that is larger than grid A by more than a factor of 2.

Grids A and B have a common surface mesh, viscous region and departure region. They differ only in the wake block representing the focus region, permitting direct comparisons of the local grid resolution's effect. Grid C serves as a more highly resolved reference with a more bespoke layout adapted for the high angle of attack flow. It eliminates the tetrahedral filling between the extruded prisms and the wake block, it includes a higher surface resolution with smaller surface aspect ratios, and its wake block covers the entire wing span. Each of these changes can be viewed as an improvement in grid quality with respect to grids A and B. The purpose of grid C is to evaluate whether the lack of these improvements in grids A and B introduces grid-related accuracy issues.

The validation and selection of a simulation model is carried out using grid A. While grid A was shown by the author in [166] and [169] to be sufficiently resolved for this type of flow at these conditions, the isolated effect of the grid is evaluated separately. The WBT0d configuration is used throughout Chapters 5 and 6. This is due to resource constraints and the historical order of the research that led to this work. Previous research [167] demonstrated that the sting has a quantifiable but very local effect on the pressure distribution and forces in steady state attached flows at the same inflow conditions. Since the forces serve as the main validation data source, the isolated effect of the sting and of the wing deformation is nevertheless quantified later in this chapter.

5.2. Method Choice and Validation

Studies conducted in preparation of the ESWI^{RP} experimental campaign had been based on URANS-type approaches [83]. The rationale is that URANS should be capable of resolving such flows under the condition of the existence of the spectral gap discussed in Chapter 3. This assumption was justified by evaluating turbulence length scales in the wake and the dominant frequencies of the wake oscillation, which are comparatively low [83]. URANS may be considered feasible for this application, as its purpose is the prediction of forces and turbulent structures impacting the wake.

As opposed to scale-resolving approaches, URANS does not require limiting temporal resolution based on reasoning via the local CFL number. It only calls for the existence of a spectral gap. Nevertheless, this study aims to achieve fair comparison between URANS and scale resolving simulations by employing a common grid and identical time step sizes. URANS' notional advantage lies in its ability to model a substantial part of the turbulence spectrum, lowering the resolution demands and decreasing the computational cost. This is partly negated by the common approach used is this validation study, which sacrifices potential computational effort savings for the sake of comparability. Above all, this enables an answer to the question of whether hybrid models are required for this type of flow.

Three different URANS turbulence models were employed, as listed in Table 5.2. Runs U1 and U2 use the Spalart-Allmaras [142] (SA) and k-ω SST [91] eddy-viscosity models, respectively, that follow the Boussinesq hypothesis of a linear constitutive relation. The SSG/LRR-g model [154] in U3 is a Reynolds stress model that solves transport equations for the Reynolds stress components individually. While potentially retaining the anisotropy of the Reynolds stress tensor, the required computational time is substantially higher due to the greater amount of transport equations that need to be solved.

The following discussion will focus on the best-performing simulation of each type. The

Tab. 5.2.: Validation runs.

run	$\kappa^{(4)}$	turbulence model
U1	1/64	URANS SA
U2	1/64	URANS SST
U3	1/64	URANS SSG/LRR-g
U4	1/1024	URANS SA
D4	1/1024	DDES SA
D5	1/64	DDES SA

URANS runs U1-U3 use the default and recommended artificial dissipation setting of $k^{(4)} = 1/64$. For TAU, it is recommended to use a setting of $k^{(4)} = 1/1024$ for DDES [11], which is the setting used in run D4. In order to isolate the effects of hybrid and URANS models and separate the artificial dissipation effects, additional URANS-SA and DDES were are conducted using $k^{(4)} = 1/1024$ (U4) and $k^{(4)} = 1/64$ (D5), respectively. Further results obtained using IDDES or DDES with other turbulence models are omitted for reasons of brevity, as DDES-SA was found to offer the best performance in the present case.

The nominal step size for the calculations was chosen by applying best practices from previous studies [41], which indicated that 100 time steps per t_∞ constitute a reasonable value, i.e. $\Delta t = 0.01 t_\infty$. Waldmann et al. [166, 168] confirmed that this does indeed deliver acceptable results for these specific inflow conditions. Spalart [141] and Mockett [94] argue that the convective CFL number in the focus region should be on the order of 1. The CFL number is estimated here using the mean velocity magnitude:

$$\mathrm{CFL} = \frac{\overline{u}\Delta t}{(\Delta x \Delta y \Delta z)^{1/3}} \tag{5.1}$$

The cell volume in the denominator of this definition may be considered a debatable choice. While this can be expected to provide reasonable results in the near-isotropic hexahedral region, the boundary layer is made up of highly anisotropic cells, skewing the results. Nevertheless, this definition is expected to yield a workable estimate of the situation in the FR. Focus is placed on the role of resolved turbulent fluctuations and their dissipation inherent in the numerical scheme and in the turbulence models themselves.

The criterion CFL < 1 holds only in a portion of the wake flow field, owing to the heterogeneity of the solution. Spatial and temporal resolution resolution effects are quantified at the end of Section 5.2.

5.2.1. General Flow Field Topology

The salient feature of the flow around the CRM at $Re_\infty = 11.6 \cdot 10^6$ and $\alpha = 18°$ is massive separation over the entire wing span, which results in unsteady forces on the wing and tailplane. Visualization of flow structures in the wake in order to understand the range of solution topologies is informative before undertaking quantitative studies. The instantaneous turbulent structures represented using isosurfaces of $\lambda_2 = -10^5 1/\mathrm{s}^{-2}$ in Fig. 5.3 attest to the chaotic nature and unsteadiness of the wake flow. The massive separation causes a large recirculation region downstream from the wing, which persists along the entire wing span.

The instantaneous isosurfaces of λ_2 visualize the typical shape of flow structures present near the wing and in the wake. The well-visible vortex pair on the leeward side of the fuselage is common to all six solutions, and is the result of squeeze-off separation from the cylindric fuselage shape as described by Hirschel et al. [53]. There is a significant difference in characteristic appearance of the flow between the URANS and hybrid models' solutions in the wing wake. The outboard flow is consistently separated in all runs and shows less pronounced differences, therefore the outboard wake flow is blanked in Fig. 5.3 for clarity.

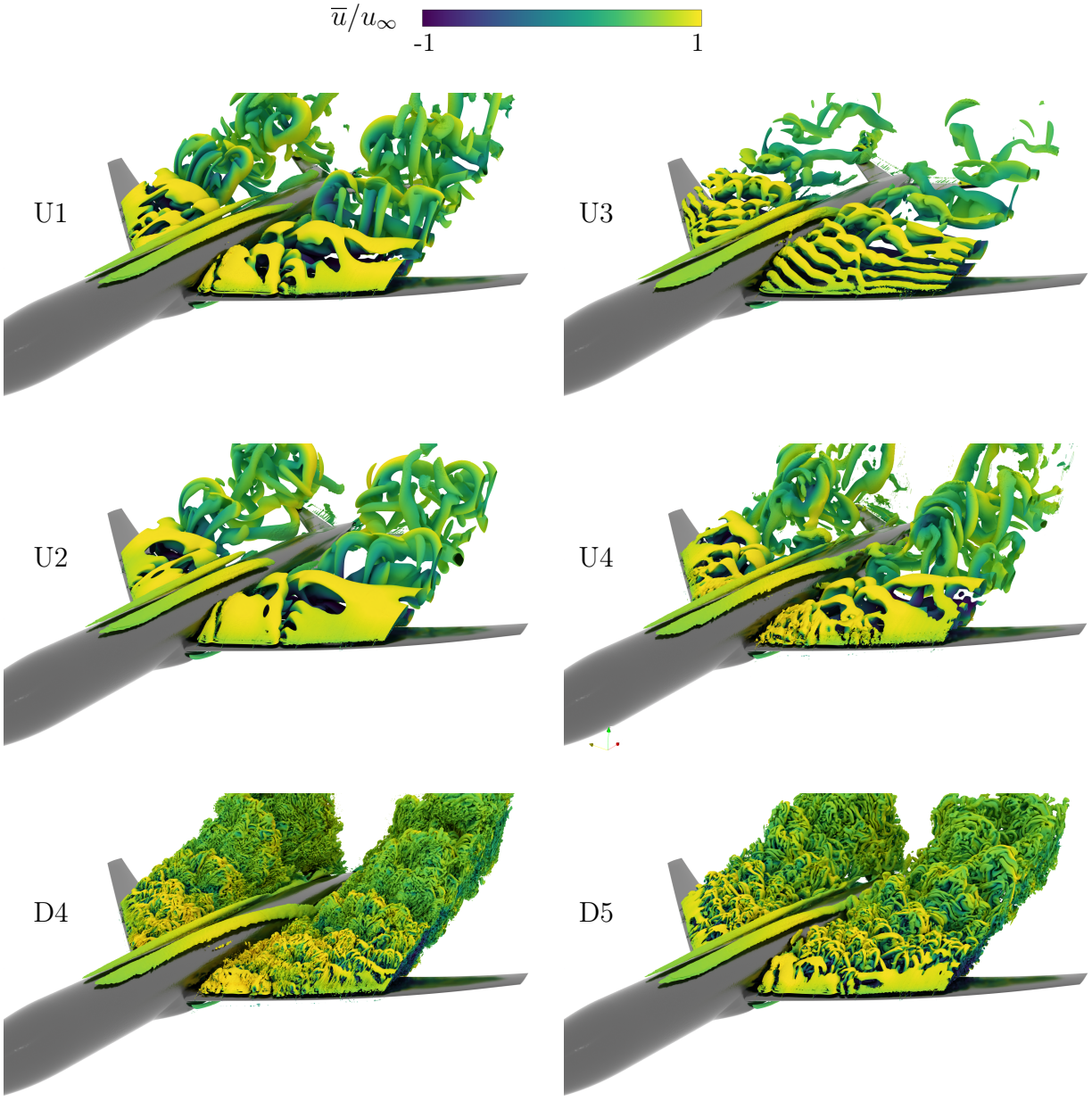

Fig. 5.3.: Isosurfaces of instantaneous $\lambda_2 = -10^5 \mathrm{s}^{-2}$ colored by streamwise velocity u. Near-surface values and outboard data $y > 0.5\,\mathrm{m}$ are not shown for clarity.

The URANS SST model (U2) predicts a continuous, almost unbroken sheet of shear flow beginning at the leading edge, decaying into discrete turbulent structures only further downstream. The SSG/LRR-g model U3 shows evenly spaced, two-dimensional and largely co-

herent vortical structures generated at the separation location near the leading edge, which remain roughly parallel to it and are convected downstream. The vortex sheet breaks up after a certain distance, with the structures becoming more random and decaying down to a certain size. This is also apparent in the result of the two runs using the SA model, U1 and U4. Although the structures near the separation differ, the size and general appearance of the vortical structures downstream of the wing are similar across all four URANS runs.

In contrast, the hybrid models in the bottom row of Fig. 5.3 predict significantly smaller turbulent structures, with little apparent coherence or order. Contrary to the URANS runs, there is little evidence of the stable sheet-type shear structure near the leading edge. D5 ($k^{(4)} = 1/64$) shows some initial alignment of the structures, however this rapidly disintegrates into three-dimensional turbulence. The D4 result ($k^{(4)} = 1/1024$) shows essentially three-dimensional turbulence beginning from the separation.

The initially two-dimensional character of the flow separating at the leading edge is a commonly observed consequence of delayed generation of resolved turbulence [162]. This is expected behavior in URANS, as small scale turbulent motion is intended to be modeled instead of resolved in accordance with the rationale of such models' design. When using hybrid RANS/LES, however, a rapid generation of resolved turbulence is desired. While the instantaneous flow field of D5 suggests the occurrence of a delay, this appears to be rectified by using a lower artificial dissipation in D4. At the same time, the U4 URANS simulation using the same dissipation settings does not appear to benefit from decreased dissipation in the same manner. While the λ_2 isosurface is less smooth than in the U1 solution, the characteristics of the vortical structures in the wake appear similar to U1. The influence of the artificial dissipation are discussed separately further below.

Validation Using Experimental Data

The lift and drag forces in Fig. 5.4 show that all simulations except the SSG run are within 10 % of the measured values. The more dissipative URANS runs U1-U3, as well as the DDES run D5, tend toward lower lift coefficients, whereas D4 and U4 are very close to the experiment. The drag values are plausible for all solutions, with the results scattered around the experimental C_D. The pitching moment C_{My} in Fig. 5.4c is significantly more revealing in terms of fundamental differences between the solutions, due to its sensitivity to the effect of the separated wake acting on the tailplane. All URANS solutions predict significantly higher magnitudes of nose-down pitching moment than the measurements. The DDES results with reduced dissipation fare better, with D4 yielding by far the best agreement with the experiment. Due to the lack of experimental tailplane pressure measurements, the reasons for this need to be inferred from other quantities.

The wing pressure distributions in Fig. 5.5 show that the CFD results and the experiments are very similar at $\eta = 60.3\,\%$ and further outboard. Most of the wing suction side in the outboard region experiences separated flow without reattachment, as evidenced by nearly constant pressure coefficient values over the surface. The constant upper side pressure is reminiscent of the base pressure of a bluff body, with the near wall flow only weakly interacting with the outer flow outside the recirculation. This is consistent across all CFD data sets, as is the pressure side c_p distribution. The situation changes further inboard, and the measured pressure distribution deviates from a constant shape. The dissipative URANS results U1-U3 and D5 tend to predict largely flat suction side pressure profiles over most of the chord,

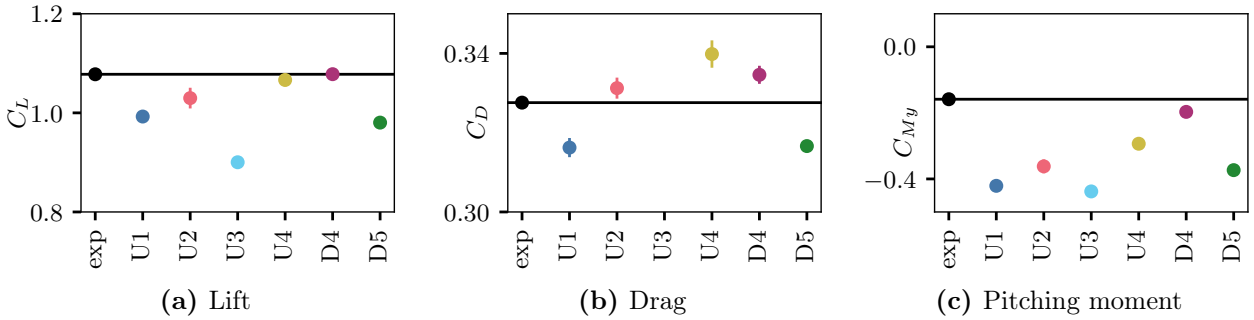

(a) Lift **(b)** Drag **(c)** Pitching moment

Fig. 5.4.: Forces and moments at $\alpha = 18°$. Vertical bars indicate the confidence bounds based on the signals's standard error where applicable.

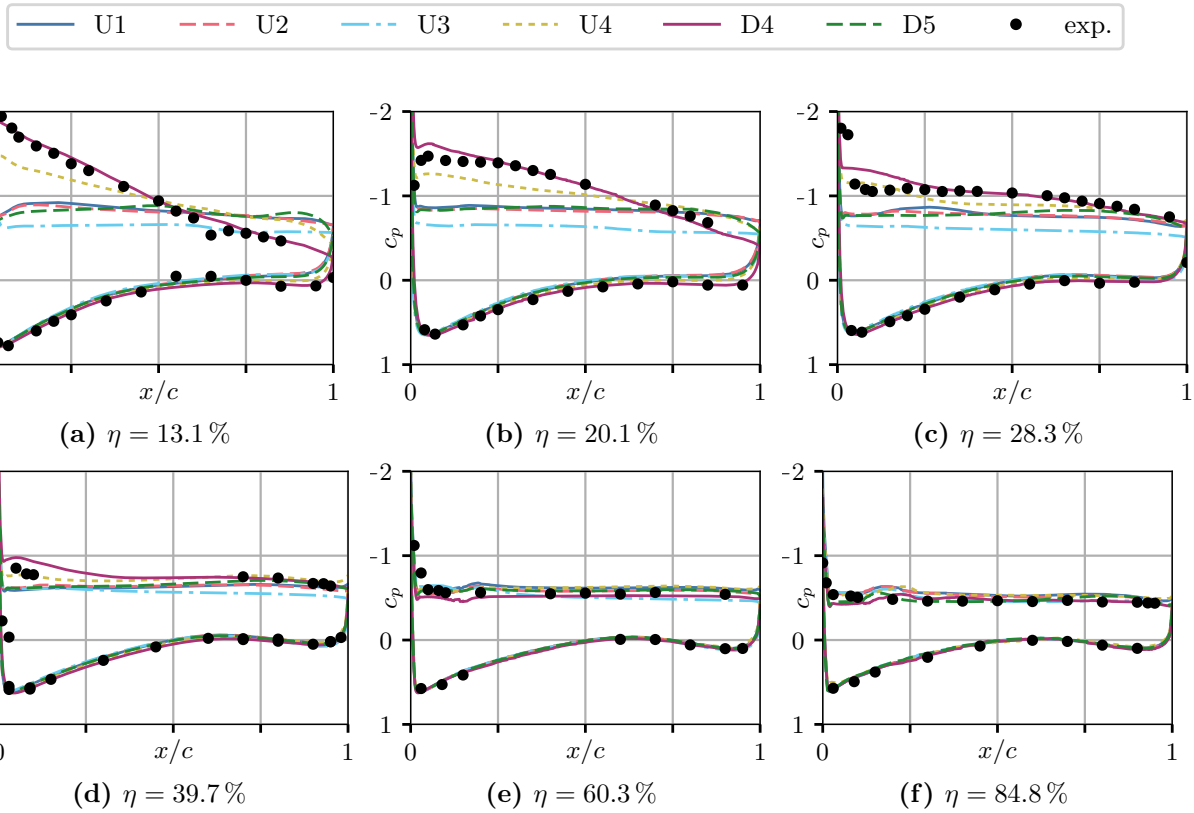

(a) $\eta = 13.1\,\%$ **(b)** $\eta = 20.1\,\%$ **(c)** $\eta = 28.3\,\%$

(d) $\eta = 39.7\,\%$ **(e)** $\eta = 60.3\,\%$ **(f)** $\eta = 84.8\,\%$

Fig. 5.5.: Wing pressure distributions at $\alpha = 18°$ for various modelling approaches. $M_\infty = 0.25$, $Re_\infty = 11.6 \cdot 10^6$, $\alpha = 18°$.

similar to the outboard locations. U4 and D4 consistently show a positive chordwise pressure gradient in Figs. 5.5a-5.5c, as does the experiment. The DDES result in particular matches the experimental data well. The large differences in inboard pressure distribution across the CFD results are consistent with the C_{My} variation in Fig. 5.4c. The local lift and the corresponding downwash strength directly determine the tailplane inflow, which strongly influences the pitching moment.

Experimental data in the wake is only available outboard, via PIV data on a slanted plane at about $\eta = 54\,\%$ and one chord downstream of the trailing edge. While the PIV sampling rate of 2000 Hz was intended for time resolved data acquisition for signal analysis, large gaps in the data render the signals extremely noisy. For instance, 58.4 % of the samples were discarded from the time series in the center of the plane of run 313, leading to a gappy signal. For this reason, spectral analysis of PIV data will be omitted. The PIV window in the mid-wing wake

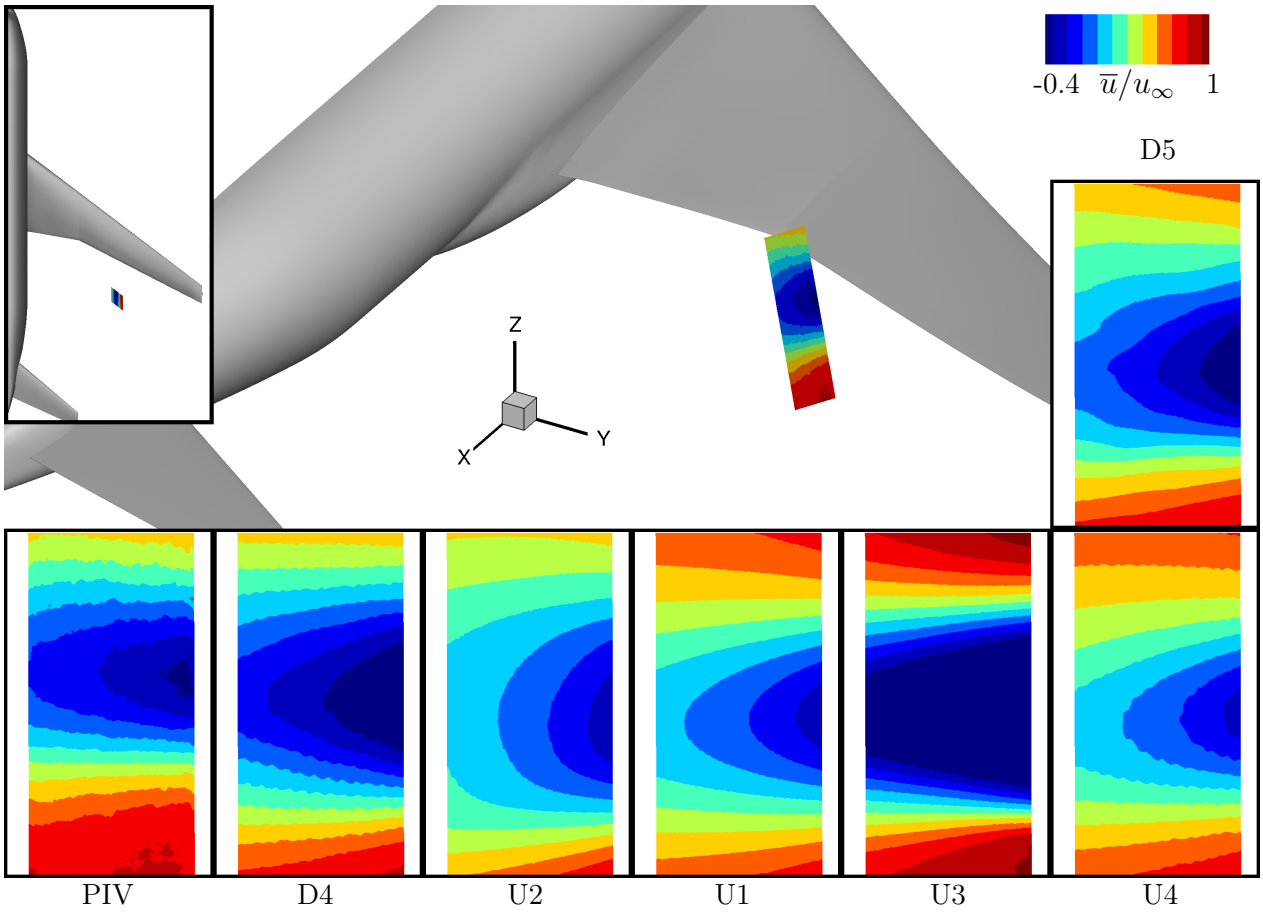

Fig. 5.6.: Location of the PIV window relative to the CRM. Inset contours: mean velocity $\overline{u}/u_\infty$ in WT coordinates. Inflow direction in the insets from the right.

and its relative position to the CRM are shown in Fig. 5.6. The inset distributions of $\overline{u}/u_\infty$ give an overview over the solution topologies. The URANS solutions U1-U3 predict either extremely small or very large vertical extents of the wake in comparison to the PIV data. As the local wing pressure distribution and the vertical position of the wake do not differ much between these simulations at this spanwise position, the differences can only be attributed to different representations of the turbulence behavior in the separated wake. However, there is no consistent trend explaining the differences in wake size. Again, D4 provides the best representation of the measurement, with a similar shape of the low velocity region. The D4 wake appears to be slightly wider in vertical direction than in the PIV data, but the overall topology is well reproduced.

As described by Waldmann et al. [166] and Waldmann et al. [170], data analysis of the wake measurements revealed discrepancies in the wake's vertical position between the simulation and experiments. The wake center in PIV at the nominal window position is systematically located above the location of the corresponding feature in CFD, irrespective of the grid or simulation setup. This is visible in the mean velocity profile on the left in Fig. 5.7. Both the overall forces and the local pressure distribution are well represented by CFD, however. Taking this into account, the local downwash and wake position can be assumed to be correctly resolved in CFD. Remaining sources of error may include erroneous resolution of wake turbulence in CFD, larger than expected influence of wind tunnel walls, or aeroelastic deformation of the support sting leading to model displacement of unknown magnitude. The

discrepancy between PIV and CFD could not be attributed to a single source of error with any certainty.

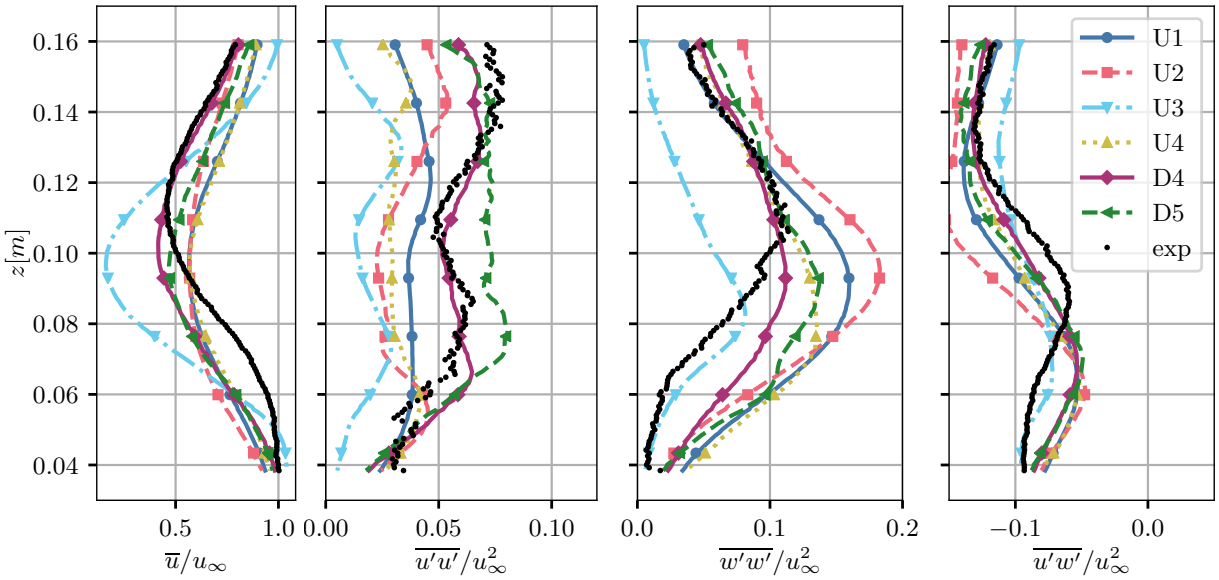

Fig. 5.7.: PIV and CFD results in the wake at $\alpha = 18°$ in wind tunnel coordinates.

Nevertheless, the comparison of quantitative data can provide insight into relative differences between the CFD results and their accuracy in terms of wake size and fluctuation characteristics. Fig. 5.7 shows first and second order statistics extracted at the center of the measurement window. Overall, the measured data is located above the CFD results and tends to indicate a narrower wake. The mean velocity is well reproduced by the DDES run D4, with the URANS results predicting less significant decrease in local velocity. SSG is the outlier, with a significantly stronger velocity deficit, while DDES run D5 underestimates the deficit. The shape of $\overline{u'u'}$ is again best reproduced by DDES, with the URANS models predicting lower fluctuation levels. All simulations predict the two local maxima of the fluctuation levels, which originate from the upper and lower edge of the wake. The vertical fluctuation is overestimated by all URANS except the SSG result. D4 matches the experimental results well in terms of magnitude and overall shape characteristics, with a widening of the wake compared to the experiment discernible in the $\overline{w'w'}$ plot. The shear stress $\overline{u'w'}$ is reasonably estimated by both DDES and U4. Overall, these results indicate good agreement between the statistics obtained from DDES and experiment, with slight discrepancies in the width of the wake.

5.2.2. Inboard Wake in CFD

The most significant differences between the modeling approaches occur in the inboard region, inside the Yehudi break and in the wake between the wing and the tailplane. There is no experimental wake data in this spanwise region, the evaluation of result characteristics and accuracy is therefore based on wing pressure distributions shown in Fig. 5.5.

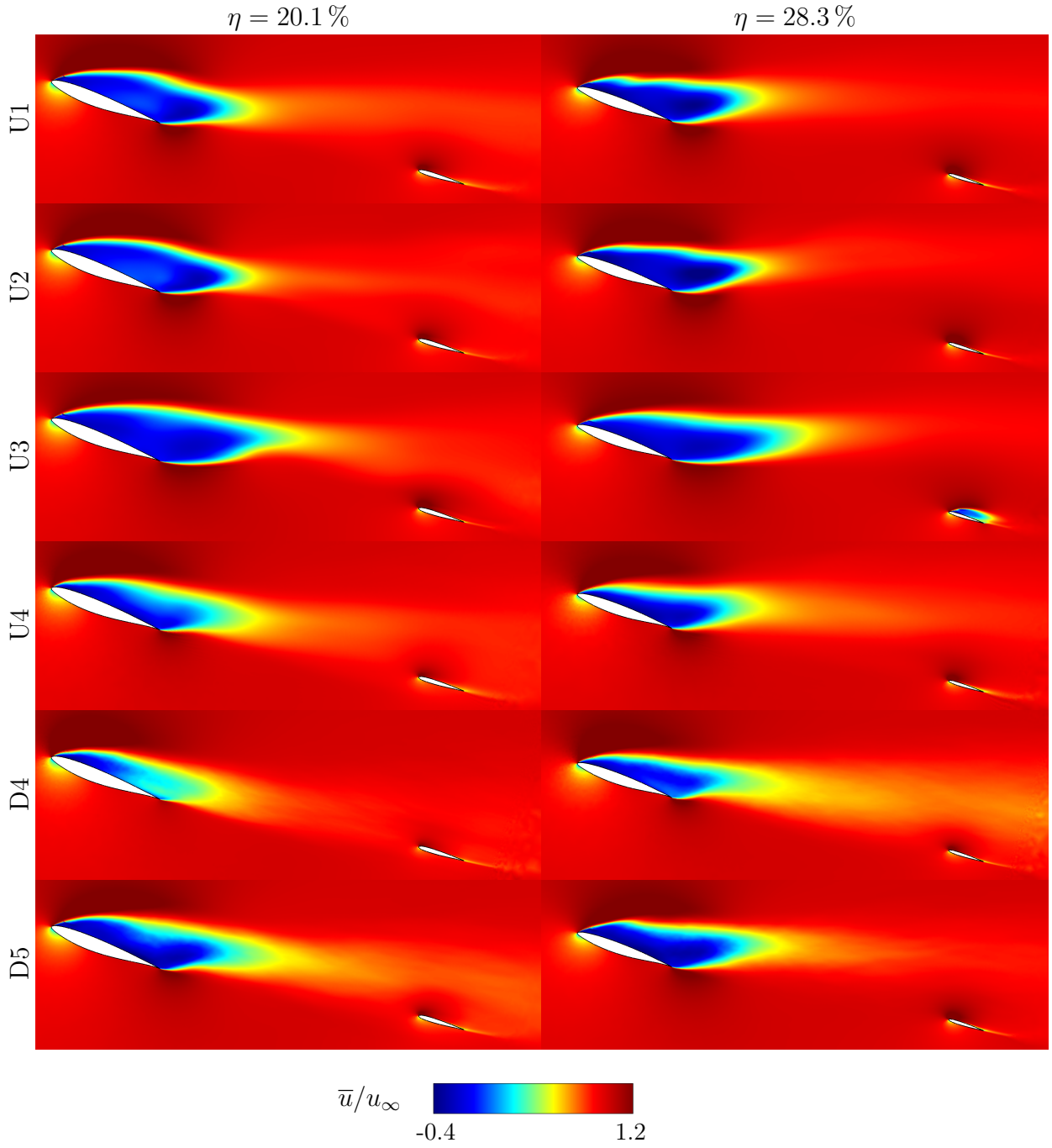

Fig. 5.8.: Inboard mean streamwise velocity distributions $\overline{u}/u_\infty$ at $\eta = 20.1\,\%$ and $\eta = 28.3\,\%$.

First and Second Order Statistics

The wake is analyzed using planar slices of the flow field volume, located at the positions of the pressure measurement rows as shown in Fig. 4.3. The shown results are aligned with the wind tunnel coordinate system WT, i.e. with the inflow horizontally from the left. The averaged streamwise velocities in the inboard wake in Fig. 5.8 show the effect the modeling approaches have on the flow topology. In the time-averaged view, large scale separation at or near the leading edge takes place in all runs and creates a recirculation region. Its shape and extent differ significantly across the simulation types. The URANS runs U1-U3 predict similar topologies at both positions, with wide and long backflow areas that extend far upward

and downstream from the wing. There is some variation between the URANS models, with the U1 model predicting the shortest backflow among them. D4, the run that most closely reproduces the measured pressure distribution by far, predicts significantly shorter backflow regions and simultaneously extended regions of low velocity in the wake. What is more, it predicts stronger downward deflection of the wake consistent with increased sectional lift. U4 and D5 predict some downwash at $\eta = 20.1\,\%$, whereas U1-U3 show largely horizontal flow off the wing. Overall, the more dissipative simulations tend to predict less downwash, larger backflow areas and shorter wakes.

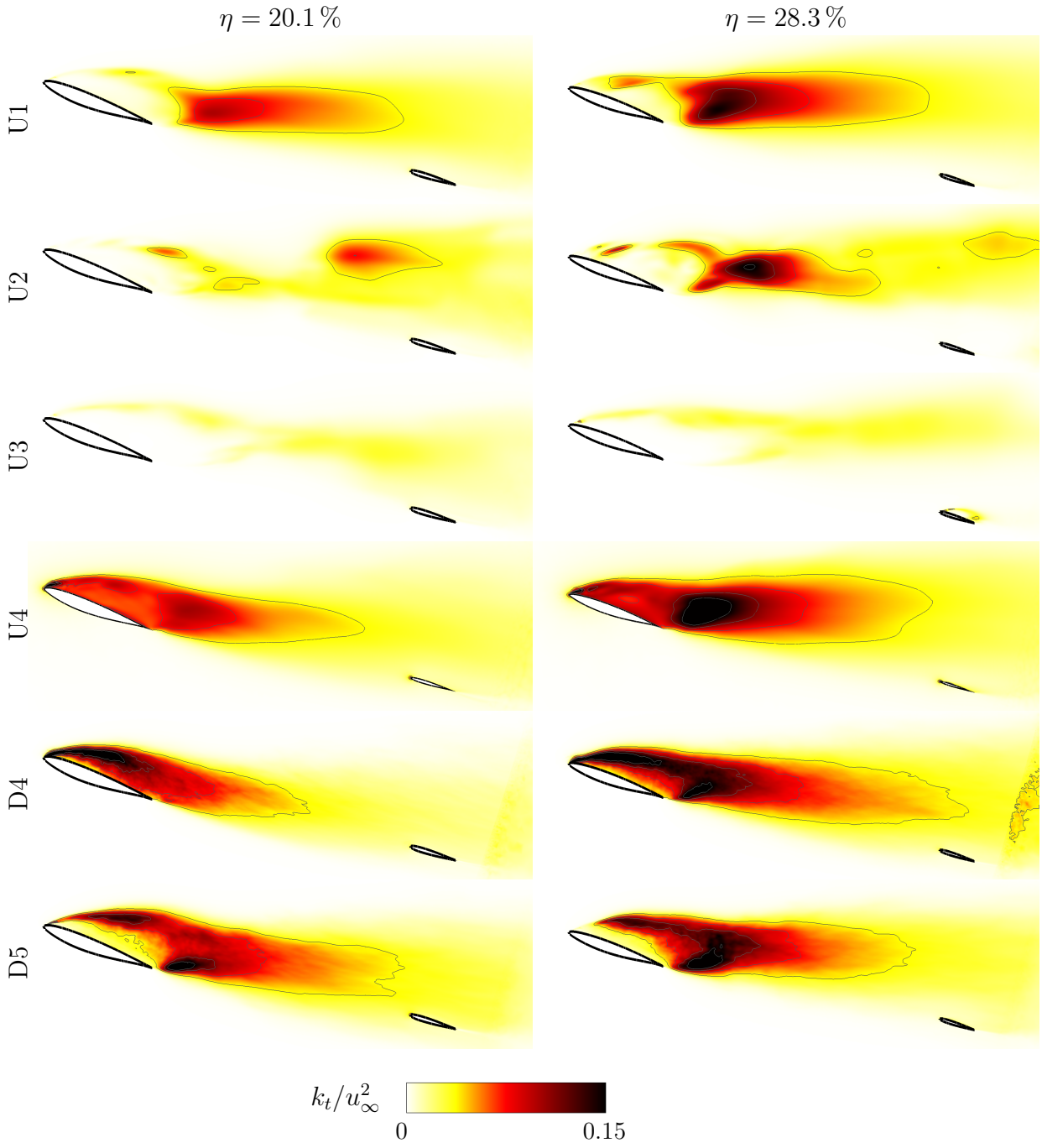

Fig. 5.9.: Inboard resolved k_t distributions at $\eta = 20.1\,\%$ and $\eta = 28.3\,\%$.

The root cause of these differences in backflow size is the effect of the separating shear

layer behavior and the momentum exchange. The distribution of resolved turbulence kinetic energy k_t shown in Fig. 5.9 quantifies these effects. The SSG/LRR-g model predicts an extremely low level of resolved fluctuations overall, with SAO (U1) and SST (U2) performing only marginally better. The broken up sheet of spanwise vortices in U3 in Fig. 5.3 does not translate to significant resolved fluctuations. There is little to no resolved k_t above the wing in U3, suggesting that there is little temporal variation of the recirculation area shape and size.

The low dissipation computations U4 and D4 display high values of k_t close to the leading edge, with this area of high fluctuation growing in size with streamwise distance. This is evidence of significant resolved turbulent motion and the enhanced mixing between the high speed outer flow and the recirculating flow. Furthermore, this explains the shorter streamwise length of the backflow regions in the low dissipation results. Most of the results involve significant levels of k_t in the wake downstream of the wing. The maximum levels of k_t reached in the wake are comparable in magnitude between the solutions. The more significant qualitative differences in terms of resolved turbulence occur in the shear layer and backflow regions. A shear layer which remains stable over a longer distance tends to shield the backflow beneath it from the high momentum outer flow and from turbulent mixing, inhibiting momentum exchange. Conversely, earlier destabilization promotes mixing and decreases the spatial separation. The shear layer in D4 becomes disorganized more rapidly than in the other results, causing an earlier onset of high resolved turbulence and a smaller area of elevated k_t. In essence, the similarity to a bluff body-like flow field diminishes with lower dissipation. The separating streamlines diverge to a lesser degree.. Judging by the agreement of the low dissipation runs with experimental results, the earlier shear layer breakdown and more rapid generation of resolved turbulence ensures a physically more accurate result. In order to achieve this, lower dissipation appears to be much more beneficial than increasing the turbulence model sophistication by replacing the one-equation SA model by SST or RSM.

5.2.3. Dissipation of Resolved Turbulence

The level of artificial dissipation significantly impacts the results in all runs. While the hybrid solutions and U4 predict significant fluctuations above the wing, this occurs only much farther downstream in the URANS results U1-U3 with $k^{(4)} = 1/64$. Lowering the dissipation in URANS has the effect of shifting the high k_t region associated with shear layer fluctuation further upstream, bringing it more in line with hybrid RANS/LES results. Similarly, the appearance of resolved k_t is shifted downstream in D5 , reflecting the stabilizing effect of artificial dissipation.

The dissipation of resolved turbulent fluctuations is a result of multiple effects, in the present case chiefly the artificial dissipation and the eddy viscosity. Using the best-performing DDES D4 as reference, two factors can be observed that are responsible for degradation of accuracy due to suppression of small scale turbulence and the consequences described above: the user-set artificial dissipation $k^{(4)}$ and the inherent dissipation associated with modeling of the small scales. These effects are investigated in isolation.

Comparing D4 and U4 with identical artificial dissipation $k^{(4)} = 1/1024$ permits isolating the effect of the modeling approach. The low artificial dissipation largely eliminates the delay in the generation of resolved fluctuations, enabling the desired quick production of turbulence.

Tab. 5.3.: Time-averaged forces and moments for different computational model approaches. Only runs pertinent to artificial dissipation discussion are shown.

configuration	C_L	$C_{L,wing}$	$C_{L,HTP}$	C_D	C_{My}
experiment	1.08			0.3276	-0.159
D4	1.09	0.784	0.318	0.3372	-0.193
D5	0.98	0.668	0.392	0.3166	-0.356
U1	0.99	0.784	0.331	0.3162	-0.420
U4	1.07	0.763	0.355	0.3398	-0.293

However, the absolute levels of k_t in Fig. 5.9 remain significantly lower in U4 compared to D4. The eddy viscosity assumption remains in place in U4 and stabilizes the flow to some degree. The inhibition of the formation of small scale turbulence does not permit the solution to attain the same levels of resolved k_t in the shear layer as the D4 solution. While lowering $k^{(4)}$ is sufficient in DDES to match the measurement data (i.e. from D5 to D4), the U4 solution suggests that in the absence of significant artificial dissipation of convective fluxes the eddy viscosity acts in a dissipative manner on the resolved gradients.

The delay in onset of resolved k_t downstream of the leading edge affects the inboard pressure distributions in Fig. 5.5. The longer the shear layer remains stable and carries the high momentum flow away from the surface, the more the suction side pressure coefficient gradient tends to remain nearly flat. U4 predicts a slope which is roughly between the constant pressure profile of the high dissipation URANS and the correct one from measurements and D4.

The URANS dissipation occurs via the action of eddy viscosity and its dampening effect on the flow field. The time-averaged eddy viscosity distribution is shown in Fig. 5.10. The sufficient grid resolution enables the DDES SA destruction term to decrease μ_t in D4 to values significantly below those in U4. The latter shows high μ_t in essentially all of the wake.

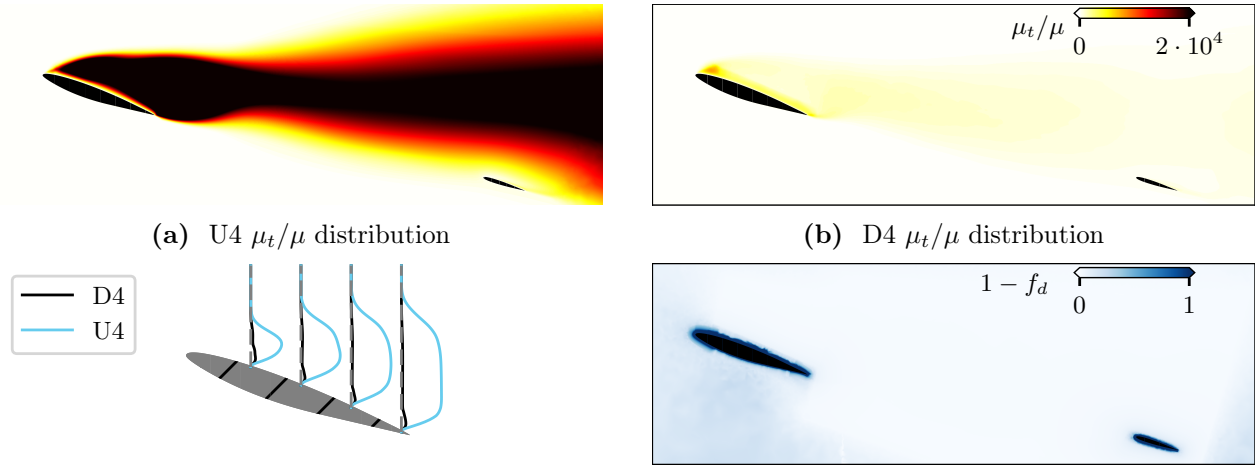

(a) U4 μ_t/μ distribution

(b) D4 μ_t/μ distribution

(c) D4 and U4 μ_t/μ profiles

(d) Distribution of $1 - f_d$ in D4

Fig. 5.10.: Time-averaged eddy viscosity and hybrid model functions at $\eta = 28.3\,\%$ for low-dissipation URANS (U4) and DDES (D4).

Fig. 5.10c shows quantitative vertical profiles of the eddy viscosity ratio μ_t/μ in the shear layer and the backflow region above the wing. The U4 solution attains values of 20000 at each

of the four shown locations, with quantitative scales omitted for clarity. This value is the solver limiter setting in this particular run, variation of which had not shown any influence on the result. While DDES reaches values on the order of 10^3 initially, the eddy viscosity decays quickly further downstream. High eddy viscosity levels like in U4 prevent the simulation from resolving the turbulent energy cascade (cf. Fig. 3.1), which can be observed via the lower resolved levels of k_t in U4 compared to D4 in Fig. 5.9. While the very low wave number region is resolved in space and time, the turbulent decay processes are modelled via the turbulence model. Imposing lower limits does not appear promising, as there is no physical justification for a particular value. What is more, the values significantly vary depending on the location and solution time. Therefore the DDES method is the more robust and accurate in this flow situation.

The mechanism acting to lower the eddy viscosity in DDES is dependent on increasing the destruction term where possible, promoting LES-like behavior. The switch between RANS and LES-like areas is controlled by the term f_d in the DDES model, which is 1 where lowering the length scale down to $C_{DES}\Delta$ is permitted. f_d approaches 0 close to walls, where it forces the model to remain in RANS mode. This is visualized for D4 in Fig. 5.10d, using the quantity $1 - f_d$ common in literature. LES-like resolution is enabled everywhere except the very wall-adjacent regions, which is desired behavior for this type of model.

Wake Flow Direction and Tailplane Impact

The above observations lead to the conclusion that the artificial dissipation plays a large role in the propagation and decay of turbulent phenomena in the hybrid simulations. In order to better understand this dependence, the isolated influence of $k^{(4)}$ is evaluated via the DDES runs at $k^{(4)} = 1/64$ (D5) and $k^{(4)} = 1/1024$ (D4). An additional result obtained with $k^{(4)} = 1/128$ is shown where appropriate, in order to visualize trends.

(a) Wake **(b)** Zoom to shear layer region

Fig. 5.11.: Contour lines of $\overline{u}/u_\infty$ in the $\eta = 28.3\%$ plane. Contour lines at $\overline{u}/u_\infty = \{0, 0.4, 0.8\}$.

The local fluctuation characteristics in the shear layer drive the shape of the separated region and the backflow. Changes to it determine the large scale characteristics of the wake. The association of mean direction of the shear layer flow and the resulting wake direction is shown in the contour plot of streamwise velocity in Fig. 5.11. The angle and general flow direction of the wake downstream do not change in isolation. Viewed more closely near the leading edge shear layer in Fig. 5.11b, the streamwise velocity isolines corresponding to $k^{(4)} = 1/1024$ are less inclined away from the surface than with high dissipation. The extent of the backflow region represented by the $\overline{u} = 0$ isoline decreases. Conversely, the region enclosed by the $\overline{u}/u_\infty = 0.8$ isoline extends furthest downstream into the wake and is more inclined downward than in the $k^{(4)} = 1/64$ case.

Quantitatively, this wake deflection can be described using the distribution of time-average

local flow angle $\xi = arctan(\overline{w}/\overline{u})$. Spatially averaging ξ over the vertical extent of the wake at each streamwise position x to obtain a local mean $\tilde{\xi}(x)$[1] results in Figs. 5.12a and 5.12d. $\tilde{\xi}(x)$ represents flow parallel to the inflow, and negative values indicate downwash. The upward deflection toward the downstream end of the plots is the upwash effect resulting from the tailplane leading edge. $k^{(4)} = 1/1024$ results in a significant downwash at both spanwise positions, while it is reduced in the higher dissipation runs, where ξ is almost zero at $\eta = 28.3\,\%$. The magnitude of ξ strongly depends on artificial dissipation and is generally consistent with the pressure distributions.

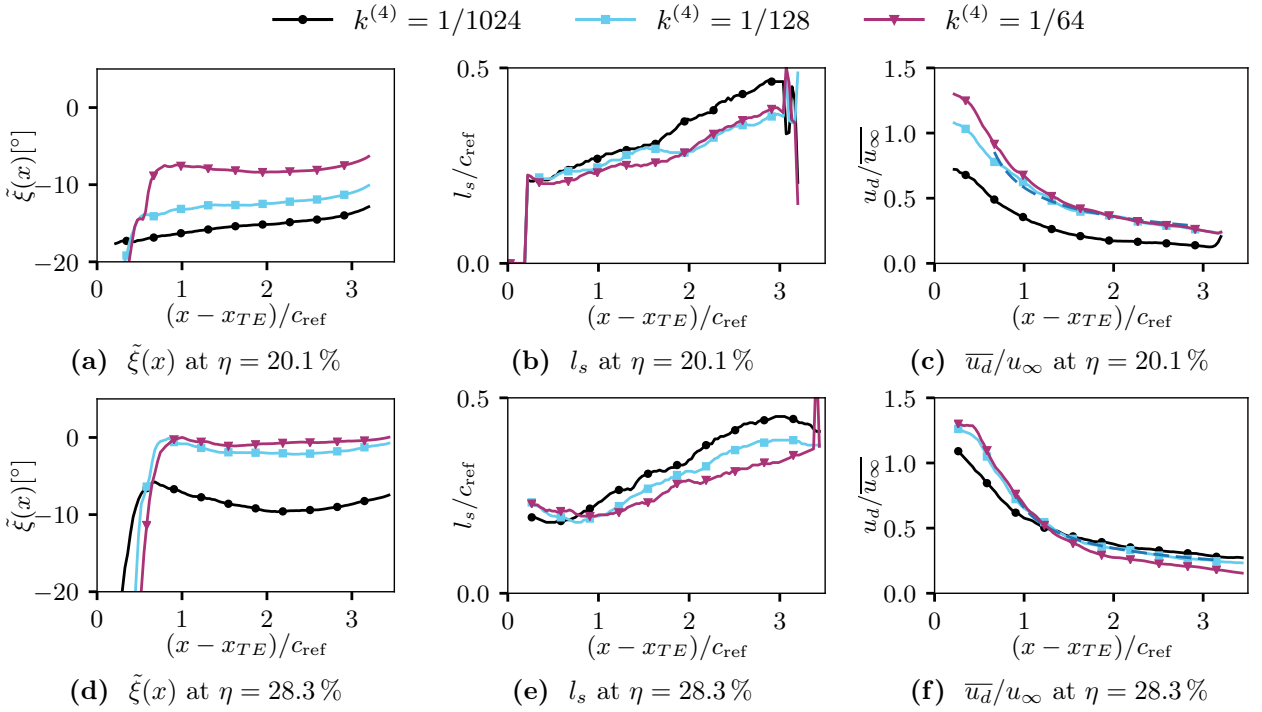

(a) $\tilde{\xi}(x)$ at $\eta = 20.1\,\%$ **(b)** l_s at $\eta = 20.1\,\%$ **(c)** $\overline{u_d}/u_\infty$ at $\eta = 20.1\,\%$

(d) $\tilde{\xi}(x)$ at $\eta = 28.3\,\%$ **(e)** l_s at $\eta = 28.3\,\%$ **(f)** $\overline{u_d}/u_\infty$ at $\eta = 28.3\,\%$

Fig. 5.12.: Streamwise evolution of inboard wake properties at $\eta = 20.1\,\%$ and $\eta = 28.3\,\%$ for 3 dissipation settings. x axis coordinate originates at the trailing edge position.

The wake half-width l_s in Figs. 5.12b and 5.12e is more noisy, with values increasing with streamwise distance after a short distance past the trailing edge. l_s reflects in quantitative terms the narrow width of the area enclosed by the $\overline{u}/u_\infty$ isolines at $k^{(4)} = 1/64$ in Fig. 5.11a compared to that at low dissipation. Although the low dissipation D4 run exhibits a decrease in the size of the near wing region where $\overline{u} < 0$ in Fig. 5.11, it has the largest values of l_s downstream from the wing.

The wake deficit $\overline{u_d}/u_\infty$ at $\eta = 20.1\,\%$ is lowest with $k^{(4)} = 1/1024$ and remains so over the entire streamwise distance. The difference due to $k^{(4)}$ is less pronounced at $\eta = 28.3\,\%$ and exists only in the very near wake close to the wing trailing edge. The large differences in initial u_d due to $k^{(4)}$ can be attributed to increased mixing due to low dissipation, which promotes a narrower recirculation region and therefore decreased loss of streamwise momentum. Effectively, increased mixing above the wing permits filling the wake with high momentum fluid from outside the wake. However, the streamwise gradient of u_d is consistently highest at high dissipation and can be seen in the slopes of u_d in the figures. This can be interpreted

[1]The averaging is carried out over a vertical extent between $-0.75c_{\mathrm{ref}}$ below the trailing edge position to $0.85c_{\mathrm{ref}}$ above it.

as a result of high artificial dissipation acting in a manner promoting the equilibration of spatial velocity gradients. Therefore, the mean size of backflow near the wing is large when the dissipation is high, while on the other hand it decreases in size much more quickly downstream. At $k^{(4)} = 1/1024$, the small scale fluctuations can therefore persist for over a longer distance and continue interacting with the outer flow, which enables the continued increase of l_s.

The above description is consistent with the high levels of k_t concentrated near the leading edge of solution D4 as opposed to D5, as seen in Fig. 5.9. At $\eta = 28.3\,\%$, the area of high k_t is large overall and persists over a longer distance. This is reversed at $\eta = 20.1\,\%$, where the early onset of resolved fluctuation in D4 reduces the recirculation area height to such an extent compared to D5 that the total amount of k_t in the wake is reduced. This causes the inboard wake downstream from the wing to become smaller in terms of k_t. This decrease is illustrated via a field slice perpendicular to the inflow in Fig. 5.13, with the two vertical lines in both images showing how the distribution of k_t differs at $\eta = 20.1\,\%$ from that at $\eta = 28.3\,\%$.

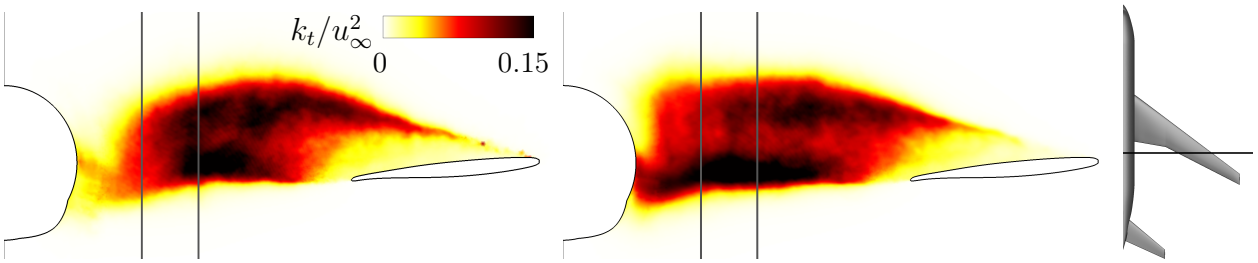

(a) $k^{(4)} = 1/1024$ (D4) **(b)** $k^{(4)} = 1/64$ (D5) **(c)** Slice position

Fig. 5.13.: Resolved turbulence kinetic energy k_t in plane perpendicular to the inflow at $x/c_{ref} = 5.7$. Vertical lines represent positions $\eta = 20.1\,\%$ and $\eta = 28.3\,\%$.

Spectral Considerations

Excessive dissipation of resolved fluctuations results in attenuation of velocity fluctuation spectra in the wake. Point data in the inboard wake obtained at the full sampling frequency of the simulation illustrates this. The points are located at the inboard slices about 1 local chord downstream from the trailing edge, with point 1 at $\eta = 28.3\,\%$ and point 2 at $\eta = 20.1\,\%$. Fig. 5.14 shows spectral densities of streamwise velocity time series at the two positions in the wake[2]. The analysis points are positioned in high-fluctuation regions in the wake at the two η stations, ensuring that high levels of k_t are present in all cases. The varying flow topologies and positions of the fluctuation maxima across the runs do not allow perfect comparability, but the spectral shapes can be nonetheless informative.

The hybrid model results D4 and D5 show a pronounced inertial range between about $f = 100\,\mathrm{Hz}$ and $f = 2000\,\mathrm{Hz}$ at both positions, which is indicated by a dashed line. The spectra deviate from the $-5/3$ line at the end of the predicted inertial range, with the amplitude drop-off occurring at slightly lower frequencies in the D5 run than in D4. The inertial range does not appear as clearly in the URANS results. U4 shows a significant drop-off at much

[2]point 1: $\eta = 28.3\,\%$, $x = 1.363\,\mathrm{m}$, $z = 0.076\,\mathrm{m}$; point 2: $\eta = 20.1\,\%$, $x = 1.153\,\mathrm{m}$, $z = 0.091\,\mathrm{m}$ in the AC system.

lower frequencies than the DDES spectra, which is expected considering the amount of eddy viscosity present in the wake. This shows that small scale turbulence cannot be reliably predicted using this method.

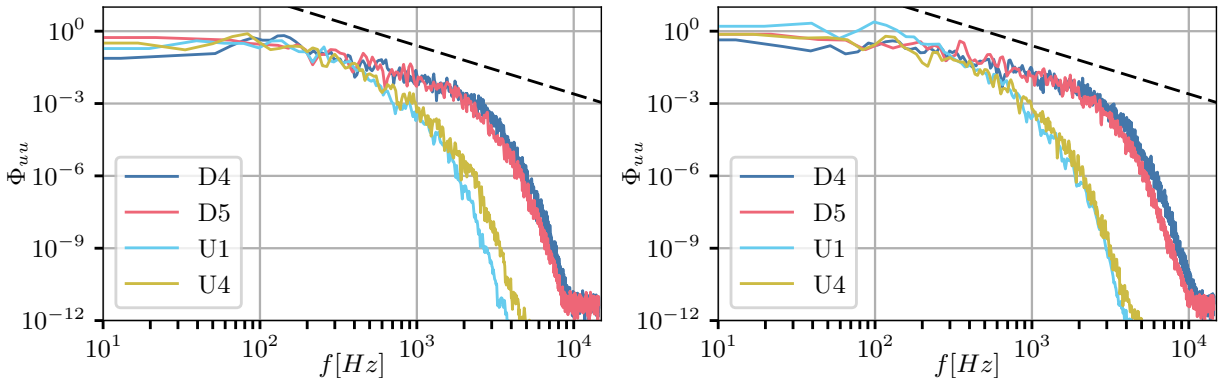

(a) point 1, $\eta = 28.3\,\%$ **(b)** point 2, $\eta = 20.1\,\%$

Fig. 5.14.: Power spectral densities of streamwise velocity u for U1, U4, D4 and D5. Dashed line represents a -5/3 slope.

Overall, strong discrepancies between URANS and DDES spectra occur only above approximately 400 Hz. This reinforces the expectation that URANS is generally capable of propagating resolved flow unsteadiness over large parts of the spectrum. Considering that major wake phenomena such as a von Kármán vortex street can be expected to occur at a Strouhal number of $Sr_d \approx 0.2$ resp. $f \approx 150\,\text{Hz}$, the propagation of these features does not appear to be a problem in URANS.

However, the turbulence conditions generated at the separation location at the wing leading edge act as the input for the formation of the turbulence field in the wake. The processes in the shear layer are associated with significantly higher frequencies than in the downstream wake itself. For instance, Wu et al. [176] showed an analysis of airfoils involving separating shear layers and vortex shedding, with the characteristic frequency of the latter being significantly higher than that of the shear layer fluctuations. As explained in Chapter 2.2.2, the frequency of mixing processes scales with the shear layer thickness. As this length scale is much smaller than the large scale structures in the wake, the associated frequencies are correspondingly higher. It is the shear layer fluctuation that needs to be properly resolved, which both U4 and D5 fail to do due to their respective sources of dissipation. While lower-frequency portions of the turbulence spectrum can be resolved with correct amplitudes, the suppression of small-scale turbulence has such a significant effect on the flow field that it alters the overall flow topology and introduces the issues described above.

URANS employing the SA model is evidently not a reasonable approach for this type of flow. Simulations using different types of turbulence models did not provide any improvement, as discussed in Sections 5.2.1 and 5.2.2. These simulations are unable to match the validation PIV data in the mid-wing wake, and they predict inboard wake topologies that are vastly different from those obtained in the D4 run. Therefore, the only feasible modeling approach amongst those presented above is the low-dissipation hybrid RANS/LES as used for run D4. The remainder of the work will focus on this type of approach and settings.

5.2.4. Spatial and Temporal Resolution

The resolution requirements and grid complexity in the low speed stall configuration are not conducive for the use of rigorous error estimation such as the grid convergence index (GCI) by Roache [116]. Spalart [141] described the difficulties in grid and time step size estimation when using DES, mostly due to the fact that a feasible test of the grid resolution Δ would require comparisons with results obtained with possibly prohibitively expensive grids of resolution $\Delta/2$. The issue is in the required physical run time of the computations. While it is possible to obtain reliable first order statistics in a reasonable time frame even for a large grid, it is not feasible to conduct multiple runs for parameter studies of inflow condition variations on such grids while expecting reasonable higher-order statistics. It is nevertheless important to understand the effects of the spatial and temporal resolution. Spalart's criterion involving the CFL number in the focus region, in this case the hexahedral wake block containing the separated wake, is used in the following. CFL_{FR} is computed via Eq. 5.1.

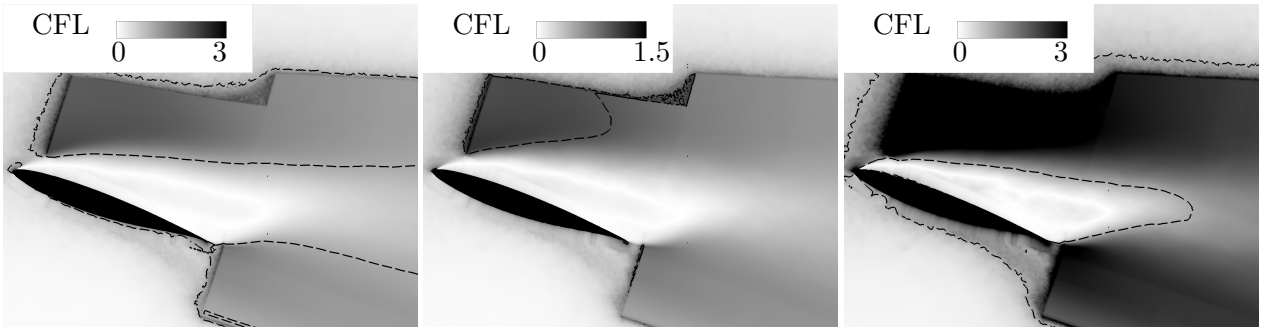

(a) run 1, $CFL_{FR} < 2$ **(b)** run 2, $CFL_{FR} < 1$ **(c)** run 3, $CFL_{FR} < 4$

Fig. 5.15.: Convective CFL number at 28.3% semispan. Dashed line denotes CFL = 1.

As with the local grid size variation described in Section 5.1, the local CFL number varies in space and should be interpreted as a characteristic, representative quantity. The characteristic $\mathrm{CFL_{FR}}$ in the focus region FR, from which the computational time step is derived via the CFL condition described in Section 5.2, is used for this purpose. A total of 6 runs at identical inflow conditions are compared in order to evaluate spatial and temporal resolution effects, with the parameters listed in Table 5.4. Runs 1-3 isolate the effect of the computational time step using grid A, while the others permit the evaluation of grid size, Δt and $\mathrm{CFL_{FR}}$.

Tab. 5.4.: Time step and grid variation.

run	Δt $[t_\infty]$	grid	$\mathrm{CFL_{FR}}$ [−]
1 (D4)	0.01	A	2
2	0.005	A	1
3	0.02	A	4
4	0.01	B	1
5	0.02	B	2
6	0.01	C	2

The distribution of CFL for runs 1, 2 and 3 using grid A in Fig. 5.15 shows that its value stays below 1 over most of the region when using $\Delta t = 0.005 t_\infty$ (run 2), while calculation D4 (run 1) with $\Delta t = 0.01 t_\infty$ reveals significant regions where CFL > 1. This does not play a large role for the pressure distribution in Fig. 5.16, showing largely matching results. The small scale variation of the mean pressure lines can be attributed to the fact that not all cases were averaged over the same duration due to the aforementioned computational constraints. Salient features such as absolute c_p levels, chordwise pressure gradients, and positions of suction peaks are well matched at all positions. This suggests that $\mathrm{CFL}_{\mathrm{FR}} < 2$ suffices at the spatial resolution of grid A.

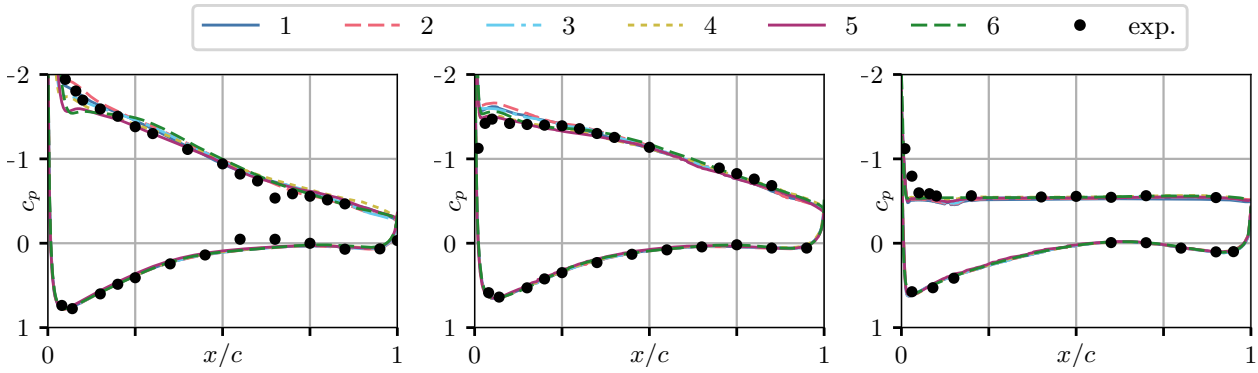

(a) $\eta = 13.1\,\%$ **(b)** $\eta = 20.1\,\%$ **(c)** $\eta = 60.3\,\%$

Fig. 5.16.: Wing pressure distributions at $\alpha = 18°$ for different grids and Δt.

Due to different resolutions in the FR, Spalart's [141] CFL number criterion leads to different physical time steps for grids A and B. For grid A, CFL $= 2$ corresponds to $\Delta t = 0.01 t_\infty$, while for grid B CFL $= 2$ corresponds to $\Delta t = 0.02 t_\infty$. Fig. 5.16 displays the agreement among the different cases, and how they stack up relative to each other. The pressure distributions suggest that the flow topologies are well reproduced by the calculations. In contrast to the above wake discussions, the inboard positions $\eta = 13.1\,\%$ and $\eta = 20.1\,\%$ are shown instead of $\eta = 28.3\,\%$, as the differences are discernible only at these positions. The pressure coefficients at the time-averaged suction peak near the leading edge differ across the cases. There is no trend in terms of temporal or spatial resolution that lends itself for an explanation, leading to the conclusion that this is a random effect and possibly attributable to very low frequency variation that cannot be captured by the collected signals during the simulated time. The pressure distribution at $\eta = 60.3\,\%$ in Fig. 5.16c is representative of the remainder of the wing, with barely visible deviations between the lines. The overall forces also vary only slightly.

Further downstream the wake, different physical time step sizes determine the maximum resolvable fluctuation frequency and the onset of the amplitude drop-off in the high frequency range of the turbulence spectrum. Fig. 5.17 shows spectra for runs 1-6 obtained at the same two points as Fig. 5.14. The shapes of the spectra suggest that high sampling rate is not decisive for the reproduction of general fluctuation characteristics. All runs show a distinct inertial range, which is shortened when coarser grids and time steps are used. The coarser resolutions do not result in qualitative changes to the accuracy, they only limit the amount of useable spectral range for data analysis.

The results suggest that a decrease of the CFL number from 2 to 1 in the wake is of limited utility, in other words that the criterion $CFL = 1$ can be relaxed just as predicted by

Spalart [141]. Even runs 3 and 5 with the coarsest time step indicate acceptable results in terms of pressure distribution and forces, although it needs to be mentioned run 5 with the combination of coarsest grid and largest time step causes a distinct shortening of the inertial region in the spectrum and early amplitude drop-off. Considering the advantage in simulation runtime and storage requirements of grid B, most of the analysis will be carried out using settings from run 4. This permits longer runtimes and improved frequency resolution.

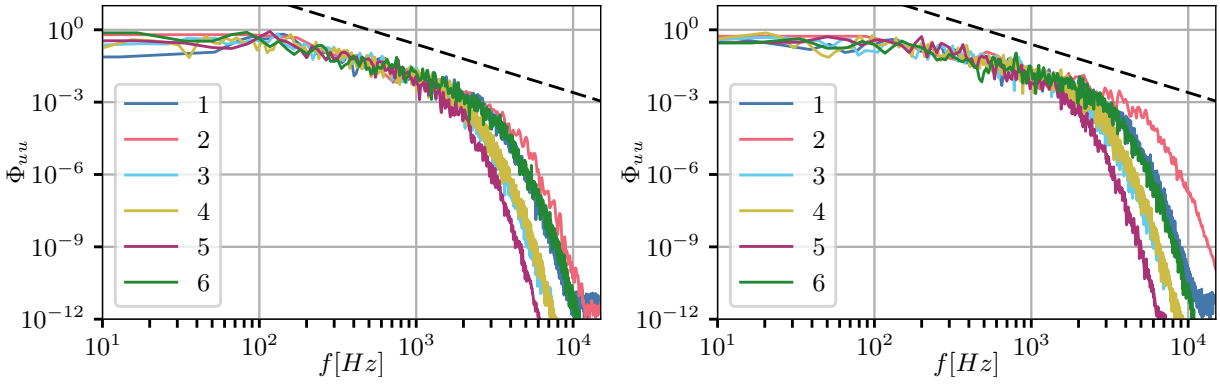

(a) point 1, $\eta = 28.3\,\%$ **(b)** point 2, $\eta = 20.1\,\%$

Fig. 5.17.: Power spectral densities of u for different resolutions. Dashed line represents $-5/3$ slope indicating inertial range.

5.3. Sensitivity to Model Configuration

The CRM exists in a WB (wing-body) and a WBTn (wing-body-tail) configuration[3], with n denoting the angle of incidence of the horizontail tailplane. Three different types of geometry were involved in the study:

- WBT0: wing-body-tail with the stabilizer at 0°, which is the nominal $1g$ free flight configuration
- WBT0d: WBT0 with aeroelastic deformation measured in the wind tunnel applied to the wing, deforming it beyond the intended $1g$ free flight shape
- WBT0ssd: WBT0d with the addition of the wind tunnel support system

WBT0d is considered the nominal configuration in this study, being close to the free flight configuration which is the one of interest from a scientific point of view. This conflicts with the goal of validation, as WBT0ssd is the configuration closest to the experimental ground truth. The modeling fidelity in terms of geometric configuration may have an effect on the results. This section shows the discrepancies arising from the comparison of WBT0d with the actual wind tunnel configuration, WBT0ssd, and the effect of including the wing deformation. The three model configurations are visualized in Fig. 5.18 with different colors highlighting the areas where changes occur. The inset zoomed-in wingtip shows that the deflection is not large and occurs mostly outboard of the regions of interest.

Accordingly, the difference in terms of forces in Table 5.5 between the deformed and undeformed wing is rather small, owing to the low magnitude of the deformation. All results

[3]The possibility of engine nacelle installation is not considered here.

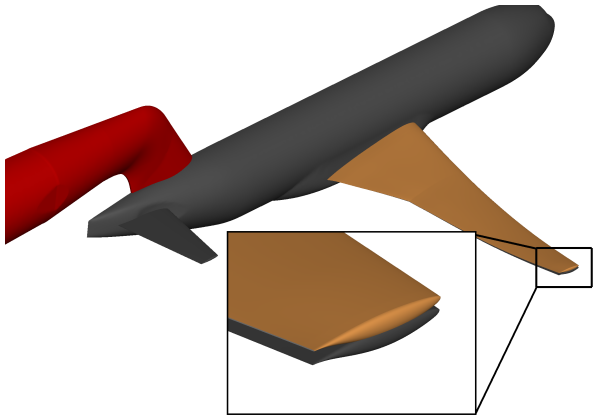

Fig. 5.18.: Configuration differences: Grey surface is baseline CRM WBT0. WBT0d deformed wing shown in yellow, WBT0ssd support system in red.

Tab. 5.5.: Time-averaged forces and moments for different CRM configurations.

configuration	C_L	$C_{L,wing}$	$C_{L,HTP}$	C_D	C_{My}
experiment	1.078			0.3276	-0.159
WBT0	1.078	0.7730	0.328	0.3386	-0.199
WBT0d	1.0868	0.7838	0.316	0.3372	-0.193
WBT0ssd	1.067	0.7752	0.286	0.331	-0.136

are within a narrow error band, with most of the variation occurring in the HTP lift and, consequently, the overall pitching moment. Wing lift is affected to a much smaller degree. The difference in tailplane lift between WBT0 and WBT0d is significantly smaller than that between WBT0d and WBT0ssd. Fig. 5.19a visualizes this, showing a consistent decrease of the $C_{L,HTP}(\eta_{HTP})$ along the tailplane span. The inboard lift coefficient differs only slightly, as the deformation has little effect there. It is more markedly reduced by the presence of the support sting (WBT0ssd), which reduces the Mach number upstream from it via the far field effect, as described in Waldmann et al. [167] and in Chapter 4.

Considering the fact that the deformation magnitude in the inboard wing region is extremely small, any difference between WBT0 and WBT0d in this area is unlikely to be be caused

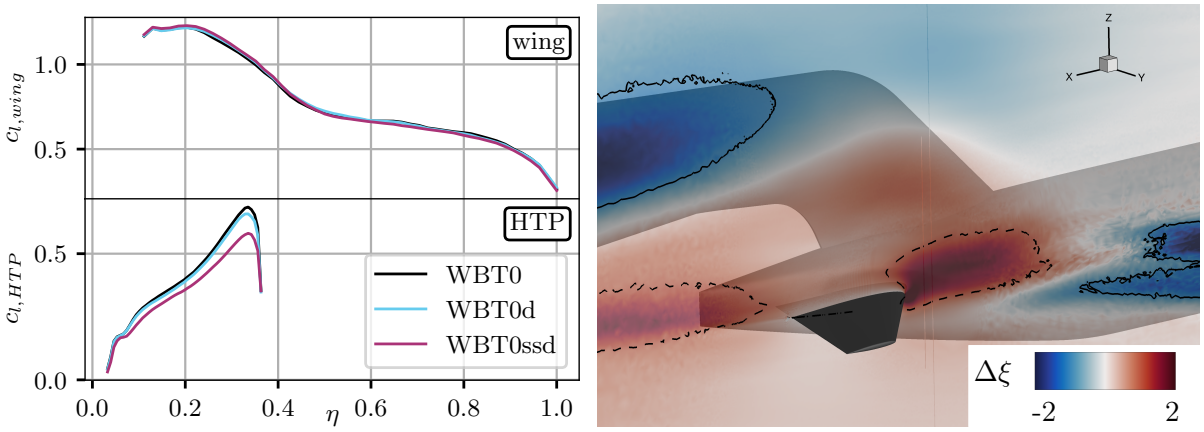

(a) Wing and HTP lift coefficient distributions **(b)** $\Delta\xi = \xi_{\mathrm{WBT0d}} - \xi_{\mathrm{WBT0ssd}}$ at $\eta = 10.7\,\%$

Fig. 5.19.: Configuration effects.

by it. More probably, the small difference is a result of imperfect statistical convergence due to limited averaging time of 50 t_∞ for WBT0. The slight increase of $C_{L,HTP}$ for WBT0d is consistent with the decrease in $C_{L,wing}$, as the latter increases the local downwash. The sting's effect on $C_{L,HTP}$ is more significant, reducing the tailplane lift over its entire span. Also, the support system's effect on $C_{L,HTP}$ is greater than on $C_{L,wing}$, which suggests that the support system influences the forces largely via local flow field modification around the aft portion of the aircraft.

This flow field modification is recognizable in Fig. 5.19b. The local flow angle in the flow field slice close to the fuselage at $\eta = 10.7\,\%$ is altered by the presence of the sting with a large diameter above and behind the fuselage. Fig., 5.19b shows the increment of the local flow field angle $\Delta\xi$ caused by the presence of the support system. The flow is diverted upward above the widest point of the sting, and downward below it. This downward deflection influences the tailplane flow, lowering the effective inflow angle of the stabilizer. This reduced $\alpha_{HTP,eff}$ results in a lower lift coefficient at the tailplane.

The drag, which is slightly overpredicted with WBT0, decreases toward the experimental value when model fidelity is improved by including the deformation and support system. The pitching moment, being the quantity that is most sensitive to flow field alterations between the wake and the tailplane, shows very little change between WBT0 and WBT0d. WBT0ssd causes an appreciable difference with respect to the other two. However, the difference in C_{My} across the configurations is significantly smaller than that across the simulation types. These results show that, while accuracy can potentially be improved by the inclusion of the support system, the WBT0d configuration which is more representative of free flight does not fundamentally alter the wake flow physics and will therefore be employed in the subsequent studies.

5.4. Sensitivity to Reynolds Number

At constant M_∞, the variation of Re represents different flight altitudes due to changing density. While the study is aimed at the investigation of stall at flight-like Reynolds numbers, a specific variation of inflow Reynolds number was conducted in order to confirm which effects can be expected. Moreover, the validation conditions at $Re_\infty = 11.6 \cdot 10^6$ chosen due to experimental constraints are far from the CRM's cruise design point of $Re_\infty = 40 \cdot 10^6$. The selected Reynolds numbers are intended to evaluate a range around the nominal value of $Re_\infty = 11.6 \cdot 10^6$ from the wind tunnel campaign. A higher value of $Re_\infty = 25 \cdot 10^6$ was selected close to the design point of the CRM in high lift configuration, which is at $Re_\infty = 24.6 \cdot 10^6$ and $M_\infty = 0.2$The lower value of $Re_\infty = 5 \cdot 10^6$ is based on the fact that it is a commonly used condition for the CRM [77, 161]. The Reynolds number is a measure of flight altitude at constant Mach number, with the high value of $Re_\infty = 25 \cdot 10^6$ corresponding to the lowest altitudes. Such

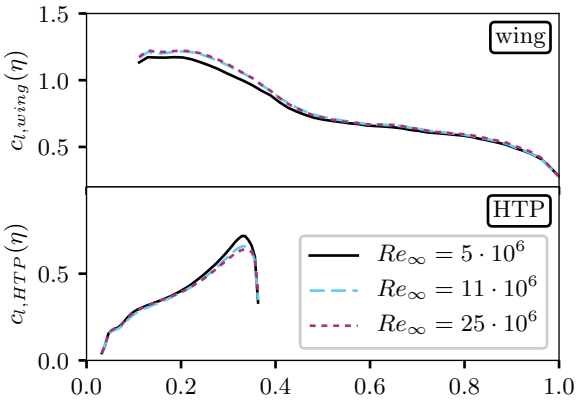

Fig. 5.20.: Spanwise distribution of wing and tailplane loads at different Re_∞.

conditions are representative of a subsonic stall occurring at altitudes of around 10000 ft.

An expansion of the simulated Reynolds number range is beneficial from the point of view of confidence in the predictive qualities of the simulation. The analysis is conducted using WBT0 and the settings from run D4, using grid B. The inflow Reynolds number is prescribed in TAU at the farfield boundary condition, which changes the inflow pressure and temperature. This means that u_∞ remains constant, causing the resolution-related properties of the simulation such as time step and CFL number to remain unchanged. The balance of inertial and viscous forces does change, however. The flow topology sees little change across the three values of Re_∞. The spanwise distributions of wing and tailplane lift coefficient in Fig. 5.20 remain similar, with especially little change in the forces above $Re_\infty = 11.6 \cdot 10^6$. This suggests that the nominal Reynolds number of $11.6 \cdot 10^6$ is representative of high Reynolds number flight, and that little change should be expected toward even higher Reynolds numbers. Lower Re_∞ causes lower inboard lift and increases tailplane lift. The increase in tailplane lift at low Reynolds number is a consequence of the decreased wing lift shown in Fig. 5.20, as the latter is associated with a decrease in downwash and an increase in $\alpha_{\text{eff},HTP}$.

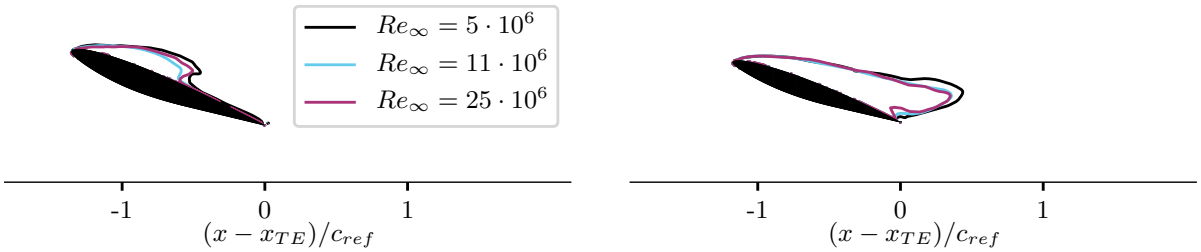

(a) $\eta = 20.1\,\%$ **(b)** $\eta = 28.3\,\%$

Fig. 5.21.: Isoline $\overline{u} = 0$ at $\alpha = 18°$ at inboard wing for three different Reynolds numbers.

The reason for the decrease in inboard lift can be found in the corresponding velocity distributions shown in Fig. 5.21. The shape of the backflow at $Re_\infty = 5 \cdot 10^6$ is elongated compared to the higher Reynolds numbers. The increased area enclosed by the isoline is a metric for the size of the recirculation area. In other words, decreasing Re_∞ causes the near wake flow field around the inboard wing section to resemble that around a body with increased bluffness. The associated loss of lift and decrease in the wing section's ability to generate downwash are consequences of this, causing increased lift at the tailplane.

5.5. Analysis of Uncertainty due to Temporal Sampling

Following the discussion of correlated statistics in Chapter 3, the expected reliability and accuracy of the obtained statistics from the hybrid RANS/LES simulation runs are evaluated before focusing on the flow physics. Parts of this section are adapted from Waldmann et al. [169].

The simulations were run over 50 t_∞ to 100 t_∞, with some exceeding 200 t_∞ depending on priority and available resources. The study in this section permits to estimate the necessary number of physical time steps for the simulation run. The main run carried out using grid B at $\Delta t = 0.01 t_\infty$ serves as benchmark, as it was run over 220 t_∞ after the initial transient.

This is a long runtime which is not possible to replicate for all cases and grids, but a useful baseline for investigation.

While means are accumulated in the solver at runtime at every grid point, postprocessing requires storage of time-resolved data. Storage of every grid point at every time step is impossible due to limited resources, therefore the postprocessing methods use planar data collected at a sampling rate below that of the unsteady simulation. Typically, only every tenth time step is written to disk and stored for later processing. A run with nominal time step of $\Delta t = 0.01 t_\infty$ therefore yields data at 10 samples per t_∞, which corresponds to a sampling rate of $f_s = 2883\,\mathrm{Hz}$. This is intended to reduce the storage requirements of the dataset. The wake point spectra in Figs. 5.14 and 5.17 indicate that this f_s is sufficiently far at the upper end of the inertial range. Considering that effects such as bluff body vortex street fluctuations can be expected to take place around $Sr_d \approx 0.2$, which corresponds to 100 Hz - 200 Hz depending on spanwise location determining d, this sampling rate f_s is assumed to suffice.

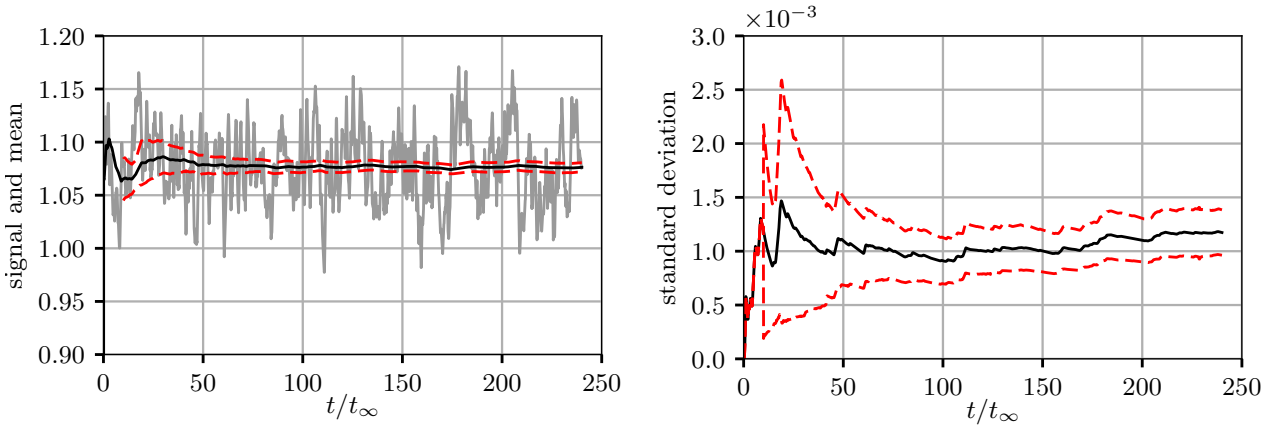

(a) Signal and running mean

(b) Running variance

Fig. 5.22.: Running statistics of the aircraft lift coefficient. Dashed lines represent confidence boundaries for each statistic according to Eq. 3.27.

Fig. 5.22a shows the overall aircraft lift signal and its running mean over the entire runtime. The running mean at each time instant t is obtained from the signal recorded from $t = 0$ until t. The running signal variance is shown in a similar manner in Fig. 5.22b. Sampled at 2883 Hz, this signal consists of $N = 2200$ samples.

Fig. 5.23 shows how the lift coefficient signals of the wing and tailplane involve vastly different time scales. Time scales are computed from the ACF via Eq. 3.25 using $R_{ii} = 0.2$ as threshold for the integration. It is interesting to note that the wing lift fluctuation is correlated over longer temporal distances than the HTP. The wing fluctuation characteristic is dominated by large scale, low frequency events, which are associated to its large surface area being subjected to large scale dynamics. While the tailplane is dominated by shorter scale events and its lift coefficient signal becomes decorrelated after 7 lags or $0.7 t_\infty$, the wing signal requires 48 samples resp. $4.8 t_\infty$. Using Eq. 3.24, these values can be converted to $N_{\mathrm{eff,wing}} = 58$ and $N_{\mathrm{eff,HTP}} = 274$ based on the 2200 total samples collected. The overall lift signal yields an intermediate value of $N_{\mathrm{eff}} = 113$. The 5 % confidence boundaries for the mean and variance estimators based on N_{eff} are drawn in Fig. 5.22, showing how the statistical accuracy increases by collecting more data. Depending on available resources, one could surmise that the cost outweighs the accuracy benefit after about 100 t_∞. However, higher statistics require even

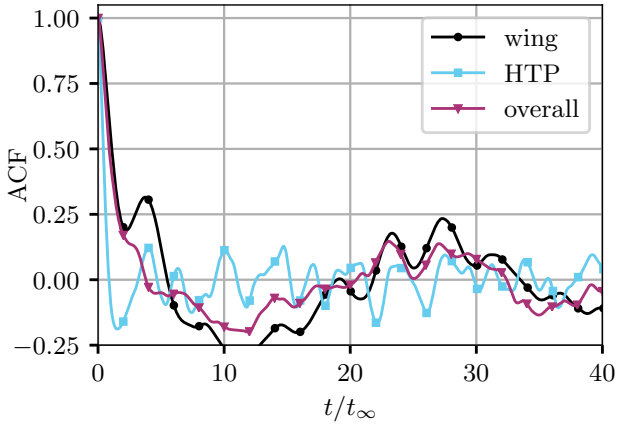

Fig. 5.23.: Autocorrelation function (ACF) of lift coefficient signals at $Re_\infty = 11.6 \cdot 10^6$, $\alpha = 18°$, DDES, grid B.

longer signals to achieve acceptable boundaries.

Spatial Distribution of Error in the Wake

The autocorrelation function, time scale and N_{eff} can be computed for any point and variable in the data set. In order to gain better understanding of the accuracy of statistics in the wake flow, this was carried out for three simulation durations: 50, 100 and 200 t_∞. A representative distribution of N_{eff} values at a single volume slice at $\eta = 28.3\,\%$ in Fig. 5.24 shows that there is considerable spatial variation across the domain. The shear layers and edges of the wake tend to lower time scales and higher N_{eff}, whereas the signals in the wake center region yield fewer effective samples.

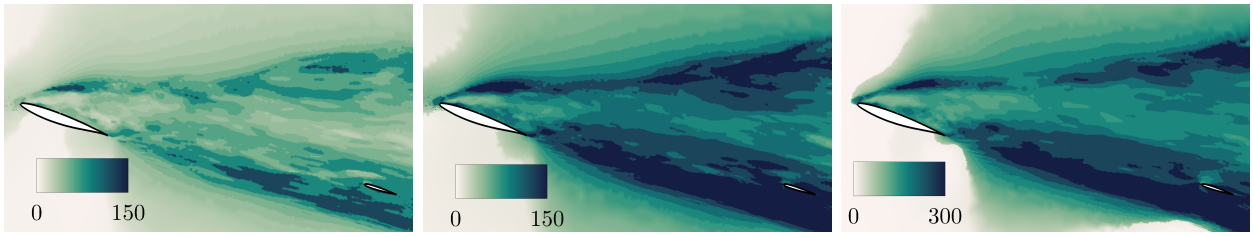

(a) $t_{\text{total}} = 50\ t_\infty$ **(b)** $t_{\text{total}} = 100\ t_\infty$ **(c)** $t_{\text{total}} = 200\ t_\infty$

Fig. 5.24.: Distribution of N_{eff} for the streamwise velocity u at $\eta = 28.3\,\%$ for three different runtimes.

The resulting uncertainty of first and second order statistics at several positions is shown in Fig. 5.25 using the confidence intervals defined by $\pm 1.96\sigma_e$, where σ_e corresponds to the appropriate σ_{mean} or $\sigma_{variance}$ computed using Eq. 3.27. The uncertainty is largest close to the centerline and decreases toward the wake edges. The first order statistics in Figs. 5.25a and 5.25c exhibit narrower confidence ranges than the second order statistics. This representation permits an overview over the uncertainties associated with the simulation of the wake flow. It is particularly the Reynolds stresses whose accuracy benefits the most from long runtimes of 200 t_∞ and above. For instance, the 95 % confidence interval for the maximum of $\overline{w'w'}/u_\infty^2$ at a distance of $1c_{\text{ref}}$ from the trailing edge in Fig. 5.25d ranges from 0.9 to 1.2 for $N = 500$. Using the full dataset of $N = 2200$ this range can be narrowed to $0.98 - 0.105$, resulting in

a more reliable prediction of the fluctuations.

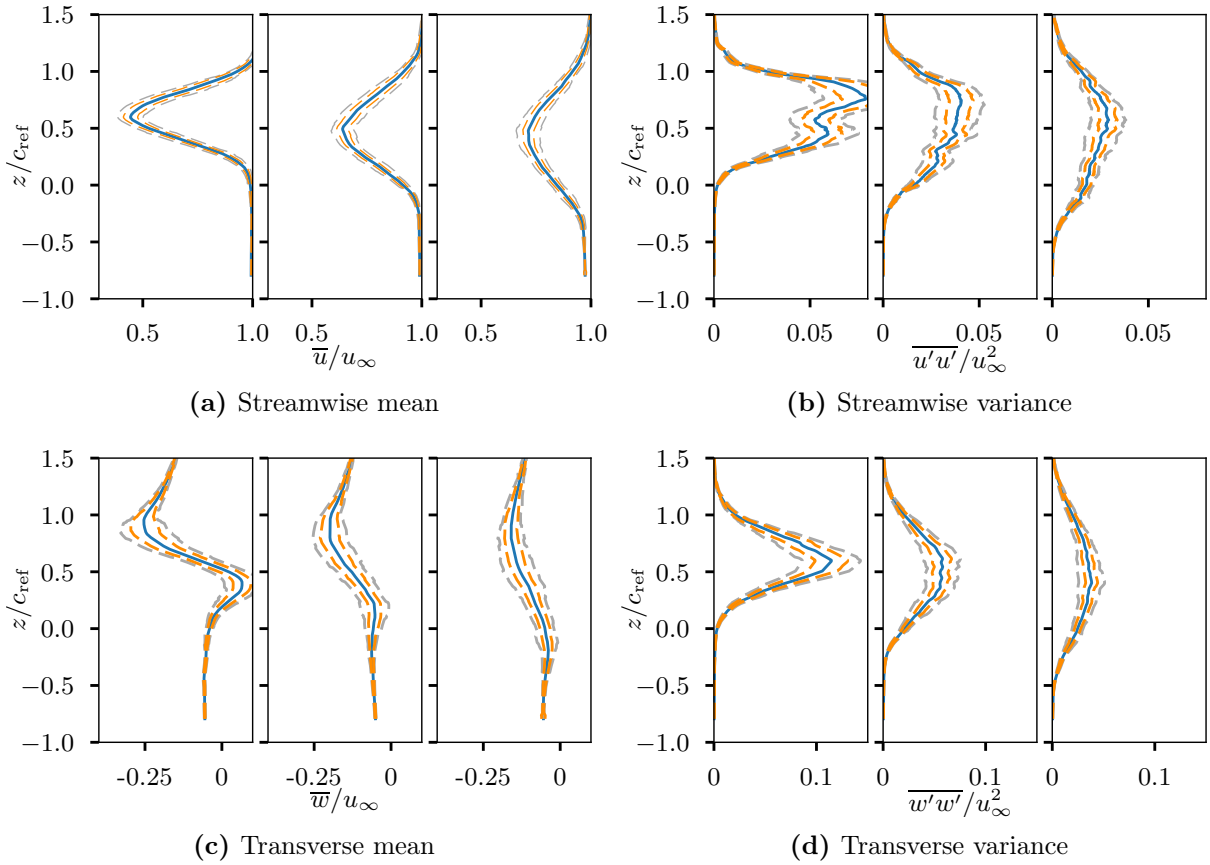

(a) Streamwise mean **(b)** Streamwise variance

(c) Transverse mean **(d)** Transverse variance

Fig. 5.25.: Uncertainty due to sampling error of first and second order velocity statistics in the wake at 5 streamwise positions ($x = \{1, 2, 3\}c_{ref}$ from the trailing edge in WT system) at $\eta = 28.3\,\%$, $\alpha = 18°$. Dashed lines indicate the range of the appropriate 95 % confidence interval at each location, orange for $N = 2200$, gray for $N = 500$.

5.6. Concluding Remarks

The validation process has shown that hybrid methods are the most feasible approach for the low speed stall condition. Dissipation of resolved turbulent fluctuations was shown to play a major role for simulation accuracy, which is one of the reasons why eddy viscosity based URANS is incapable of reaching the same degree of fidelity as DDES. While URANS is able to reasonably propagate turbulence in the wake, the dissipation of small scale shear layer instabilities prevents the formation of the correct wake topology. This is also true for excessively high artificial dissipation settings in DDES, making $k^{(4)}$ a crucial parameter. Temporal resolution acts in a similar manner, with too coarse values leading to excessive dissipation. Overall, the best-performing DDES computations are able to replicate forces, moments and pressure distributions with a high degree of accuracy and show a great degree of grid independence. The free flight configuration WBT0d provides a reasonable approximation of the flow physics. The wake predicted by CFD is slightly wider than in the PIV measurement, indicating that the resolution of the mixing processes in the shear layer may be still slightly too dissipative.

CHAPTER 6

Wake Flow in Low Speed Stall

Having identified appropriate spatial and temporal resolutions, solver parameters, and the hybrid RANS/LES method as the proper simulation approach, the characteristics of the wake and the tailplane loads can be more thoroughly investigated at varying flight conditions. The significant unsteadiness of the flow in low speed stall shows that such conditions cannot realistically occur in a static manner. The significant unsteadiness associated with large scale flow separation at this $\alpha = 18°$ can be expected to constantly change α in free flight. While dynamic analysis and coupling with flight mechanics is out of the scope of this study, comparison of flow phenomena at different static conditions can help further the understanding of the underlying physics. The wake study will be carried out at three different inflow conditions in terms of angle of attack, with the conditions listed in Table 6.1. Most of the focus is on the validation case from Chapter 5, $\alpha = 18°$ and $Re_\infty = 11.6 \cdot 10^6$, with the effects occurring due to α variation described where applicable.

Tab. 6.1.: Low speed stall flow conditions.

$Re \cdot 10^{-6}$	M_∞	α	T_{ref}	p_{ref}
11.6	0.25	16°, 18°, 20°	115 K	303 kPa

Static measurement of aeroelastic deformation via SPT has some inherent temporal resolution, with the result being an implicit temporal average. The significance of the deformation unsteadiness is unknown, and its proper characterization would require further experimental studies. However, having ascertained that the magnitude of model wing deformation isof low relevance for the low speed stall case, a constant deformation will be used in all simulations across the three angles of attack. It needs to be pointed out that the assumption of small deformation magnitude cannot be applied to full scale aircraft, it is merely a consequence of focusing on the vastly stiffer wind tunnel model.

This chapter aims to provide an overview over different aspects of the wake flow. Section 6.1

focuses on the general topology of the wake, beginning with an exploratory overview over the overall three-dimensional shape and investigating the interaction between spanwise lift distribution and the wing wake. Quantitative differences in wake direction and size between the three angles of attack are also shown. Section 6.2 discusses the dynamic characteristics of the flow separation via POD. The results of the large scale overall fluctuation characteristics are juxtaposed to characteristics of the turbulent fluctuations at different locations in the wake in Section 6.3.

6.1. Separation and Flow Topology in Post Stall

6.1.1. Three-Dimensional Separation and Flow Topology

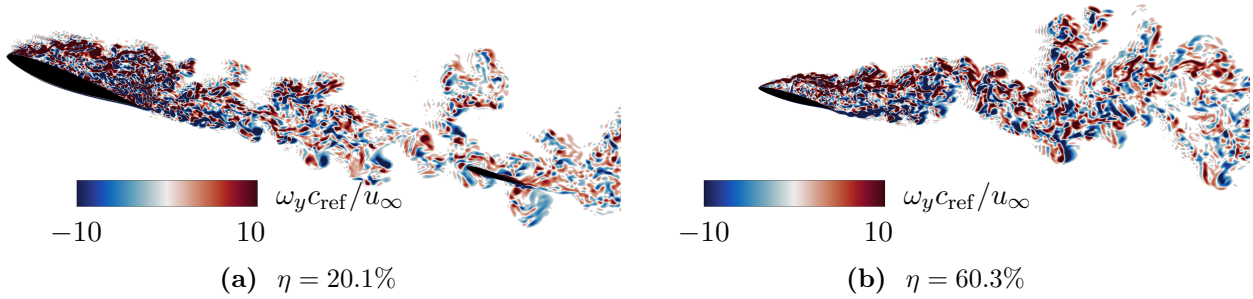

(a) $\eta = 20.1\%$ **(b)** $\eta = 60.3\%$

Fig. 6.1.: Instantaneous spanwise vorticity ω_y inboard and outboard at $\alpha = 18°$.

The validation chapter showed that leading edge separation and a resulting turbulent shear layer occur across most of the wing span. This shear layer forms the upper boundary of the recirculation area, and its length and stability vary significantly over the span. As the pressure distributions had suggested, the wing wake can be roughly divided into two regions with different flow regimes, inboard and outboard of the Yehudi kink. The inboard region is characterized by strong interactions of turbulent dynamics with the wing suction side pressure, with the shear layer fluctuations situated close to the surface. The outboard wing involves shear layer instabilities that occur farther away from the surface. The load fluctuations are therefore significantly more pronounced over the inboard wing. The precise nature of the difference between inboard and outboard flow characteristics, as well as the position of the switchover, are investigated in the following.

The instantaneous spanwise vorticity ω_y in Fig. 6.1 and on the left wing in Fig. 6.2 visualizes the difference. Outboard, the narrow region of high ω_y in Fig. 6.1b immediately downstream of the leading edge is largely undisturbed over a length of about one third of the local chord. The shear layer disintegrates only after significant streamwise distance. High negative ω_y is visible behind the trailing edge, but with less clear spatial structure. Inboard, the flow is much more chaotic starting at the leading edge, with resolved vortical structures visible above the surface over the entire chord. There is no discernible contiguous shear layer like at the outboard position, it consists of discrete vortices.

The time-averaged vorticity confirms this, with a long narrow region of $\overline{\omega_y}$ in Fig. 6.3b suggesting little spatial scatter of vorticity in the outbard wake. The shape of positive $\overline{\omega_y}$ near

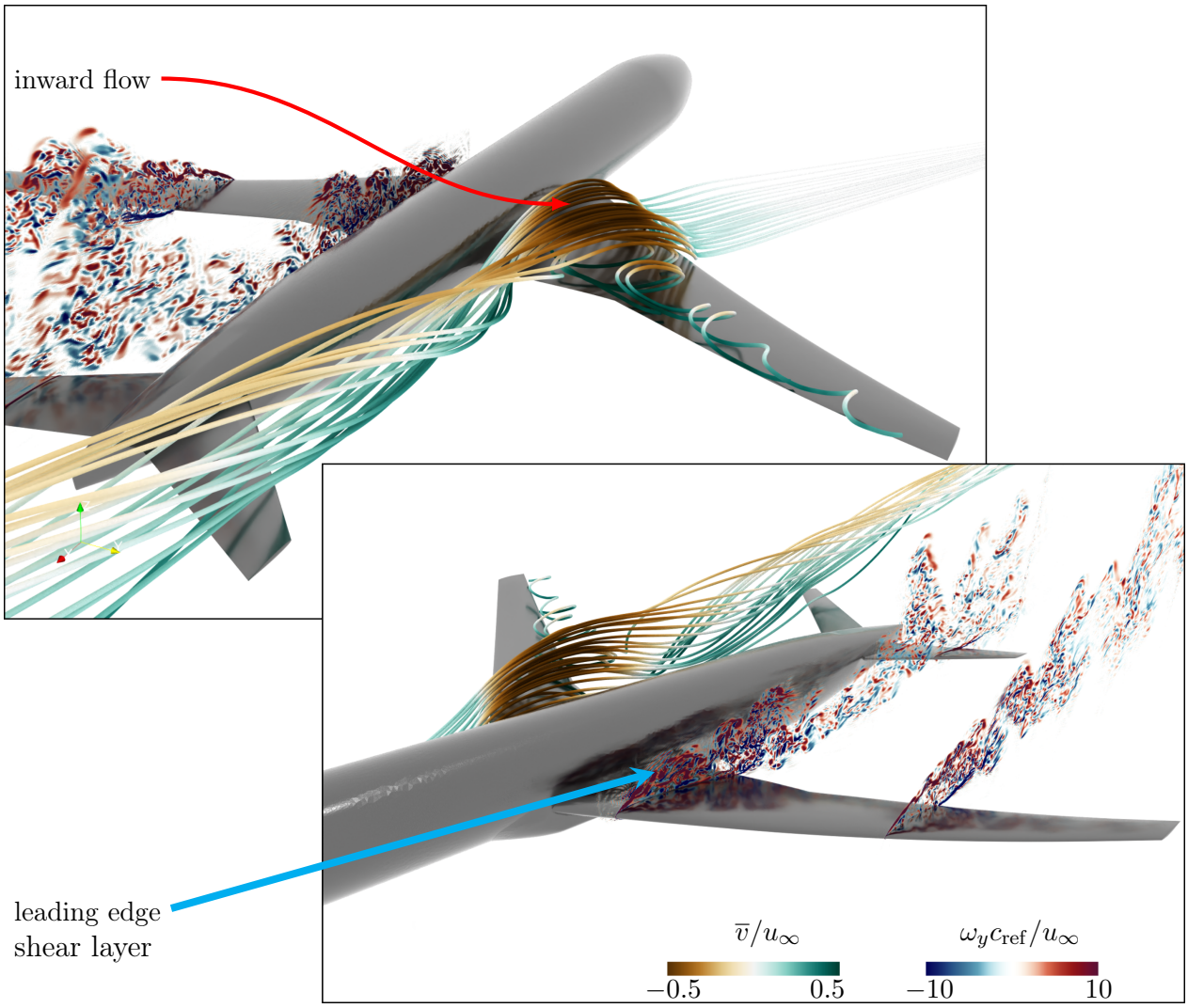

Fig. 6.2.: Time-averaged streamlines at inboard wing and instantaneous spanwise vorticity component ω_y in two slices inboard and outboard at $\alpha = 18°$. Streamlines are colored by mean spanwise velocity $\overline{v}$. ω_y is mirrored to the left wing for clarity, with $|\omega_y| < 500$ omitted.

the inboard leading edge in Fig. 6.3a is smeared and more spatially distributed. Comparing the top and bottom rows of Fig. 6.3, the decrease of $\overline{\omega_y}$ coincides with a strong increase of resolved shear stress $\overline{u'w'}$. This is especially well visible outboard. The symmetry of the $\overline{u'w'}$ distribution in Fig. 6.3d and the shape and lack of downward deflection of the streamlines in Fig. 6.3b resemble a prototypical bluff body flow configuration with the downstream streamlines largely parallel to the inflow, such as shown in Fig. 2.5. The delayed destabilization of the outboard shear layer shifts the region of noteworthy resolved fluctuations significantly further downstream.

The inboard flow field in Fig. 6.3c is much less symmetric and contains a large area of resolved negative $\overline{u'w'}$ above the wing, i.e. strong momentum exchange between streamwise outer flow and the induction of a downward fluctuating velocity component. The earlier discussion of artificial dissipation established a link between the streamwise position of this fluctuation region and the surface pressure fluctuation, suggesting the high momentum outer flow intermittently penetrates toward the wing surface. The maximum values of resolved shear stress are nevertheless similar at both positions.

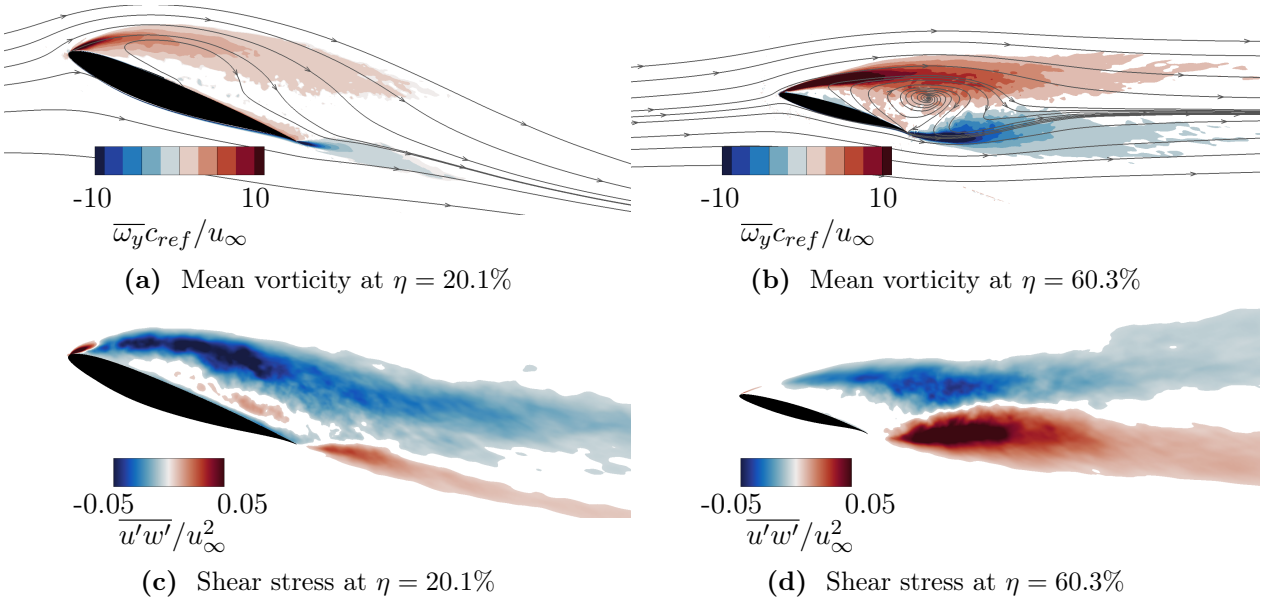

(a) Mean vorticity at $\eta = 20.1\%$ **(b)** Mean vorticity at $\eta = 60.3\%$

(c) Shear stress at $\eta = 20.1\%$ **(d)** Shear stress at $\eta = 60.3\%$

Fig. 6.3.: $\overline{\omega_y} c_{ref}/u_\infty$ (top row) and $\overline{u'w'}/u_\infty^2$ (bottom row) at $\alpha = 18°$. Mean in-plane streamlines are superimposed on the mean vorticity.

6.1.2. Forces and Load Distributions

According to lifting line theory, the lift of a wing can be represented using a bound vortex of varying strength $\Gamma(\eta)$ at the quarter chord line [108]. The spanwise variation of lift is evident in the chordwise pressure distributions in Fig. 6.4, in the spanwise distributions of circulation $\Gamma(\eta)$ in Fig. 6.5a, and the lift coefficient $c_l(\eta)$ in Fig. 6.5b. Fig. 6.5a additionally shows the spanwise gradient of the bound vortex strength, $\gamma(\eta) = \partial\Gamma/\partial\eta$.

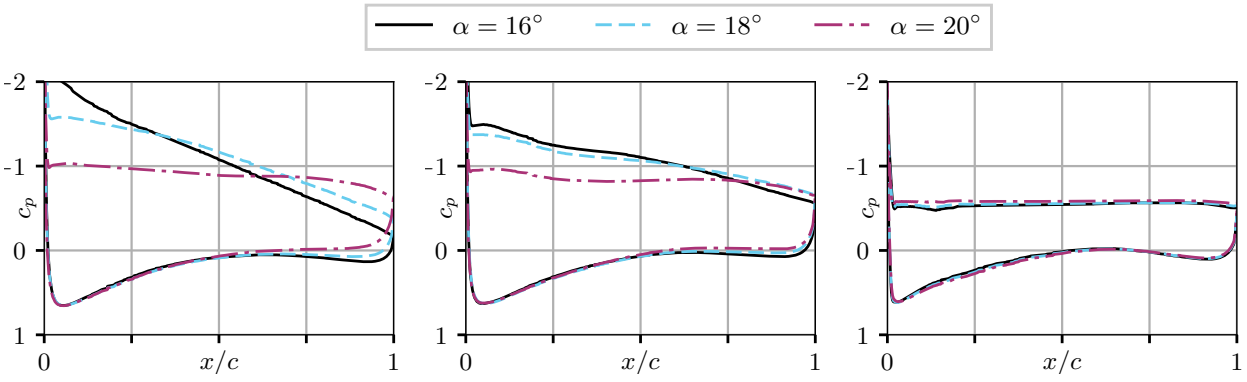

(a) $\eta = 20.1\,\%$ **(b)** $\eta = 28.3\,\%$ **(c)** $\eta = 60.3\,\%$

Fig. 6.4.: Wing pressure distributions for three angles of attack at $M_\infty = 0.25$, $Re_\infty = 11.6 \cdot 10^6$.

The outboard wing flow is barely affected by variation of the angle of attack between 16° and 20°, with the pressure distribution in Fig. 6.4c and the values of Γ for $\eta \gtrapprox 0.5$ in Fig. 6.5a appearing largely identical across the three α settings. Most of the differences across the angle of attack range are confined to the inboard region, with similar circulation Γ for $\alpha = 16°$ and $\alpha = 18°$ and markedly lower values for $\alpha = 20°$. In effect, the adverse chordwise pressure gradient observed on the wing upper side decreases in magnitude with increasing angle of attack in Figs. 6.4a and 6.4b. The inboard local lift decreases at higher α due to the lack of a pronounced low pressure region over the upstream portion of the wing. Upper side c_p is mostly

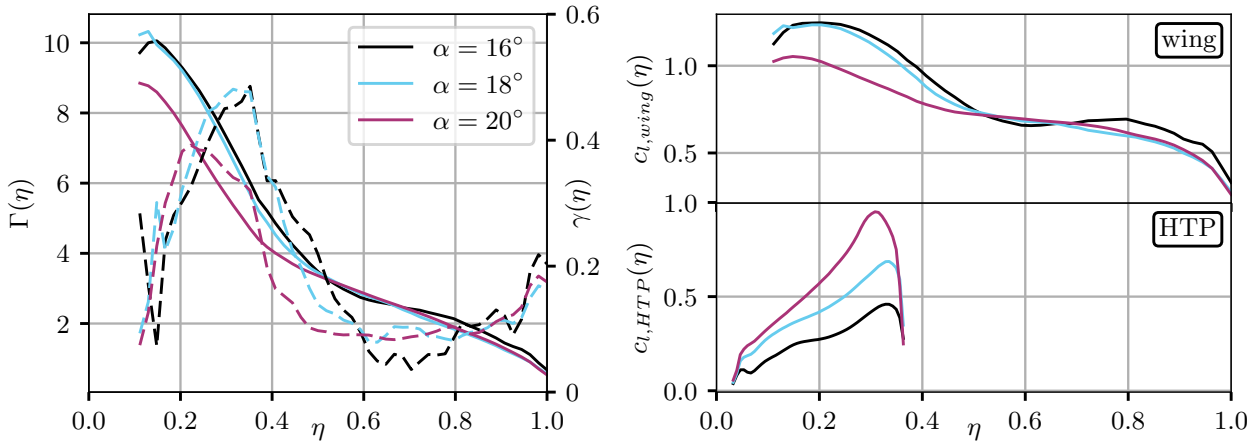

(a) Spanwise distribution of Γ (left-hand y axis, solid lines) and γ (right-hand y axis, dashed lines).

(b) Time-averaged $c_L(\eta)$. Legend as in a).

Fig. 6.5.: Spanwise distributions of c_L and circulation characteristics.

flat for $\alpha = 20°$, consistent with a separated airfoil pressure distribution. Correspondingly, the distribution of $\Gamma(\eta)$ in Fig. 6.5a shows the highest values for the lowest α.

However, the largely equal inboard circulation Γ in Fig. 6.5a at the two lower α values does not necessitate the same shape of the c_p distributions at the corresponding positions. The suction side pressure at $\eta = 20.1\,\%$ in Fig. 6.4a shows more lift generated at $\alpha = 16°$ by the front part, while $\alpha = 18°$ shows less pressure recovery and higher lift in the rear of the chord downstream of a crossover point at about $x/c \approx 0.35$. These differences largely cancel out each other in terms of circulation and lift, explaining the similar Γ at the corresponding spanwise positions.

Tab. 6.2.: Time-averaged forces and moments at three different angles of attack.

α	C_L	$C_{L,wing}$	$C_{L,HTP}$	C_D	C_{My}
16	1.079	0.819	0.215	0.285	-0.110
18	1.090	0.792	0.314	0.3446	-0.190
20	1.040	0.690	0.458	0.373	-0.382

The quantitative and qualitative differences between the three angle of attack conditions show that the lift response to α input is highly nonlinear. Both the distribution of wing lift in Fig. 6.5b and its magnitude $C_{L,wing}$ in Table 6.2 are similar at $\alpha = 16°$ and $\alpha = 18°$, while $\alpha = 20°$ shows a large decrease. This is counteracted by an increase of $C_{L,HTP}$, which grows significantly with α due to the diminishing downwash which causes an increase of the tailplane inflow angle. What is more, the relative increase of $C_{L,HTP}$ caused by $\Delta\alpha$ is much higher than the change in $C_{L,wing}$. The tailplane inflow conditions determining $C_{L,HTP}$ are strongly influenced by the downwash from the inboard wing. The spanwise distribution of the lift coefficient in Fig. 6.5b shows that the forces vary significantly and that the lift coefficient is very high near the tailplane tip. This bears both the danger of local separation and causes high tailplane root moments.

6.1.3. Shape of Near and Far Wake

The wake shape shown in Fig. 6.2 is consistent with the spanwise distribution of circulation $\Gamma(\eta)$ in Fig. 6.5a, with the maximum local lift occurring inboard and decreasing significantly in the region of the Yehudi break. The inboard wing is responsible for most of the lift force. The spanwise gradient $\gamma(\eta) = \partial\Gamma/\partial\eta$ induces longitudinal vorticity ω_x in the wake. High values of $\gamma(\eta)$ are attained between approximately $\eta = 0.2$ and $\eta = 0.4$ in Fig. 6.5a. This is coincident with the diffuse region of elevated ω_x in Fig. 6.6. In agreement with the generic considerations by Harper and Maki [48], the outboard flow separates at the leading edge and forms a vortex which curves in streamwise direction and departs the wing surface.

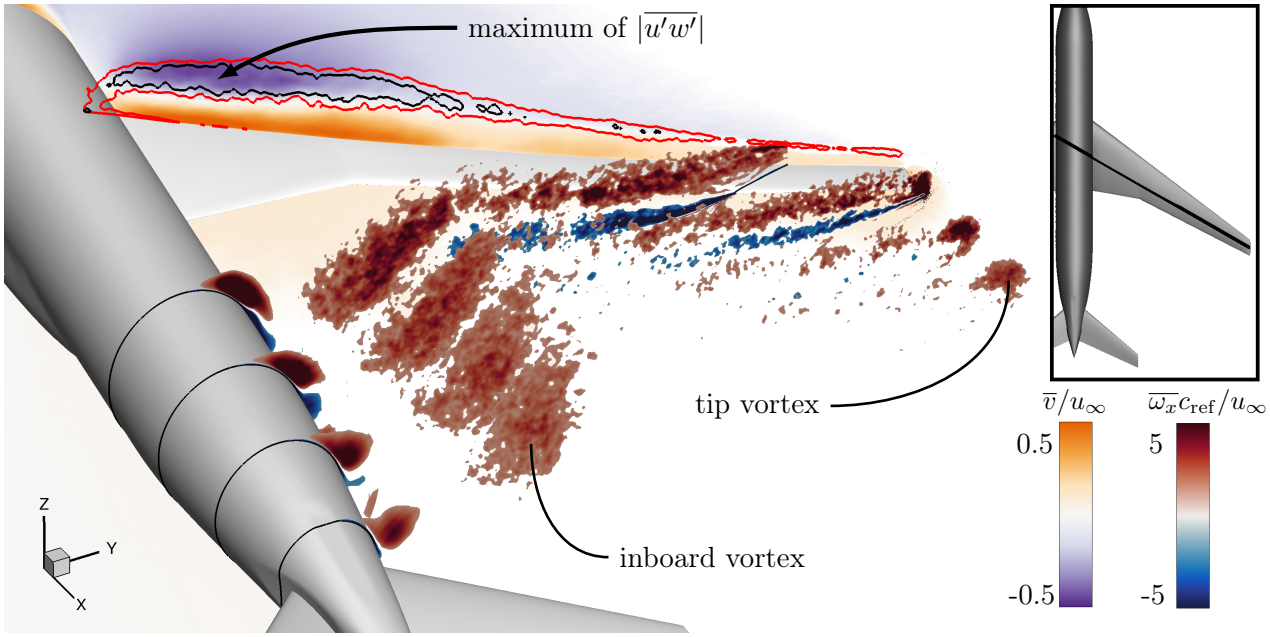

Fig. 6.6.: Contours of time-averaged spanwise velocity $\overline{v}/u_\infty$ in a slice parallel to the outboard trailing edge and contours of time-averaged streamwise vorticity in multiple slices in the wake at $\alpha = 18°$. Red and black contour lines represent $\overline{u'w'}/u_\infty^2 = \{0.05, 0.1\}$. Wing-aligned slice position shown on top right.

Above the wing, the vorticity is visible as a spanwise counterflow. The distribution of spanwise velocity $\overline{v}/u_\infty$ in a slice parallel to the wing leading edge in Fig. 6.6 shows a stratified structure, consistent with the lifting line theory's prediction of a longitudinal counterclockwise vorticity over the entire half span. The outer flow far above the wing is orientated inward with $\overline{v} < 0$, whereas the inner flow moves fluid toward the tip.

The shear stresses indicating regions of high momentum exchange between outer and inner flow are concentrated in regions of the highest (spanwise) inward and streamwise velocity. The maximum of the shear stress $\overline{u'w'}$ between streamwise and vertical velocity fluctuations is indicated in Fig. 6.6, just above the white shaded region of the slice representing $\overline{v} = 0$. The superimposed contours of $\overline{u'w'}$ show that it is high over most of the inboard wing. $\overline{v}$ attains values on the order of $\pm 0.5 u_\infty$, suggesting a large amount of momentum being transferred from streamwise inflow velocity to counterflowing outer (positive v) and inner (negative v) velocity components over the inboard wing.

The surface streamlines in Fig. 6.7 visualize the direction of the wall shear. The outboard

recirculation is oriented in roughly parallel lines and few changes in direction, with a bias to outboard orientation. At the same time, the inboard streamline pattern indicates a curved shape near the wing root. The pattern is generally consistent with swept wing stall observations by Schütte [130] and Zhang et al. [180]. There is a change in spanwise direction across the inner 40 % of the wingspan, with the streamlines oriented inward in the leading edge region. A distinct kink in the surface streamlines is visible at about a quarter of the chord. The local inward orientation observed here may be explained by intermittent breakdown of the shear layer, which allows high momentum outer flow with its inward component to penetrate it and reach the surface.

In an attached swept wing flow, the surface streamlines simply curve outward, more so than the inviscid streamlines at the boundary layer edge. Hirschel [52] describes how the longitudinal vorticity in a wake is reflected in the opposite orientation of the flow at the edge of the boundary layer flow on the upper (inward) and lower (outward) wing sides. In this present case, the outward spanwise flow is already detectable above the upper side upstream from the trailing edge. The outward curvature of the upper side skin friction lines shown for attached flows by Hirschel et al. [53] is visible in Fig. 6.7, despite the fact that no attached boundary layer is present.

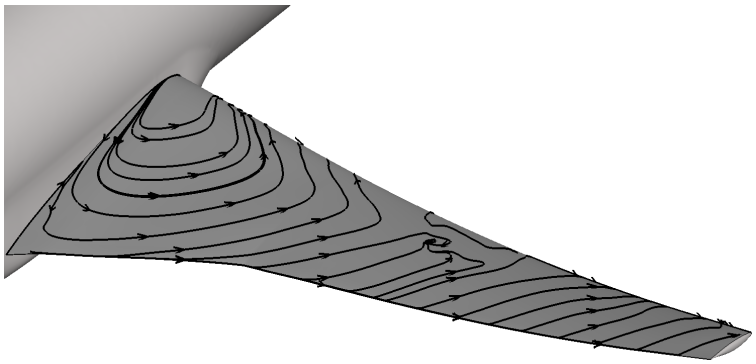

Fig. 6.7.: Time-averaged surface streamlines derived from intergration of the local wall friction coefficient vector.

The axis of the resulting longitudinal time-averaged vortical structure in the wake coincides roughly with the maximum of the gradient $\gamma(\eta)$ near the Yehudi break, positioning it just inboard of the HTP tip. Its counter-clockwise rotation (viewed from downstream) imposes a spanwise distortion of the tailplane inflow angle and $\alpha_{HTP,eff}$. This process deforms the wake and twists it into a vortical structure which persists downstream. This deformation remains visible with increased distance in the wake, demonstrated in Fig. 6.8 viewed from downstream. The inboard region of the wake is dominated by large regions of spanwise resp. transverse velocity of opposite signs, making up the large vortex in Fig. 6.6. The velocity magnitudes decrease with streamwise distance, shown from left to right in Fig. 6.8. The structures are initially deformed due to close proximity to the wing trailing edge and the influence of the outboard wing. The shape becomes less complex downstream, with the visible structures becoming more rounded and uniform.

The twisting and roll-up of the separating wake into the distinct longitudinal vortex at different angles of attack is visualized via the shape of the isosurface of $\overline{u}/u_\infty = 0.5$ in Fig. 6.9. A slice through the isosurfaces from Figs. 6.9a-6.9c at $x/c_{\text{ref}} = 7$ is shown in Fig. 6.9d to facilitate direct comparison of the positions. The isosurfaces indicate that this features's position shifts in spanwise direction depending on α, which is again consistent with Harper and Maki. The longitudinal rotating motion entrains high momentum outer flow from above the wake inward and down. This increases the local streamwise velocity and causes

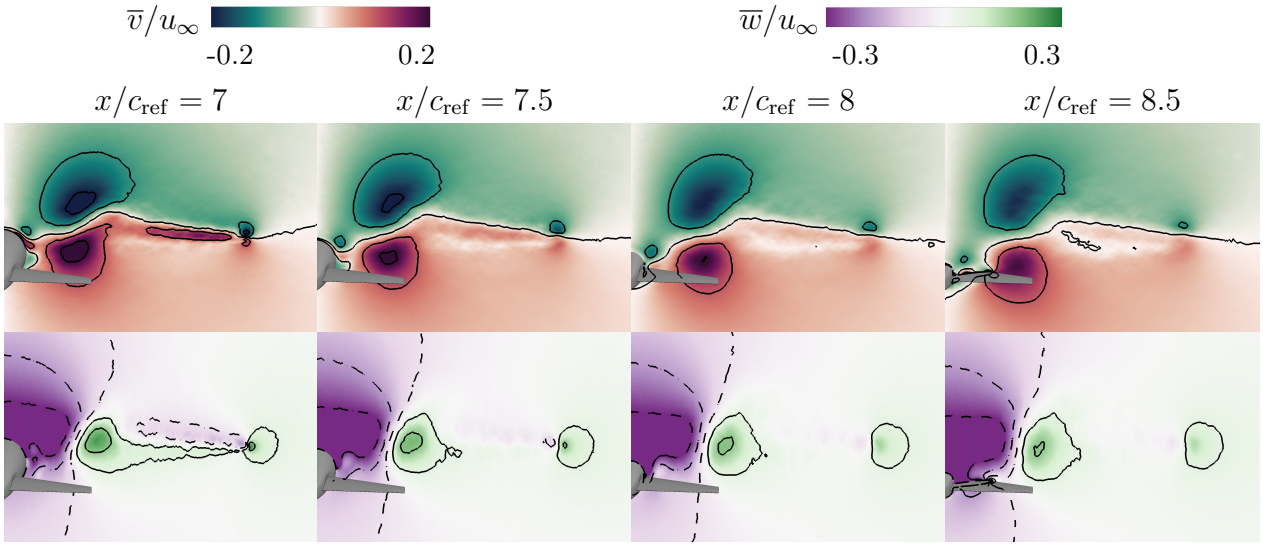

Fig. 6.8.: Mean spanwise and transverse velocities in the wake at $\alpha = 18°$. Dashed contour lines in the bottom row represent negative values.

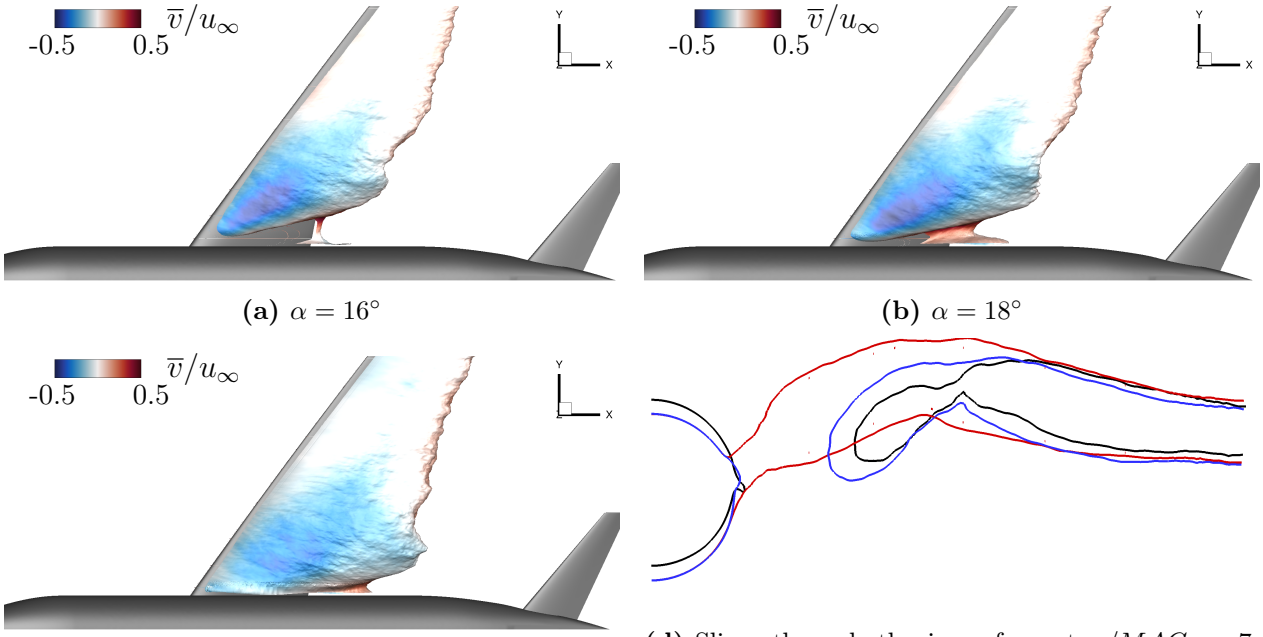

(a) $\alpha = 16°$

(b) $\alpha = 18°$

(c) $\alpha = 20°$

(d) Slices through the isosurface at $x/MAC = 7$. ——: $\alpha = 16°$, ——: $\alpha = 18°$, ——: $\alpha = 20°$

Fig. 6.9.: Top views of $\overline{u}/u_\infty = 0.5$ isosurface colored by mean spanwise velocity $\overline{v}$.

the isosurface of $\overline{u}/u_\infty = 0.5$ to retreat from the fuselage in Figs. 6.9a and 6.9b. This occurs slightly farther outboard at $\alpha = 16°$ than at $\alpha = 18°$. The isosurface deformation is much less pronounced at $\alpha = 20°$ in Fig. 6.9c, as expected from the weaker vortex induced by the lower $\gamma(\eta)$.

Recirculation Area and Wake Size at Different Angles of Attack

Despite the streamlined shape of the wing section, the leading edge separation at the high angles of attack encountered in this work creates a wake flow that exhibits characteristics similar to that behind a bluff body. The three-dimensional vortical motion described above

distorts the flow in spanwise direction. Increased α values cause a proportionate increase in the projected height d of the wing section, a quantity which is characteristic for the bluff body-like behavior and is associated with streamline divergence, as described in 2.2.1.

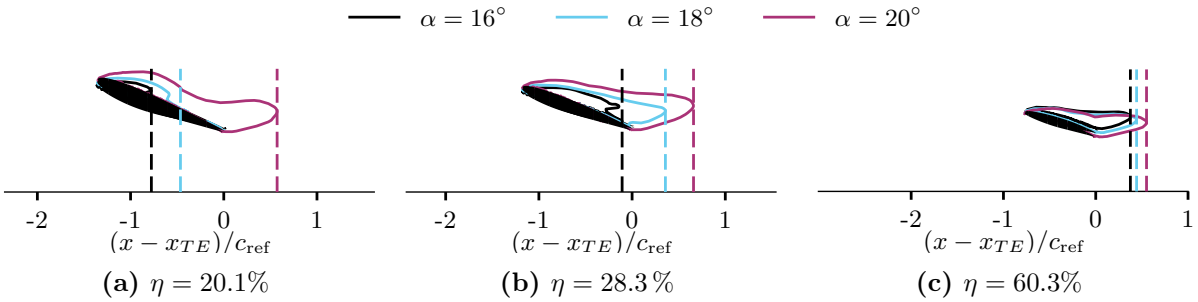

(a) $\eta = 20.1\%$ **(b)** $\eta = 28.3\,\%$ **(c)** $\eta = 60.3\%$

Fig. 6.10.: Time-averaged extent of the recirculation area delimited by contours of $\overline{u} = 0$ at three spanwise positions for three angles of attack. Colored dashed lines mark the streamwise location of the rear stagnation point.

The extent of the backflow region is described using the isoline of zero mean streamwise velocity $\overline{u} = 0$ and its farthest downstream position (i.e. the rear stagnation point [29]) as characteristic features. Fig. 6.10 shows the isoline shapes relative to the wing section at three spanwise positions, with the dashed lines emphasizing the streamwise location of the rear stagnation points. The inboard backflow ($\eta = 20.1\,\%$, Fig. 6.10a) is largest at $\alpha = 20°$, with lower α significantly decreasing its size. The $\overline{u} = 0$ isoline extends far downstream into the wake at $\alpha = 20°$, whereas it moves upstream and above the wing at the lower angles of attack. The differences diminish at $\eta = 28.3\,\%$ (Fig. 6.10b), but are still significant. At the outboard wing, the differences between the three angles of attack decrease even further, the flow shapes become more similar. The locations are listed in Tab. 6.3 for reference. Fig. D.1 in the appendix gives an overview of the time-averaged velocity field for all three positions and angles of attack.

Tab. 6.3.: Streamwise location of the rear stagnation point at different angles of attack and spanwise locations. Data in absolute WT coordinates.

Plane	$\alpha = 16°$	$\alpha = 18°$	$\alpha = 20°$
$\eta = 20.1\%$	0.891	0.924	1.118
$\eta = 28.3\%$	1.029	1.086	1.142
$\eta = 60.3\%$	1.198	1.211	1.232

The varying backflow size is accompanied by a variation of the location of resolved turbulent fluctuations. As observed in the discussion of dissipation variation in the previous chapter, the shear layer fluctuation interacts with wing surface pressure fluctuation. This interaction varies with α and spanwise position, with the locations of the regions of high resolved k_t relative to the wing shown in Fig. 6.11. At the outboard positions represented by $\eta = 60.3\,\%$ in the right-hand column of Fig. 6.11, there is little variation due to α. As with $\overline{u}$, there is little variation due to α outboard, represented by the contours of resolved k_t at the $\eta = 60.3\,\%$ position in the right column of Fig. 6.11. At this location, the regions of elevated k_t are symmetrical with respect to the horizontal and have almost identical shapes at each α, with

only the streamwise positions and maximum k_t magnitudes being variable. The resolved fluctuations above the wing are relatively weak. Lower α promotes earlier onset of resolved k_t, while high α shifts it downstream. The streamwise positions of maximum k_t roughly coincide with the stagnation point location in Fig. 6.10, which is on the order of magnitude of one local chord downstream of the trailing edge. The area above the outboard wing is largely quiescent with low values of k_t.

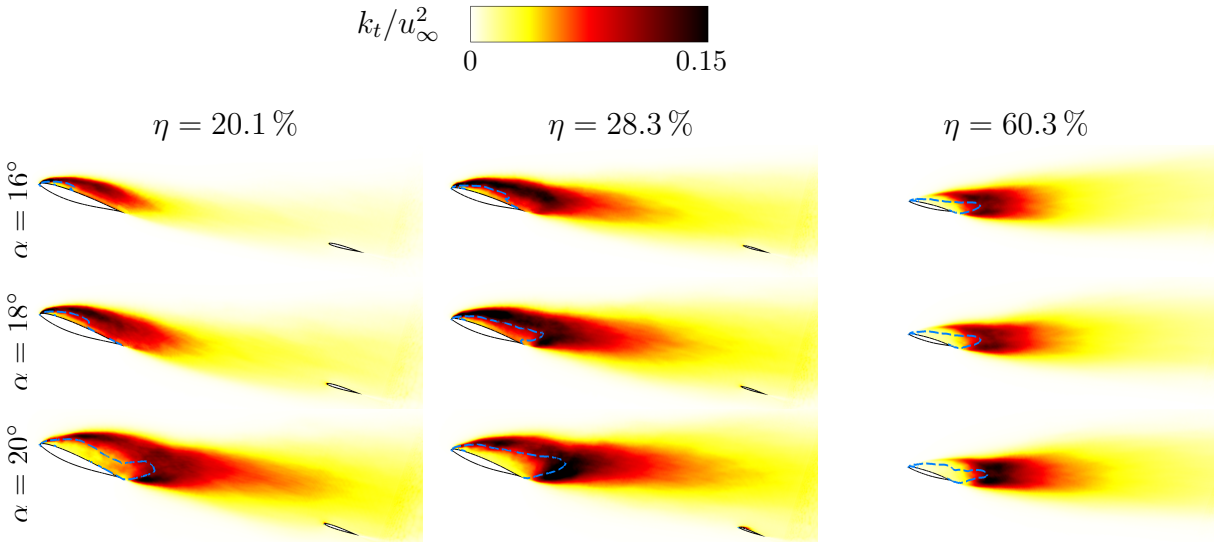

Fig. 6.11.: Turbulence kinetic energy k_t/u_∞^2 at $Re_\infty = 11.6 \cdot 10^6$. Dashed blue line represents $\overline{u} = 0$.

At the inboard positions $\eta = 20.1\,\%$ and $\eta = 28.3\,\%$ in Fig. 6.11, the differences across the α values are more significant. More of the fluctuations occur above the wing as opposed to downstream from it. The resolved fluctuations beginning close to the leading edge cause high k_t above the wing at $\eta = 20.1\,\%$ and $\eta = 28.3\,\%$, without the downstream displacement visible at $\eta = 60.3\,\%$. Lower α causes less streamline divergence by the wing section due to smaller projected area d, this results in the elevated k_t region being positioned lower and with less space between it and the wing surface. The wing upper surface is also less inclined relative to the inflow direction, further reducing the distance between the high shear area and the surface. Close vertical proximity between shear layer and the wing causes a larger amount of pressure fluctuation on the wing surface. In contrast, the high angle of attack of $\alpha = 20°$ increases the vertical distance of the fluctuation region from the surface by such an amount that a largely quiescent region of low k_t can be observed directly above the surface of the inboard wing in Fig. 6.11. Similar to the flow pattern at $\eta = 60.3\,\%$, this is associated with a significantly farther downstream position of the rear stagnation point in Fig. 6.10. The variation of this position due to α is equally well visible at $\eta = 20.1\,\%$. The major difference with respect to the outboard flow pattern is that there is a qualitative difference in topology due to α in the inboard wake. In cases with large backflow region and a rear stagnation point downstream of the trailing edge ($\eta = 28.3\,\%$, $\alpha = 18°$), a second area of elevated k_t can be observed behind the wing. It becomes progressively smaller when the backflow region decreases in size, such as at $\eta = 28.3\,\%$ for $\alpha = 16°$.

In conclusion, three types of fluctuation pattern can be visually distinguished in Fig. 6.11:

- I: Nearly symmetrical k_t maxima downstream of the wing, as at $\eta = 60.3\,\%$ for each α. Little resolved fluctuation at the leading edge

- II: Significant fluctuation in the leading edge shear, little resolved k_t near the trailing edge ($\eta = 20.1\,\%$ at $\alpha = 16°$ and $\alpha = 18°$, $\eta = 28.3\,\%$ at $\alpha = 16°$)
- III: Significant leading edge fluctuation and a second distinct fluctuation region associated with the trailing edge or the overall wake downstream ($\eta = 20.1\,\%$ at $\alpha = 20°$, $\eta = 28.3\,\%$ at $\alpha = 18°$ and $\alpha = 20°$)

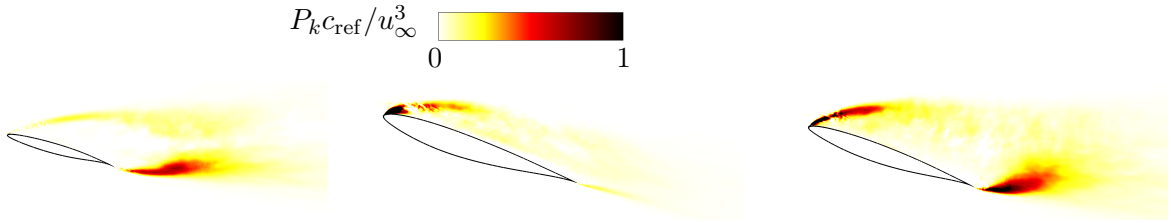

(a) Type I ($\eta = 60.3\,\%$, $\alpha = 18°$) **(b)** Type II ($\eta = 20.1\,\%$, $\alpha = 16°$) **(c)** Type III ($\eta = 28.3\,\%$, $\alpha = 18°$)

Fig. 6.12.: Production of resolved turbulence kinetic energy for the three flow topology types. Data in parentheses denotes the specific solution shown as example.

The spatial distribution of the production term of k_t, P_k, in Fig. 6.12 is largely concentrated in the areas immediately downstream of the leading and trailing edge at $\eta = 28.3\,\%$. The regions where significant production takes place are of roughly equal size in the type III topology. The overwhelming amount of energy production occurs immediately downstream of the edges, with most of the resolved stresses being the result of transport from these production locations. Type II locations ($\eta = 20.1\,\%$, $\alpha = 16°$ in Fig. 6.12b) involves significant turbulence production only at the leading edge, which causes high levels of k_t over most of the wing upper surface. Little P_k occurs at the trailing edge, explaining the lack of resolved k_t and Reynolds stresses at that location. The type I configuration shown in Fig. 6.12a has a mostly symmetric distribution of of production regions, mostly coinciding with the locations of high k_t seen in Fig. 6.11.

The following trends can be observed:

- The rear stagnation point moves aft with outboard distance and with increased α.
- Outboard flow patterns are similar across the α range in terms of backflow region size and fluctuation topology.
- The size of the quiescent low fluctuation region above the wing is smaller inboard than outboard at constant α. This is also true for the overall size of the backflow. This decrease is counteracted when α is increased, and the large backflow extends further inboard. In other words, fluctuation type II extends over a larger distance at lower angles of attack, while increasing α shifts the flow towards type III.
- The appearance of a high k_t region near the trailing edge is associated with a rear stagnation point position downstream of the trailing edge.

The variation in backflow size precipitates a change in wake velocity deficit $u_d = \max(\overline{u} - u_\infty)$. Large backflow causes high initial u_d which decreases downstream in the wake. u_d is shown in Fig. 6.13 for the three cases at the inboard and outboard wing. As with the backflow, the differences are largest in the inboard region, with the highest angle of attack consistently generating the largest wake u_d. Further downstream at $\eta = 20.1\,\%$, u_d remains highest at $\alpha = 20°$ (Fig. 6.13a), consistent with the physically largest backflow and associated amount of low momentum turbulent flow. At $\alpha = 20°$, thewake deficit is also larger at $\eta = 28.3\,\%$

than at $\eta = 20.1\,\%$. The retreat of the wake from the fuselage caused by the longitudinal vorticity is responsible for this, effectively decreasing the wake size. This effect, showcased in Fig. 6.9d, is least pronounced for $\alpha = 20°$ and explains the small difference of u_d between the two positions at that α.

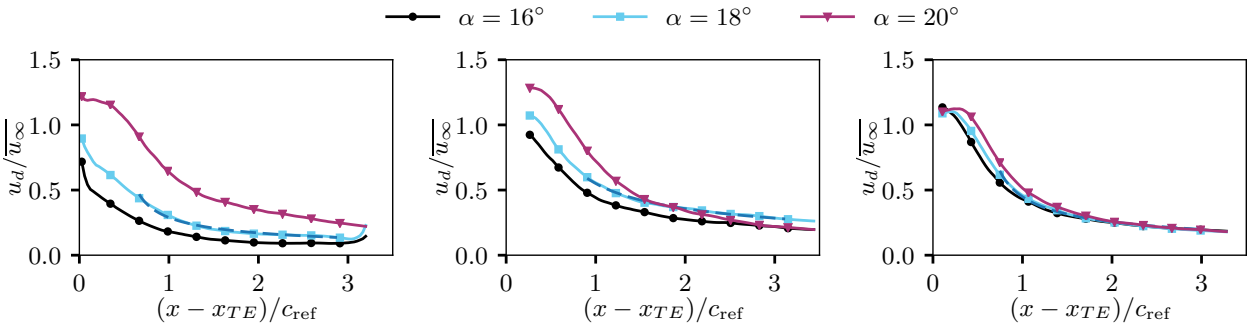

(a) $\eta = 20.1\,\%$ **(b)** $\eta = 28.3\,\%$ **(c)** $\eta = 60.3\,\%$

Fig. 6.13.: Magnitude of wake velocity deficit $|\overline{u_d}|$ for three angles of attack, plotted over distance from the trailing edge.

The differences behind the outboard wing (Fig. 6.13c) are significantly smaller and exist only in the near wake region at $(x - x_{TE})/c_{\text{ref}} < 1$; the curves nearly collapse on top of each other downstream of this position. Similar to the observations for different artificial dissipation settings, the streamwise gradient of u_d is largest when its initial magnitude is large due to increased extent of the backflow. This wake deficit recovery therefore is consistently largest for $\alpha = 20°$ at all spanwise positions. This causes the initially high u_d at $\eta = 28.3\,\%$ at $\alpha = 20°$ to drop below the corresponding value at $\alpha = 18°$ after $(x - x_{TE})/c_{\text{ref}} \approx 1$.

A wake's momentum thickness is obtained by integrating

$$\Theta(x) = \int_{-\infty}^{\infty} \frac{u}{u_\infty}\left(1 - \frac{u}{u_\infty}\right) dz \tag{6.1}$$

at each location x. As explained by Patel and Scheuerer [103], plane wakes tend to involve a Θ which remains constant over x. Despite the large scale longitudinal vorticity, this is largely valid in the CRM's wake as shown in Fig. 6.14. A short distance past the trailing edge, within c_{ref} in the shown cases, the flow reaches such a state where the values of $\Theta(x)$ remain nearly constant.

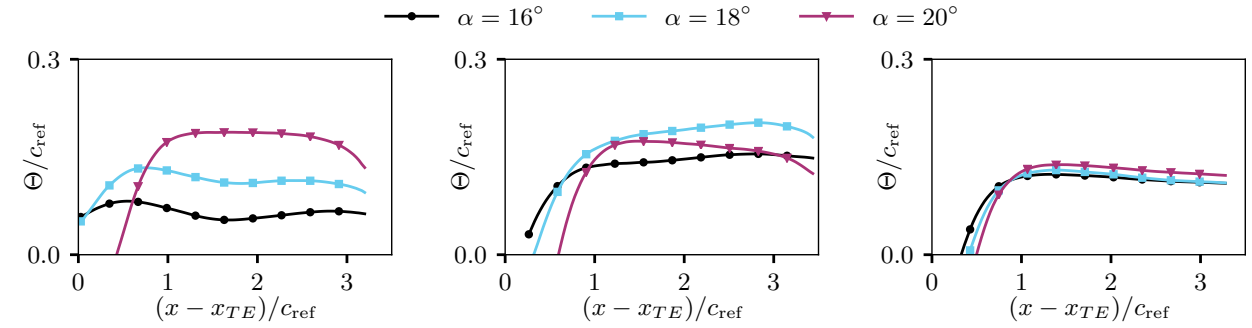

(a) $\eta = 20.1\,\%$ **(b)** $\eta = 28.3\,\%$ **(c)** $\eta = 60.3\,\%$

Fig. 6.14.: Magnitude of momentum thickness Θ for three angles of attack.

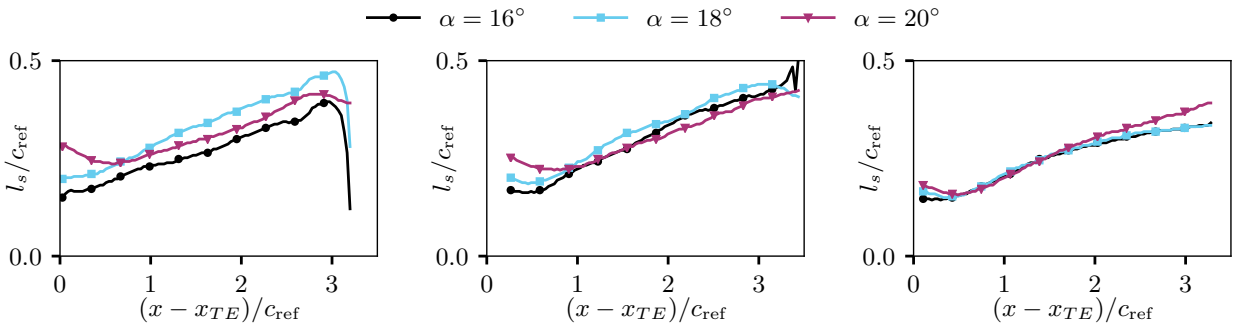

(a) $\eta = 20.1\,\%$ **(b)** $\eta = 28.3\,\%$ **(c)** $\eta = 60.3\,\%$

Fig. 6.15.: Wake half-width l_s for three angles of attack.

Tennekes and Lumley's plane wake model [151] from Chapter 2 involves a wake half-width l_s as characteristic length scale, which is the vertical distance between the wake centerline and the location where $u - u_\infty = 0.5u_d$. The flow asymmetry associated with nonzero lift gives rise to two values of l_s, one for the upper and lower side of the wake. Patel and Scheuerer [103] use the vertical distance between the two locations of $u - u_\infty = 0.5u_d$, while Thomas and Liu [152] employ the average of the two distances from the centerline. The present investigation uses the second notation. l_s is shown in Fig. 6.15 at three different spanwise positions. The length scale at $\alpha = 20°$ shows large values close to the wing. The large initial values are a consequence of the large backflow region size. At about one c_{ref} distance from the trailing edge, l_s of $\alpha = 20°$ decreases to values similar to and slightly lower than at $\alpha = 18°$. All three solutions exhibit similar wake halfwidths at this distance. The exception occurs far inboard at $\eta = 20.1\,\%$, where the halfwidth $\alpha = 16°$ is significantly smaller than in the other runs. This can be traced to the spanwise retreat of the wake away from the fuselage at this angle of attack; here the wake is essentially so narrow that l_s drops significantly.

Thomas and Liu observed that asymmetric wakes spread more quickly than symmetric ones and exhibit a roughly linear rate of spread. The latter is supported by the present data, as l_s evolves for the most part in a linear fashion in the inboard wake.

Downwash Direction

The decrease in local wing lift coefficient at higher angles of attack apparent in Fig. 6.5 leads to lower magnitudes of vertical flow deflection from the inflow direction downstream of the wing, which is measured via the downwash angle ξ. A higher aircraft α has therefore a twofold influence on $\alpha_{HTP,\text{eff}}$ in accordance with Eq. 2.1, in that $\alpha_{HTP,\text{eff}}$ increases by the increment of α and by the decreased magnitude of ξ. The tailplane's $\alpha_{HTP,\text{eff}}$ therefore disproportionately increases with higher overall α values.

The downwash angle can be seen in Fig. 6.16, where the streamwise evolution of $\overline{\xi}(x)$ is shown in terms of an average across the wake in transverse direction at several streamwise positions. This transverse average can be used as a metric for the bulk wake flow direction. The averaging domain is constant for all α and spans from $z = -5\,\text{mm}$ to $z = 25\,\text{mm}$ in the wind tunnel coordinate system. The pure averaging of the velocity angle ignores momentum and the differences in the width of the wake, but it gives in impression of the differences in the downwash direction. Large deflection magnitudes can be observed in the near wake, with a sharp turn toward constant values coinciding with each case's location of the rear

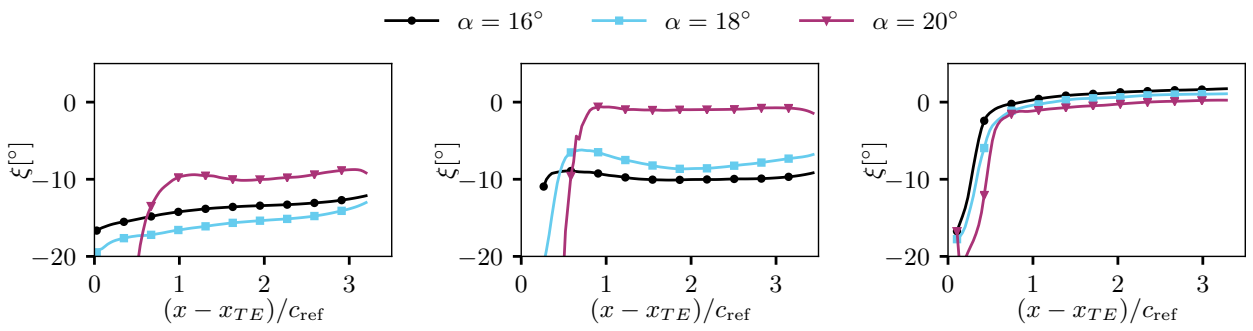

(a) $\eta = 20.1\%$. **(b)** $\eta = 28.3\,\%$. **(c)** $\eta = 60.3\%$.

Fig. 6.16.: Downwash angle ξ averaged over time and over the vertical extent of the wake between $z = -0.05\,\mathrm{m}$ and $z = 0.25\,\mathrm{m}$.

stagnation point about $0.5..1c_{\mathrm{ref}}$ downstream of the trailing edge. While the near wake and recirculation region involve significant streamwise gradients of $\overline{\xi}$, the flat shape downstream is indicative of linear propagation toward the tailplane with little change in direction.

The ξ magnitude at $\alpha = 20°$ is consistently the lowest one in the inboard wing wake. $\alpha = 16°$ and $\alpha = 18°$ cause approximately equal ξ at $\eta = 28.3°$. At $\eta = 20.1°$, the spatial averaging causes a low ξ magnitude at $\alpha = 16°$ due to the narrowness of the wake. The differences across α are largely confined to the inboard locations. The values at the outboard position in Fig. 6.16c are similar across the α range, which is consistent with the smaller differences in local lift at this location. ξ is highest at $\alpha = 16°$ despite largely similar Γ at this location in Fig. 6.5a. However, the local gradient $\gamma(\eta = 60.3°)$ associated with longituginal wake vorticity is highest at $\alpha = 16°$, due to the vortical structure being further outboard than at higher α. The outboard side of this wake vortex induces an upward velocity component, which suffices to cause local wake upwash at $\alpha = 16°$ at this position.

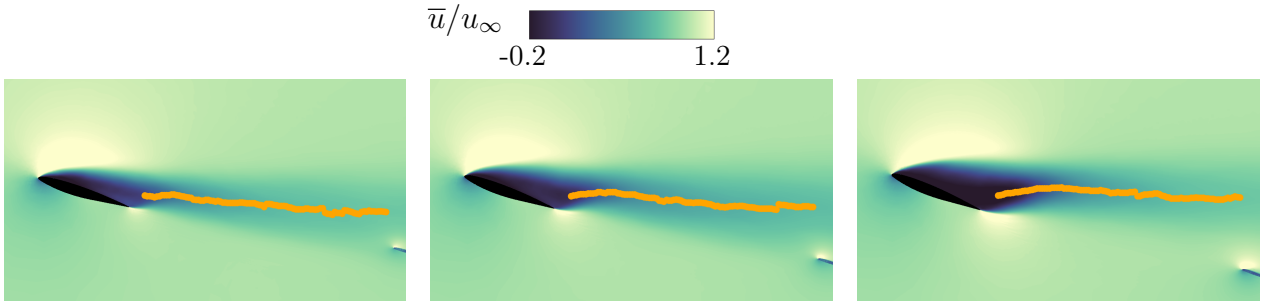

(a) $\alpha = 16°$ **(b)** $\alpha = 18°$ **(c)** $\alpha = 20°$

Fig. 6.17.: Time averaged mean streamwise velocity and superimposed locations of wake center based on $\overline{u}$ at $\eta = 28.3\,\%$.

A more quantitative measure for the downwash is obtained by determining the vertical position of the minimum streamwise velocity $\overline{u}$ at each streamwise location, i.e. $z(u_{min}(x))$. The mean velocity distributions in $\eta = 28.3\,\%$ with overlaid locations of the minimum are shown in Fig. 6.17. The roughly linear shape is leveraged by applying a linear fit downstream of the rear stagnation point, resulting in the fits shown in Fig. 6.18. The quality of the fits is reasonable and enables assessment of a downwash angle and a wake slope, except in the close inboard region at $\alpha = 16°$ due to the same reasons as above associated with the vanishing wake. The linear fit for this case is a rough approximation and was carried out only in the

middle portion of the wake, before the large undulation far downstream in Fig. 6.18a.

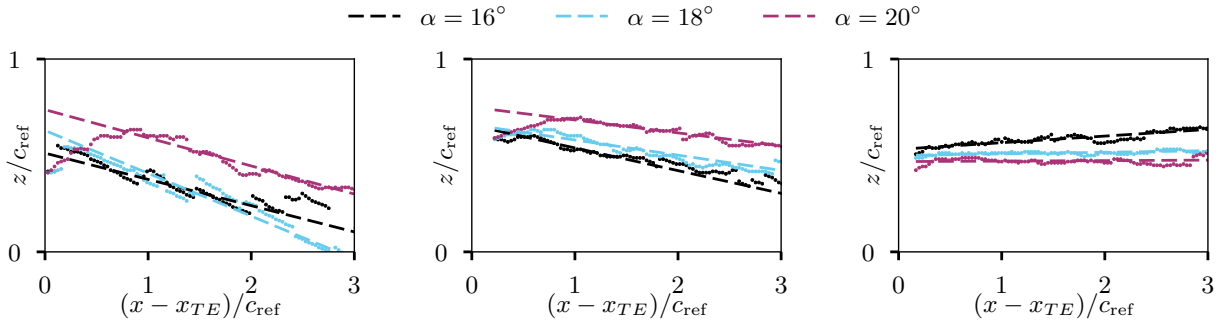

(a) $\eta = 20.1\,\%$ **(b)** $\eta = 28.3\,\%$ **(c)** $\eta = 60.3\,\%$

Fig. 6.18.: Time-averaged position of the velocity minimum at each streamwise position, dashed lines showing ξ_{lin}.

The resulting wake slope angles ξ_{lin} are listed in Table 6.4. Generally, ξ_{lin} increases in magnitude toward the fuselage. The $\eta = 28.3\,\%$ slopes are large at the two lower angles of attack, with $\alpha = 20°$ causing less deflection. While $\alpha = 16°$ causes the highest lift, its absolute downwash angle ξ in the inflow coordinate system is similar to that of $\alpha = 18°$ at $\eta = 28.3\,\%$. However, the difference $\Delta\xi_{lin} = \xi_{lin,\alpha=16°} - \xi_{lin,\alpha=18°}$ is far smaller than the angle of attack increment $\Delta\alpha = 2°$. ξ describes the deflection relative to the inflow, and the $\alpha = 16°$ achieves similar deflection at lower angle of attack. $\xi_{\alpha=16°}$ is even smaller at $\eta = 20.1\,\%$, which is due to the small size of the wake and the difficulty in properly capturing a minimum. These wake slope angles are used for the definition of the coordinate system WC which is employed in parts of the wake turbulence analysis below. WC is oriented with its streamwise axis parallel to the local wake centerline. It is obtained by rotating the WT system by ξ_{lin} around the PMR.

Tab. 6.4.: Wake centerline slope angles of the linear wake portion ξ_{lin} at different angles of attack and positions.

Plane	$\alpha = 16°$	$\alpha = 18°$	$\alpha = 20°$
$\eta = 20.1\%$	-1.4	-6.9	-3.8
$\eta = 28.3\%$	-5.3	-5.4	-4.0
$\eta = 60.3\%$	2.0	0.5	0.1

6.1.4. Concluding Remarks

The topology of three-dimensional wake flow was investigated, and its shape was associated with the wing lift distribution. Three distinct combinations of k_t production locations were identified. Among those, the presence of significant k_t near the trailing edge correlates with whether the rear stagnation point is located upstream or downstream of the trailing edge. All three solutions predict a large separated wake with significant longitudinal vorticity propagating downstream. The spanwise position of this vortical structure varies with α. The outboard separation is little affected by this vortical structure and does not change with α.

Its position shifts inboard at higher α, which significantly alters the separation characteristics at the inboard locations. While the recirculation almost disappears at $\alpha = 16°$ at $\eta = 20.1\,\%$, it retains a large spatial extent and produces significant k_t at $\alpha = 20°$. The increase of inboard wake size at high α was quantitied via plane wake halfwidth l_s and momentum thickness Θ. Furthermore, the inboard wake is more asymmetric than the outboard wake. The degree of asymmetry partially translates to increased downwash, which was quantified via linear interpolation and determination of ξ_{lin}.

6.2. Dynamics of Separation and Wake

> To caricature, it has jokingly been said that, once one has eliminated all features of a flow that one understands, what remains is turbulence.
>
> Mathieu and Scott, *An Introduction to Turbulent Flow* [88]

The multiscale broadband turbulence in the wake is chaotic, but nevertheless contains features that can be interpreted and associated with physical phenomena. Modal analysis, especially low order modeling approaches such as POD, offers a way to separate quasi-periodic and large scale motion from small scale turbulence. This type of analysis will be applied in the following in order to gain an understanding of the dynamic processes in the turbulent wake. The spectral characteristics of the tailplane loads can be associated with these dynamics.

6.2.1. Proper Orthogonal Decomposition Analysis of Longitudinal Wake Slices

POD decomposes fluctuating turbulent motion in the wake and orders the resulting modes according to the fluctuation energy represented by them by way of solving the eigenvalue problem for the correlation matrix constructed from the dataset. The resulting low order models permit reconstruction of fluctuating time series using arbitrary numbers of modes. The POD method was applied to the time series of planar data sets. The method is generally agnostic to the structure of the input data, as the inputs are flattened into a 1D array in each temporal snapshot. Simultaneous POD of multiple variables involves stacking the arrays at each time step. Each snapshot array forms a column of the input matrix, with the latter having $(N_{\text{vars}} \cdot N_{\text{points}})$ rows and $N_{\text{snapshots}}$ columns. All three velocity components are used, implying $N_{\text{vars}} = 3$. The decomposition of the velocity field results in spatial modes ϕ_i and associated temporal coefficients a_i.

POD eigenvalues obtained for five longitudinal planes using u, v and w at $\alpha = 18°$, based on $N_{\text{snapshots}} = 1500$ representing 150 convective times t_∞, are distributed as shown in Fig. 6.19. The dataset obtained at $\alpha = 18°$ will be explored before highlighting the differences occurring due to α. The relative magnitude of the eigenvalues λ_i of the first 16 modes at five different spanwise positions in Fig. 6.19a reveal the presence of significant low order modal structure. Pairwise grouping of modes can be observed, with several modes having a counterpart with similar energy in the eigenvalue spectrum. Such pairing is often indicative of convective structures propagating through the flow field. The modes of the first pair each account for about 4-6% of the total fluctuation energy, while the second pairs contribute about 3-4%

each. The higher order modes above the discernible pairs show slowly decreasing energy levels. The $\eta = 60.3\,\%$ slice contains only one noteworthy mode pair, which dominates significantly over the rest. The $\eta = 20.1\,\%$ position shows the lowest degree of structure in the sense of mode pairing and distinctiveness, with the lowest mode pair contributing the least percentage of energy among the planes. $\eta = 39.7\,\%$ shows the most distinct pairing in terms of relative energy. While some low order structure is present, mode 16 in each plane contributes about one fifth of the energy of the corresponding mode 1. This decrease by only a factor of five indicates that the flow possesses a complexity that may not necessarily be easily captured by reducing it to only few modes. This can be expressed as relative information content RIC, which represents the cumulative eigenvalue magnitude of modes, i.e. $\mathrm{RIC}(k) = \Sigma_{i=1}^{k}\lambda_i / \Sigma_{i=1}^{N}\lambda_i$. This can be used as a guideline for reconstruction, as it gives an indication over how many modes would be required to represent a certain fraction of energy, or information. Fig. 6.19b shows that about 500 modes are required in order to accumulate and reproduce 90 % of the fluctuation energy. Nevertheless, the lowest order mode pairs can be expected to provide insight into the most significant dynamic processes in the wake.

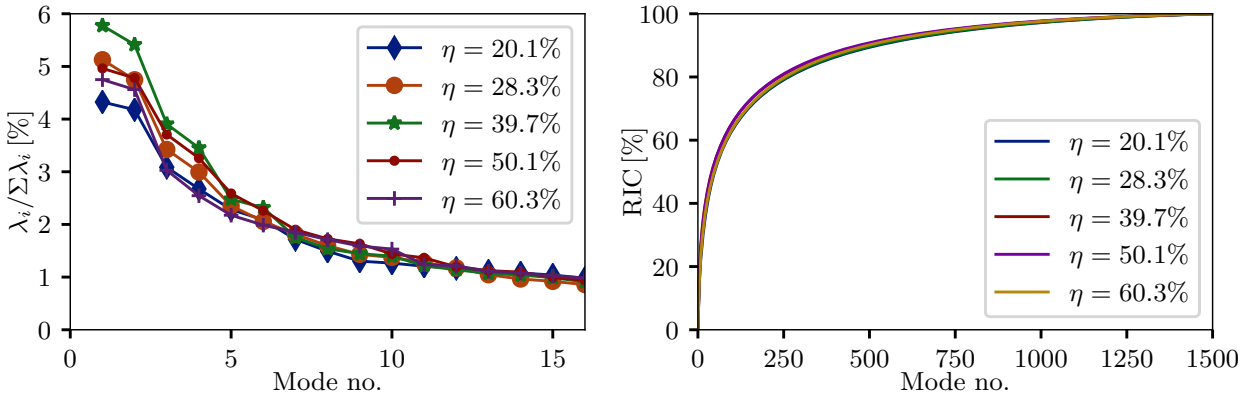

(a) Mode energy percentages **(b)** Relative information content

Fig. 6.19.: POD mode eigenvalues in wake slices at $\alpha = 18°$.

The mode shapes of the first four modes at $\eta = 28.3\,\%$, which form two pairs with similar eigenvalue levels in Fig. 6.19a, are shown in Fig. 6.20. Each velocity component is shown separately. The first two modes are spatially concentrated in the near wake and above the wing, representing the low order dynamics of the recirculation region. The fluctuations are strongly three-dimensional, with the spanwise component v alternating in a manner similar to u. The vertical velocity w shows its highest values near the trailing edge and immediately downstream, however these structures do not propagate far downstream. The magnitude of fluctuations associated with these modes decreases downstream of the rear stagnation point. This observation can be interpreted as these modes being concentrated in the recirculation zone, with a certain amount of correlation to downstream wake features. The second mode pair ϕ_3 and ϕ_4 is mostly located behind the wing in the wake itself, with some additional footprint in the recirculation region upstream of the stagnation point. However, these latter areas have lower magnitudes of ϕ than the wake. The mode shapes in the wake reveal significant spatial order with alternating features. The vertically alternating shapes of the u modes and the aligned w fluctuation patterns resemble a vortex street. These modes indeed represent the vortex street-like motion as previously observed by Zimmermann et al. [182]. This is consistent with interpretation of paired modes by other authors, often associating the occurrence of mode pairs with alternating oscillation motion [159] [174].

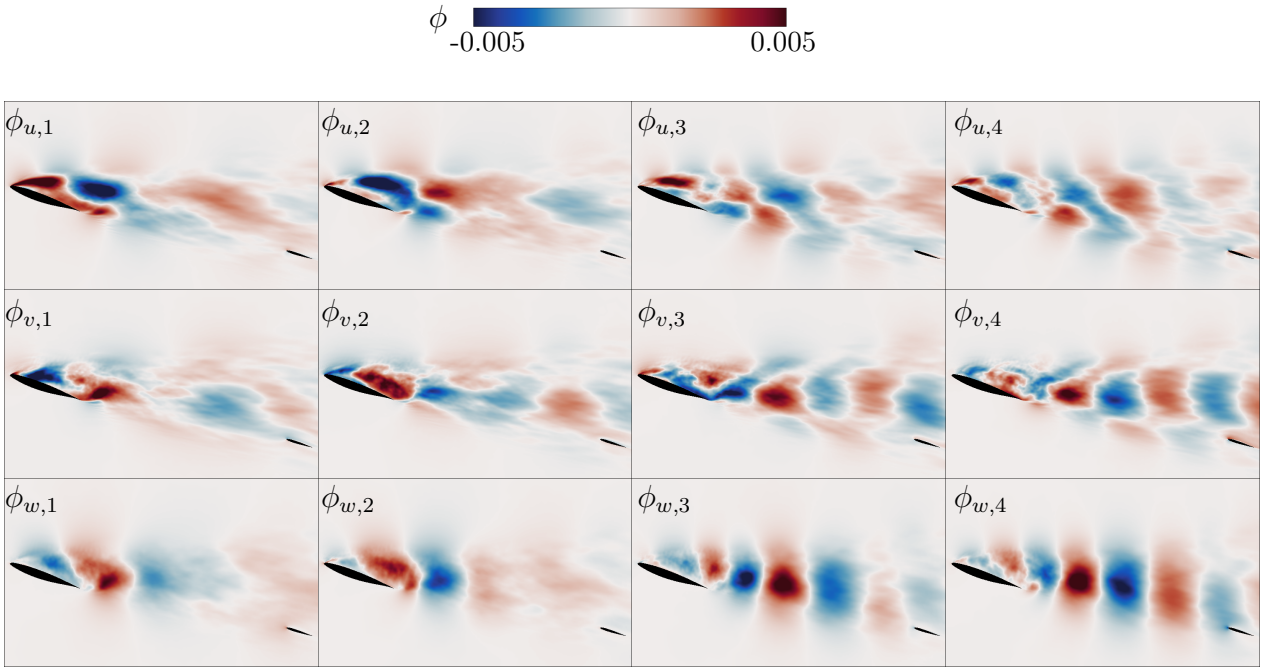

Fig. 6.20.: First four POD modes at $\eta = 28.3\%$ and $\alpha = 18°$, coupled POD.

However, this feature is not a canonical planar vortex street with purely transverse velocity fluctuations. Modes 3 and 4 involve significant alternating structures of the spanwise velocity component v in the second row of Fig. 6.20, coinciding with the w pattern. This is reasonable in light of the three dimensional character of the flow in the inboard region. This observation suggests that the mean longitudinal vortical motion described at the beginning of Section 6.1 is modulated by other oscillating features. In comparison to the first mode pair, ϕ_3 and ϕ_4 are comparatively pure wake modes and extend far into the wake toward the tailplane, which makes these features likely candidates for load fluctuation on the tailplane at their associated frequencies. Their appearance is very similar to the NACA0012 example introduced in Chapter 3.

The apparent spatial order of the mode shapes manifests itself in the temporal evolution of the mode coefficients a_3/a_4 (top panel of Fig. 6.21b), which exhibit a large amount of periodicity. This pair is particularly highlighted due to its association with the wake vortex street. The spectra of the first eight modes are shown in Fig. 6.21a in a pairwise manner to showcase the associations. As in the rest of this section, the Strouhal number on the horizontal axis is computed using the mean aerodynamic chord c_{ref}, situations where it scales with the local projected body height d are indicated specifically. The first two of the pairs in the figure represent narrowband phenomena with spectral densities each containing a prominent peak, at $Sr_{c_{\mathrm{ref}}} = 0.22$ and at $Sr_{c_{\mathrm{ref}}} = 0.5$, respectively. The latter corresponds to $Sr_d = 0.22$ at this location. The prominence of these amplitude peaks suggests that these features can be distinguished and separated in spectral space. The spectra overlap significantly, visualized using magnitude square coherence MSC in Fig. 6.21b. The frequency ranges with high amplitude coincide with MSC values of nearly 1. The spectral separation is not perfect, as exemplified by a secondary spectral peak in a_3 near $Sr_{c_{\mathrm{ref}}} \approx 0.25$ in Fig. 6.21a. This is not coherent with any feature in a_4, which is a result of modal mixing or spectral spillover between the first and second mode pairs.

The coherent mode pairs are phase shifted by $\pi/2$ with respect to each other in the respective

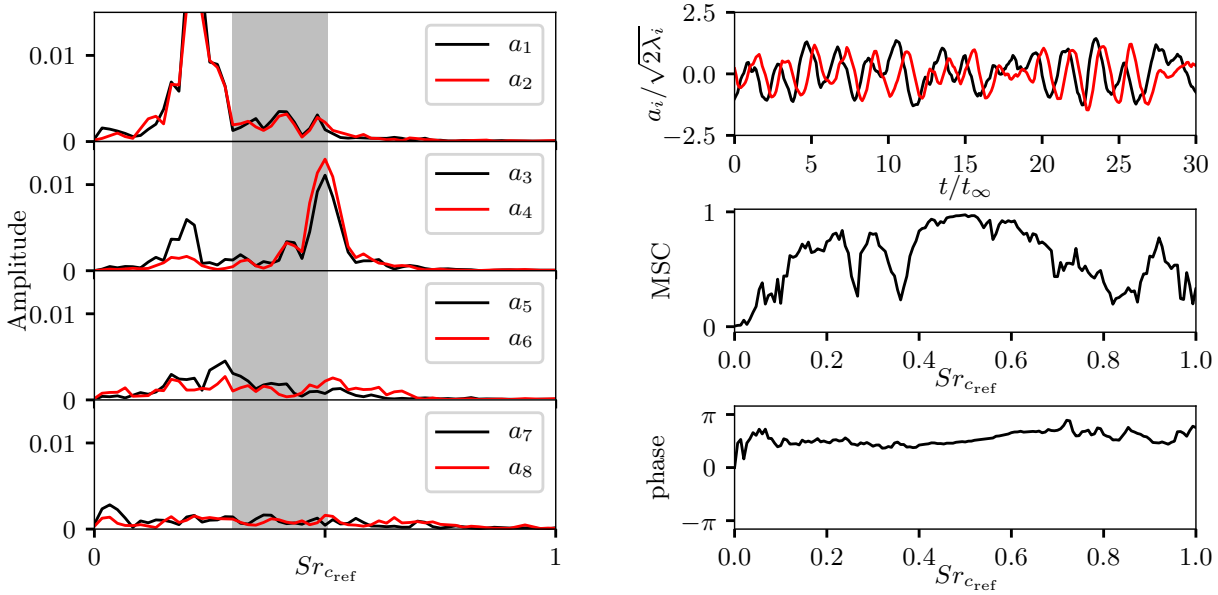

(a) Power spectral densities of coefficient signals a_1 to a_8. Each panel shows a pair, y axis scaling is in arbitrary units. Shaded region denotes range of Strouhal numbers $Sr_d = 0.09...0.22$ based on the local value of d.

(b) Signal time series a_3 and a_4 (top panel) and their interactions (center and bottom panel).

Fig. 6.21.: POD coefficient signal characteristics at $\eta = 28.3\,\%$, $\alpha = 18°$.

frequency regions. The constant shift of the first two modes is shown in the lower panel of Fig. 6.21b. Such coherence and constant phase shift is indicative of periodic oscillation and downstream transport of alternating features, as expected in a von Kármán vortex street type flow. Such phenomena have been described by Wolf [174] for afterbodies, Mulleners et al. [99] for separated airfoil flow or van Oudsheusden et al. [159] for square cylinders. In comparison to the first two mode pairs, there is little order in the higher modes. While there is some amount of pairwise coherence (such as between a_5 and a_6), there are no noteworthy peaks that may indicate prominent flow structures. These modes cannot be readily used for interpretation of single-frequency spatial features. However, they cannot be discounted when considering their contribution to overall fluctuations, as they represent a significant fraction of fluctuation energy.

Fig. 6.22 shows the spectral densities for the first eight mode coefficients at 20.1 %, 39.7 % and 60.3 % of span. The POD results inboard at $\eta = 20.1\,\%$ display significantly less discernible structure than $\eta = 28.3\,\%$ discussed above. There is more severe spectral mixing, with all but the first mode pair showing broadband characteristics with few peaks. This is consistent with the eigenvalue distribution in Fig. 6.19, where only the first mode pair is discernible as such. It is spatially concentrated above the wing and describes an oscillation of the shear layer and recirculation region, as indicated on the left of Fig. 6.23. The high values of the streamwise u component in the spatial shape suggest a strong variation of the streamwise extent of the recirculation region.

The $\eta = 39.7\,\%$ position just outboard of the yehudi kink involves a bimodal spectral structure in Fig. 6.22b, with the first mode pair around $Sr_{c_{\mathrm{ref}}} \approx 0.25$ being more pronounced than the von Kármán wake structure at $Sr_{c_{\mathrm{ref}}} \approx 0.5$. However, the first and second mode pair spectra contain mixed frequencies and are not fully independent. As such, the u component

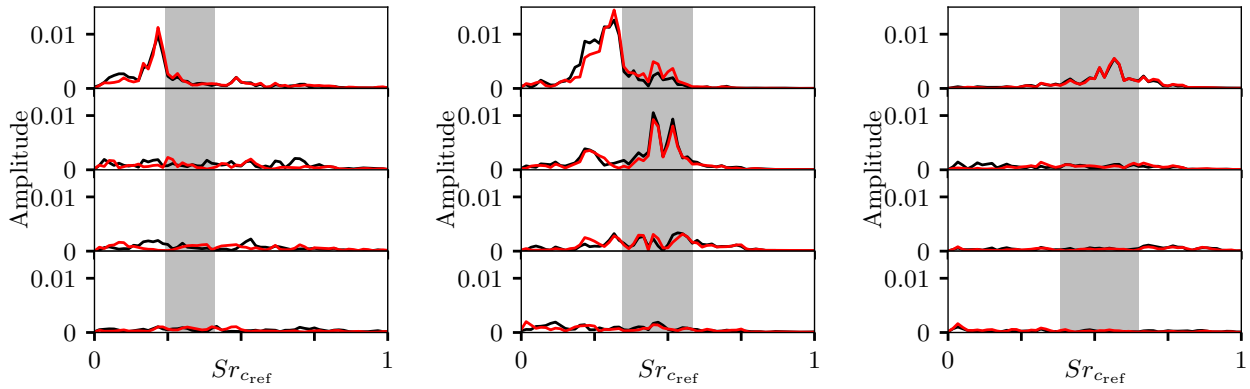

(a) $\eta = 20.1\,\%$ **(b)** $\eta = 39.7\,\%$ **(c)** $\eta = 60.3\,\%$

Fig. 6.22.: POD spectra for first eight modes at different longitudinal planes for $\alpha = 18°$, $Re_\infty = 11.6 \cdot 10^6$. Shaded region denotes range of Strouhal numbers $Sr_d = 0.09...0.22$ based on the local value of d. The vertical arrangement of spectra and the coloring are the same as in Fig. 6.21a.

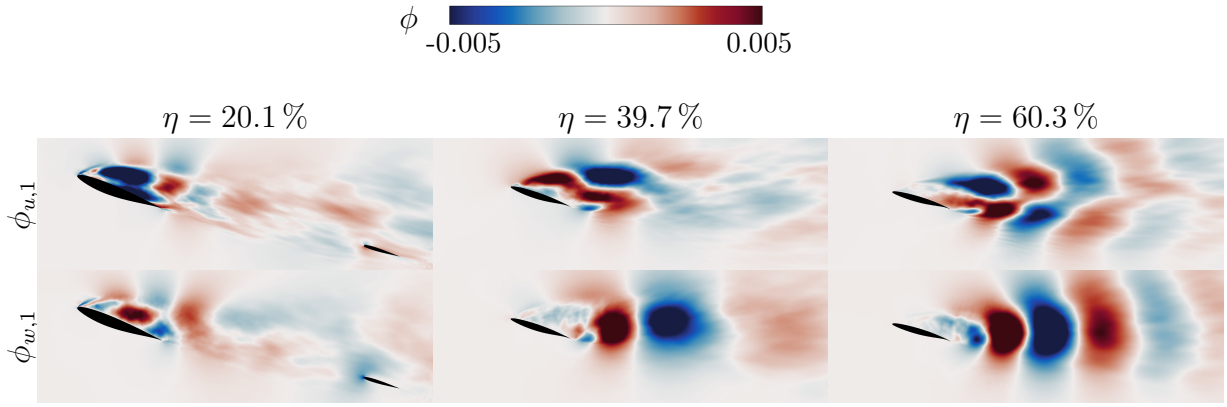

Fig. 6.23.: u and w components of the first POD mode at $\eta = 20.1\,\%, 39.7\,\%, 60.3\,\%$ at $\alpha = 18°$.

distribution of the first mode pair in Fig. 6.23 is of similar appearance as that at $\eta = 20.1\,\%$. The outboard positions exhibit only one significant mode pair, as represented by the $\eta = 60.3\,\%$ position in Fig. 6.23. The von Kármán mode pair at $Sr_{c_{\mathrm{ref}}} = 0.55$ shows almost perfect coherence between the spectral densities of the two modes in Fig. 6.22c, which lie almost indistinguishably on top of each other. There is no low order shear layer mode comparable to those at the inboard locations, most of the POD modal content is in the wake.

In the upper rows of the inboard spectral density plots in Figs. 6.21a and 6.22, there is some indication of a fluctuation taking place around $Sr_{c_{\mathrm{ref}}} \approx 0.06$, which converts to $Sr_d \approx 0.03$. Barring statistical inaccuracies due to inherently short simulation runtimes, this may be associated with features found in literature. Berger et al. [22] suggest the existence of an axial pumping motion, i.e. a lengthening and shortening of the recirculation zone. This feature can be quite prominent, as shown by Wolf [174] for a rocket afterbody. These authors argue that this feature is not associated with alternating oscillation motion and therefore does not generate a POD mode pair. In the present flow field this feature is extremely weak in comparison to the large scale oscillations taking place between $Sr_{c_{\mathrm{ref}}} = 0.22$ and $Sr_{c_{\mathrm{ref}}} = 0.5$.

In general, the outboard wing flow is dominated by two-dimensional structures mostly located behind the wing section. Their appearance is very similar to the NACA0012 example case, with ordered features alternating in streamwise direction. The higher modes do not show any structure. The vertical line representing the expected von Kármán frequency of $Sr_d = 0.22$

shows that the actual frequency is somewhat lower. One plausible reason is that this location does not exist in isolation from the inboard wake and is part of the three-dimensional wing wake. There may be influence of the lower-frequency inboard fluctuation, or a lock-in to the frequency of the oscillation which is dominant in absolute energy terms.

The flow inboard of the Yehudi break involves strong spanwise motion and intermittent shear layer breakdown, which strongly impacts the formation of the wake. A connection between POD modal properties and the separation characteristics can be made. This latter phenomenon is more chaotic and intermittent than the regular von Kármán motion downstream of the wing, which is reflected in the increasing irregularity of the POD results at $\eta = 20.1\,\%$.

Recirculation Dynamics

The low order POD mode at $Sr_{c_{\text{ref}}} = 0.22$ associated with the near wake and backflow region can be used to help explain the local load fluctuations on the inboard wing. The time series of the local lift coefficient $c_L(\eta)$ in Fig. 6.24a and the associated spectral densities in Fig. 6.24b reveal that the spectra of local sectional loads are comparable to the feature occurring at $Sr_{c_{\text{ref}}} = 0.22$ in the wake revealed by POD. This can be seen as indication of an interaction between fluctuation of the recirculation bubble size and the local wing lift dynamics. What is more, the Power Spectral Density (PSD) shows that the pure wake mode at $Sr_{c_{\text{ref}}} = 0.5$ has little influence on the wing lift fluctuation and does not cause increased amplitudes at this frequency. This is consistent with the notion that the far wake influences the bluff body only to a minor degree.

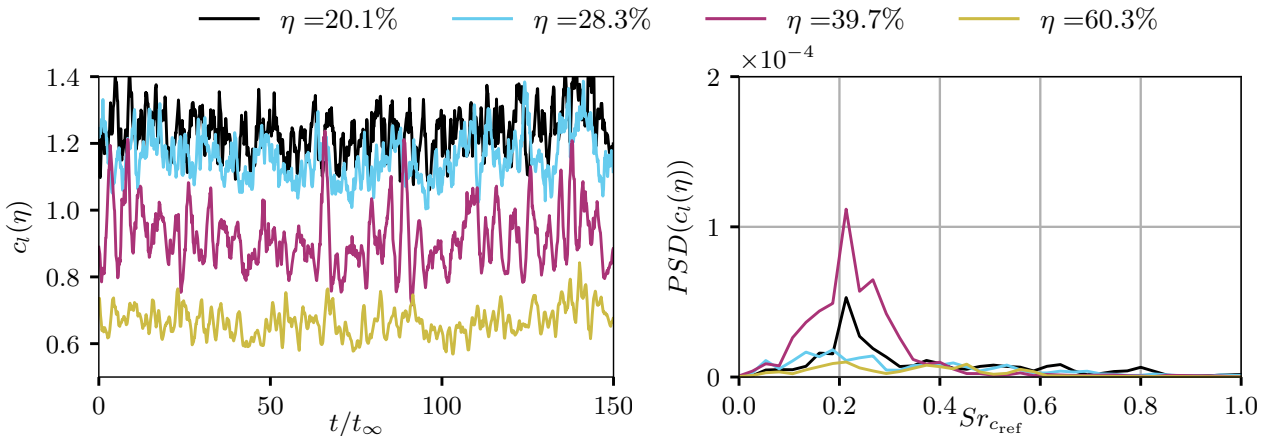

(a) Time signal **(b)** Power spectral density

Fig. 6.24.: Lift coefficient fluctuation $c_l(\eta)$ at $\alpha = 18°$.

While the Strouhal numbers of the von Kármán wake mode partially scale with the local projected body height d, the peaks in Fig. 6.24b all occur at the same frequency, or $Sr_{c_{\text{ref}}}$. This suggests that this phenomenon cannot be explained by analogy of 2D bluff body wake flow, but is rather a feature characteristic for this particular 3D swept wing. A POD analysis of the wing upper side pressure coefficient c_p underlines this, with the first mode pair in Fig. 6.25b showing strongly coherent spectra with peaks at $Sr_{c_{\text{ref}}} = 0.22$. The shapes of these modes in Fig. 6.25a show strong fluctuations across the inboard half of the wing, not confined to a single spanwise location. The highest values are near the leading edge, although much of the inner wing surface is involved. The spatial distribution of the mode pair and

the positions of the maxima relative to each other suggest complex spanwise and chordwise oscillative motion. This is consistent with the earlier observation that significant inward spanwise flow velocities can be observed in this area.

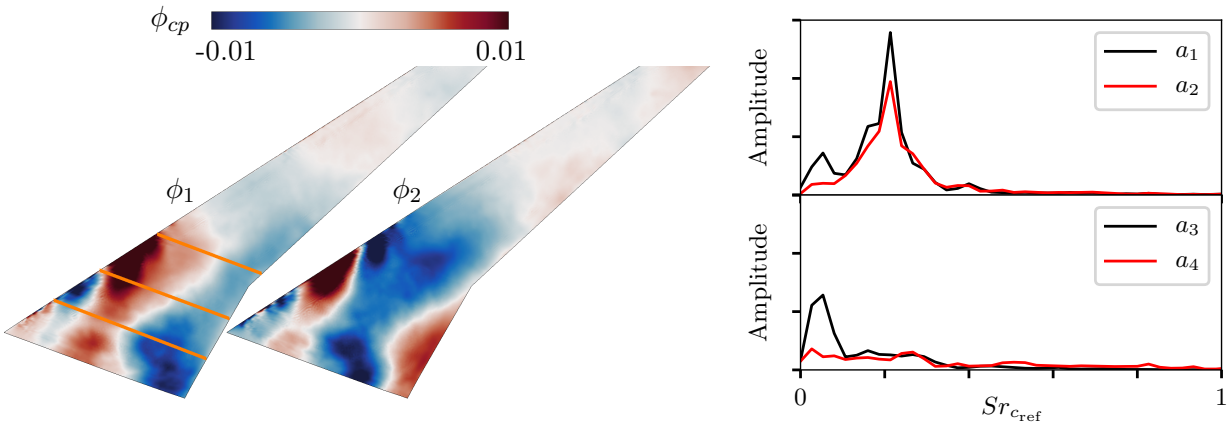

(a) Mode shapes ϕ_1 and ϕ_2. Orange lines on wing surface indicate positions of longitudinal slices $\eta = 20.1\,\%$, $\eta = 28.3\,\%$, $\eta = 39.7\,\%$.

(b) Power spectral densities of mode coefficients

Fig. 6.25.: Low order POD modes of surface c_p.

The location of the high pressure fluctuation area near the leading edge suggests that there is strong intermittent fluctuation of the flow in this region. Fig. 6.26 shows two instantaneous snapshots in the shear layer region via a slice parallel to the leading edge at about 20 % local chord (B). A longitudinal slice at $\eta = 39.7\,\%$ is added for clarity (A). The slices are colored by instantaneous spanwise velocity v. The stratification of inward (blue) and outward (red) spanwise flow is highly variable in space and time, with a strongly serrated isoline $v = 0$ (white). As was shown using time-averaged surface streamlines in Fig. 6.8, near-surface flow

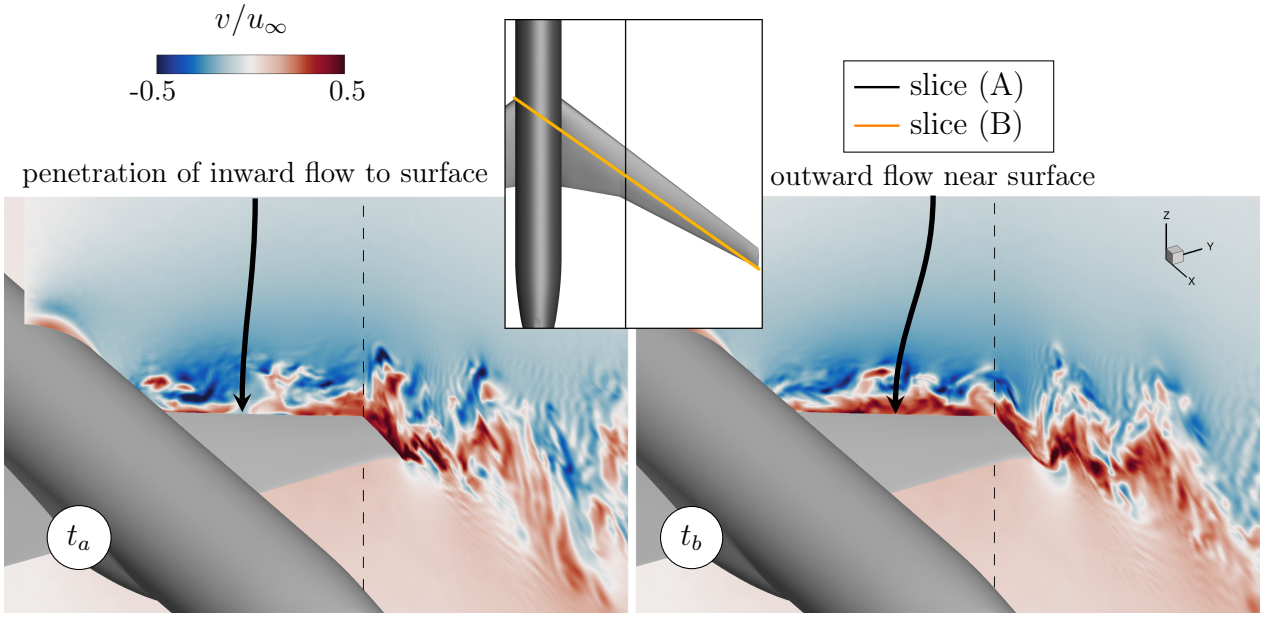

Fig. 6.26.: Instantaneous spanwise velocities at $\alpha = 18°$. Contours in a longitudinal slice at $\eta = 39.7\,\%$ (A) and a slice parallel to the wing leading edge (B). Slice positions are indicated in the inset view. Dashed black line indicates intersection between the two slices.

has a spanwise velocity component with an outward orientation on average, with the exception of the near leading edge region where the streamlines are curved in inward direction. The shear layer between the inner and outer flow is not straight and coplanar with a longitudinal plane, but rather three-dimensional with significant spanwise components. Any temporary breakdown of the shear layer permits high momentum inward flow to reach close to the wing surface, contributing inward components to the time-averaged surface streamlines. Fig. 6.26 shows such an instant on the left-hand side (t_a), when blue shaded inward flow reaches far down to the surface over the inward wing. At the other instant (right-hand side of Fig. 6.26, t_b), the near-wall flow is directed outward, with the shear layer visible at a distance above the wing. This intermittent penetration of high momentum fluid toward the surface results in large scale undulation of the shear layer. It can be considered intermittent breakdown of the shear layer, but no reattachment takes place. This oscillating feature is responsible for the strong pressure fluctuation in the leading edge region shown in the spectra in Fig. 6.25b.

The mode shape pair of surface POD in Fig. 6.25a suggests that most of the coherent motion related to this phenomenon occurs near the leading edge. However, the mid-chord part of the inboard wing does not show the same degree of alternation between the two mode shapes. The leads to the conclusion that the phenomenon responsible for the $Sr_{c_{\mathrm{ref}}} = 0.25$ oscillation originates at the leading edge. The resulting turbulent shear layer contains broadband fluctuation which impacts the surface, most prominently far inboard and at lower α. This is a consequence of the swept wing's longitudinal separation vortex predicted by Harper and Maki [48]. It rolls up on itself, with its upper side impinging disturbances on the rear part of the inboard wing surface. In other words, the majority of fluctuations occurring there do not arrive directly from the leading edge via near wall flow, but rather via the vortical structure. This may explain the lesser degree of clear alternating pattern on the rear wing surface, compared to the mode shape near the leading edge.

On the other hand, near the Yehudi break the shapes of the POD mode pair do indicate alternating surface pressure oscillation consistently over most of the local chord. In other words, the alternating positive and negative contributions of the mode pair are consistent with a locally chordwise oscillation direction. This is particularly evident along the $\eta = 39.7\,\%$ line shown in Fig. 6.25a, indicating locally nearly chordwise propagation of oscillations associated with this fluctuation mode. This is consistent with the extremely regular $c_l(\eta = 39.7\,\%)$ signal in Fig. 6.24a, in which the $Sr_{c_{\mathrm{ref}}} = 0.22$ fluctuation dominates. In contrast to the other $c_l(\eta)$ signals further inboard, the lift fluctuation is not contaminated by other flow features and remains visible over the entire local chord.

The resulting pressure fluctuation footprint at different locations is shown in terms of spectral densities of c_p along four chordwise lines on the wing upper surface in Fig. 6.27. High fluctuation amplitudes can be observed at the inboard locations (Figs. 6.27a, 6.27b) near the leading edge, which extend over a large frequency range. Apart from these, there is a prominent spectral plateau around $Sr_{c_{\mathrm{ref}}} = 0.22$ over the rear half of the chord. The reason for relative dominance of the $Sr_{c_{\mathrm{ref}}} = 0.22$ peak in the spectrum of $c_l(\eta = 39.7\,\%)$ in Fig. 6.24b is visible in Fig. 6.27c, as the spectral peak persists over most of the chord. At $\eta = 28.3\,\%$, this feature is broken up around mid-chord. The shear layer undulation associated with this frequency dominates the lift coefficient spectrum at $\eta = 39.7\,\%$. The inboard positions' spectra are less distinctive due to the loss of clear peaks at mid-chord. Fluctuations at the outboard positions (Fig. 6.27d) do not show distinct spectral features, reaffirming that the outboard shear layer does not appreciably affect surface pressure fluctuations.

While the phenomenon associated with $Sr_{c_{\mathrm{ref}}} = 0.22$ is three dimensional and occurs over the

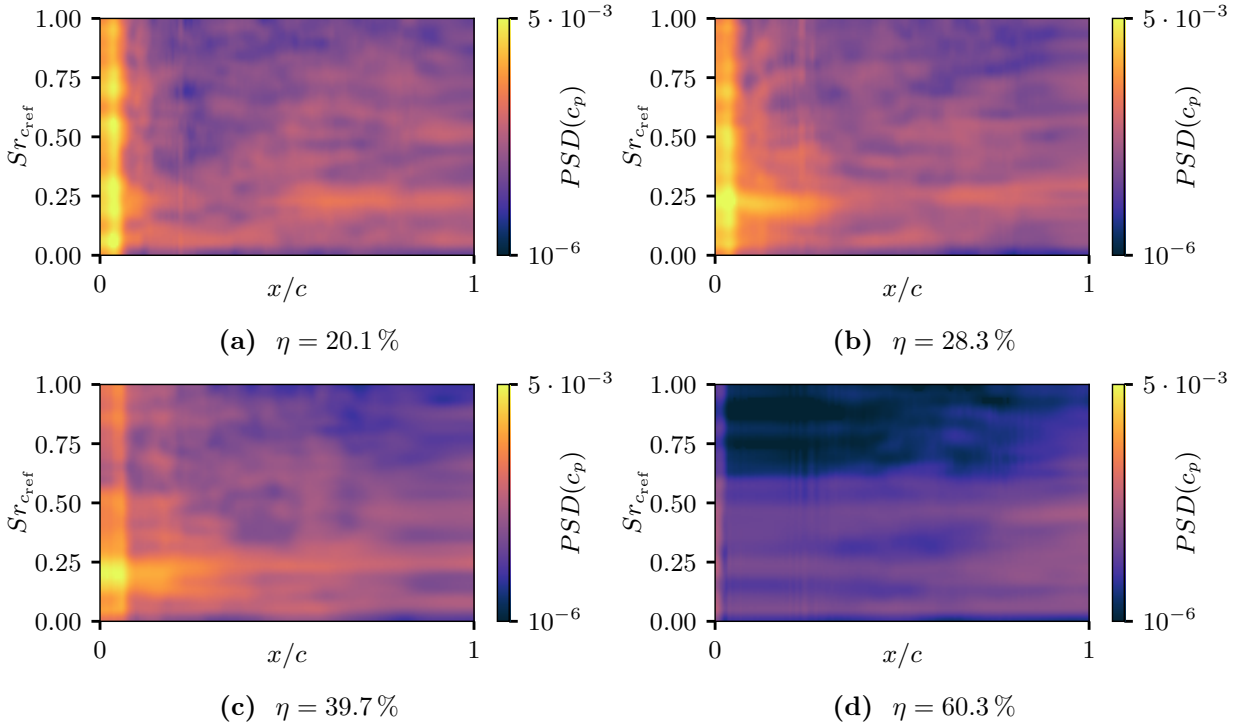

(a) $\eta = 20.1\,\%$ **(b)** $\eta = 28.3\,\%$

(c) $\eta = 39.7\,\%$ **(d)** $\eta = 60.3\,\%$

Fig. 6.27.: Power spectral density of wall c_p along the local chord, $\alpha = 18°$.

inboard third of the wing, it dominates at $\eta = 39.7\,\%$ to such an extent that the regularity of the local sectional lift signal $c_l(\eta = 39.7\,\%)$ in Fig. 6.24a can be used to elucidate the flow mechanisms. The POD coefficient signals of the entire wing surface pressure coefficient and the longitudinal wake slice at that position are compared in Fig. 6.28a. The mode coefficient signal $a_{2,surf}$ of the wing surface POD analysis aligns closely with the signal of the lift coefficient fluctuation $c_l(\eta = 39.7\,\%)$. A time window of $20t_\infty$ is plotted, which contains several periods of all signals. $a_{2,surf}$, $a_{2,\eta}$ and $c_l(\eta = 39.7\,\%)$ show a significant degree of correlation with multiple coincident peaks, although there are superimposed fluctuations at other frequencies. The largest peaks occur at temporal distances consistent with the $Sr_{c_{\mathrm{ref}}} = 0.22$ amplitude, which corresponds to a period of $4.5t_\infty$. The two instants, t_a and t_b, correspond to low and high lift situations, respectively. Fig. 6.28b visualizes the corresponding chordwise pressure coefficient distributions, with t_a and t_b marked in red and black and the intervening temporal snapshots plotted in light gray.

Figs. 6.29a and 6.29b visualize the instantaneous streamwise velocities at t_a and t_b, respectively. The low lift situation at $t_a = 82.6t_\infty$ in Fig. 6.28a coincides with a smooth and homogeneous backflow region in Fig. 6.29a. There is little spatial variation of the negative streamwise velocity u across its extent, i.e. there is bulk reversed flow above the wing with few disturbances. The corresponding instantaneous chordwise pressure distribution for t_a (red line in Fig. 6.28b) is mostly flat, with the exception of a slight suction peak that can be associated with a small pocket of high upstream velocity close to the leading edge. The instantaneous dividing line between high speed outer flow and the recirculation is angled away from the surface and maintains a relatively straight shape with only small scale undulations.

During maximum lift at $t_b = 85t_\infty$ in Fig. 6.29b, this dividing line is much more undulated and closer to the wall in the upstream part. A region of high speed outer flow (B) entrained by the shear is present. A rollup motion with the corresponding high backflow velocity region close to the wall (A) results in a significant spanwise vorticity at this location. This vortical

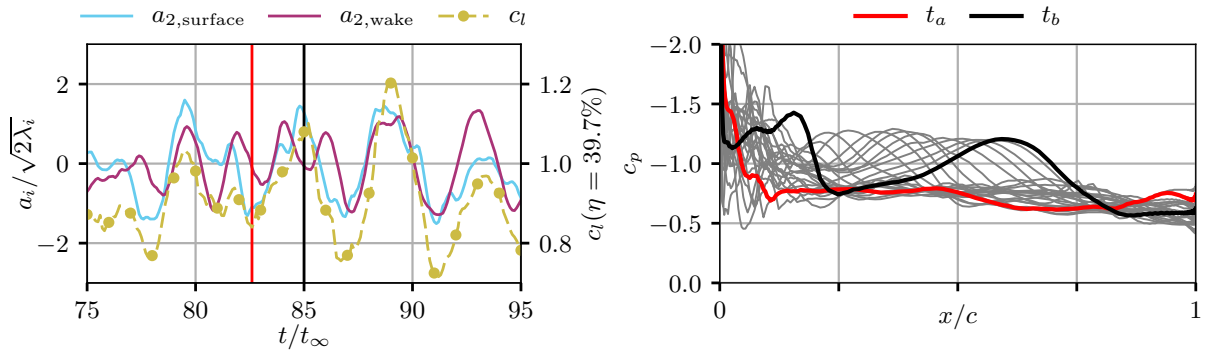

(a) Signals of $c_l(\eta = 39.7\,\%)$, POD wake mode a_2 at $\eta = 39.7\,\%$, and the POD surface mode $a_{2,\text{surface}}$.

(b) Temporal evolution of c_p distributions.

Fig. 6.28.: Temporal evolution of local flow features at $\eta = 39.7\,\%$ during a lift increase period from t_a to t_b.

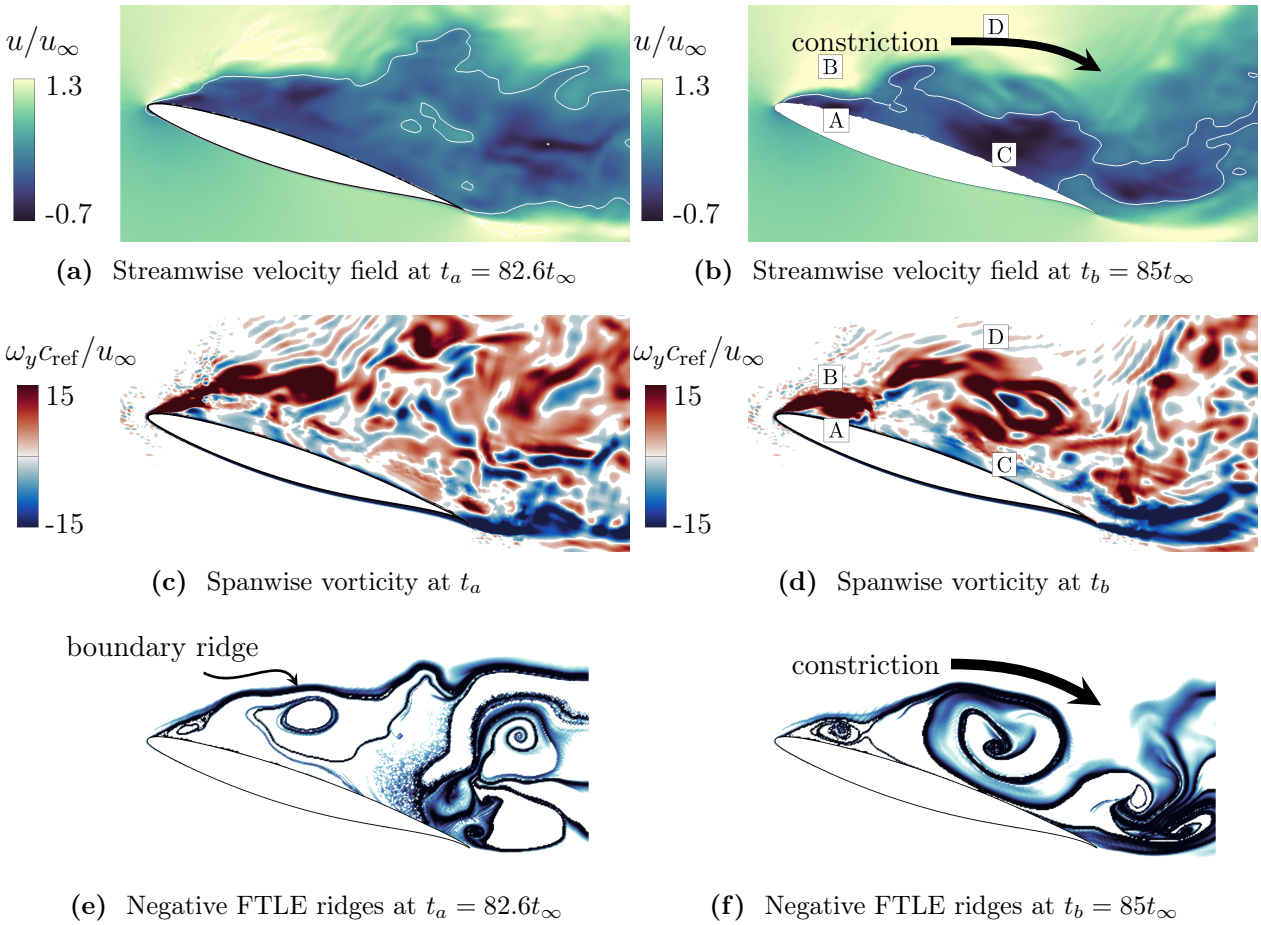

(a) Streamwise velocity field at $t_a = 82.6t_\infty$

(b) Streamwise velocity field at $t_b = 85t_\infty$

(c) Spanwise vorticity at t_a

(d) Spanwise vorticity at t_b

(e) Negative FTLE ridges at $t_a = 82.6t_\infty$

(f) Negative FTLE ridges at $t_b = 85t_\infty$

Fig. 6.29.: Local flow features at $\eta = 39.7\,\%$ during a lift increase period from t_a to t_b.

structure is at $x/c \approx 0.2$ and creates a local c_p decrease in Fig. 6.28b. Further downstream, there is a second, larger region of upstream velocity (C) and a corresponding region of high downstream velocity fluid (D) above the backflow region. The combination of high velocities at C and D causes a wide hump of negative c_p in Fig. 6.28b.

The vortical features at t_b can be visualized using instantaneous vorticity ω_y and ridges of

negative Finite Time Lyapunov Exponent (FTLE) in Fig. 6.29f. The vorticity in Figs. 6.29c and 6.29d provides an impression of the vortical motion, however the large scale structure is superimposed by small scale turbulence which generates spurious vorticity everywhere in the wake. The computation of the FTLE permits the identification of Lagrangian Coherent Structures (LCS). The application here is similar to separated airfoil wake application presented by Steinfurth and Haucke [145], with the corresponding theoretical background described by Shadden et al. [133]. The FTLE field is computed by placing a cartesian plane around the area of interest and interpolating the instantaneous velocity field on it. Afterwards, trajectories of passive particles starting at each point of the interpolated grid are integrated via a 4th order Runge-Kutta method. The integration is carried out in negative temporal direction in order to obtain attracting material lines, over a finite time of 2 t_∞ with a time step of 0.05 t_∞. The plotted FTLE field results from the eigenvalue computation of the Cauchy-Green deformation tensor obtained from the integration, as specified by Shadden et al. [133]. Contiguous regions of high FTLE are termed *ridges* and tend to inhibit flow across them. The structures associated with AB and CD both result in spiral-shaped FTLE ridges in Fig. 6.29f, indicating rotating motion at this location. The FTLE topology at t_a in Fig. 6.29e shows little by way of rotation, involving a single, slightly curved ridge separating outer and inner flow. This shall be called boundary ridge in the present context. This uppermost ridge forming the edge of the backflow region is rolled up into rotating features in t_b. The boundary ridge approaches closer to the wing surface in several locations in t_b compared to t_a. The ridge rollup of the feature CD is associated with a strong downward displacement of the high speed outer flow at t_b, whereas the boundary ridge is undisturbed at t_a and continues a mostly upward trajectory even downstream from the trailing edge.

Judging by the two snapshots and the temporal c_p evolution, the vortex structure CD visible at t_b originates near the leading edge and is propagated downstream over time between t_a and t_b. The history of the instantaneous chordwise pressure distributions at the intervening time steps between t_a and t_b in Fig. 6.28b indicates that it travels from about $x/c = 0.2$ to its final position over multiple time steps. The magnitude of the c_p depression traveling downstream remains approximately constant, however the low pressure region becomes wider as it travels downstream. The rotating motion is fed energy by the high momentum outer fluid, but it does not grow in the vertical direction. Instead, it spreads in streamwise direction and causes low c_p over a larger portion of the chord. At the same time, the AB vortical structure begins to grow, causing additional lift at the upstream part of the wing section. At t_b, the right side of the CD vortex has reached the trailing edge, resulting in reduction of lift with further downstream motion after t_b.

As the phenomenon is so closely tied to the first two POD modes, they are used for reconstruction of the velocity field time series. The resulting reconstructed velocity snapshots for the low and high lift instants t_a and t_b are shown in Figs. 6.30a and 6.30b. These reconstructed field topologies reflect the oscillation of the recirculation region, including the increased upstream and downstream velocities in the region CD at t_b. It is important to note that the POD modes of the entire analyzed plane do not capture the small scale undulations of the shear layer itself, but rather the effect of that motion on the wake plane. They do show the effect of backflow constriction and downward motion associated with structure CD in the rear part of the airfoil. As a result of the POD analysis, the near wing flow oscillates between the two states at $Sr_{c_{\mathrm{ref}}} = 0.22$. This oscillation involves velocity fluctuations across a large area, i.e. the POD mode describing it is spatially more spread out than the local shear layer motion causing it.

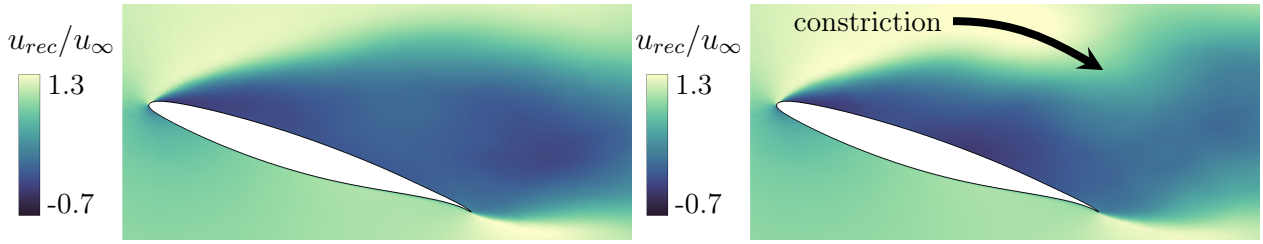

(a) Reconstructed u at $t_a = 82.6t_\infty$ **(b)** Reconstructed u at $t_b = 85t_\infty$

Fig. 6.30.: Streamwise velocities reconstructed using 2 modes at t_a and t_b.

6.2.2. Phase Assignment using POD

The clear correlation between the local sectional c_l signal and the POD wake mode exists only at $\eta = 39.7\,\%$. In the region of interest further inboard, visualization of the backflow region states like in Fig. 6.28 is more difficult. The c_l signal is significantly more contaminated by higher frequency broadband content. Nevertheless, the first mode pair is still associated with the same type of backflow oscillation and represents a periodic undulation of the shear layer.

The fluctuation pattern of the first modes is indeed reflected in the oscillation of the recirculation area size. Again, two representative snapshots are selected in order to visualize the effect of low order dynamics on the flow field, with $t_c = 87t_\infty$ and $t_d = 89t_\infty$. The instantaneous velocity distributions at t_c and t_d in Fig. 6.31 are overlaid with contours of the u component of mode 1, i.e. $\phi_{u,1}$ from Fig. 6.20. Like at $\eta = 39.7\,\%$, there is alternating expansion (t_c, Fig.6.31a) and contraction (t_d, Fig.6.31b) of the backflow region. The region of high streamwise velocity u above the trailing edge at t_d spatially coincides with the local maximum of the $\phi_{u,1}$ mode.

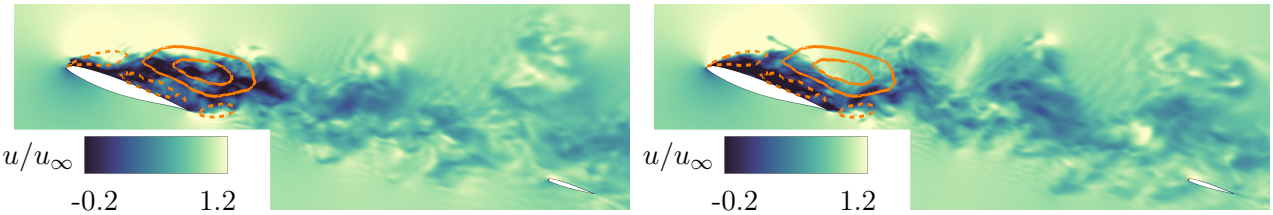

(a) $t_c = 87t_\infty$ **(b)** $t_d = 89t_\infty$

Fig. 6.31.: Instantaneous u at $\eta = 28.3\,\%$ overlaid with contours of the $\phi_{u,1}$ mode from Fig. 6.20, displayed here using lines only for positive (solid) and negative (dashed) regions.

The fact that the alternating oscillation of the shear layer associated with a fluctuation of the entire backflow region occurs at nearly-constant harmonic frequency, and represents the highest energy POD mode pair, makes these two modes a useful phase reference. Perrin et al. [104] and van Oudsheusden [159] carried out similar procedures on cylinder-like geometries, while Mulleners and Rütten [99] described airfoil wake oscillations at static stall using this approach. The constant phase shift of the modes a_1 and a_2 permits a global phase identification without requiring a designated, separate phase indicator signal.

The simplest low order model is based on a flow field reconstruction using the mean value and the first mode pair. The fact that the first mode pair constitutes only about 12 % of the total fluctuation energy in the current POD analysis should not be confused for irrelevance, as the RIC values in Fig. 6.19 relate to the entire plane in which POD was computed. The above discussion has shown that such models may be sufficiently representative. Assuming a

phase relation between the two modes, the coherent oscillation phenomenon can be described as a function of phase angle ψ instead of t by setting

$$a_1(\psi) = \sqrt{2\lambda_1}\sin(\psi) \qquad a_2(\psi) = \sqrt{2\lambda_2}\cos(\psi). \tag{6.2}$$

At any given time t, $\psi(t)$ can be obtained from the values of the mode coefficients via

$$\psi(t) = \arctan\frac{\sqrt{2\lambda_1}a_1(t)}{\sqrt{2\lambda_2}a_2(t)} \tag{6.3}$$

and describes the angular position in the phase space spanned by the two modes. ψ evolves quasi-linearly in time. The reconstructed low order model then reads:

$$u_{rec}(\psi) = \overline{u} + a_1(\psi) + \phi_{u,1} + a_2(\psi)\phi_{u,2} \tag{6.4}$$

The mode coefficients are orthogonal per definition of the POD mode, but not independent. a_1 and a_2 form a disk or ellipse in phase space. An ideal single-frequency uninterrupted oscillation phenomenon would arrange the normalized coefficients on a unit circle [99], whereas the actual data of the first mode pair at $\eta = 28.3\,\%$ is shown in Fig. 6.32a. Each snapshot from the time signal corresponds to a point in the plot. The wide distribution is owed to the complexity of the flow field and the associated randomness, as indicated by the smeared and wide spectral peaks of the a_1 and a_2 modes in Fig. 6.21. The points are not random samples forming a circle, they result from a strongly distorted circular pattern. This is similar to observations described by Mulleners and Raffel [99] in a simpler flow situation involving mild airfoil stall.

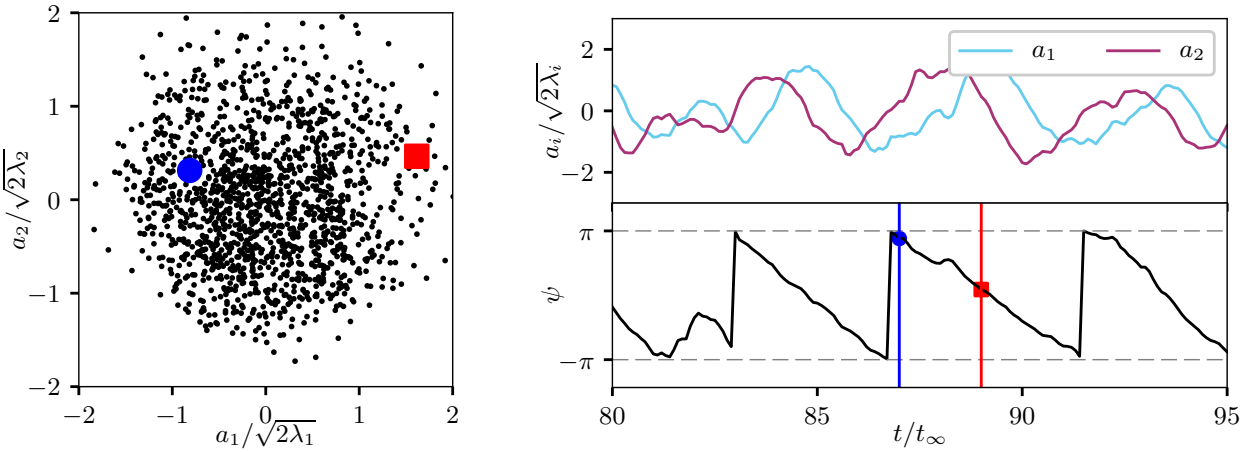

(a) POD coefficient phase space

(b) Mode coefficients a_1 and a_2, and their phase angle ψ over time

Fig. 6.32.: Phase relationship between POD modes a_1 and a_2 at $\eta = 28.3\,\%$. Red vertical line and ■ indicate t_c, blue vertical line and ● denote t_d.

The position of the samples in Fig. 6.32a can be represented in polar coordinates with respect to the space spanned by a_1 and a_2, i.e. a distance from the origin and the angle ψ. The time series of flow field realizations, represented by planar slices at $\eta = 28.3\,\%$ from the unsteady simulation, are binned according to ψ using 48 segments spanning all possible value ranges between 0 and 2π. This corresponds to a bin width of $\Delta\psi = 2\pi/48 = 7.5°$. The distance

from the origin is ignored in this case, as it did not provide any gain in information. Van Oudsheusden et al. [159] discussed the influence of bin width $\Delta\psi$ and arrived at the conclusion that POD-based phase averaging is efficient in the sense that relatively low bin fillings suffice for this purpose. The 48 segments correspond to 31 samples per segment on average in the present case. The locations of t_c and t_d in phase space are highlighted in Fig. 6.32a, showing the locations corresponding to $\psi_c = \pi$ and $\psi_d = 0$, respectively. The plot of ψ in Fig. 6.32b provides a representation of ψ's approximately linear evolution over time.

Averaging over each realization within the bins including ψ_c and ψ_d yields the phase average. This process is applied to two time series: the full original data set of the flow at $\eta = 28.3\,\%$, and to the reconstruction obtained using modes 1 and 2 via Eq. 6.4. In both cases, the resulting samples belonging to ψ_c and ψ_d are averaged and shown in Fig. 6.33. The remarkable similarity between the upper and lower row, i.e. phase averages obtained from the two mode low order model and the original time series, is another indicator for the feasibility of the low order model. Both the shape change of the upper edge of the recirculation area and the constriction of the backflow above the trailing edge at $\psi = 0$ is recognizable in both averages and match the characteristics suggested by the shape of the modes themselves in Fig. 6.20. Even though the low frequency modes are superimposed by higher frequency motion and turbulence, their structure is so dominant that they remain readily visibile in the phase average. This is consistent with observations by Liberzon et al. [78], who described the quality of reconstruction and low truncation errors when using few POD modes. They concluded that evaluating the representativity of the POD result based only on energy percentage or RIC is not sufficient. This is consistent with Lumley's [81] idea of compactness in the context of POD, i.e. of structures that do not significantly change when more modes are added.

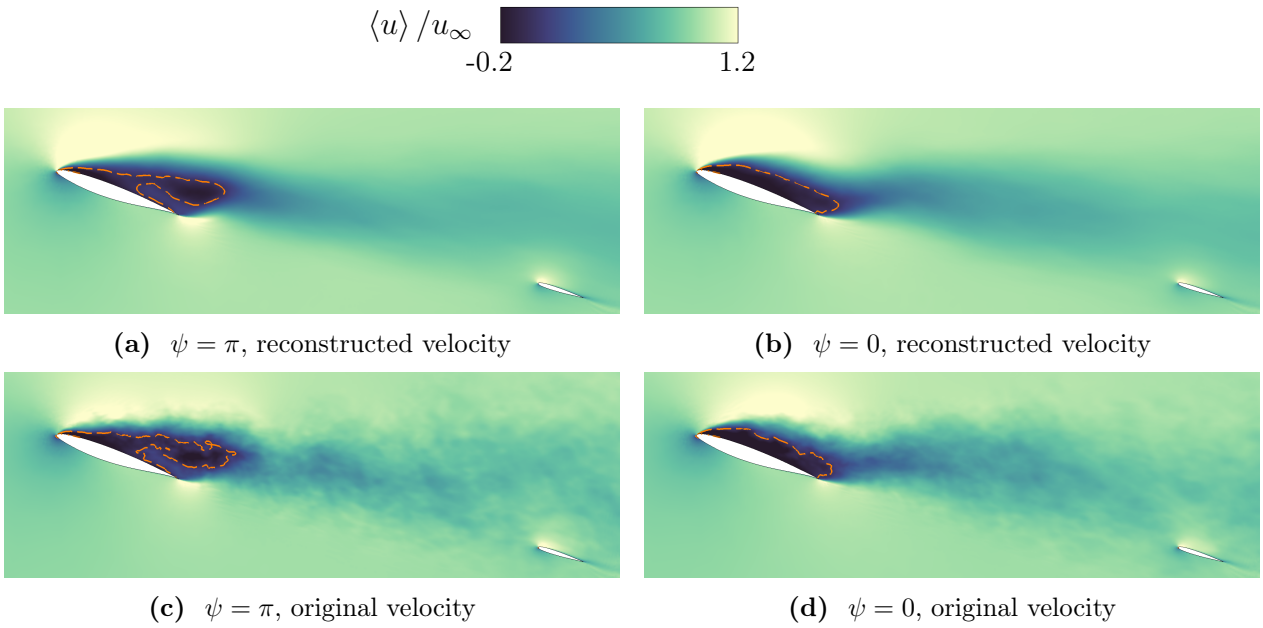

(a) $\psi = \pi$, reconstructed velocity

(b) $\psi = 0$, reconstructed velocity

(c) $\psi = \pi$, original velocity

(d) $\psi = 0$, original velocity

Fig. 6.33.: Phase average of original (top row) and reconstructed (bottom row) streamwise velocity at $\eta = 28.3\,\%$ at two different phase angles. Dashed orange line denotes $\overline{u} = 0$.

6.2.3. Changes in Dynamics due to Angle of Attack

The analysis of wake dynamics and sectional lift force fluctuations was carried out for all three angles of attack. The wing sectional lift was computed at 100 spanwise positions at each time step. Accumulating the signals and applying Welch's [171] spectral density estimation method with 3 overlapping time series segments to each position yields a spectral map which reveals characteristic fluctuation distributions depending on α.

The spectral maps in Fig. 6.34 show fluctuation characteristics of the local lift distributions. The maps show consistently high amplitudes at all conditions below approximately $Sr_{c_{\mathrm{ref}}} \approx 1$, with most significant amplitudes below $Sr_{c_{\mathrm{ref}}} = 0.3$. This is consistent with the surface POD mode at $Sr_{c_{\mathrm{ref}}} = 0.22$ at $\alpha = 18°$, and can be observed over most of the inboard wing ($\eta < 0.4$) at $\alpha = 16°$ as well. All three cases exhibit the strongest fluctuations in the inboard region, with a significant drop-off beyond the Yehudi's location at about $\eta = 37\%$. The $\alpha = 20°$ case shows significantly decreased high frequency fluctuation amplitudes above approx. $Sr_{c_{\mathrm{ref}}} = 1.0$ even inboard, which is a consequence of the larger size recirculation area with greater spatial separations between shear layer and wing surface. The small scale turbulence in the shear layer does not propagate downward to affect the surface pressure at this α as much as in the lower angle of attack cases. Instead, only the very large scale/low frequency wake motion can be detected in the lift coefficient fluctuation, and the amplitudes $Sr_{c_{\mathrm{ref}}} < 0.3$ remain high. Compared to this, $\alpha = 16°$ and $\alpha = 18°$ exhibit similar characteristics. The low level of fluctuation close to the fuselage at $\eta < 0.15$ at $\alpha = 16°$ can be explained by the retreat of the rotating longitudinal vortex in outboard direction, which was discussed above using Fig. 6.9.

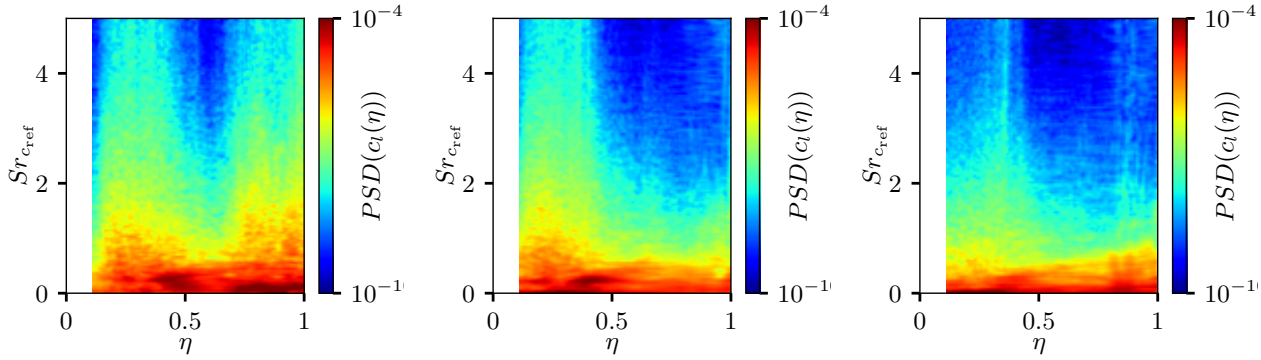

(a) $\alpha = 16°$ **(b)** $\alpha = 18°$ **(c)** $\alpha = 20°$

Fig. 6.34.: Spectral maps of section lift coefficients $c_l(\eta)$ at $Re_\infty = 11.6 \cdot 10^6$.

The same POD analysis procedure was carried out at $\alpha = 16°$ and $\alpha = 20°$. The mode topologies remain similar in terms of shape, therefore representation of mode shapes are omitted. Only spectral densities of the lowest order modes are shown at three spanwise positions in Figs. 6.35 and 6.36, which is sufficient for an overview in comparison to Fig. 6.22. Strouhal number scaling with c_{ref} is used throughout, since few direct correlations with projected height d can be observed.

The low order mode coefficient spectra $\alpha = 16°$ at $\eta = 20.1\,\%$ (Fig. 6.35a) are very similar to those at $\alpha = 18°$. Only one mode pair is discernible, corresponding to the $Sr_{c_{\mathrm{ref}}} = 0.22$ fluctuation and no von Kármán-like features at $Sr_{c_{\mathrm{ref}}} = 0.5$ are present. The spectra at $\eta = 28.3\,\%$ in Fig. 6.35b are somewhat more smeared and show less spectral separation

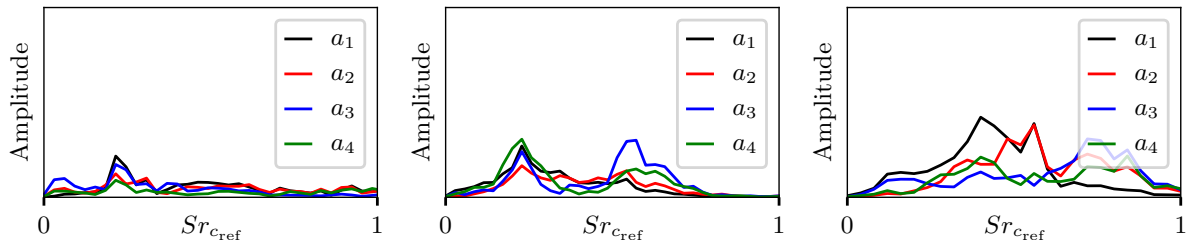

(a) $\eta = 20.1\,\%$ **(b)** $\eta = 28.3\,\%$ **(c)** $\eta = 60.3\,\%$

Fig. 6.35.: Power spectral densities of POD coefficients at $\alpha = 16°$, $Re_\infty = 11.6 \cdot 10^6$, linear scales.

than those at the same position at $\alpha = 18°$. One explanation for this may be the tighter coupling and interaction between the leading edge shear layer and the wake at $\alpha = 16°$ due to the overall compactness of the wake features at lower α. The larger physical distance between recirculation and downstream wake at $\alpha = 18°$ decreases interactions between these phenomena, increasing the sharpness of the peaks. Apart from these differences, the main fluctuation frequencies are similar. The low frequency recirculation mode occurs at the same frequency $Sr_{c_{\text{ref}}} = 0.22$ as at $\alpha = 18°$. The higher von Kármán wake mode occurs at a slightly higher $Sr_{c_{\text{ref}}}$, which is consistent with lower projected height d due to lower α.

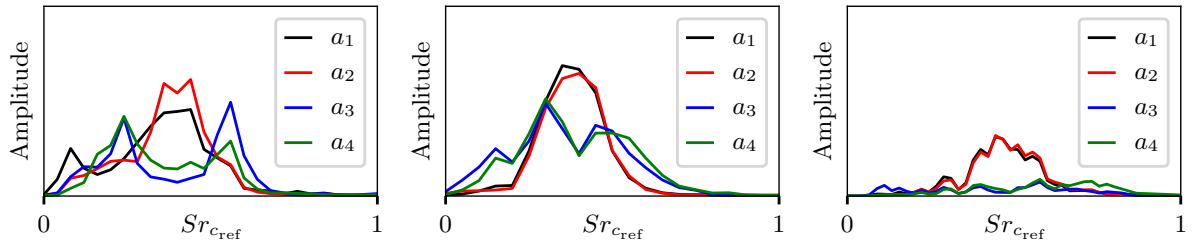

(a) $\eta = 20.1\,\%$ **(b)** $\eta = 28.3\,\%$ **(c)** $\eta = 60.3\,\%$

Fig. 6.36.: Power spectral densities of POD coefficients at $\alpha = 20°$, $Re_\infty = 11.6 \cdot 10^6$, linear scales.

The POD results at $\alpha = 20°$ in Fig. 6.36 differ somewhat from those observed at the two lower angles of attack. Although the POD coefficient signals are not cleanly harmonic at $\alpha = 18°$, they are still much more variable in terms of frequency at $\alpha = 20°$. While the two significant flow features at $\alpha = 18°$ are separated into separate mode pairs with one spectral peak each, there are broad regions of high amplitude $\alpha = 20°$ at both $\eta = 20.1\,\%$ and $\eta = 28.3\,\%$. These indicate that the fluctuation dynamics are somewhat less regular at this α than at the other two. Here, the low order dynamics are represented by two mode pairs, with the spectra of a_3 and a_4 occurring at similar frequencies to those at the lower angles of attack. The spectra of the modes a_1 and a_2 show high amplitude regions at frequencies between those of the second mode pair's peaks. This lack of separation makes the interpretation of these modes more difficult than for the flow features at $\alpha = 18°$. However, the fact that the peaks of a_3 and a_4 at $\eta = 20.1\,\%$ and $\eta = 28.3°$ occur at frequencies so similar to those at $\eta = 28.3\,\%$ and $\alpha = 18°$ is an indication that similar dynamics take place. In fact, the appearance spectral peaks of a_3 and a_4 in Fig. 6.36a at these frequencies is an indication that the dynamics at $\eta = 20.1\,\%$ and $\alpha = 20°$ behave similarly to those at $\eta = 28.3\,\%$ and $\alpha = 18°$. This agrees with the observations from 6.1.3 that the wake extends inboard closer to the fuselage at higher α. The position at $\eta = 20.1\,\%$ shifts from a type II pattern at $\alpha = 18°$ to type III at $\alpha = 20°$. The broadening of the spectral features continues when considering the dynamics further outboard, where the von Kármán mode at $\alpha = 20°$ is less prominent in spectral space of the

POD coefficients than at the lower α. This is one drawback of the POD method, as there is no way to fully avoid spectral mixing. Methods such as Dynamics Mode Decomposition (DMD) or Spectral POD (SPOD) may help alleviate these issues.

6.2.4. Concluding Remarks

The POD analysis provides insight into the large scale, energy carrying structures present in the wake, which are associated with the k_t field investigated in Section 6.1.3. Modal structure consisting of two mode pairs was identified at most of the investigated inboard positions which exhibit type III distribution of k_t identified in Section 6.1.3. One pair is associated with recirculation region dynamics above the wing, and the other with a von Kármán vortex street in the wake. The latter is most clearly identifiable in the outboard wake, which also exhibits the largest degrees of symmetry as per Section 6.1. The recirculation mode is barely detectable at these locations, consistent with the lack of significant k_t production above the wing in the type I configuration.

The mode pair associated with recirculation region dynamics was used to carry out phase averaging, the results of which were leveraged to identify the two recirculation region shapes at opposite angles in phase space. It can be shown via comparison of phase averaged original and reconstructed velocity time series, that most of the information on the recirculation region dynamics is contained in the low order mode pair, despite its comparatively low contribution to the overall turbulence kinetic energy of the wake plane.

Furthermore, the influence of α on wake dynamics and wing pressure fluctuation was evaluated based on POD. The increased bluffness of the wake at high α causes less broadband surface pressure fluctuations, as most of the elevated k_t areas remain further away from the surface.

6.3. Quantitative Characteristics of Wake Turbulence

Having discussed the three dimensional separation topology and the large scale separation dynamics in the wake, the turbulent phenomena in the wake are investigated in the following. The focus is primarily on the $\eta = 28.3\,\%$ plane, with spanwise difference highlighted where appropriate.

The first part in Section 6.3.1 involves analysis of the Reynolds stresses and their anisotropy in the inboard wake at the three different α inflow conditions. Following this, turbulence characteristics are investigated more in depth in Section 6.3.2, separately highlighting processes in the shear layer and in the downstream wake. Signal analysis of turbulent fluctuations and momentum exchange characteristics are used to describe the structure of the separated wake. At the end in Section 6.3.3, this knowledge of the turbulent fluctuations is used to determine spatial correlation characteristics and turbulent length scales in the wake.

6.3.1. Turbulent Stresses in Separated Flow

As described via Fig. 6.11, the separation and wake at $\alpha = 18°$ and $\eta = 28.3\%$ involve two distinct regions of fluctuation, termed type III in Section 6.1.

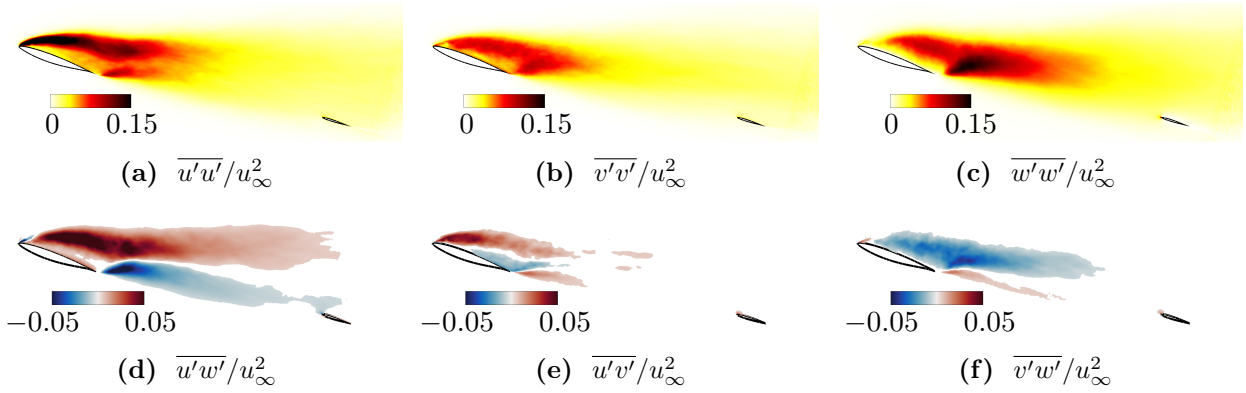

(a) $\overline{u'u'}/u_\infty^2$ **(b)** $\overline{v'v'}/u_\infty^2$ **(c)** $\overline{w'w'}/u_\infty^2$

(d) $\overline{u'w'}/u_\infty^2$ **(e)** $\overline{u'v'}/u_\infty^2$ **(f)** $\overline{v'w'}/u_\infty^2$

Fig. 6.37.: Resolved Reynolds stress components at $\alpha = 18°$ and $\eta = 28.3\,\%$.

The resolved fluctuation components in Fig. 6.37 show that these maximaof k_t are associated with different elements of the Reynolds stress tensor. The large scale dynamic processes associated with the leading edge separation result in extremely high values of streamwise normal stress $\overline{u'u'}$, which decrease further downstream. The low order, high energy POD modes also involve primarily streamwise fluctuations, underscoring this. On the other hand, the transverse normal component $\overline{w'w'}$ is highest behind the wing and in the wake, reflecting the large scale vertical wake motion also revealed via POD. The momentum exchange between streamwise and transverse fluctuations $\overline{u'w'}$ is mostly coincident with high $\overline{u'u'}$ and occurs mostly over and near the wing surface, with comparatively low values in the wake. The highest velocities and velocity gradients exist in this region, causing significant shear stress. The same is true for the streamwise-spanwise shear component $\overline{u'v'}$, which is significant downstream from the swept leading edge.

Despite this, the components related to spanwise motion are of lower magnitude than the others, but not negligible. Normal spanwise stress $\overline{v'v'}$ occurs mostly in the leading shear layer and a short distance downstream of the trailing edge. There is significant interaction $\overline{v'w'}$ downstream of the trailing edge, which is consistent with the large scale longitudinal vorticity ω_x observed above in Section 6.1.3. That vortical structure is detectable in the time averaged velocity field, but is difficult to capture in instantaneous data. The rotation about the x-axis implies flow with varying velocity components v and w. Fluctuation of these velocities over time results in significant Reynolds stress $\overline{v'w'}$.

Anisotropy of Turbulence

The stress components in Fig. 6.37 are distributed unequally, showing that the resolved Reynolds stress tensor $\overline{u_i u_j}$ involves some degree of anisotropy. This imbalance between the fluctuation directions and components can be quantified via the anisotropy tensor a_{ij}, which is obtained from the Reynolds stress tensor via

$$a_{ij} = \frac{\overline{u_i u_j}}{2k_t} - \frac{1}{3}\delta_{ij} \tag{6.5}$$

The anisotropy tensor is dimensionless, has zero trace and vanishes identically in the case of isotropy [112]. The transformation of the resolved Reynolds stress tensor to the anisotropy tensor via Eq. 6.5 isolates the anisotropy properties, which gives rise to visualization and quantification of the directional properties of turbulent fluctuations. Analysis of a_{ij} provides

information on the shape of the Reynolds stress tensor. This is achieved by computing the three invariants of a_{ij}, the first of which is the trace and therefore equals 0 by definition. The second and third invariants are

$$\begin{aligned} II_a &= a_{ij}a_{ji} \\ III_a &= a_{ij}a_{jk}a_{ki} \end{aligned} \tag{6.6}$$

and define a space that contains all possible shapes of the Reynolds stress tensor, or anisotropy states. The invariants describe the magnitudes of the tensor eigenvalues λ_i relative to each other. The classification of turbulence states using anisotropy representation amounts to the description of the energy ellipsoid [19]. This is a model representation of the anisotropy state in terms of a geometrical shape determined by the relative magnitude of its semi-axes. Three equal eigenvalues $\lambda_1 = \lambda_2 = \lambda_3$ define a perfectly spherical ellipsoid without preference for any direction, while differences in eigenvalues may stretch or squeeze it into a non-spherical ellipsoid.

The anisotropy of the wake along the centerline, as defined by ξ_{lin} in Fig. 6.18, is visualized in Fig. 6.38. Invariant values are plotted along the centerline from the trailing edge position to $(x - x_{TE})/c_{\text{ref}} = 3$. The latter position roughly corresponds to around the mid-chord of the tailplane. In this Anisotropy Invariant Map (AIM) by Lumley and Newman [82], the flow tends toward the isotropic corner at $II_a = III_a = 0$ with increasing streamwise distance. The state in this lower corner represents isotropic turbulence with fluctuation energy distributed equally across the directional components. Most of the values along the wake centerline are not far from this state. Zoomed-in views are given in Figs. 6.38b-6.38d, as most of the points are close to the corner of the AIM.

The color coding of the point samples corresponds to streamwise position. As the wake centerline is well above the tailplane, it does not seem to be influencing the local anisotropy state. The purple samples in the recirculation above the trailing edge start out away from the turbulence map edges, albeit still close to the isotropic state at the bottom. Past the rear stagnation point in the far wake, they move toward the right-hand limit of the map. This boundary represents an axisymmetric expansion of the Reynolds stress tensor with three nonzero eigenvalues, one of which being larger than the other two. This is equivalent to one principal stress component being larger than the other two [136]. The dominant vertical normal stress $\overline{w'w'}$ in the wake in Fig. 6.37 is responsible for this.

With increasing downstream distance, the eigenvalues tend toward equilibrium and the tensor approaches a spherical shape. The flow develops further toward isotropy and moves downward along the axisymmetric expansion line in the AIM. While a fully isotropic state of resolved turbulence is never reached in Fig. 6.38, the centerline values at $\alpha = 16°$ and $\alpha = 18°$ approach values closest to it. This is an effect of the smaller wake size at the smaller α values, which promotes the most thorough mixing of low momentum wake flow with outer flow and accelerates isotropization. The opposite is true at $\alpha = 20°$ due to the larger wake extent.

A drawback of the representation in Fig. 6.38 is that it is difficult to visually ascertain the degree of isotropy in the flow due to bias inherent in the AIM's construction. In order to rectify this feature of Lumley's [82] AIM, Banerjee et al. [19] proposed representation of the anisotropy tensor using a convex combination of basis matrices representing limiting states of the stress tensor — one-component, two-component and three-component turbulence. These

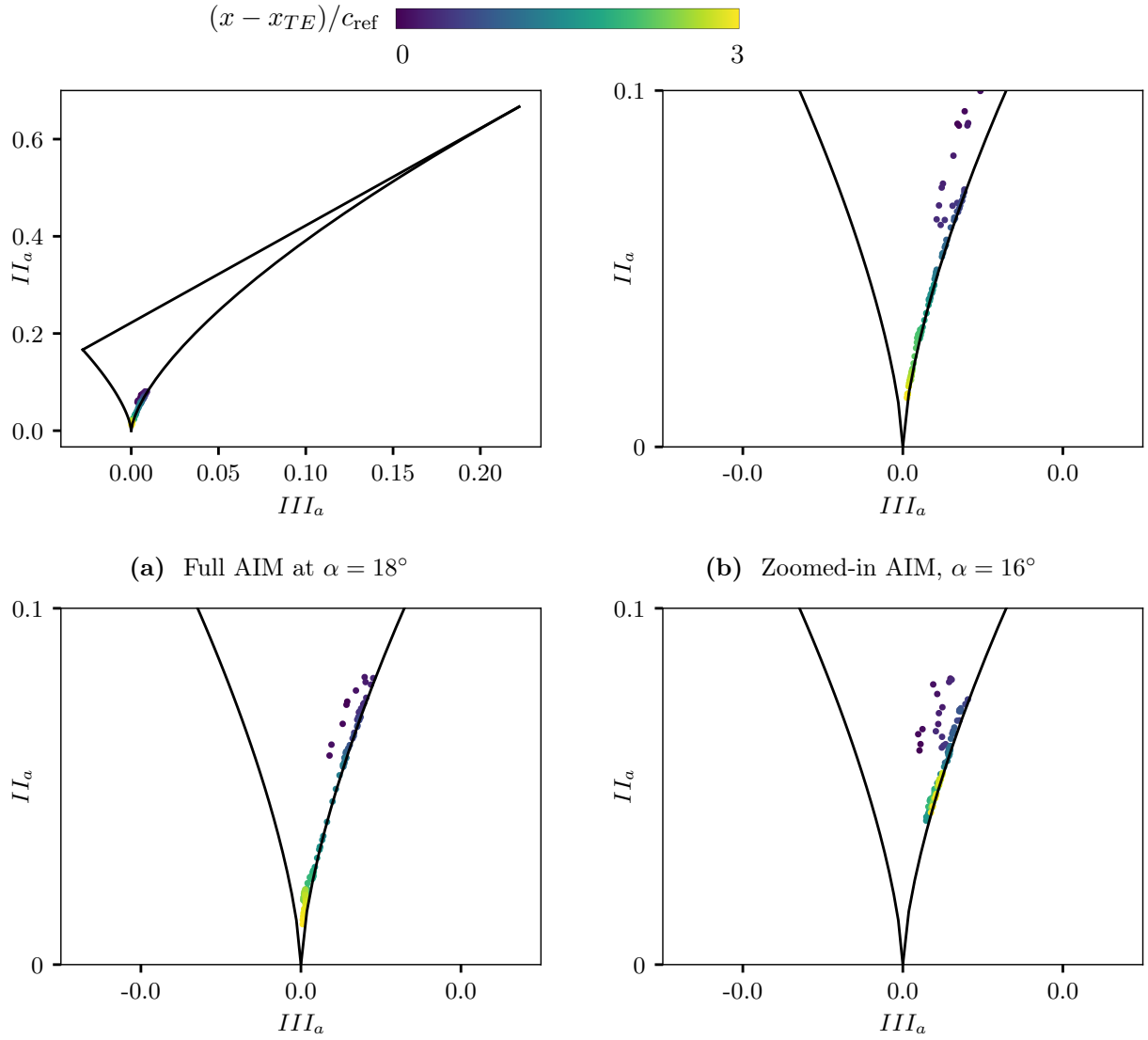

(a) Full AIM at $\alpha = 18°$

(b) Zoomed-in AIM, $\alpha = 16°$

(c) Zoomed-in AIM, $\alpha = 18°$

(d) Zoomed-in AIM, $\alpha = 20°$

Fig. 6.38.: Anisotropy map showing fluctuations along the time averaged wake centerline (ξ_{lin} shown in Fig. 6.18) at $\eta = 28.3\,\%$. Point colors represent distance along the wake centerline. Color coding is shown in Fig. 6.38a,.

states are mapped to barycentric metrics C_{1c}, C_{2c} and C_{3c}, respectively, via

$$\begin{aligned} C_{1c} &= \lambda_1 - \lambda_2 \\ C_{2c} &= 2(\lambda_2 - \lambda_3) \\ C_{3c} &= 3\lambda_3 + 1, \end{aligned} \tag{6.7}$$

which are mapped to Euclidean coordinates x_B and y_B:

$$\begin{aligned} x_B &= C_{1c} + C_{3c}\frac{1}{2} \\ y_B &= C_{3c}\frac{\sqrt{3}}{2}. \end{aligned} \tag{6.8}$$

This representation permits the construction of a barycentric map in order to avoid the distortion and nonlinearity inherent in Lumley's invariant map. A triangular map is used to represent all possible states in Euclidean space, with the top vertex being associated with $C_{3c} = 1$ and the lower right vertex with $C_{2c} = 1$. The shape of the limiting states can be chosen arbitrarily, the equilateral triangle is typically used for equal weighting. In this representation, the isotropic state is at the top corner where $C_{1c} = C_{2c} = 0$ and $C_{3c} = 1$. Banerjee et al. [19] showed that Lumley's AIM is visually biased towards representing axisymmetric or near-isotropic stress tensor shapes, which is indeed the case in Fig. 6.38 with most points located close to isotropy. In the barycentric maps in Fig. 6.39, the anisotropy state at the beginning of the extracted line is in the center of the triangle, moving toward the upper corner representing isotropy in looping, meandering paths. There is some bias toward the axisymmetric expansion boundary represented by the right-hand boundary of the triangle. This representation reveals that, even at the far downstream location at the end of the extracted line near the tailplane, some distance still remains between the data point and the top vertex of the triangle. This is true even in the $\alpha = 16°$ case, which can be expected to most rapidly converge to isotropy due to the smallest wake size.

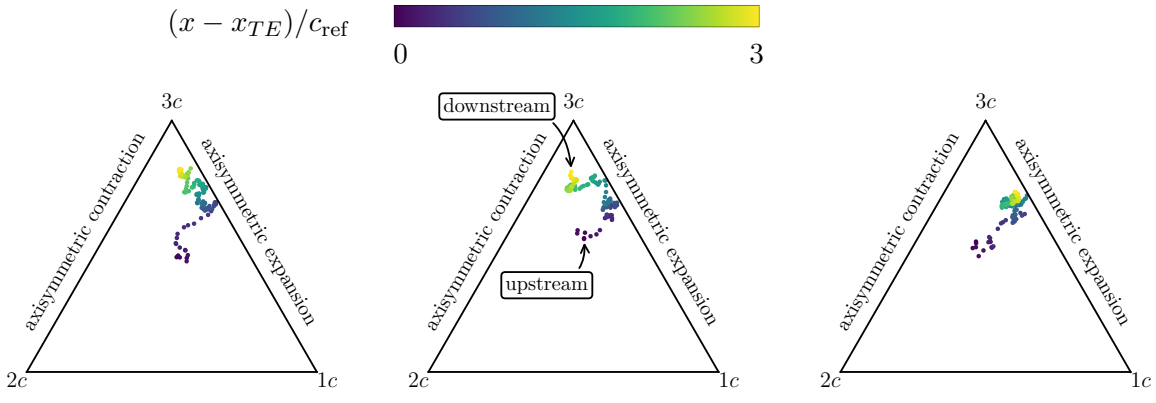

(a) $\alpha = 16°$ **(b)** $\alpha = 18°$ **(c)** $\alpha = 20°$

Fig. 6.39.: Anisotropy map showing fluctuations along the time averaged wake centerline. Point colors represent distance along the wake centerline. The locations $1c$, $2c$ and $3c$ denote one-component, two-component and three-component turbulence, respectively.

Extracting data at points or along a line makes comparison difficult across different flow conditions and large amounts of data. Emory and Iaccarino [35] proposed a method to increase the data density in order to better visualize spatial variations. Their method involves mapping the barycentric metrics C_{ic} to magenta, yellow and cyan channels for $i = \{1, 2, 3\}$. The resulting colormap permits a representation of the turbulence states for two-dimensional data via the CMY color space. Each possible location inside the triangle has its own color triplet. This representation is of a more qualitative nature, with the mapping between anisotropy states and color components given in Fig. 6.40a.

The bulk of the flow inside the wake at each α in Fig. 6.40 is shaded cyan, showing that it is close to the isotropic state $3c$. The upper and lower wake boundaries contain purple colors, which is a combination of cyan and magenta. Pure magenta ($1c$) represents one-component turbulence with one eigenvalue much larger than the other two. The purple shade is associated with the line connecting $1c$ and $3c$ and represents the locally increased tendency to axisymmetric turbulence. The leading edge shear involves a curved region with more clear magenta shades extending over about one quarter of the local chord marked in

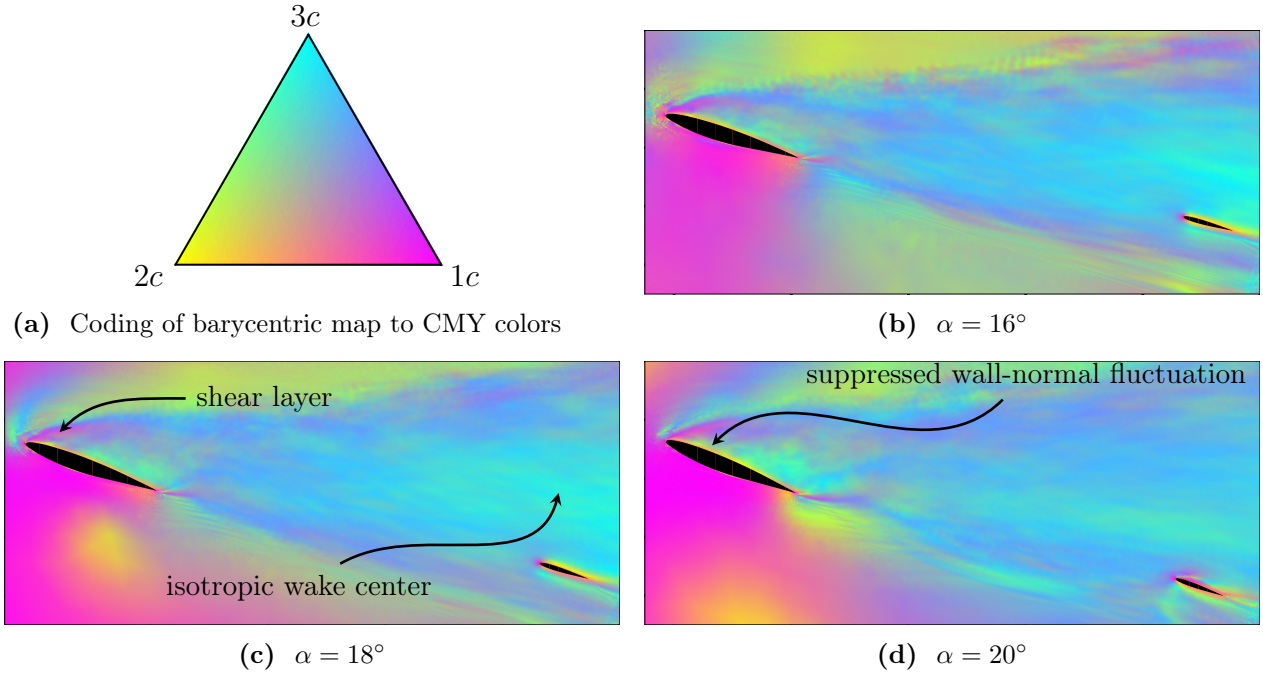

(a) Coding of barycentric map to CMY colors

(b) $\alpha = 16°$

(c) $\alpha = 18°$

(d) $\alpha = 20°$

Fig. 6.40.: Anisotropy componentiality contours at $\eta = 28.3\,\%$. Color coding given in Fig. 6.40a with magenta: one-component, yellow: axisymmetric two-component, cyan: isotropic three-component.

Fig. 6.40c, showing that the axisymmetric expansion along the $1c$ - $3c$ edge is even more pronounced and the values tend toward $1c$. This reflects the large values of $\overline{u'u'}$ in Fig. 6.37 in comparison to the other stress components. It needs to be kept in mind that the latter, direct representation of the shear stresses is oriented with the used coordinate system. The representation based on a_{ij} describes by how much one principal normal stress dominates over the other two, agnostic of the coordinate directions. The curved shape of the shear layer region roughly follows the local mean flow direction. The bias toward $1c$ at this location indicates that the normal stress component tangential to the mean streamlines dominates over the perpendicular and spanwise ones. The highest angle of attack in Fig. 6.40d involves the longest such region of magenta shades, which is consistent with the shear layer extending over the longest streamwise distance at this α.

The thin slivers of yellow shades near the upper surfaces of the wing and tailplane at each α are indicative of two-component axisymmetric turbulence. This effect is due to the fluctuations normal to the wall being suppressed, resulting in one greatly reduced eigenvalue. Away from the wall and toward the wake, this situation equilibrates and shifts toward $3c$ via green shades. The tailplane inflow in the $\eta = 28.3\,\%$ slice tends to be affected by the lower edge of the wake, particularly so at $\alpha = 20°$ in Fig. 6.40d. While the HTP leading edge is positioned in a mostly cyan region of the componentiality contours at $\alpha = 16°$ and $\alpha = 18°$ (Figs. 6.40b and 6.40c, respectively), it is in a region more affected by axisymmetric turbulence due to wake edge influences at $\alpha = 20°$, indicated by the shift toward purple.

6.3.2. Turbulence Statistics and Signal Analysis

Local characteristics of the wake turbulence fluctuations in the $\eta = 28.3\,\%$ plane are scrutinized more closely in the following, in order to gain an understanding of the mechanisms occurring in different portions of the wake. As the descriptions above and the k_t distribu-

tions in Fig. 6.11 have shown, the far inboard wake nearly vanishes at $\alpha = 16°$. Therefore the $\eta = 28.3\,\%$ position serves as the baseline for discussion, as it enables the most consistent comparison. Analysis of turbulence characteristics and velocity signals will be carried out at lines and points extracted from the flow field. In accordance with the findings from the separation dynamics analysis, the portion of the flow field encompassing the backflow and the leading edge shear layer will be evaluated separately from the wake flow downstream of the trailing edge. Signal analysis at specific points along the shear layer at $\alpha = 18°$ provides more insight into the turbulent mixing processes. This enables the quantification of the turbulent fluctuations in the crucial shear layer region in a detailed manner.

Shear Layer and Recirculation Region

An instantaneous streamwise velocity snapshot of the backflow region is shown in Fig. 6.41 along with vertical lines used for data extraction. The green vertical lines are positioned at $x/c_{\text{local}} = \{0.2, 0.4, 0.6, 0.8, 1.0\}$. Three points SL1, SL2 and SL3 are arranged along the shear layer at equal streamwise spacings, with point SL3 located above the trailing edge. They are positioned at 40 %, 70 % and 100 % of the local chord c_{local}[1] and at the respective vertical position of the k_t maximum. Fig. 6.41 shows the locations of the points relative to the wing in the WT coordinate system. Contours of $\overline{u}$ are overlaid using dashed lines to give an impression of the time-averaged bluff body flow shape. The precise positions of the points in the WT coordinate system are shown in the table in Fig. 6.41.

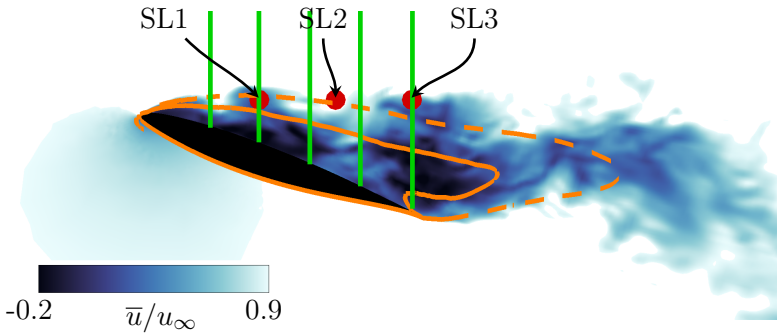

point	x	z	x/c
SL1	0.88	0.178	0.4
SL2	0.94	0.175	0.7
SL3	1.00	0.158	1.0

Fig. 6.41.: Shear layer point positions at $\eta = 28.3\,\%$. Red symbols represent points SL1, SL2, SL3. Velocity contour colors are cut off above $0.9u_\infty$, overlaid orange lines indicate $\overline{u}/u_\infty = 0$ (solid) and $\overline{u}/u_\infty = 0.4$ (dashed).. Green vertical lines represent extraction locations.

Mean velocity profiles and other quantities extracted at the five vertical lines above the wing surface and along the shear layers are shown in Fig. 6.42. The vertical profiles are shifted in horizontal direction in order to be distinct from each other, with a dashed black line showing the zero reference at each position. The scale of the horizontal data is drawn using a double headed arrow for each such plot.

The mean velocities in Fig. 6.42a show how the mean shear is initially concentrated in a narrow area close to the surface, rapidly spreading vertically with downstream distance. The crossing of the velocity profile over the $\overline{u} = 0$ line shows that significant upstream velocity (i.e. backflow) on the order of up to $-0.15u_\infty$ can be detected over the entirety of the wing upper surface at $\alpha = 20°$. Time-averaged backflow velocities exist only to a significantly reduced extent at the lower angles of attack. At $\alpha = 16°$ and $\alpha = 18°$, the far downstream

[1] c_{local} is defined as the streamwise distance between leading and trailing edge.

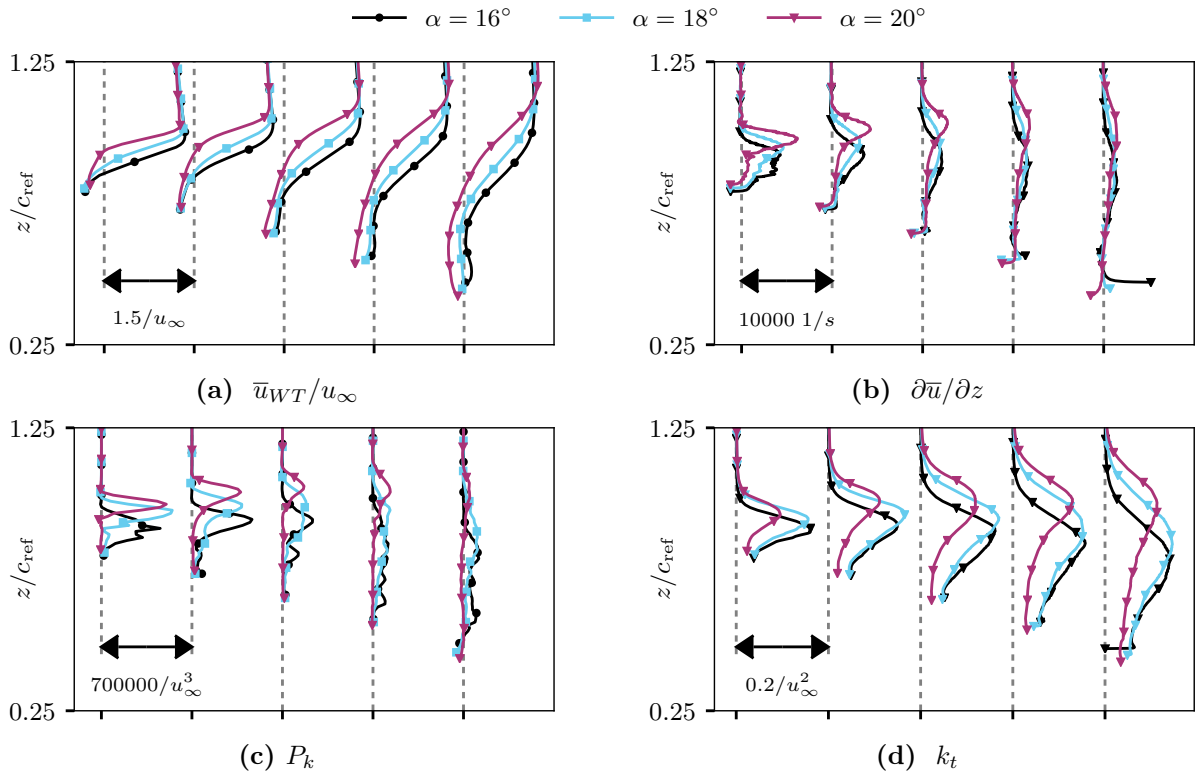

Fig. 6.42.: Profiles of shear layer quantities at $\eta = 28.3\,\%$, WT coordinate system. Vertical profiles are extracted at positions shown via green lines in Fig. 6.41, with plots horizontally offset by a constant amount for clarity. Grey dotted lines represent zero value at each of the five position. The scale is given in each figure using a double arrow.

positions do not cross over the $\overline{u} = 0$ and $\overline{u}$ remains positive over the entire height.

The change in mean velocity, i.e. from the undisturbed outer flow above to the inner flow inside the recirculation, occurs over a narrow vertical extent at the upstream positions in Fig. 6.42a. Therefore, there is a strong vertical velocity gradient $\partial\overline{u}/\partial z$ in Fig. 6.42b. This is most significant for $\alpha = 20°$ whose gradient attains the highest values with a narrower peak compared to $\alpha = 16°$ and $\alpha = 18°$. The wider gradient peak at the lower α values indicates that the dissipation and associated widening of the mean shear begins further upstream than at $\alpha = 20°$. The high shear is also located farther above and away from the surface at high α, with the $(\partial\overline{u}/\partial z)_{max}$ positions in Fig. 6.43d arranged in increasing order corresponding to angle of attack. The resolved turbulence kinetic energy k_t (Fig. 6.42d) is arranged in a similar manner. The positions of maximum k_t nearly coincide with those of the maximum gradients. However, although high α consistently causes the highest local $\partial\overline{u}/\partial z$ everywhere (Fig. 6.43a), it causes the lowest maximum magnitude of k_t. The corresponding production term P_k in Fig. 6.42c reveals that most of the turbulence production associated with the shear layer occurs in the upstream part, and that the high k_t values near the trailing edge in Fig. 6.42d are mostly transported turbulence from the leading edge region. The production decreases after about 60 % of the local chord. Upstream, the narrow production peak can be attributed to the strong shear inside the shear layer. Further downstream, the majority of P_k occurs down below inside the recirculation region, i.e. the shear layer can be considered fully disintegrated at this point. The high α case of $\alpha = 20°$ forms the exception again, with the maximum P_k occurring at the height of the shear layer even at the farthest downstream position shown in Fig. 6.42c. This is due to the shear layer at this α being more stable over

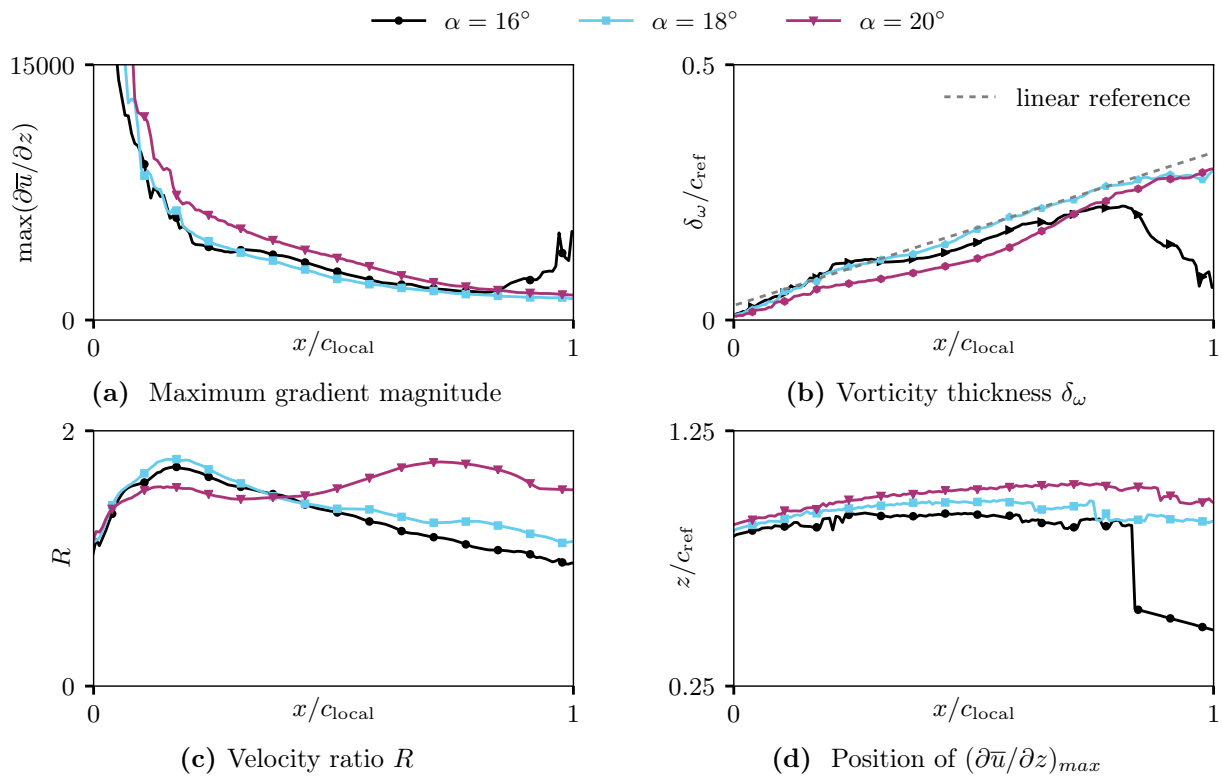

(a) Maximum gradient magnitude

(b) Vorticity thickness δ_ω

(c) Velocity ratio R

(d) Position of $(\partial\overline{u}/\partial z)_{max}$

Fig. 6.43.: Shear layer quantities along the shear layer length.

a longer distance than at low angles of attack.

The vorticity thickness δ_ω initially grows with streamwise distance at all positions. The growth shown in Fig. 6.43b is distinctly non-linear, as opposed to 2D airfoil flows. A dashed line approximating a linear growth with a slope of $0.27\,\mathrm{m}^{-1}$ is added to visualize this. The shapes are comparable to those obtained in a similar DES-based study by Le Pape et al. [72]. They observed an initial delay in δ_ω increase due to what they judged to be insufficient resolution. In another similar case on a stalled helicopter rotor blade, Richez et al. [114] obtain a δ_ω slope of 0.36, which is larger than the plane mixing layer value of 0.2. This increase is due to the presence of recirculation, which agrees with the presently observed value of 0.27.

$\alpha = 20°$ tends to show the lowest values of δ_ω and $\partial\delta_\omega/\partial x$ of the three cases, at least initially. This is most prominently visible via a locally decreased slope and increased curvature of the δ_ω function at approximately 25 % of the local chord at $\eta = 28.3\,\%$ in Fig. 6.43b. This is consistent with the dependence of the thickness spreading rate $\partial\delta_\omega/\partial x$ on the velocity ratio R shown in Fig. 6.43c. R is not constant in this case due to the presence of the wing and generally nonplanar flow. The low initial R for $\alpha = 20°$ causes δ_ω to drop below the values of the lower angles of attack. The comparatively low value of R at high α results from the shape of the recirculation region, as seen via the $\overline{u} = 0$ isoline in Fig. 6.10 or in more quantitative terms in Fig. 6.42a. At high α, the outer velocity constituting U_1 in the definition of R in Eq. 2.2 is slightly lower than at lower α over the upstream stations, while the backflow velocity U_2 is similar across the α values. The magnitude of U_2 downstream is significantly higher for $\alpha = 20°$ than at the lower angles of attack. This difference in R over the rear part of the wing is another result of the significantly larger backflow at high α, whereas the mostly disintegrated state of the shear layer over the rear part at lower α contributes to consistent

decrease of ΔU and therefore R. $R_{\alpha=20°}$ increases significantly above the other values after about 30 % of the local chord, which leads to an increase in δ_ω and a larger slope $\partial\delta_\omega/\partial x$ downstream.

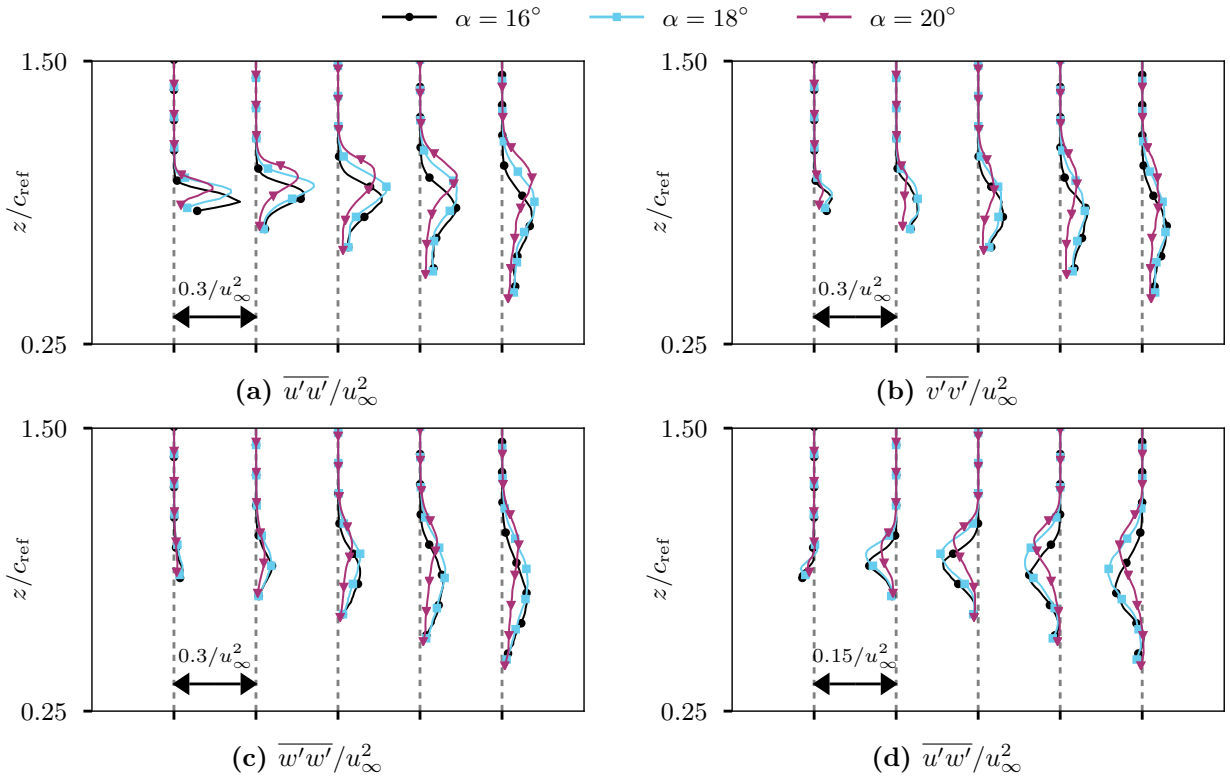

Fig. 6.44.: Reynolds stresses in the shear layer for three angles of attack and $\eta = 28.3\,\%$. Lines are at 20%, 40%, 60%, 80%, 100% of local chord.

The make-up of the Reynolds stresses leading to the k_t distributions in Fig. 6.42d is plotted separately in Fig. 6.44. The shapes of $\overline{u'u'}$ are arranged similarly to k_t. The significant anisotropy near the leading edge described in Section 6.3.1 is for the most part a result of the dominance of $\overline{u'u'}$ over the other normal components. This is the case in particular in the upstream part of the shear layer, at each angle of attack. The differences between the three normal components decrease with streamwise distance, as shown using componentiality colors in Fig. 6.40. The difference between streamwise (Fig. 6.44a) and both the spanwise (Fig. 6.44b) and the vertical (Fig. 6.44c) components remain large at $\alpha = 20°$ until the trailing edge, where $\overline{v'v'}$ and $\overline{w'w'}$ decrease significantly compared to $\overline{u'u'}$. The mixing processes in the upstream part of the shear layer appear to be more intense at lower angles of attack, redistributing and equilibrating the normal stresses more rapidly. At the same time, turbulence keeps being produced over the rear part of the shear layer at $\alpha = 20°$ according to Fig. 6.42c. This can be attributed to the high streamwise velocity ratio R in the rear shear layer at that α, as it causes the strongest counterflow velocities and can therefore be expected to cause the highest streamwise fluctuation magnitudes. The shear stress representing momentum exchange between u and w in Fig. 6.44d is negative over the entire shear layer and its peak magnitude does not change significantly between the 40 % and the 100 % positions. This shear stress is a consequence of the momentum transfer from streamwise to vertical fluctuations, i.e. a part of the decreasing $\overline{u'u'}$ serves to maintain roughly constant $\overline{u'w'}$.

Higher Order Statistics

This process of feeding the high speed streamwise flow momentum into the reciculation is termed entrainment. Sandham et al. [124] described the process of entrainment of free-stream, undisturbed fluid into the mixing region. This is achieved via small-scale nibbling along the boundary or by engulfing of fluid pockets via large scale vortical motion. This process results in a characteristic statistical distribution of the temporal velocity samples. Skewness S and kurtoris K represent the deviation from a Gaussian distribution, with the former quantifying the asymmetry and the latter the flatness or peakiness of a given distribution. For the streamwise velocity u, they are defined as follows:

$$S_u = \frac{(u-\overline{u})^3}{\sigma_u^3} \qquad K_u = \frac{(u-\overline{u})^4}{\sigma_u^4} \tag{6.9}$$

The fluctuations in the present shear layer are distinctly non-Gaussian and the profiles do not adhere to $S = 0$ and $K = 3$ in Fig. 6.45, as they would if the distribution was Gaussian. As described by Carlier and Sodjavi [27], skewness of longitudinal velocity u on the high speed side of a mixing layer tends to negative values, and jumps to positive values on the low speed side. The corresponding distributions in Fig. 6.45a support this, with skewness values of u reaching $S_u = -3$. The w velocity distribution is also skewed, albeit toward positive values on the high speed side.

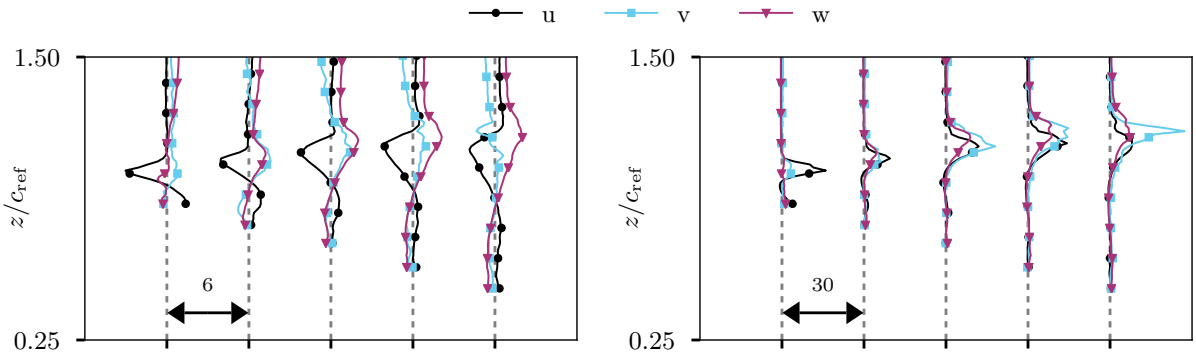

(a) Skewness **(b)** Excess kurtosis

Fig. 6.45.: Profiles of skewness and kurtosis of the three velocity components in the shear layer at $\alpha = 18°$ and $\eta = 28.3\,\%$. Lines are at 20%, 40%, 60%, 80%, 100% of local chord.

This indicates that the outer flow being disturbed by low momentum (hence reduced u) flow rising upward (hence increased w) from inside the recirculation region. The negative S_u peak is mirrored on the lower side of the layer by increased skewness of comparable magnitude, at least at the two upstream locations. This represents intermittent entrainment of high momentum outer fluid into the backflow. Although the S_u profile is not entirely symmetrical, it represents momentum exchange comparable to canonical shear layers from literature [27]. The symmetry is even less pronounced in the S_w profiles, and largely absent for S_v. The former can be attributed to the fact that the presence of the wing surface below the shear layer inhibits vertical motion, in particular inside the backflow region. The S_v profile behaves similarly to S_w in the upstream part of the shear layer, with values around 0 over most of the height. The spanwise fluctuation distribution is less skewed than that of u, showing less of a trend toward one side of the mean.

The fourth statistical moment, or kurtosis, designates the peakedness of the distribution. The

excess kurtosis $K_u - 3$ is employed, whose value is 0 for a Gaussian distribution. Fig. 6.45b shows that K_u is close to zero inside the backflow and increases drastically in the shear layer region, indicating leptokurtic distributions. These deviate from Gaussian distributions by having a high, narrow peak and heavy tails, i.e. the most commonly occurring samples are close to the mean while the extreme values tend to be far from it. K_u reaches its highest values at the two upstream positions, whereas the peak values of K_v and K_w are initially low and increase further downstream. Carlier and Sodjavi [27] described similar sharp increases of K in the shear layers associated with increased intermittency. K_v is particularly high at the trailing edge position with values exceeding 20, suggesting extreme events taking place that are far from the mean velocity. These locations are mostly outside of the turbulent flow and are characterized by smooth velocity signals.

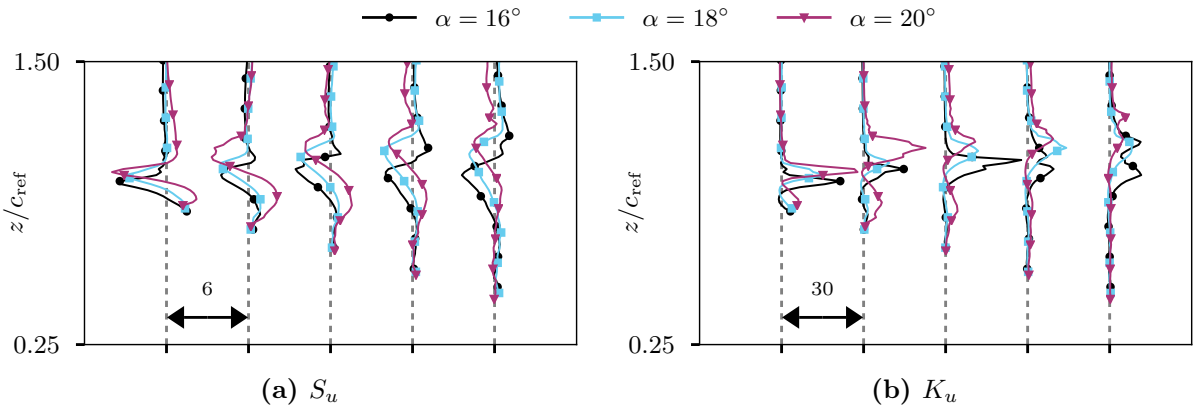

Fig. 6.46.: Skewness and kurtosis of streamwise velocity in the shear layer at $\eta = 28.3\%$ at three angles of attack. Line legend as in Fig. 6.42. Lines are at 20%, 40%, 60%, 80%, 100% of local chord.

The profiles in Fig. 6.46 show how these higher moments vary with α. While the $\alpha = 20°$ case shows the aforementioned quasi-symmetrical shape of S_u with a changing sign over its height across most of the positions, this symmetry rapidly becomes indistinguishable at lower α. This is due to the decreased volume and velocity of the bulk backflow below the shear layer, which causes less pronounced positive skewness with the strong negative skewness dominating. Effectively, the $\alpha = 20°$ shear layer, at a greater distance from the wing surface and a value of R that remains close to constant, most closely resembles a canonical counterflow shear layer. This is supported by the degree of symmetry of S_u across that shear layer. This less-symmetrical downstream S_u shapes at lower α are indicative of entrainment of high streamwise momentum flow into the backflow with the associated deceleration, and without the reciprocal ejection of low momentum flow outward. The absence of a quiescent region between the high k_t area near the trailing edge at low α and the full breakdown of the shear layer before the trailing edge essentially removes distinguishable outer flow and backflow. The dominating negative S_u is an indication that the momentum exchange becomes a one-way transfer process from the outer flow to the inner flow. The excess kurtosis of u in Fig. 6.46b indicates that the phenomena causing large negative skewness are comparatively extreme events causing heavy tails in the distribution of u, as large values of K_u spatially coincide with large negative S_u. As in Carlier et al. [27], the negative S_u peak and the coincident K_u peaks are situated slightly above the maximum gradient location shown in Fig. 6.43d, on the high speed side of the mixing region.

More details can be deduced from studying point signals along the shear layer. Local data is extracted at the points SL1-SL3. The time signal traces in Fig. 6.47 show how the signals

fluctuate over a large range of values with a high variance, which is the definition of the resolved Reynolds stress. There is initially (i.e. at SL1) significant low frequency periodicity in the u signal discernible with the naked eye. This apparent structure in the u signal gradually disperses toward SL3, with the signal becoming more chaotic and broadband. The v and w components do not exhibit comparable characteristics that are so readily visible.

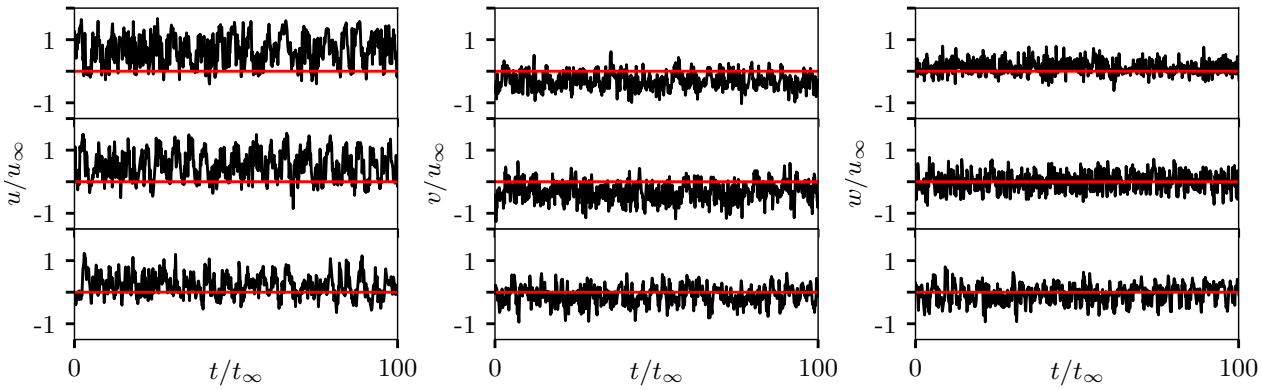

(a) u/u_∞ **(b)** v/u_∞ **(c)** w/u_∞

Fig. 6.47.: Velocity signals at the positions SL1 (top), SL2 (middle), SL3 (bottom) in the upper shear layer at $\alpha = 18°$. Red line indicates zero in all panels.

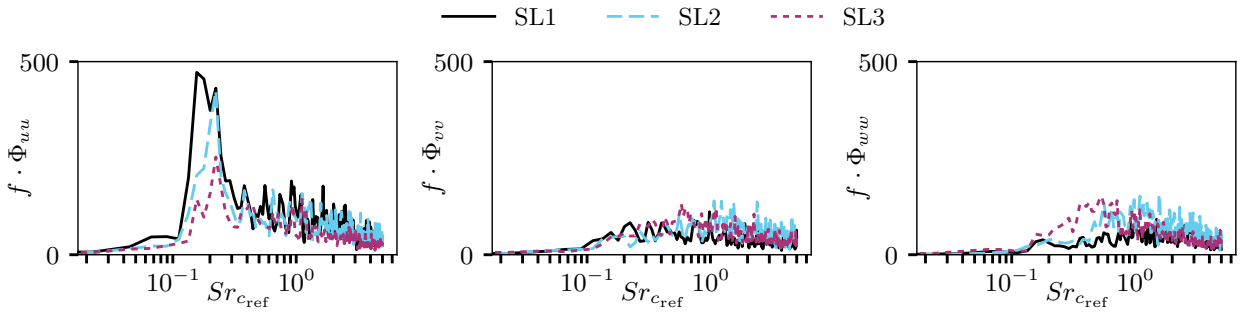

(a) u/u_∞ **(b)** v/u_∞ **(c)** w/u_∞

Fig. 6.48.: Premultiplied power spectral densities of velocity at the positions SL1, SL2 and SL3 in the upper shear layer at $\alpha = 18°$.

The power spectral densities are shown in Fig. 6.48 using a premultiplied spectral representation, which is variance-conserving. The low frequency oscillation visible in the u signal corresponds to the peak at $Sr_{c_{\mathrm{ref}}} = 0.22$ which dominates the spectrum of u in Fig. 6.48a. The peak persists at SL2, and diminishes markedly toward SL3 at the trailing edge. It is still prominent at that location, however. SL3 is located in the area near the maximum of the $\phi_{u,1}$ POD mode, showing how the coherent fluctuation extracted via POD is reflected in the unfiltered point spectra. The SL1 v signal shows some noteworthy amplitudes at the same frequency as u. However, these amplitudes rapidly decrease with streamwise distance and no peaks are discernible anymore at location SL2. This is consistent with the attribution of the $Sr = 0.22$ mode to a phenomenon occurring at the leading edge and propagating in streamwise and inboard direction. Most of the spectral content in terms of v shifts to higher frequencies with downstream distance. In the spectrum of w, the amplitudes in in the range around $Sr = 0.22$ are nearly negligible. Most of the fluctuation of the transverse velocity

is associated with broadband shear layer turbulence, and not with the large scale feature originating at the leading edge seen in POD. Both v and w contain significant fluctuation energy in the mid frequency region above $Sr_{c_{\text{ref}}} = 0.5$. Apart from the low frequency peak at $Sr_{c_{\text{ref}}} = 0.22$ attributable to the large scale fluctuations, the broadband and high frequency turbulent fluctuations increase with streamwise distance. Generally, it can be observed that the initially dominant u fluctuation at $Sr_{c_{\text{ref}}} = 0.22$ diminishes over the length of the shear layer, whereas the w fluctuations between the von Kármán frequency and $Sr_{c_{\text{ref}}} = 1$ increase with downstream distance.

In the section on separation dynamics (Sec. 6.2), the nature of the shear layer undulation was visualized via instantaneous velocity distributions and reconstructed data. When considering spatially fixed points, displacement of the shear layer results in the point alternating between being immersed in the backflow and being exposed to the outer flow. The strong spectral peaks in the PSD plots of the different signals in Fig. 6.48 give an indication on the common nature of the phenomenon occurring at this frequency. The POD mode signal coefficients were observed to be not perfectly periodical, but with varying degree of coherence over time. The inherent low-pass filtering carried out by applying POD makes those signals more easily interpretable, and the regular magnitude squared coherence as shown in Fig. 6.21b is a useful measure for their analysis. The point signal amplitudes SL1-3 are distributed over much broader frequency ranges and are more intermittent. Consequently, coherence analysis of velocity componets at the fixed points is carried out via continuous wavelet transform (CWT), as this permits evaluation of temporal variations of signal characteristics or interactions. Computation of wavelet spectra is based on the work by Torrence and Compo [155]. The wavelet coherence W is based on the wavelet cross-spectrum between two signals and has values between 0 and 1, similar to the computation of Magnitude Squared Coherence (MSC) based on the cross-spectral density using Fourier transformation. In this instance, the Morlet wavelet is used to compute the coherence between u and w at points SL1, SL2 and SL3. The results in Fig. 6.49 show the contours of coherence over the entire time series and over a range of frequencies. Coherence between streamwise and vertical velocities attains its highest values around lower order POD frequency $Sr_{c_{\text{ref}}} = 0.22$ at SL1 and SL2. This frequency is highlighted using the horizontal line in Fig. 6.49. This is also true at SL3 as well, however at this location there is also high coherence at very low frequencies.

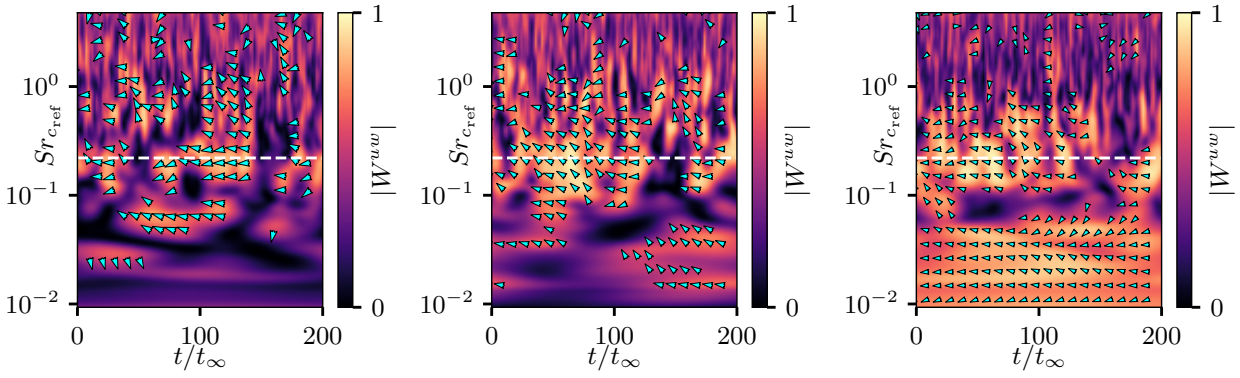

(a) SL1 **(b)** SL2 **(c)** SL3

Fig. 6.49.: Wavelet coherence $|W^{uw}|$ between u and w at SL1, SL2 and SL3 at $\alpha = 18°$. Dashed horizontal line indicates $Sr_{c_{\text{ref}}} = 0.22$. Arrow direction indicates phase angle, right-facing arrows represent 0 and phase increasing in counter-clockwise direction. Arrows are drawn on evey 100th point of the grid.

The wavelet coherence computation also provides phase information at each frequency. Phase information is superimposed on the coherence contours in Fig. 6.49 using arrows in regions where $|W^{uw}| > 0.5$. Arrows to the right indicate a phase angle of 0 between the two signals, while arrows to the left indicate a phase angle of π. This representation is only a rough guideline, as arrows are drawn on only every 100th sample for clarity. Nevertheless they visualize the general phase relation in temporal and spectral space where high coherence is present. Reversed phase situations with phase angle π occur during most of the shown runtime around $Sr_{c_{\mathrm{ref}}} = 0.22$, as high values of u associated with this fluctuation mode typically coincide with downward motion, and vice versa. The same level of coherence does not exist at higher frequencies. The intermittency does not fundamentally alter the phase relation at a given frequency, such as the drop in $|W^{uw}|$ at SL3 between $t/t_\infty = 120$ and $t/t_\infty = 150$. Similar intermittent loss of coherence occurs at SL1 and SL2 at the same frequency, as well. Every time, the coherence and phase relationship reestablishes after this period.

As the position of the shear layer in space along the chord is known, further quantities can be derived. For instance, power spectral density can be computed for each point from separation until the streamwise position above the trailing edge. The power spectral densities of the u fluctuation along shear layer points extracted at the position of maximum local k_t are shown in Fig. 6.50. Initially, the fluctuations are strongest in the very low frequency range, gradually expanding across the frequency range with downstream distance. Increasingly high amplitudes are attained in the Strouhal number range between 0 and 1 above the rear part of the wing surface.

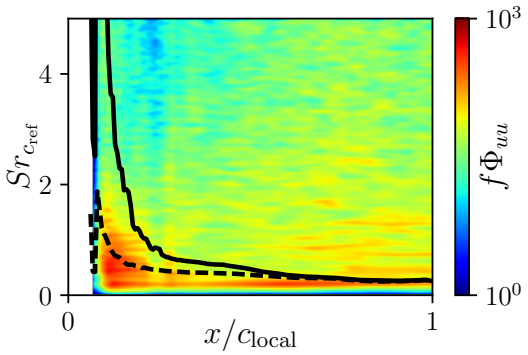

Fig. 6.50.: Fluctuation spectrum along the shear layer. Solid line shows most amplified f_{KH,δ_ω}, dashed line shows f_{KH,δ_Θ}.

As indicated in the point spectra of u in Fig. 6.48a, the $Sr_{c_{\mathrm{ref}}} = 0.22$ oscillation originates in the front part of the wing section and persists over the entire chord length. The theory explained in Chapter 2 enables prediction of a most amplified frequency for a planar mixing layer based on δ_ω, which is given as $f_{KH,\delta_\omega}(x) = 0.135\Delta\overline{U}/\delta_\omega(x)$ by Le Pape et al. [72] based on Huerre and Rossi [60]. The most amplified frequency is therefore dependent on the local shear layer thickness and is an indication which frequencies will most likely occur and be preserved. The solid line representing $Sr_{\delta_\omega}(x) = 0.135$ is overlaid on top of the spectral contours in Fig. 6.50. Other authors studying configurations with shear layers detaching from three-dimensional bodies, such as Pain et al. [102] for rocket afterbodies or Richez et al. [114] for rotor blades, reported satisfactory agreement of observed shear fluctuations with predicted Kelvin-Helmholtz fluctuations based on either δ_ω or δ_Θ. Pain et al., in particular, showed a rough correspondence between high amplitude regions in the spectral map and the predicted frequency, with the latter overpredicting the frequency especially in the upstream part of the shear layer. The same occurs in Fig. 6.50. The frequency based on momentum thickness is given by Huerre and Rossi as $f_{KH,\delta_\Theta} = 0.032\Delta\overline{U}/\delta_\Theta(x)$. The dashed line in Fig. 6.50 consequently shows $Sr_{\delta_\Theta}(x) = 0.032$, which tracks the high amplitude region of the spectral map reasonably well. Considering the difference between the simple planar mixing layer for which these theoretical frequencies are derived, and the complex swept wing flow present in this case, this can be

assessed as excellent agreement. This result may in part explain the the preference of the separation dynamics for the $Sr_{c_{\mathrm{ref}}} = 0.22$ frequency.

Momentum Exchange

Fig. 6.51 shows the bivariate Gaussian kernel density estimate of the streamwise turbulent velocity fluctuations u' versus w' at SL1, SL2 and SL3. Each panel gives a two-dimensional representation of the joint probability density function (PDF) and the histograms of u and w on the margins.

The shape of the point histograms shows how the third and fourth order statistics profiles in Fig. 6.45 are associated with local distributions. The most extreme values of S and K are above and below maximum shear, wheras points SL1-SL3 are specifically located precisely at the local maximum shear stress. Nevertheless, the histograms of u are distinctly non-normal. There is significant skew, which decreases over the streamwise distance. The distribution of u at SL3 is significantly more symmetric than at SL1. The w histograms are remarkably symmetrical and show little skewness. While the K_u profiles above and below maximum shear involve extremely high values, the u histograms at the top of Fig. 6.51 tend toward platykurtic shapes, i.e. wide-peaked distributions. For instance, K_u has a value of -0.95 at SL1, which is significantly different from the Gaussian value of 3 or the values of up to 20 in Fig. 6.45.

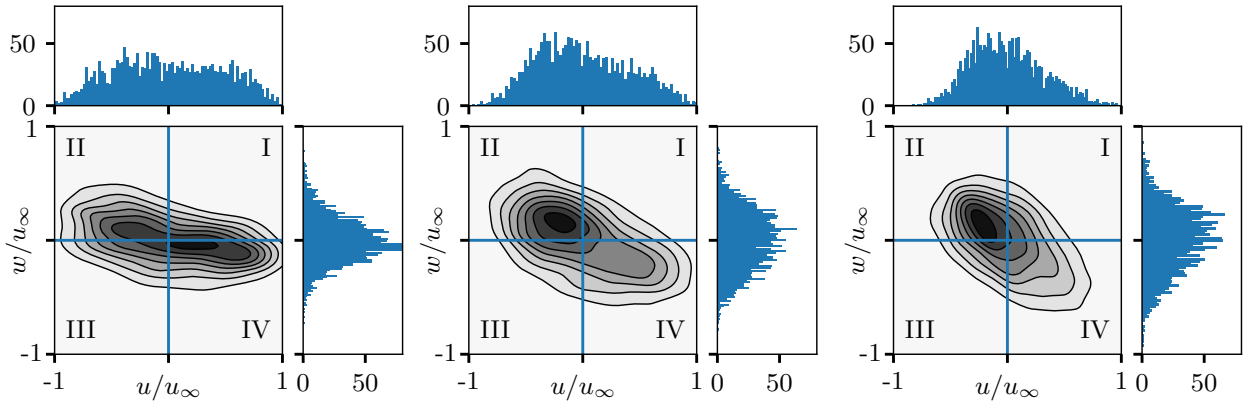

(a) SL1 **(b)** SL2 **(c)** SL3

Fig. 6.51.: Contours of joint probability density functions with the associated u and w histograms at SL1, SL2, SL3. u histogram shown on top and w to the right, with common scaling. The range of u'/u_∞ and w'/u_∞ is from -1 to 1 in all panels.

The aforementioned association of positive u' with negative w' and vice versa is visualized via the joint PDFs in Fig. 6.51. The characteristic elongated ellipsoidal shape of the distribution at SL1 deforms with downstream distance and becomes more circular toward the trailing edge with minor and major semi-axies becoming more similar. The orientations of the elliptic shapes of the PDF contours change, and the semi-axes rotate in clockwise direction with streamwise distance. The vertical fluctuations increase in magnitude, while the streamwise component decrease. This rotation is also caused by turbulent transfer of momentum from u' to w'.

Apart from providing detailed information on the distribution and interaction of the turbulent fluctuations at one point, the plotted PDFs broadly visualize the prevalence of the four

possible combinations of the signs of u' and w'. Quadrant analysis of these combinations permits the quantification of events in the shear flow and their relative importance. Four types of events can be identified, corresponding to the four quadrants visible in the joint PDF plots in Fig. 6.51. The associated names are given according to the original nomenclature by Willmarth and Lu [173]:

- I: $u' > 0$, $w' > 0$, outward interaction
- II: $u' < 0$, $w' > 0$, ejection
- III: $u' < 0$, $w' < 0$, inward interaction
- IV: $u' > 0$, $w' < 0$, sweep

While this terminology reflects the original usage of quadrant analysis in boundary layers, it is well applicable to the present shear layer separating an outer flow and a turbulent inner recirculation zone. In each time series at each point, the quadrant analysis counts the number of samples belonging in each bin, along with their instantaneous magnitude. The former is computed by counting the occurrence of each of the four quadrants and is expressed as their fractions of the overall number of samples N. This quantity is termed the duration fraction D_i, i.e. the proportion of time which is spent in quadrant i. The instantaneous magnitudes of $\overline{u'w'}$ can be used to derive a stress fraction, which is the contribution of each quadrant to the overall resolved shear stress as described by Raupach [113]:

$$S_i = \langle u'w' \rangle_i / \overline{u'w'} \tag{6.10}$$

The angle brackets represent a conditional averaging based on quadrants:

$$\langle u'w' \rangle_i = \frac{1}{N} \sum_{n=1}^{N} u(n)'w(n)'I_i \tag{6.11}$$

The indicator I_i equals 1 for a temporal sample if $u'w'$ is in quadrant i, and 0 otherwise. The fractions are defined so that:

$$\sum_{i=1}^{4} |D_i| = 1 \qquad \sum_{i=1}^{4} |S_i| = 1 \tag{6.12}$$

For presentation purposes along the vertical lines across the shear layer, the utility of S_i is limited due to achieving locally large values $S_i > 1$ in areas where the magnitude of $\overline{u'w'}$ is small or crosses zero. The absolute stress contributions of each quadrant are used instead of the fractions S_i, as demonstrated for wind turbine wake shear analysis by Hamilton et al. [47]. Departing from Hamilton et al.'s nomenclature, the stress contributions do not use the same symbol as the fractions, and are referred to in the following as $C_i = \langle u'w' \rangle_i$ instead. This approach permits clearer visualization of the different quadrant contributions, and intuitive visual validation due to the sum of all quadrant contributions at one point equaling $\overline{u'w'}$.

Ejection and sweep events are the main contributors, corresponding to momentum exchange events with upward-moving low momentum fluid (ejection) and downward-moving high momentum fluid (sweep). A similar result was presented by Longo et al. [79] for the shear layer and wake of a stalled airfoil. The profiles of D_i and C_i in Fig. 6.52 reveal how the early shear layer at 20 % of c_{local} involves contributions of all quadrants in a similar measure, with

positive contributions of C_I and C_{III} arranged above the negative peaks of C_{II} and C_{IV}. However, only D_I has a high local value. The low duration D_{III} at the height of high stress C_{III} indicates that rare events with high magnitude are responsible for that quadrant's stress contribution. Conversely, the stress due to quadrant I is generated by frequent occurrence of the corresponding combination of signs.

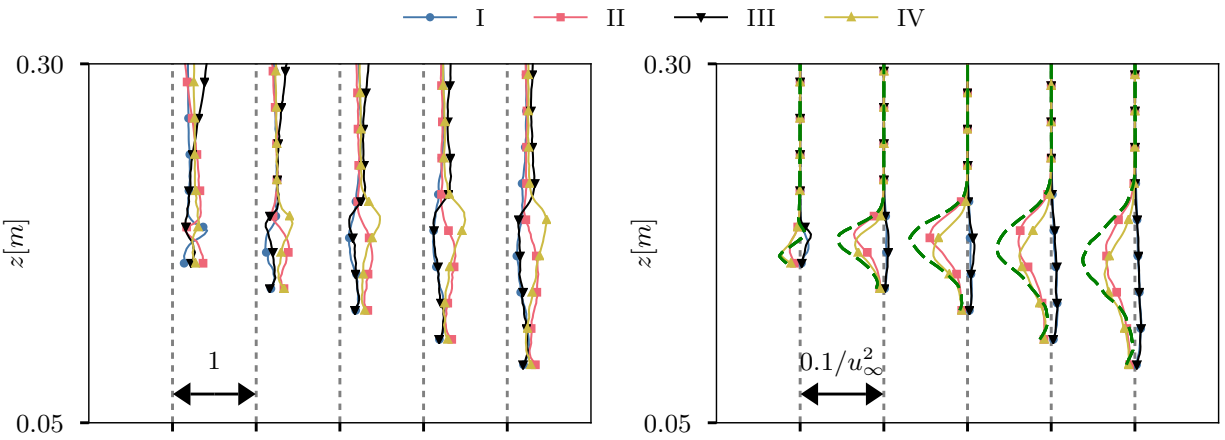

(a) Duration fraction D_i **(b)** Stress contributions C_i

Fig. 6.52.: Quadrant analysis in the shear layer at $\alpha = 18°$. Dashed green line in **(b)** denotes total shear stress $\overline{u'w'}$.

Further downstream and starting at 40 % of c_{local}, the negative $\overline{u'w'}$ in the high shear region is mostly a combination of ejection and sweep events, II and IV. This is consistent with the orientation of the joint PDF in Fig. 6.51. The overall shear stress $\overline{u'w'}$ is the sum of $C_I ... C_{IV}$ at each location. It is notable that the locations of the maxima of D_i and C_i do not coincide for these quadrants. The maximum of D_{IV} is well above the the maximum magnitude positions of both $\overline{u'w'}$ and C_{IV}. At the trailing edge, sweep (IV) accounts for almost 50 % of occurrences at the z position of its maximum in Fig. 6.52a, while ejection events (II) contribute significantly more shear stress in terms of C_{II} at this location despite occurring more rarely. This combination occurs all over the shear layer above the maximum magnitude of $\overline{u'w'}$, and is mirrored below that maximum. This can be summarized as follows:

- At $z > z(|\overline{u'w'}|_{max})$, most of the stress is contributed by ejection (high C_{II}), despite sweep events occurring more frequently ($D_{IV} > D_{II}$).
- At $z < z(|\overline{u'w'}|_{max})$, most of the stress is contributed by sweep (high C_{IV}), despite ejection events occurring more frequently ($D_{II} > D_{IV}$).

These combinations occur consistently at the four downstream positions shown in Fig. 6.52. These observations suggest that the events that contribute the most to overall shear stress occur infrequently. This is indicative for the existence of large scale structures with large swings in velocity, whose frequency is low due to their size.

Wake

An analogous analysis is carried out in the wake downstream from the trailing edge at $\eta = 28.3\,\%$. Contrary to the shear layer analysis above, the coordinates and velocity components are transformed to the WC coordinate system. This results in the bulk of the flow being for

a large part aligned with the x_{WC} direction, simplifying the analysis. The wake downwash angle of $\xi_{lin} = 5.4°$ derived in Section 6.1.3 is used as the x axis direction. The wake centerline analysis points WC1, WC2 and WC3, shown in Fig. 6.53, are placed at distances of 1, 2 and 3 local chords c_{local} downstream from the trailing edge. Their positions in the WC coordinate system are listed in Table 6.5. Additionally, far wake points FW1 and FW2 are placed at $(x - x_{TE})/c_{\text{local}} = 3$, and FW3 upstream of the HTP. The term far wake is used liberally here, as the distance of the points from the wing does not fit the classical definition of wake from Chapter 2. Vertical lines extracted across the wake at the positions of the points WC1-WC3 are used to visualize changes across the width of the wake.

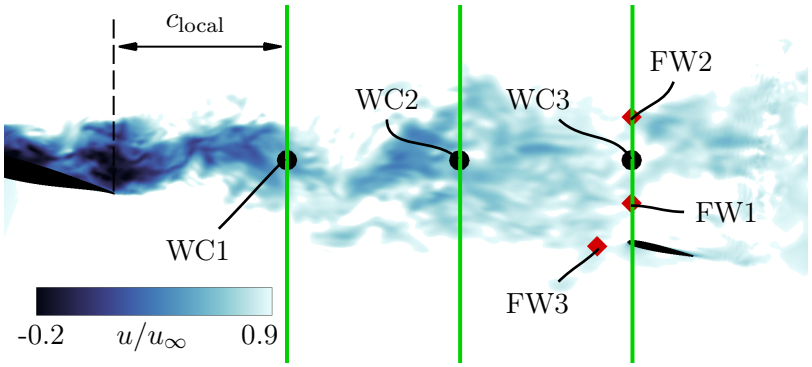

Fig. 6.53.: Point positions at $\eta = 28.3\,\%$. Instantaneous velocity contour colors are cut off above $0.9u_\infty$. Green vertical lines represent extraction locations.

Plane	x_{WC}	z_{WC}
WC1	1.238	0.133
WC2	1.461	0.133
WC3	1.684	0.133
FW1	1.684	0.078
FW2	1.682	0.189
FW3	1.638	0.022

Tab. 6.5.: Positions of the wake analysis points at $\alpha = 18°$.

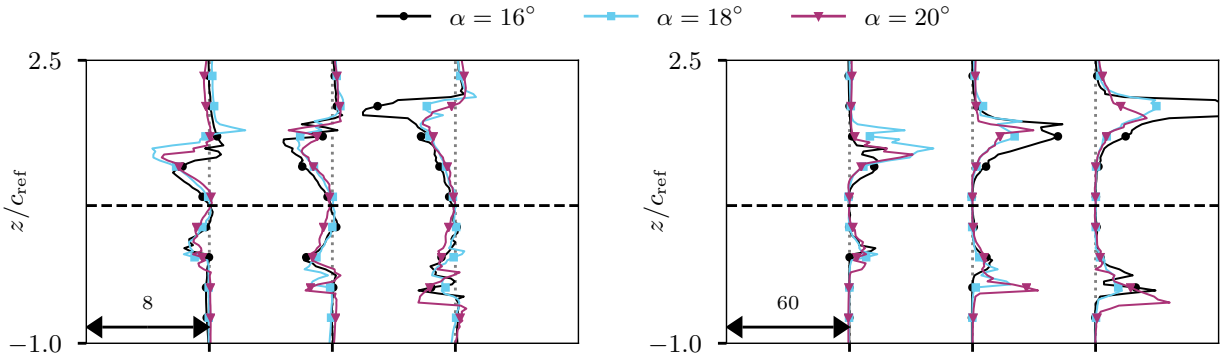

(a) S_u **(b)** K_u

Fig. 6.54.: Skewness and kurtosis of streamwise velocity in the wake at $\eta = 28.3\,\%$ at three angles of attack. Three streamwise positions shown, at $(x - x_{TE})/c_{\text{local}} = \{1, 2, 3\}$ as indicated in Fig. 6.53. Dashed horizontal lines represent position of the wake centerline. Coordinates in WC system.

In terms of turbulence statistics, the wake has characteristics similar to two mixing layers positioned above each other. The third and fourth order statistics are shown in Fig. 6.54. The wider the wake, the farther the shear layers are spaced apart. The shear layers are characterized by significant nonzero values of S_u and K_u, while most of the wake center is much closer to Gaussian values. Viewed from the high speed outer flow outside and below the wake, S_u initially becomes negative when approaching the wake. The emergence of low momentum disturbances with $u' < 0$ and $w' < 0$ from inside the wake slows down the outer flow and skews the distribution. The same can be observed at the same position when

approaching the wake from above, with a positive w' component transporting fluid with low streamwise momentum outside. In contrast to the simple mixing layer, there is no symmetry about the shear layer axis in the sense of a positive S_u value inside the wake mirroring the negative one outside. Instead, S_u tends to zero in the wake. The same is true for K_u, which has an even more distinct region with values around 0. The excess kurtosis values in Fig. 6.54b indicate that the velocity distributions are close to Gaussian in the wake center, becoming highly leptokurtic outside of the high shear regions. This is due to the higher intermittency and the existence of more outliers far from the mean than for a corresponding normal distribution.

There is visible asymmetry of the wake itself in the statistics, in the sense that the upper edge initially causes higher values of both S_u and K_u. Some equilibration between upper and lower edge occurs, with the values largely similar near the downstream position. The only exception is the upper wake edge at $\alpha = 16°$, which involves high skewness and kurtosis magnitudes.

Point Analysis

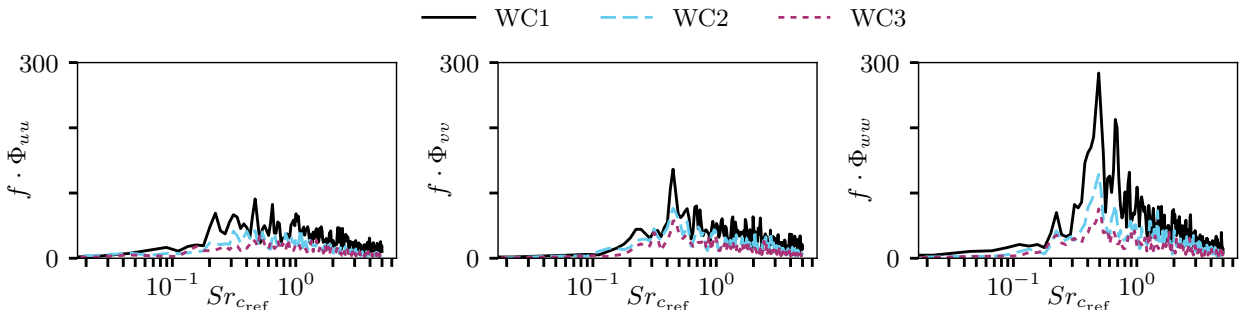

(a) u **(b)** v **(c)** w

Fig. 6.55.: Premultiplied power spectral densities of velocity at the positions WC1, WC2, WC3 along the wake centerline at $\alpha = 18°$.

Spectral analysis of the centerline points WC1-WC3 shows the association of local motion with the low order dynamics from Section 6.2. The premultiplied point spectra in Fig. 6.55 show that most of the signals involve a high amplitude peak around $Sr_{c_{\mathrm{ref}}} = 0.5$, coinciding with the von Kármán mode. u and v velocities also involve higher frequency fluctuations. However, these latter phenomena decay more rapidly than the von Kármán frequency, which remains the most dominant feature at the farthest downstream point WC3. This is especially true for the transverse velocity w fluctuation. The conservation of the von Kármán feature is a result of its global instability characteristic and its large scale. Other, more local effects occurring at higher frequency are subject to more significant dissipation and tend to remain local.

The backflow region fluctuation at $Sr_{c_{\mathrm{ref}}} = 0.22$ is visible in the spectrum of the streamwise velocity u in Fig. 6.55a. However, the streamwise fluctuations along the centerline are nearly negligible compared to the vertical fluctuations in Fig. 6.55c. The u spectrum loses the bump at $Sr_{c_{\mathrm{ref}}} = 0.22$ and the peak shifts to higher frequencies with downstream distance. Even close to the wing at WC1, the peak at $Sr_{c_{\mathrm{ref}}} = 0.5$ has higher amplitude than the lower frequency one. These observations confirm the insight from the POD analysis, which

showed that the low frequency separation mode is not transported very far into the wake as a coherent feature. The fluctuations due to the von Kármán mode are more significant already at WC1 and persist well into the downstream wake region. In the v and w spectra along the centerline, it is the only fluctuation mode that is visible at all. With a view to tailplane loads, the von Kármán mode can be therefore expected to be more important in this regard than the $Sr_{c_{\text{ref}}}$ separation fluctuation.

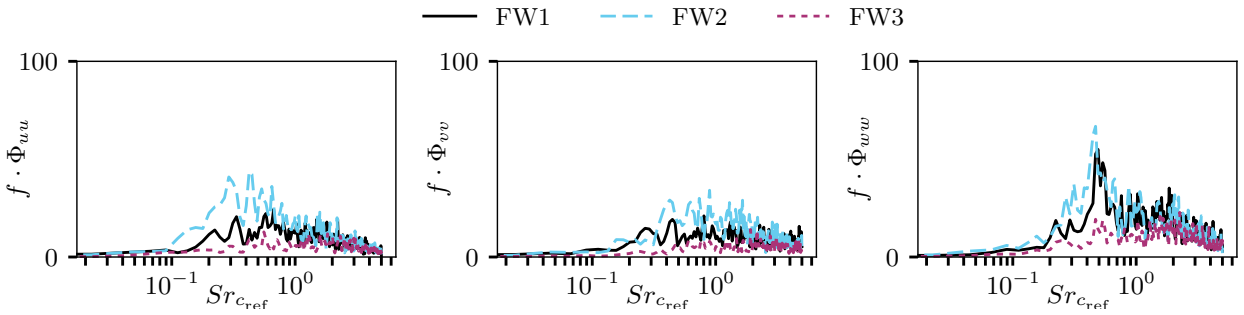

(a) u **(b)** v **(c)** w

Fig. 6.56.: Premultiplied power spectral densities of velocity at the far wake position points FW1-FW3 at $\alpha = 18°$.

The $Sr_{c_{\text{ref}}} = 0.22$ amplitude peak reemerges away from the centerline, most notably to near the upper wake edge at FW2 in Fig. 6.56. The points FW1 and FW2 are located three local chords downstream of the trailing edge. Despite the significant amount of mixing that has occurred over this distance, and the visible increase in symmetry in Fig. 6.54, the upper and lower edge of the wake differ significantly in their spectral contents. Point FW1 on the lower edge shows little content at the backflow-related frequency $Sr_{c_{\text{ref}}} = 0.22$, whereas point FW2 at the upper wake edge exhibits significant such oscillations of the streamwise velocity u. While the modal analysis of the wake tends to emphasize the large scale coherent motion such as the von Kármán mode downstream of the trailing edge, the FW2 spectra show that the oscillations originating with strong local events like the $Sr_{c_{\text{ref}}} = 0.22$ mode associated with separation are transported with the mean flow. They do not persist as a coherent mode, but they are sufficiently energetic to be detectable at far downstream locations.

Spectral density maps of the streamwise velocity u extracted along the three vertical lines at $(x - x_{TE})/c_{\text{local}} = \{1, 2, 3\}$ are shown in Fig. 6.57. At the upstream position in Fig. 6.57a, the amplitudes are distributed rather evenly over most of the frequency range. The pattern at the two downstream locations indicate a concentration of large scale low frequency fluctuations near the upper edge of the wake. The amplitude drops off across the entire frequency range everywhere at $(x - x_{TE})/c_{\text{local}} = 2$ compared to $(x - x_{TE})/c_{\text{local}} = 1$, but the upper edge fluctuation becomes more prominent. This process continues toward the $(x - x_{TE})/c_{\text{local}} = 3$ location in Fig. 6.57c, where the slight asymmetry of the low frequency amplitude distribution remains visible. The vertical location of maximum amplitude in Fig.6.57c is also the approximate location of point FW2.

The shapes of S_u and K_u in Fig. 6.54 indicate nearly Gaussian velocity distributions along the centerline, which is shown to be true for both u and w in Fig. 6.58. There is little skew in both of the distributions, and the u distribution is only initially slightly platykurtic at WC1 with a sub-Gaussian flat peak with $K_u < 3$. Both u and w components' variance decreases with downstream distance, as the wake centerline Reynolds stress decreases. The

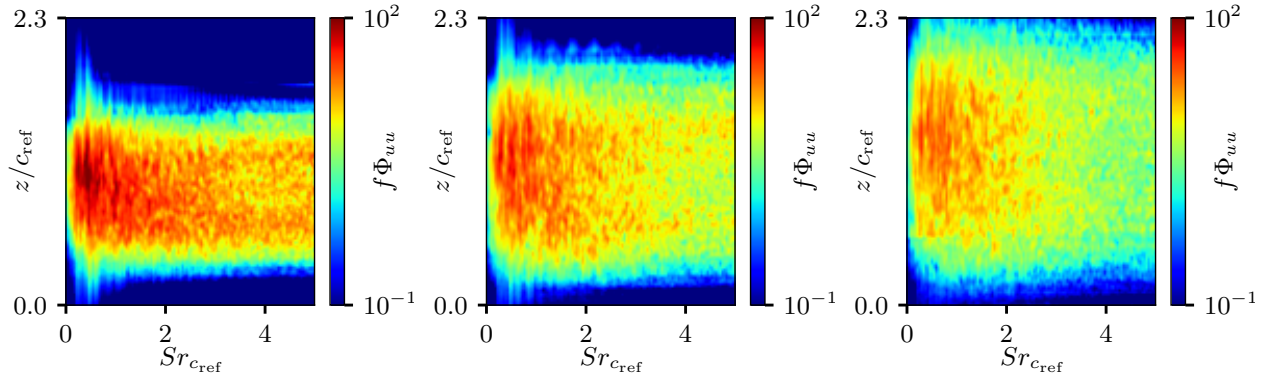

(a) $(x - x_{TE})/c_{\mathrm{ref}} = 1$ **(b)** $(x - x_{TE})/c_{\mathrm{ref}} = 2$ **(c)** $(x - x_{TE})/c_{\mathrm{ref}} = 3$

Fig. 6.57.: Power spectral density of streamwise velocity u along vertical lines at $\eta = 28.3\,\%$, $\alpha = 18°$. Data extraction lines located at $(x - x_{TE})/c_{\mathrm{ref}} = \{1, 2, 3\}$ in WC coordinates.

PDFs remain roughly circular, only decreasing in magnitude. There is little preference for any specific velocity component, in accordance with the isotropy in this region shown in Fig. 6.40. Some residual anisotropy is visible at WC1, with w' fluctuations stronger than u' causing a slight elongation in vertical direction. Still, the joint PDF shapes are much more circular than the ellipsoidal ones for the shear layer points SL1-SL3.

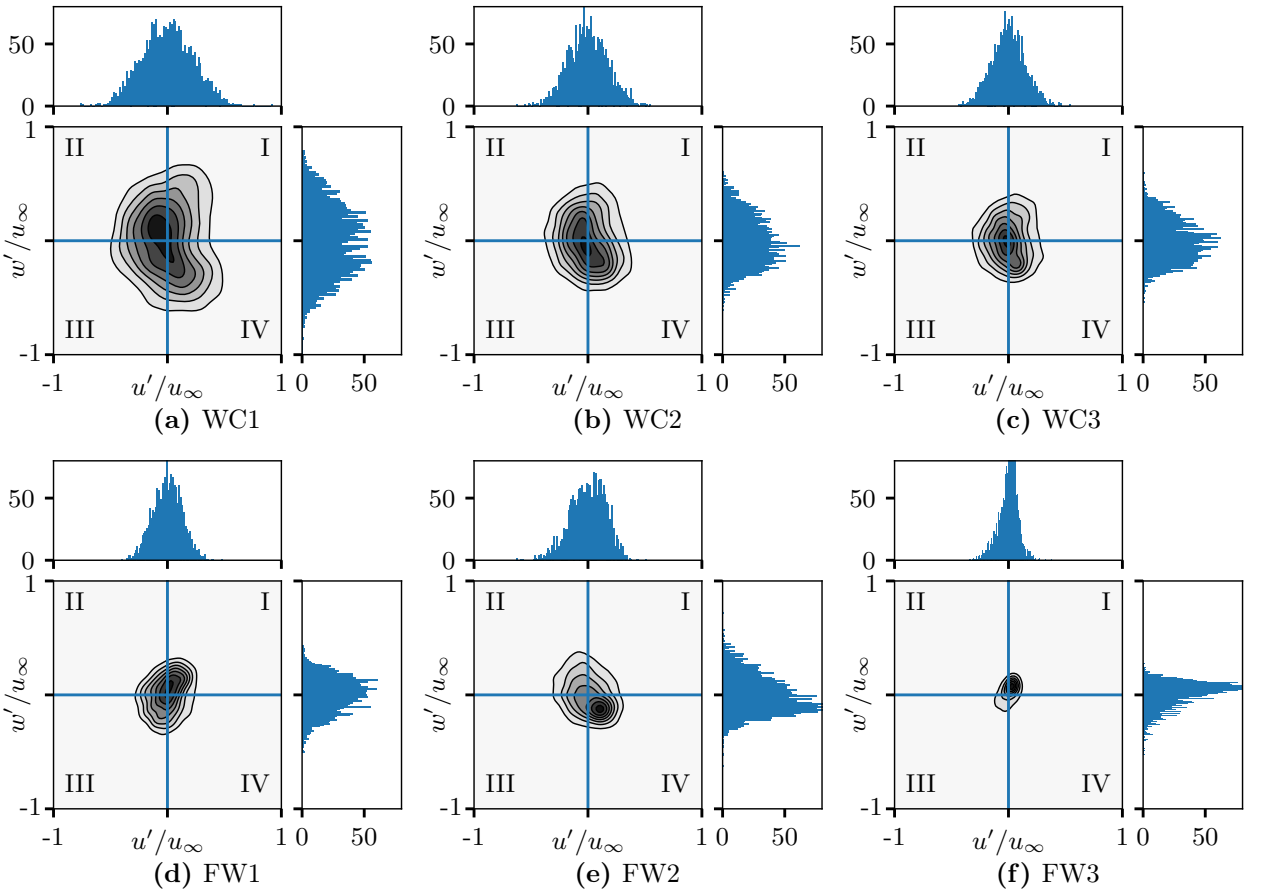

(a) WC1 **(b)** WC2 **(c)** WC3

(d) FW1 **(e)** FW2 **(f)** FW3

Fig. 6.58.: Contours of joint probability density functions with the associated u and w histograms at WC1-3 and FW1-3. u histogram shown on top and w to the right of the contour plots, with common scaling.

The distributions across the wake at FW1-FW3 in the lower row of Fig. 6.58, away from the

wake centerline, are different in terms of joint PDF shape. The upper (FW2) and lower (FW1) points are characterized by rotated and slightly elongated PDFs in Figs. 6.58d and 6.58e. The point FW3 is mostly outside the actual wake, as indicated by the small diameter of the shown PDF in Fig. 6.58f. The corresponding histograms are somewhat skewed. These locations are not in the maximum shear regions, much rather they show the gradual departure from the conditions seen at centerline. These shapes correspond well to the mixing layer observations described by Carlier and Sodjavi [27] and to the SL1-SL3 data in Fig. 6.51.

With regard to quadrant analysis, most samples at the lower points FW1 and FW3 are concentrated in quadrant I of the PDFs, while the PDF of upper point FW2 has its center of mass in quadrant IV. These configurations result from the entrainment of outer flow into the wake. The entrained fluid has higher streamwise momentum ($u' > 0$) and moves into the wake ($w' > 0$ at lower edge, $w' > 0$ at upper edge). The prevalence of sweep events at FW2 is similar to the characteristic of the leading edge shear layer points.

The terminology does not apply to the lower edge, where the same type of event associated with transfer of high momentum from outer flow with $u' > 0$ into the wake ($w' > 0$) occurs in different quadrants. Recognizing that ejection and sweep events are much more common than interaction events in a wake flow, Antonia and Browne [18] termed both quadrants II and III, i.e. those where $u' < 0$, ejection. Both I and IV with $u' > 0$ are sweep quadrants. This is a useful characterization, as the PDF at the lower point FW1 in Fig. 6.58d is rotated by 90° with respect to that of FW2 in Fig. 6.58e, while describing fundamentally the same process.

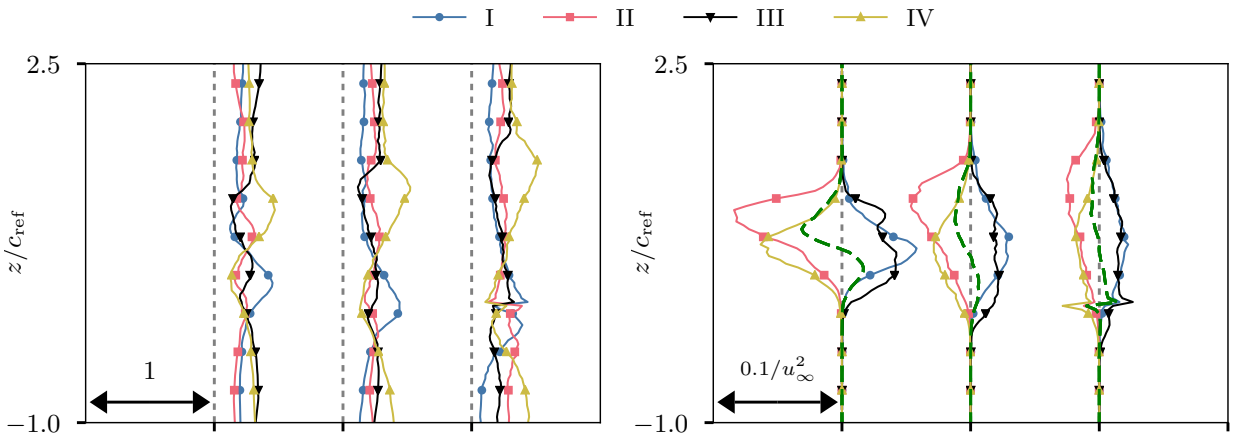

(a) Duration fractions D_i **(b)** Stress contributions C_i

Fig. 6.59.: Quadrant analysis in the wake at $\alpha = 18°$. Lines are at $(x - x_{TE})/c_{\mathrm{ref}} = \{1, 2, 3\}$. Dashed green line in **(b)** denotes total shear stress $\overline{u'w'}$. Coordinates in WC system.

The distribution of duration fractions and quadrant stress contributions in the wake in Fig. 6.59 shows that the upper wake edge involves similar combinations of duration fraction and shear contribution as the leading edge shear layer. For instance, fluctuations at the upper wake edge at the first position $(x - x_{TE})/c_{\mathrm{ref}} = 1$ involve high magnitude ejection events which dominate with high absolute C_{II}. However, it is D_{IV} that shows the most frequent occurrence at that location. This combination is visible just above the maximum magnitude of $\overline{u'w'}$ corresponding to the upper wake edge. The frequency of ejection events in terms of D_{II} increases deeper inside the wake, while their magnitude C_{II} decreases. The distributions occur in the same manner on the lower edge, only with quadrant II replaced

by III and IV by I. There is some degree of symmetry about the wake centerline in the D_i profiles in Fig. 6.59a. The C_i distributions show that the two shear layers cannot be analyzed in full isolation, despite their distance. Where the leading edge shear layer involves mostly only quadrants II and IV, in the wake there are significant values of C_{III} and C_I in the upper edge area. The same is true for the lower edge. Overall, this results in the quadrant C_i values being significantly larger than $\overline{u'w'}$, which is their sum.

6.3.3. Scales and Correlations of Turbulence

Apart from the temporal point statistics described above, the flow unsteadiness and the large scale motion can be described using spatial and temporal correlations of the fluctuating flow field. The correlation tensor between the velocities at two points x_0 and $x_0 + x'$ is defined as follows:

$$R_{uu}\left(x_0, x'\right) = \frac{1}{N} \sum_{t=0}^{N} u'\left(x_0\right) u'\left(x_0 + x'\right) \tag{6.13}$$

$R\left(x_0, x'\right)$ is the normalized cross-correlation coefficient between the velocity signal at location x_0 and a second location displaced by x', i.e. $x_0 + x'$. Eq. 6.13 is defined for the u velocity component and can be used for any of the other solution signals. $R\left(x_0, x'\right)$ permits quantification of spatiotemporal relationships between points. Fixing x_0 and iterating x' over an entire wake slice yields a distribution of correlation coefficients in the field, which provides an impression of the locations which are influenced by the fluctuating events occurring at x_0 [132].

The spatial structure near the wake point SL2 is shown in in Fig. 6.60a. The contours of $R_{uu}(SL2, x')$ have an elliptical shape and are elongated in streamwise direction. The non-circular shape is a consequence of the anisotropy of the correlation tensor. The significant correlation of u over a substantial streamwise distance in this region suggests the existence of coherent streamwise motion over a signficant distance inside the shear layer. This is indicated by the elongated shape of the positive correlation coefficient region. Both the point spectra at SL2 and the POD analysis indicate that the most energetic low order motion at this location has a dominant streamwise component, which is consistent with this R_{uu} distribution. The distinct adjacent region of $R_{uu} < 0$ above the shear layer indicates that increased velocity in the shear layer typically coincides with decreased velocity above it.

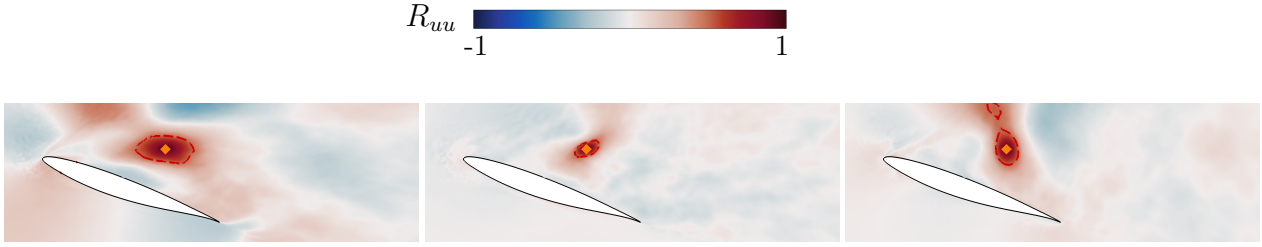

(a) $R_{uu}(SL2)$ **(b)** $R_{vv}(SL2)$ **(c)** $R_{ww}(SL2)$

Fig. 6.60.: Two-point correlations at point SL2 in the upper shear layer at $\eta = 28.3\,\%$, $\alpha = 18°$, WT coordinates.

Regions of high R_{vv} and R_{ww} with respect to SL2 in Fig. 6.60 are much more compact in space. R_{vv} is slightly elongated in wall normal direction. The transverse velocity correlation R_{ww}

with alternating positive and negative extrema in streamwise direction suggest streamwise propagation of spanwise-oriented vortical structures. The positive and negative correlation areas are formed by the opposite velocities at the upstream and downstream side of the vortex. This is comparable to the experimentally observed two-point correlation of Kelvin-Helmholtz vortices behind a backward facing step described by Scharnowski and Kähler [127]. The correlation extends above and below the shear layer, which shows how bulk upward and downward motion influences the direction of flow at larger distances from x_0.

The spatial extent of contiguous correlated regions tends to increase downstream from the trailing edge. R_{uu} is shown for four different points in the near wake in Fig. 6.61. Representative upper and lower wake edge locations (Figs. 6.61a and 6.61d) are shown along with the wake centerline points WC1 and WC2 in Figs 6.61b and 6.61c, respectively. The upper and lower points are situated at the same streamwise position as WC1, i.e. $1c_{\mathrm{ref}}$ downstream from the trailing edge. They are visualized instead of the FW1 and FW2 points, as the correlation shape is visually more discernible at the upstream location.

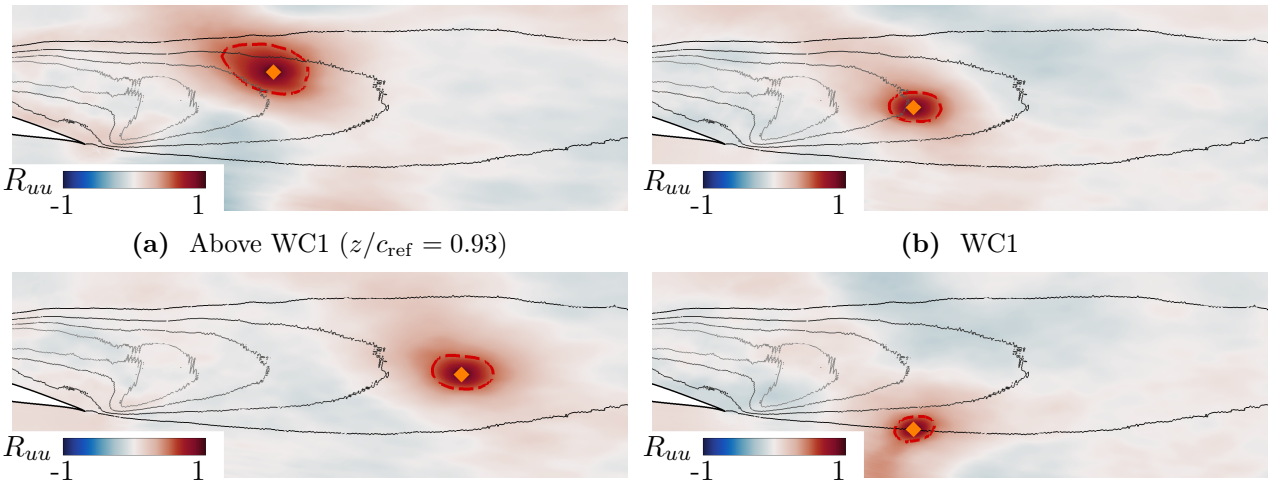

(a) Above WC1 ($z/c_{\mathrm{ref}} = 0.93$) **(b)** WC1

(c) WC2 **(d)** Below WC1 ($z/c_{\mathrm{ref}} = 0.36$)

Fig. 6.61.: Two-point correlations in the wake at $\eta = 28.3\,\%$ and $\alpha = 18°$, WC coordinates. Colors show R_{uu} ranging from -1 to 1, grey lines show distribution of k_t.

The correlation coefficient distributions of the upper and lower edge points are rotated toward the wake. These orientations match the joint PDF distributions shown for the upper and lower far wake points FW1 and FW2 in Fig. 6.58 discussed above. The area correlated with the lower edge point is somewhat smaller than that correlated with the upper edge point, i.e. the fluctuations occurring at the lower edge are more local in nature and have a smaller size scale. The point associated with the upper shear layer is more elongated in streamwise direction. The correlation footprint is also spatially larger than that in the lower shear layer, suggesting a larger size of the associated turbulent structures. The centerline points have an elongated correlation coefficient distribution aligned with the local wake flow direction parallel to the centerline.

The size of the correlated regions is a common metric for the length scale of turbulence. The integral length scale tensor L_{ij} at x_0 is formed from the correlation of velocity component i in direction j via Eq. 6.13 and its integration over all x' in the desired direction:

$$L_{ij}(x_0) = \int_0^\infty R_{ij}(x_0, x')dx' \tag{6.14}$$

The formal integration boundary of ∞ is replaced by a fixed value in practical use. It can be run until the first zero crossing ($R_{uu} = 0$) or until a fixed value > 0 is achieved in order to ensure robust computation of the integral everywhere. It is possible to fit an exponential function to the initial part of the function, but the direct computation proved sufficiently robust in this case. These length scales can be defined for any combination of variable and direction. The longitudinal integral length scale L_{uu} is in common use, correlating the streamwise velocity in streamwise direction. It is often employed as a measure of the large scale eddies, as defined by Pope [107] for homogeneous and isotropic turbulent flows. While neither of these conditions is strictly fulfilled, L_{uu} can serve as a useful qualitative proxy measure for comparison across different locations and flow conditions.

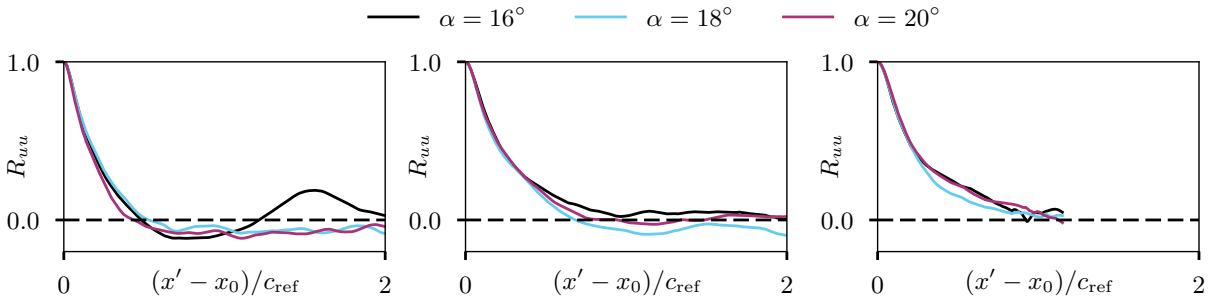

(a) $x_0/c_{\mathrm{ref}} = 1$ **(b)** $x_0/c_{\mathrm{ref}} = 2$ **(c)** $x_0/c_{\mathrm{ref}} = 3$

Fig. 6.62.: Correlation functions R_{uu} with x_0 at WC1, WC2 and WC3, $\eta = 28.3\,\%$.

Comparative shapes of the correlation function R_{uu} are shown for three angles of attack at the wake centerline points WC1-3 at $\eta = 28.3\,\%$ in Fig. 6.62. The shapes of the correlation functions and their changes over streamwise distance are similar at different α values, with no consistent trend which could be attributed to α. The downstream position in Fig. 6.62c visualizes the difficulty with obtaining R_{uu} near the edge of the highly resolved grid region, as the integration needs to be stopped shortly after the threshold is reached due to irregularities appearing at higher Δx, when the flow transitions from the grid's focus region into more coarsely resolved regions. Fig. 6.62b showcases why it is not useful to choose $R = 0$ as stopping condition for integration, as the turbulent nature of the wake and imperfect sampling due to finite simulation runtime may cause spurious long-distance correlation. $R_{uu} = 0.1$ was chosen as threshold for this reason.

Obtaining spatiotemporal correlations for many locations can be computationally expensive, and computing L_{uu} for a point involves the computation of two-point correlations with a large number of points in the vicinity. On the other hand, autocorrelations are much more easily derived as they only involve point signals without spatial correlations. Autocorrelation can be used to estimate L_{uu} via Taylors's hypothesis. This involves the assumption that turbulence is homogeneous and does not change in space, i.e. turbulent structures convect with the local velocity without significant change or deformation. This permits the computation of a length scale purely from a local time scale and propagation velocity. The time scale τ is the integral over time lags of an autocorrelation ρ, i.e. a quantity that is much more easily obtained from a flow field. The scales can thus be obtained as follows:

$$L_{Taylor}(x_0) = \overline{u} \cdot \tau = \overline{u} \int_0^\infty \rho(t', x_0) dt' \qquad \rho(t', x_0) = \frac{\overline{\phi(t)\phi(t+t')}}{\overline{\phi(t)\phi(t)}} \tag{6.15}$$

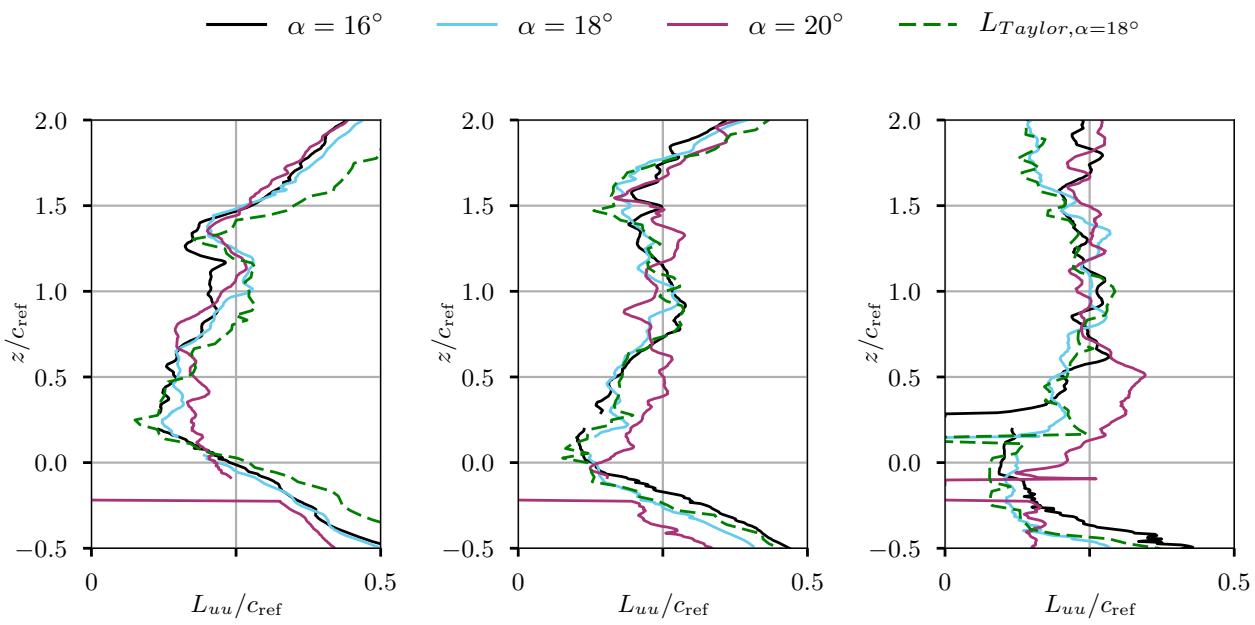

(a) $x/c_{\text{local}} = 1$ **(b)** $x/c_{\text{local}} = 2$ **(c)** $x/c_{\text{local}} = 3$

Fig. 6.63.: Integral length scale L_{uu} at three positions downstream of the trailing edge, WC system. The distortion at the lower edge is caused by integration approaching the tailplane.

Length scale profiles at $\eta = 28.3\,\%$ across vertical lines through WC1-WC3 in the wake are shown as a function of transverse coordinate z in Fig. 6.63. The strong increases toward the upper and lower margins of the plots are spurious effects outside the wake, where rare and intermittent disturbances cause slow oscillations which lead to artificially inflated correlation distances. Discounting such data and retaining only values in the region between $z/c_{\text{ref}} = 0$ and $z/c_{\text{ref}} = 1.5$, the length scale is on the order of $L_{uu} \approx 0.2c_{\text{ref}}$ everywhere in the wake, which corresponds to roughly $L_{uu} \approx 0.4d$ at $\eta = 28.3\,\%$ ignoring the slight variation due to α.

Wake L_{uu} tends to be largest around the wake center, where large scale processes and bulk motion dominate. L_{uu} tends to decrease at the upper and lower wake edges, where the smaller-scale shear layer effects due to mixing between outer flow and wake flow tend to decrease the characteristic scales. This is especially true at the lower edge, where the values decrease to about half of the centerline value. The profile becomes more symmetric with streamwise distance. The L_{uu} profile shapes are largely unchanged by the angle of attack, indicating that wake motion has a characteristic longitudinal length scales of about $0.4d$ in most regions of the flow.

$L_{uu,Taylor}$ derived using the temporal autocorrelations is also included in the figures for $\alpha = 18°$ in order to evaluate its accuracy. It provides essentially the same information as L_{uu} based on two-point correlation, with similar increases in the upper part of the wake and the equlibration of the length scales with streamwise distance. The approximate fulfilment of the Taylor hypothesis is an indicator that the large scale turbulent structures convect downstream with little change. It can be explained by the production term of k_t acting as a source of resolved turbulence upstream near the leading and trailing edges. By consequence, the turbulence observed further downstream in the wake is predominantly a result of transport from upstream, with local production playing a much smaller role. The local mixing effects do not appear to invalidate Taylor's hypothesis to a significant degree. Its use permits the

analysis of integral length scales everywhere in the flow field, with the profiles in Fig. 6.63 increasing confidence in the validity of the $L_{uu,Taylor}$ values.

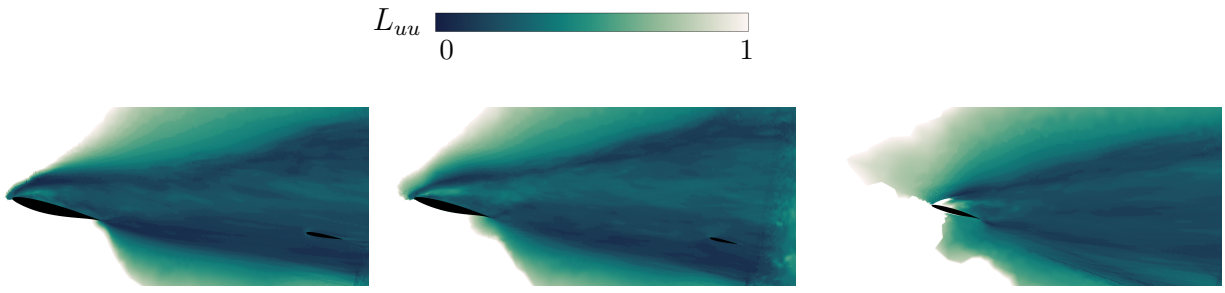

(a) $\eta = 20.1\,\%$ **(b)** $\eta = 28.3\,\%$ **(c)** $\eta = 60.3\,\%$

Fig. 6.64.: Integral length scales $L_{uu,Taylor}/c_{\text{ref}}$ using Taylor's hypothesis, $\alpha = 18°$, WC system. Contours cut off above $L_{uu}/c_{\text{ref}} = 1$.

The spatial distributions of Taylor-based longitudinal length scales $L_{uu,Taylor}$ are shown in Fig. 6.64. The structure is similar across all spanwise positions, with upper and lower wake edges involving smaller integral length scales compared to the center. The wake center length scales at $\eta = 28.3\,\%$ reach values greater than $0.2c_{\text{ref}}$, whereas they are significantly smaller at the edges. The recirculation region between the wing surface and the leading edge shear layer involves large scales approaching $L_{uu}/c_{\text{ref}} > 0.5$. This is due to the low frequency shear layer dynamics described in Section 6.2.

The topology with a large isotropic wake core involving relatively large length scales near the centerline and decreased values toward the edges is rather distinct at $\eta = 28.3\,\%$. It does exist at $\eta = 20.1\,\%$ in Fig. 6.64a, albeit to a lesser degree. Here, $L_{uu,Taylor}$ does not reach as high values in the wake center as at $\eta = 28.3\,\%$. The overall distributions are similar, but the decreased wake width at $\eta = 20.1\,\%$ translates to less space for persistence of larger scales in the wake. Rather, the upper and lower wake edges interact with each other in a more direct manner. The small scale turbulence in the upper and lower wake edges inhibits the formation of a distinct wake center region with large scales.

The outboard length scales in Fig. 6.64c are of similar magnitude to those inboard in absolute terms. This means that they are significantly larger with respect to the local projected wing height d. There is a wide wake core with large scale turbulence, bounded by narrow strips of small length scales above and below. The overall symmetric appearance of the outboard wake is once again visible via L_{uu}.

6.3.4. Concluding Remarks

This section focused on the quantitative characteristics of turbulent flows in the leading edge shear layer bounding the recirculation region, and in the wake downstream from the wing trailing edge. Second order statistics such as Reynolds stresses, and third and fourth order statistics were evaluated to demonstrate the behavior of turbulent fluctuations and its similarity to canonical shear layer flows from literature. Quadrant analysis and point signal statistics were analyzed to obtain a complete picture of fluctuation characteristics, and of their evolution with downstream distance. The von Kármán wake mode dominates most of the wake fluctuations. Despite this, spectral features associated with large scale dynamics structures can be detected in parts of the wake. Analysis of turbulence length

scales shows that length scales based on Taylor's frozen turbulence hypothesis provide a feasible approximation of the integral length scales in the wake.

6.4. Wake Propagation and Tailplane Loads

While understanding the wing forces and wake dynamics is important in and of itself, the manner in which the unsteady wake propagates from the location of its origin to the aircraft tail needs to be focused on. The interaction of the fluctuation with the tail forces determines the way in which the massive separation affects the overall aircraft forces and moments. In the following, the propagation of wake structures is evaluated and the spectral characteristics of the tail loads are investigated. This is intended to enable a deeper understanding of the aircraft loads at the prescribed flow conditions.

The turbulent fluctuations generated at the wing and in the wake propagate toward the tailplane with a characteristic bulk velocity depending on the wake characteristics. The large and small scale fluctuations that contribute to the turbulent wake flow impinge on the tailplane and generate fluctuating loads.

6.4.1. Wake Meandering

Foti et al. [40] and Howard et al. [56] described the concept of wake meandering in the context of wind turbine wake flows, whereas Mulleners et al. [99] termed the concept "wake undulation" and employed it for mildly separated airfoil flows with vortex shedding. The concept is to analyze each instantaneous velocity snapshot individually and obtain statistics from the resulting data set. The instantaneous velocity field in a longitudinal slice contains all resolved velocity scales, but a large scale meandering pattern can be determined even with the naked eye. The wake meander can be defined using the local minima of the instantaneous streamwise velocity u at each x position. This is shown as dots superimposed on the instantaneous velocity field in Fig. 6.65a at a time t_i, defining the position $z_{meander}(x, t_i)$ of the large scale meandering wake. The distribution of the minima is noisy and can be expected to introduce spurious information during further processing, which make the analysis of the large scale features more difficult. Howard et al. [56] proposed the employment of a spatial low-pass filter in order to improve the signal to noise ratio. The cutoff for the 5th order Butterworth filter is set to $k_{cut} = 0.04m^2$. The largest length scale that can be feasibly resolved in the near field between the wing and tailplane is about 0.6 m or $3.3c_{\mathrm{ref}}$, which is roughly the distance between wing and tailplane. Most of the smaller scale fluctuations are filtered out. With the integral length scales L_{uu} determined above being of a similar magnitude to k_{cut}, this cutoff wavenumber is a reasonable choice for the study of large scales. A sensitivity study of the results with respect to different k_{cut} values showed robust behavior of the resulting detection. The resulting meander signature obtained using the filter is shown as an orange line for a single temporal snapshot in Fig. 6.65a.

The shape permits representation of the wake meander as a simple function of streamwise distance x. Measuring the minima and maxima of this function and their respective distances at each time step yields the characteristics of the meandering motion. The wavelength Λ is

[2] This corresponds to one half of the projected height of the bluff body d, consistent with Howard's suggestion in [56].

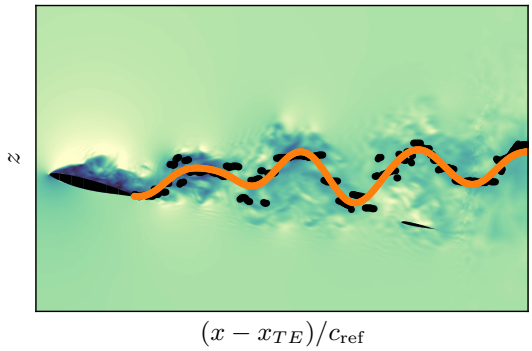

(a) Contours of instantaneous u, $min(u)$ at each streamwise position indicated by black dots. Orange line shows low-pass filtered signal.

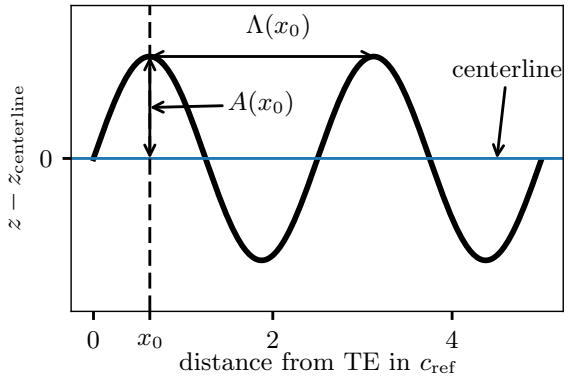

(b) Definition of A and Λ in the meander pattern

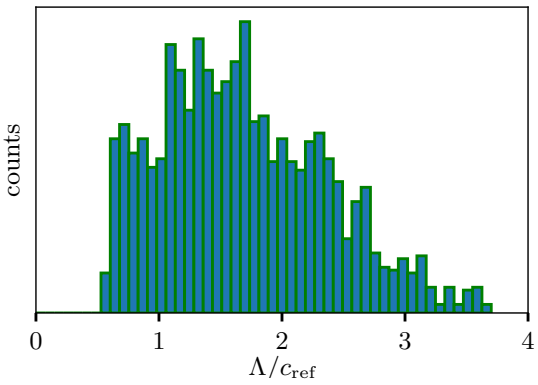

(c) Histogram of all detected wavelengths

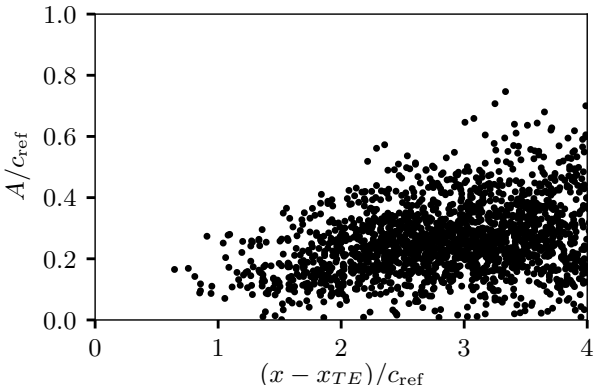

(d) Detected A/c_{ref} over x

Fig. 6.65.: Wake meandering at $\alpha = 18°$, $\eta = 28.3\%$.

defined as the spatial distance between consecutive minima or maxima of the low-pass filtered shape, cf. Fig. 6.65b. For statistics collection, the location corresponding to a wavelength is the halfway position between two such consecutive extrema. The amplitude A and wavelength Λ are associated at the same location. These definitions are chosen corresponding to Foti et al. [40].

Fig. 6.65c shows a typical histogram of the detected meander wavelengths of the entire run history over $150t_\infty$ at $\alpha = 18°$. The distribution is skewed with a long tail toward high values of $\Lambda/c_{\mathrm{ref}} = 3$, with most of the values between 1 and 2. The largest scales of meandering in the histogram's long tail to the right are of the same order of magnitude as the distance between the wing trailing edge and the HTP. Reasonable statistics of the evolution of Λ over x would require much longer domains far downstream of the aircraft, which is not within the scope of this study.

The amplitudes A, on the other hand, can be evaluated over the entire domain. A is measured as the perpendicular distance to the linear fit over the wake centerline as shown in Fig. 6.65b. The values of A increase slightly with streamwise distance, as shown in Fig. 6.65d. This is indicative of the spreading of the wake that occurs over distance. While the computation of the wake half-width l_s provides a scale, the statistics of A also permit determining a vertical position of the wake and its most extreme extents. This was determined by taking the maximum and minimum positions of detected amplitude at each possible streamwise location, the result of which is plotted in Fig. 6.66. The maximum vertical width of the wake close to the airfoil is on the order of the projected height d and increases rapidly

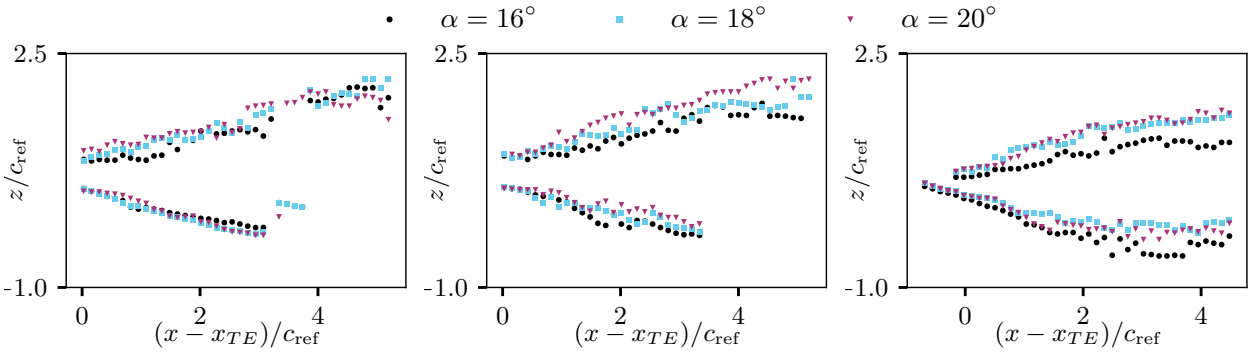

(a) $\eta = 20.1\%$ **(b)** $\eta = 28.3\%$ **(c)** $\eta = 60.3\%$

Fig. 6.66.: Wake maximum extent via extrema of A over streamwise distance. Only every 10th sample is shown for clarity. WC system.

with downstream distance. Like l_s, the maximum vertical extent $A_{max}(x)$ increases roughly linearly with streamwise distance x, in particular inboard. An apparent asymptotic behavior of the expansion can be surmised, especially at $\alpha = 16°$, but it is not achieved within the streamwise distance before reaching the tail. It does occur more clearly outboard at $\eta = 60.3\,\%$ in Fig. 6.66c, where the vertical positions of the minima and maxima cease to grow linearly after about $3c_{\text{ref}}$.

6.4.2. Propagation Speed

Despite the three dimensional phenomena in the wake, the large scale meandering structures predominantly propagate downstream at a characteristic velocity. Their impact on the tailplane is therefore delayed by the time necessary to traverse the distance between the location where the wake is created and the tailplane. The position of the peaks and troughs of the meander shape lends itself to the estimation of the disturbance propagation velocity in streamwise direction. The space-time representation of the wake shapes over time in Fig. 6.67 includes distinct minima and maxima of the flow. The slope of position x versus time t of these extrema remains largely consistent over time and can be averaged to about $\overline{u}/u_\infty = 0.8$ for $\alpha = 18°$. The same value is obtained at $\alpha = 20°$, while a higher value of $\overline{u}/u_\infty = 0.88$ results for $\alpha = 16°$.

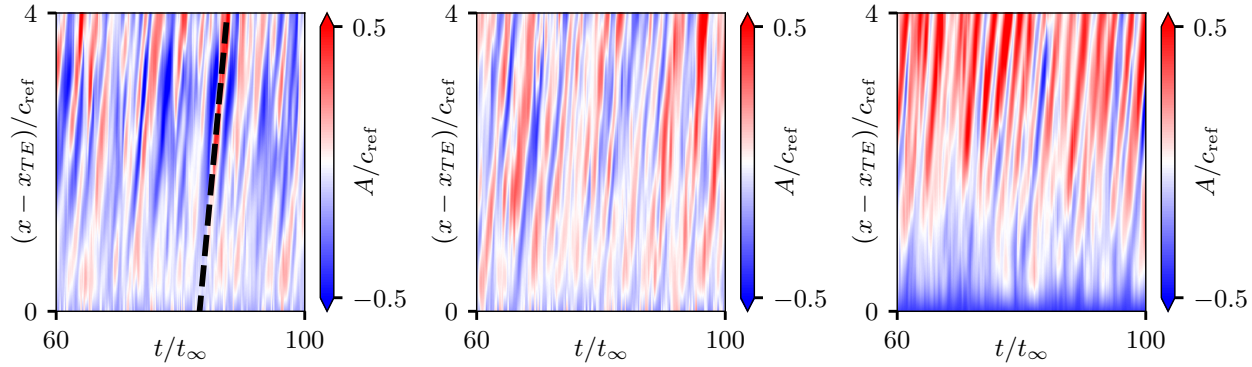

(a) $\alpha = 16°$ **(b)** $\alpha = 18°$ **(c)** $\alpha = 20°$

Fig. 6.67.: Space-time plot of low-pass filtered meander function over time at $\eta = 28.3\,\%$. Dashed green line in Fig. 6.67a indicates typical slope of a ridge.

The above is a direct result obtained from flow physics. A different, proximate measure for the propagation velocity can be derived from the fluctuating lift signals of the wing and tailplane at the same spanwise position. The local lift coefficient $c_l(y)_{\text{wing}}$ and $c_l(y)_{\text{HTP}}$, evaluated at the same absolute position y, are correlated due to transport of flow features being largely aligned with the streamwise direction x_{WT}. The cross-correlation of the two signals at a given spanwise position $y = const.$ can be computed by the following, assuming jointly wide-sense stationary stochastic processes:

$$\rho(\Delta t, y) = \frac{\overline{c_{l,\text{wing}}(t, y) c_{l,\text{HTP}}(t + \Delta t, y)}}{\sigma(c_{l,\text{wing}}(t, y))\sigma(c_{l,\text{HTP}}(t, y))}. \tag{6.16}$$

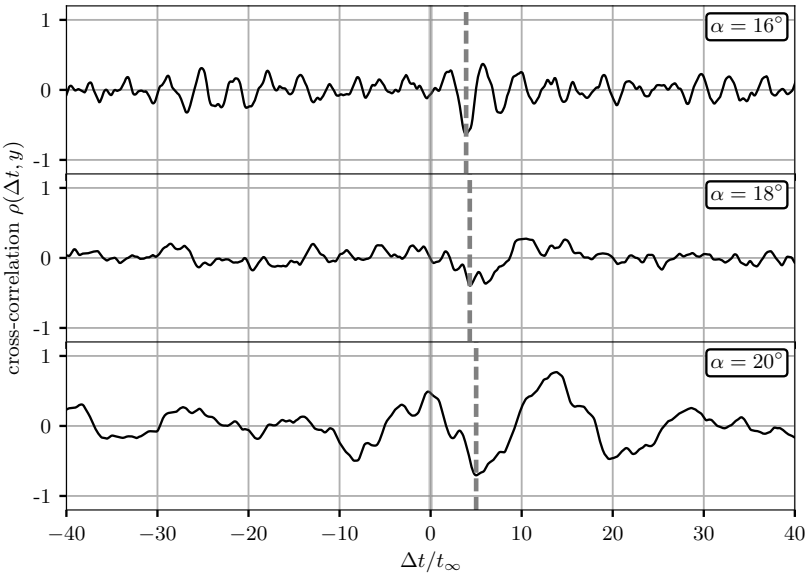

Fig. 6.68.: Cross-correlation of the local wing lift at $\eta = 28.3\,\%$ and the corresponding spanwise position on the tailplane. Vertical dashed line indicates lag of highest absolute correlation coefficient.

$\rho(\Delta t, y)$ is shown in Fig. 6.68 for $\eta = 28.3\,\%$. The plots show a significant amount of noise, and the ρ values do not approach close to 1. The wing lift is only weakly impacted by the downstream wake phenomena which influence the tailplane lift the most. Nevertheless, the first local peak of negative correlation at each angle of attack with a positive delay can be reasonably assumed to represent the delay inherent in the propagation of large scale features from wing to tail. This represents an inverse relationship between wing and tail forces at the same spanwise position. The lag increases with angle of attack, with $t_{\text{delay},16^\circ} = 1.35 \cdot 10^{-2} s$, $t_{\text{delay},18^\circ} = 1.49 \cdot 10^{-2} s$ and $t_{\text{delay},20^\circ} = 1.70 \cdot 10^{-2} s$. These delays can be associated with the propagation velocity of the flow phenomena causing forces on the wing and the tailplane. The resulting values are $0.88 u_\infty$, $0.80 u_\infty$ and $0.70 u_\infty$, respectively, which is a very good match with the speeds computed via direct tracking of the large scale structures. Only the velocity at $\alpha = 20^\circ$ is appreciably different from that obtained from the wake meandering. This may reflect inaccuracies in the cross-correlation method and in the estimation of Λ at different angles of attack. Both estimation methods are affected by deficiencies: the amplitude detection for the wake meandering approach suffers from a small number of detectable peaks relative to the domain length, while the cross-correlation ignores the actual flow phenomena and is based on pure force signal comparison. Nevertheless, both results do indicate that the velocity scales with the wake width. Higher angles of attack flows tend to exhibit the lowest

propagation velocities and vice versa.

6.4.3. Tailplane Interaction

The time-averaged tailplane loads in terms of C_L were explored in Section 6.1.2, concluding that the tailplane lift is largely determined by the wing downwash angle ξ and the resulting effective HTP inflow direction. This results in a $C_{L,HTP}$ that is twice as large at $\alpha = 20°$ than at $\alpha = 16°$ in Table 6.2. The time series of $C_{L,HTP}$ are shown in Fig. 6.69 and visualize the unsteadiness of the phenomena. Both the mean levels of $C_{L,HTP}$ and the oscillations increase with higher α. A result obtained using URANS at $\alpha = 18°$ (run U4 from Chapter 5) is shown for reference.

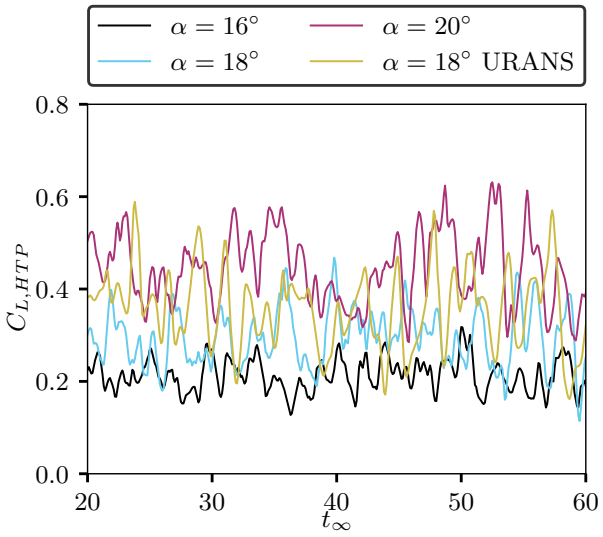

Fig. 6.69.: Time series of tailplane forces.

Most of the local lift differences occur near the tip of the HTP, which is close to the wing's $\eta = 28.3\,\%$ station discussed above. While the means of the tailplane lift signals increase strongly with α in Fig. 6.70a, the signal variance as a measure of load fluctuations does not grow by similar amounts. Its increase from $\alpha = 18°$ to $\alpha = 20°$ is smaller than that from $\alpha = 16°$ to $\alpha = 18°$.

The premultiplied spectra of $C_{L,HTP}$ in Fig. 6.70b reflect this and reach similar levels at the two higher α. The spectra were obtained using Welch's method and 7 signal bins each, in this case prioritizing statistical significance and reliability of the observed amplitude peaks over spectral resolution, which suffers as a result. While the overall variance is similar, the distribution of high fluctuation amplitudes across the frequency range is different between $\alpha = 18°$ and $\alpha = 20°$. The tailplane lift coefficient spectra reflect the observations made via POD at $\eta = 28.3\,\%$ and $\eta = 20.1\,\%$ in Figs. 6.22, 6.35 and 6.36 remarkably well. $C_{L,HTP}$ exhibits two peaks at $\alpha = 18°$ at the same Strouhal numbers as the POD wake modes, $Sr_{c_{\text{ref}}} = 0.22$ and $Sr_{c_{\text{ref}}} = 0.5$. A similar bimodal structure is visible at $\alpha = 16°$, where is is shifted to higher frequencies. At the same time, there is a broad spectral bump at $\alpha = 20°$, reflecting the spectral shape of the predominant wake POD modes at that α. Generally, POD wake data can be considered a good predictor of tailplane loads.

The reasons for the differences in the spanwise distribution of tailplane load variance can

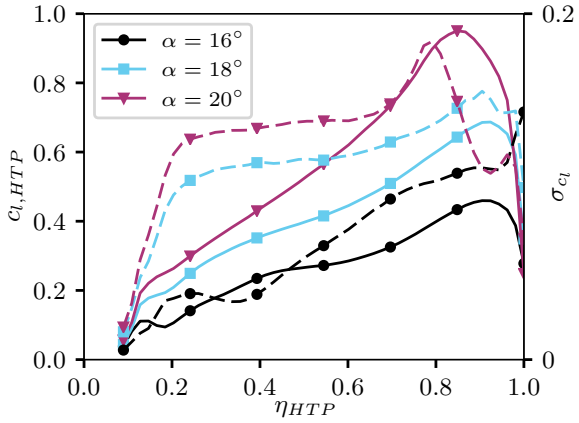

(a) Spanwise distribution of $c_{l,HTP}$ (solid lines, left y axis) and its standard deviation σ_{c_l} (dashed lines, right-hand y axis).

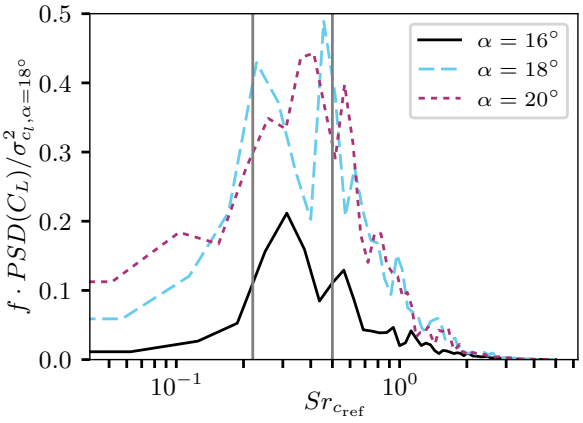

(b) Premultiplied spectral density of the tailplane lift coefficient, nondimensionalized by the signal variance at $\alpha = 18°$. Vertical lines indicate the two main modal frequencies identified at $\alpha = 18°$ using POD.

Fig. 6.70.: Tailplane loads at three angles of attack.

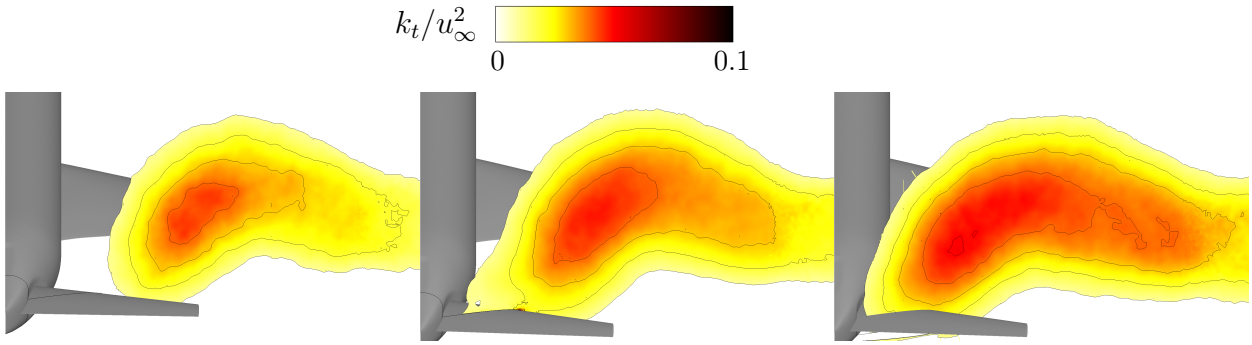

(a) $\alpha = 16°$ **(b)** $\alpha = 18°$ **(c)** $\alpha = 20°$

Fig. 6.71.: k_t/u^2_∞ at $x/c_{\mathrm{ref}} = 8.5$. Volume slice is fixed in WT system.

be visualized via resolved k_t just upstream of the HTP leading edge, shown in Fig. 6.71. Using k_t as a measure for the presence of a turbulent wake, its physical extent is significantly smaller at the lowest angle of attack. The spanwise maximum of k_t in Fig. 6.71a is positioned above the tailplane tip, while higher α move this region of maximum k_t further inboard. The turbulent fluctuations impinging on the tailplane represented by k_t are the source of the load fluctuation on the tailplane. This is the reason why the local lift fluctuation near the tip at $\alpha = 18°$ in Fig. 6.70a is higher than that at $\alpha = 20°$, as the maximum k_t is located further inboard in the latter case.

While the increase of time-averaged tailplane load with increasing α is intuitive, the less significant increase of its fluctuation requires further discussion. Assuming that the majority of tailplane load fluctuations occurs due to incoming turbulence, the greater magnitude of resolved k_t in the wake seen in Fig. 6.11 should cause larger fluctuations. This is counteracted not only by spanwise differences, but also by the vertical distance between the wake and the tailplane visualized in Fig. 6.72.

While $\alpha = 20\,\%$ in Fig. 6.72c involves the highest magnitudes of k_t in the wake center, the wake passes largely above the tailplane at this spanwise position. The high k_t regions move closer to the tailplane at lower angles of attack. This is visualized using the purple line

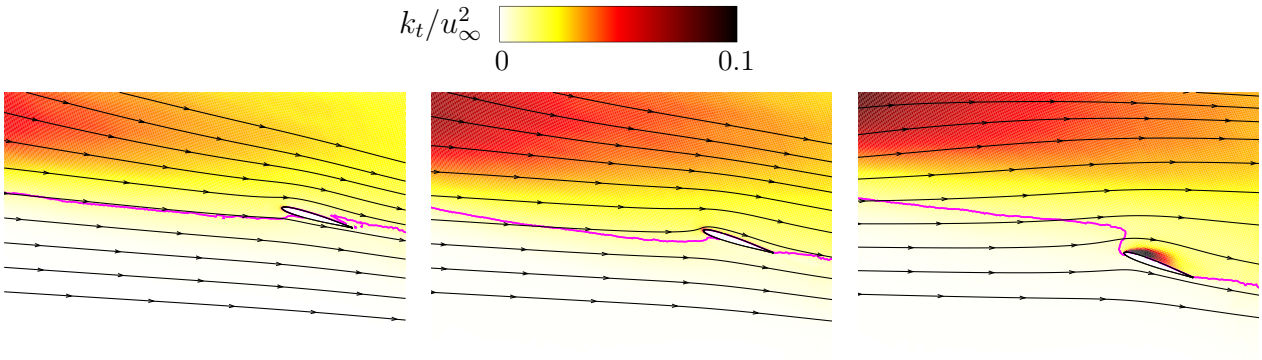

(a) $\alpha = 16°$ **(b)** $\alpha = 18°$ **(c)** $\alpha = 20°$

Fig. 6.72.: Resolved k_t/u_∞^2 at $\eta = 28.3\,\%$ near the tailplane and time-averaged in-plane streamlines. Purple isoline denotes $k_t/u_\infty^2 = 0.01$.

superimposed on the k_t contours, which represents the isoline of $k_t/u_\infty^2 = 0.01$. It is positioned near the tailplane leading edge in Figs. 6.72a and 6.72b, and is clearly shifted upward at $\alpha = 20\,\%$. The wake at high angle of attack therefore involves the highest fluctuation levels, however its influence on the tailplane load fluctuations is counterbalanced by the reduced impingement of strong turbulent fluctuation on the HTP.

The flow field in Fig. 6.72c also provides the reason for the high local values of c_l near the tip at $\alpha = 20°$. As the downwash decreases at higher α, the tailplane re-emerges from the wake into the comparatively undisturbed freestream below it. The streamlines in Fig. 6.72c indicate a effective high angle of attack for the tailplane at this position. This α_{eff} is sufficiently large to cause local flow separation. This is indicated by the elevated value of k_t in Fig. 6.72c above the tailplane surface, which represents significant turbulence kinetic energy which does not originate from the wake.

6.4.4. Concluding Remarks

The propagation of the fluctuating flow from the wing to the wake was evaluated using two different methods, based on velocity field analysis and on force measurements signals only. The agreement between the two approaches increases confidence in the feasibility of the study and shows that the propagation velocity of the large scales tends to decrease at high α and with increased size of the wake. Irrespective of the propagation velocity, spectral analysis of the tailplane lift coefficient shows how the flow structures generated at the wing cause load fluctuations with their corresponding frequencies. As such, both the leading edge fluctuation and the von Kármán wake mode can be detected in terms of load amplitudes at the tailplane. The relative position of the tail with regard to the fluctuating turbulent wake was shown to play a role for the loads, demonstrating that the increase in load fluctuations due to increase α diminishes past $\alpha = 18°$. This is due to the tailplane being moved outside of the wake's path.

CHAPTER 7

Conclusion

This work explores the nature of flow phenomena occurring in low speed stall conditions on a representative commercial transport aircraft configuration. The Common Research Model was used with the goal of employing an aircraft geometry for which a large amount of research already exists. Validation data for flight-relevant Reynolds number aircraft flows provided by the ESWI^{RP} project was leveraged to derive proper simulation approaches for flow conditions of such complexity. The work involves two main aspects: the establishment of a specifically validated simulation strategy and an in-depth analysis of the time-resolved flow physics obtained using the chosen method.

Simulation Aspects

The inherent unsteadiness of the flow needs to be reproduced by time-accurate simulation of the flow field. Spatiotemporal resolution, computational model choice, geometric representation and inherent differences between computational and experimental data sets need to be taken into account. The validation case of $Re_\infty = 11.6 \cdot 10^6$, $M_\infty = 0.25$, $\alpha = 18°$ as per ESWI^{RP}'s run 313 was selected based on the amount of available data for comparison. Leveraging previous work by the author and the Aircraft Aerodynamics working group, a series of bespoke grids was created with appropriate local resolution in regions of interest.

A wide variety of simulation runs using unsteady RANS and hybrid RANS/LES methods were undertaken, of which four URANS results and two DDES results are used for comparison in this work. The results show that:

- With the same background model and otherwise equal parameters, URANS shows excessive dissipation of small scale fluctuations compared to DDES
- Differences in fluctuation characteristics in the leading edge shear layer cause stark differences in pressure distribution, which is most significant at the wing measurement

stations inboard from the Yehudi break

- The erroneous separated flow field results in the URANS runs cause force and moment results with large deviation from experimentally measured values
- Artificial dissipation plays a significant role, excessive values of $k^{(4)}$ cause similar problems to occur in DDES
- Only the combination of low artificial dissipation and hybrid models is capable of providing accurate results in agreement with experimentally measured forces, moments and pressures
- The best-performing simulation shows remaining discrepancies with regard to the PIV data, mainly in the wake width. This may be attributable to excessive widening of the wake due to dissipation.

Closer study results in the conclusion that URANS, while principally able to resolve the large scale characteristics which are responsible for the majority of loads, is not feasible for this type of simulation. Proper representation of the leading edge fluctuation was observed to be critical for the formation of the correct flow topology in the wake. Only the hybrid methods are capable of this in the present context, and were employed for the studies of the flow physics.

Apart from computational model choice, grid and time step size were evaluated via wake flow field analysis. Maximum time step size and grid resolution, as well as their relation to the convective CFL number, were derived from these results. These outcomes can serve as basis for future studies. The inherent configuration differences between wind tunnel and computational model were taken into account by running comparative simulations with the selected DDES method. The wing deformation of the wind tunnel model has a negligible effect at the investigated flow conditions. The wind tunnel mounting system does have a local effect which alters the quantitative results in terms of forces and moments. It does not, however, change the wake physics in appreciable qualitative terms.

Flow Physics

Static low speed stall was shown to be characterized by massive separation over the entire wing in a time-averaged sense, which results in a large scale separated unsteady and highly turbulent flow behind the wing. The separated region is deformed by longitudinal vorticity which occurs due to the planform and shape of the main wing and the associated spanwise circulation gradient. The size of the wake scales with the angle of attack, increasing at higher α. Similarly, the longitudinal vortex moves inboard with increasing α. This is associated with a reduction in wake size far inboard. These observations are consistent with the existing literature on low speed stall on moderately swept wings.

The separated wake shows characteristics of a bluff body flow, with separation at the leading edge and large recirculation areas above the wing. The size of the recirculation and the location of the rear stagnation point vary with spanwise location η and angle of attack α. Three distinct types of turbulence generation topology were identified according to the main location where turbulence production occurs: downstream from leading edge above the wing, downstream from trailing edge, and both. The wake characteristics show little change due to α outboard of the Yehudi break. Conversely, the asymmetry and downwash angle are

strongly affected by α in the inboard wake.

Recirculation Area Fluctuation

The fluctuation characteristics were further elaborated using modal analysis and POD, showing that the different fluctuation phenomena involve different frequency ranges. The low frequency fluctuation above the inboard wing at $\eta = 28.3\,\%$ was analyzed via phase binning based on POD results. Periodic alternation of the backflow region between shortened and elongated shapes could be associated with different locations in phase space. Spectral analysis, joint statistics and wavelet coherence analysis of locations along the shear layer helped elucidate the momentum exchange and entrainment processes, whereby high speed outer flow is periodically entrained downward towards the wing surface and thus shortens the backflow region. Analysis of the Reynolds stress tensor components and the higher order statistics provides insight into differences of the turbulence effects in this high shear region. Quadrant analysis of the shear stress indicates that the majority of momentum transfer between streamwise and vertical directions is indeed accomplished by low frequency events. The events contributing the largest amounts of shear stress are comparatively rare. This is consistent with the predominant low frequency features in the Fourier spectra, and was confirmed by high coherence between u and w in the corresponding frequency range employing wavelet cross-spectra.

Wake Turbulence

The turbulent wake is transported downstream toward the tail, imparting loads on its surface. The spectral content associated with backflow recirculation is detectable in parts of the wake even at large downstream distances. Mostly, von Kármán vortex street type fluctuations dominate the large scale dynamics. These fluctuations occur near the $Sr_d \approx 0.22$ oscillation frequency which is frequently referred to in literature for various kinds of bluff body flows. Despite the three dimensional character of the wake and noticeable longitudinal vorticity, many of turbulence phenomena show properties of plane wakes. The turbulence statistics reveal a wake center region characterized by near-isotropic turbulence and comparatively large turbulence length scales of up to $L_{uu} \approx 0.2/c_{\mathrm{ref}}$. The wake center is bounded above and below by mixing regions which interact with the outer flow, exhibiting shear layer-like profiles of Reynolds stresses, skewness and kurtosis. More significant anisotropy of the Reynolds stress tensor occurs in these regions, tending to axisymmetric oscillations with strong shear stress $\overline{u'w'}$.

Both the recirculation region fluctuation and the pure wake fluctuation relate to the vortex street visible in the spectra of the tailplane loads. Time-averaged tail loads and their fluctuation amplitudes both increase with angle of attack. However, these increases are counteracted at higher α by the tailplane moving outside of the path of the wake.

Limitations and Research Outlook

The overarching motivation for this type of work, as laid out in the introduction, is the advancement of understanding of extreme conditions in the flight envelope for the purpose

of increasing safety and efficiency.

Considering the magnitude of the occurring loads, structural motion is to be expected. Adding unsteady deformation and aeroelastic coupling to a simulation are further steps significantly increasing complexity, but also offering potential benefits in terms of accuracy. For the same reason, the load coefficients encountered in this work show that the concept of static stall is difficult to translate to free flight. The significant fluctuation of forces and moments alters separation locations and the center of pressure, modulating the pitch angle and α. The inflow boundary condition α can be held constant in CFD for the type of fundamental study such as the present work, but coupling CFD with flight mechanics studies is necessary to fully understand an aircraft's behavior after entering stall conditions.

In addition to this, geometrical features of actual aircraft such as deployed high lift devices, engine nacelles with associated engine exhaust stream, flap track fairings and other complexities may be added in order to improve simulation fidelity. All of these aspects have been researched to various degrees and referred to in Chapter 1, but their combination with simulation of post stall behavior appears to be a worthy research objective.

The post stall conditions focused on in this work are associated with complex flow dynamics and require high fidelity computational methods. Despite this, the simulations are aided by the fact that the very high angles of attack cause the location of flow separation to remain relatively fixed near the leading edge of the wing. At more moderate angles of attack, the separation line may move in space and modulate the turbulent wake flow by superimposing much lower frequency oscillations. In order to close the gap between linear-regime attached flow and post-stall unsteady flow, additional research effort needs to be spent with simulation at moderate angles of attack.

The low speed stall is but one part of the Mach number regime. Transonic flight near design conditions involves different stall mechanisms via shock induced separation. Moderate Mach numbers at high angles of attack may also trigger transonic phenomena due to high local velocities. Expanding the Mach number range is therefore paramount for full understanding of an aircraft's behavior beyond the envelope boundaries. Significant research has been conducted in the past years focusing on transonic regime, but investigations of aircraft stall over an entire Mach number range would be a large scale undertaking.

APPENDIX A

RANS Turbulence Models

For the sake of completeness, the transport equations for the two-equation (SST) and Reynolds stress models (SSG/LRR-g) used in this work are presented in the following. The SST model by Menter [91] involves the solution of transport equations for the modeled turbulence kinetic energy k and the specific dissipation rate ω:

$$\frac{\partial \rho k}{\partial t} + \frac{\rho u_j k}{x_j} = P - \beta^* \rho \omega k + \frac{\partial}{\partial x_j}\left[(\mu + \sigma_k \mu_t)\frac{\partial k}{\partial x_j}\right] \tag{A.1}$$

$$\frac{\partial \rho \omega}{\partial t} + \frac{\rho u_j \omega}{x_j} = \frac{\gamma}{\nu_t} P - \beta \rho \omega + \frac{\partial}{\partial x_j}\left[(\mu + \sigma_\omega \mu_t)\frac{\partial \omega}{\partial x_j}\right] + 2(1 - F_1)\frac{\rho \sigma_{\omega 2}}{\omega}\frac{\partial k}{\partial x_j}\frac{\partial \omega}{\partial x_j} \tag{A.2}$$

The Reynolds stress model approach calls for the direct solution for the Reynolds stress components via six additional transport equations. They have the following form:

$$\frac{\partial \tau_{ij}}{\partial t} + \frac{\partial \tau_{ij} u_k}{\partial x_k} = \rho(P_{ij} + \Pi_{ij} - \varepsilon_{ij} + D_{ij} + M_{ij}) \tag{A.3}$$

Reynolds stress models include separate terms for production (P_{ij}), redistribution (Π_{ij}), dissipation (ε_{ij}), diffusion (D_{ij}) and fluctuating mass flux (M_{ij}) of each Reynolds stress tensor component. The SSG/LRR-g model combines the Speziale-Sarkar-Gatski and Launder-Reece-Rodi models with a transport equation for the quantity g [154].

APPENDIX B

Experimental Settings

The wind tunnel conditions used to conduct $ESWI^{\mathrm{RP}}$ experiments at the Reynolds numbers relevant for this work are:

Tab. B.1.: Overview of experimental conditions.

run	Re_∞	M_∞	$T[K]$	q/E	$p[kPa]$
313	11.6	0.25	115	0.0987	303
256	16.85	0.25	115	0.0674	445

Useable wake data is only available at the lower Reynolds number, while deformation was measured only at the higher one. Schulte am Hülse [128] demonstrated that the deformation magnitude varies proportionally to q/E, which enables deformation scaling across the Reynolds number settings.

APPENDIX C

Solver Parameters

The following solver parameters were used in the unsteady hybrid RANS/LES runs. Settings which have been varied in order to study their effects are not listed and are discussed in Chapter 5.

Tab. C.1.: TAU computational parameters for CRM simulations.

TAU parameter	value
multigrid scheme	5w
linear solver CFL	2
convective flux for turbulence equations	Roe
grid metric	`Cell_vertex`
inner iterations per time step	100
Prandtl number	0.72
Gas constant	$296.8\,\mathrm{J\,kg^{-1}\,K^{-1}}$
Sutherland constant	$111\,\mathrm{K}$
Sutherland reference temperature	$300.55\,\mathrm{K}$
Sutherland reference viscosity	$17.81 \cdot 10^{-6}\,\mathrm{Pa\,s}$
Central convective meanflow flux	`Skew_symmetric_kok`

APPENDIX D

Wake Quantities in Low Speed Stall

Fig. D.1 shows the distribution of the time-averaged velocity $\overline{u}$ field for three η positions and three angles of attack.

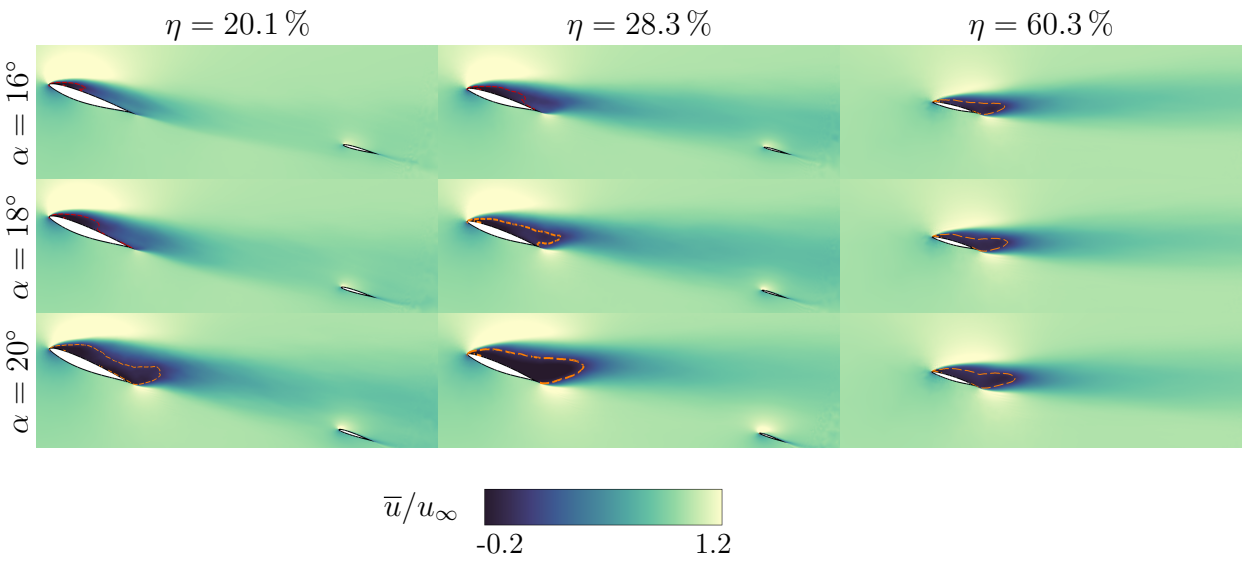

Fig. D.1.: Mean streamwise velocity $\overline{u}/u_\infty$ at $Re_\infty = 11.6 \cdot 10^6$. Dashed orange line represents $\overline{u} = 0$.

Bibliography

[1] Image from Airbus web site. https://www.airbus.com/aircraft/passenger-aircraft/a350xwb-family/a350-900.html, . retrieved on 31 July 2019.

[2] Airbus Global Market Forecast 2018-2037. https://www.airbus.com/aircraft/market/global-market-forecast.html, . Accessed on 25 June 2019.

[3] Aviation Safety Network website. https://news.aviation-safety.net/2019/01/01/aviation-safety-network-releases-2018-airliner-accident-statistics/. Accessed on 11 November 2019.

[4] Boeing Commercial Market Outlook 2019-2038. https://www.boeing.com/commercial/market/commercial-market-outlook/. Accessed on 25 June 2019.

[5] IATA 20-Year Air Passenger Forecast, Press Release No. 62. https://www.iata.org/pressroom/pr/Pages/2014-10-16-01.aspx. Accessed on 25 June 2019.

[6] Synopsis of Lift, Drag and Vortex Frequency Data for Rigid Circular Cylinders. Research Division Bulletin 300, Washington State University, College of Engineering, Pullman, WA, 1966.

[7] Loss of Control on Approach, Colgan Air, Inc., Operating as Continental Connection Flight 3407, Bombardier DHC-8-400, N200WQ, Clarence Center, New York, February 12, 2009. Technical Report NTSB/AAR-10/01, National Transportation Safety Board, Washington, D.C., 2010.

[8] Safety Investigation Following the Accident on 1 ST June 2009 to the Airbus A330-203, Flight AF447. Technical report, Bureau d'EnquÃłtes et d'Analyses, 2012.

[9] Airplane Upset Recovery Training Aid Rev. 3. https://www.icao.int/safety/loci/auprta/index.html, 2017. Accessed: 2019-03-21, published February 2017.

[10] ICAO Annual Report 2017. https://www.icao.int/annual-report-2017/Pages/

the-world-of-air-transport-in-2017-statistical-results.aspx, 2017. Accessed on 25 June 2019.

[11] *TAU-Code User Guide*, 2017.

[12] European Union Aviation Safety Agency Explanatory Note to Decision 2019/005/R. https://www.easa.europa.eu/sites/default/files/dfu/ExplanatoryNotetoDecicion2019-005-R.pdf, 2019. Accessed: 2019-06-25, published February 2019.

[13] CS-25: Certification Specifications and Acceptable Means of Compliance for Large Aeroplanes, Amendment 23, July 2019.

[14] A. Abbas-Bayoumi and K. Becker. An industrial view on numerical simulation for aircraft aerodynamic design. *Journal of Mathematics in Industry*, 1(1):10, Dec 2011. ISSN 2190-5983. doi: 10.1186/2190-5983-1-10. URL https://doi.org/10.1186/2190-5983-1-10.

[15] G. Abdrashitov. Tail Buffeting. Technical Report Report No. 395, Central Aero-Hydrodynamical Institute, Moscow, 1939.

[16] S. K. Advani and J. A. Schroeder. Global Implementation of Upset Prevention & Recovery Training. AIAA Modeling and Simulation Technologies Conference, San Diego, CA. doi: 10.2514/6.2016-1430, AIAA 2016-1430, Jan 2016.

[17] J. D. Anderson. *Fundamentals of Aerodynamics*. McGraw Hill, New York, 1984.

[18] R. A. Antonia and L. W. B. Browne. Quadrant analysis in the turbulent far-wake of a cylinder. *Fluid Dynamics Research*, 2(1):3–14, aug 1987. doi: 10.1016/0169-5983(87)90013-x.

[19] S. Banerjee, R. Krahl, F. Durst, and C. Zenger. Presentation of anisotropy properties of turbulence, invariants versus eigenvalue approaches. *Journal of Turbulence*, 8(32): 1–27, 2007. doi: 10.1080/14685240701506896.

[20] C. M. Belcastro, J. V. Foster, G. H. Shah, I. M. Gregory, D. E. Cox, D. A. Crider, L. Groff, R. L. Newman, and D. H. Klyde. Aircraft Loss of Control Problem Analysis and Research Toward a Holistic Solution. *Journal of Guidance, Control, and Dynamics*, 40(4):733–775, 2017. doi: 10.2514/1.G002815.

[21] L. H. Benedict and R. D. Gould. Towards better uncertainty estimates for turbulence statistics. *Experiments in Fluids*, 22:129–136, Apr. 1996.

[22] E. Berger, D. Scholz, and M. Schumm. Coherent Vortex Structures in the Wake of a Sphere and a Circular Disk at Rest and under Forced Vibrations. *Journal of Fluids and Structures*, 4:231–257, 1990.

[23] J. Blazek. *Computational Fluid Dynamics: Principles and Applications*. Elsevier, Kidlington, Oxford, UK, 2001. ISBN 0080430090.

[24] J. Boussinesq. Essai sur la theéorie des eaux courantes. In *Memoires presentés par divers savants á lácademie des sciences de línstitut de France, XXIII*, page 660. Paris, France, 1877.

[25] C. P. Britcher, C. W. Alcorn, and W. A. Kilgore. Subsonic sting interference on the drag of a family of slanted-base ogive-cylinders. *AIAA Paper 89-2006-CP*, Jan. 1989.

[26] G. L. Brown and A. Roshko. Turbulent shear layers and wakes. *Journal of Turbulence*, 13(51):1–32, 2012. doi: 10.1080/14685248.2012.723805. URL `https://doi.org/10.1080/14685248.2012.723805`.

[27] J. Carlier and K. Sodjavi. Turbulent mixing and entrainment in a stratified horizontal plane shear layer: joint velocity-temperature analysis of experimental data. *Journal of Fluid Mechanics*, 806:542–579, Oct. 2016. doi: 10.1017/jfm.2016.592.

[28] H. Choi and P. Moin. Grid-point requirements for large eddy simulation: Chapman's estimates revisited. *Physics of Fluids*, 24(011702), 2012.

[29] D. J. Craze. On the Near Wake Behind a Circular Disk. *6th Australasian Hydraulics and Fluid Mechanics Conference, Adelaide, Australia*, pages 282–286, Dec. 1977.

[30] J. D. Crouch, A. Garbaruk, and M. Strelets. Global Instability Analysis of Unswept- and Swept-Wing Transonic Buffet Onset. In *2018 Fluid Dynamics Conference*, page 3229, 2018.

[31] J. Dandois. Experimental study of transonic buffet phenomenon on a 3D swept wing. *Physics of Fluids*, 28(1):116, 2016.

[32] S. Deck. Zonal Detached Eddy Simulation of the Flow around a High-Lift Configuration. *AIAA Journal*, 43(11):2372–2384, Nov. 2005.

[33] D. Depres, R. Reijasse, and J. P. Dussauge. Analysis of Unsteadiness in Afterbody Transonic Flows. *AIAA Journal*, 42(12):2541–2550, Dec. 2004.

[34] R. P. Dwight. Heuristic a posteriori estimation of error due to dissipation in finite volume schemes and application to mesh adaptation. *Journal of Computational Physics*, 227:2845–2863, 2007. doi: 10.1016/j.jcp.2007.11.020.

[35] M. Emory and G. Iaccarino. Visualizing turbulence anisotropy in the spatial domain with componentality contours. In *Annual Research Briefs 2014*, pages 123–138. Center for Turbulence Research, 2014.

[36] J. A. Escobar, C. A. Suarez, C. Silva, O. D. Lopez, J. S. Velandia, and C. A. Lara. Detached-Eddy Simulation of a Wide-Body Commercial Aircraft in High-Lift Configuration. *Journal of Aircraft*, 52(4):1112–1121, 2015. doi: 10.2514/1.C033164.

[37] B. F. R. Ewald, editor. *Wind Tunnel Wall Correction*. AGARDograph 336. NATO Research and Technology Organisation, Oct. 1998. ISBN 92-836-1076-8. AGARD-AG-336.

[38] S. Farokhi, S. Mirsafian, T. Sherwood, and M. Ewing. Prediction of Antisymmetric Buffet Loads on Horizontal Stabilizers in Massively Separated Flows, Phase II. final report DOT/FAA/AR-99/27, U.S. Department of Transportation, Federal Aviation Administration, 1999.

[39] J. R. Forsythe, K. D. Squires, K. E. Wurtzler, and P. R. Spalart. Detached-Eddy Simulation of the F-15E at High Alpha. *Journal of Aircraft*, 41(2):193–200, Mar. 2004.

[40] D. Foti, X. Yang, M. Guala, and F. Sotiropoulos. Wake meandering statistics of a model wind turbine: Insights gained by large eddy simulations. *Physical Review Fluids*, 1(044407):1–25, 2016. doi: 10.1103/PhysRevFluids.1.044407.

[41] P. P. Gansel, S. A. Illi, S. Krimmer, T. Lutz, and E. Krämer. Unsteady CFD Simulation of the NASA Common Re-search Model in Low Speed Stall. *High Performance Computing in Science and Engineering '13*, pages 439–453, ISBN 978-3-319-02164-5 2013.

[42] C. M. Garcia, P. Ryan Jackson, and M. H. Garcia. Confidence intervals in the determination of turbulence parameters. *Experiments in Fluids*, 40:514–522, 2006.

[43] H. C. Garner, editor. *Subsonic Wind Tunnel Wall Corrections*. AGARDograph 109. NATO Research and Technology Organisation, Oct. 1966. ISBN 92-836-1076-8.

[44] M. Gopalakrishnan Meena, K. Taira, and K. Asai. Airfoil-Wake Modification with Gurney Flap at Low Reynolds Number. *AIAA Journal*, 56(4):1348–1359, 2018.

[45] A. Gorbushin, S. Bosnyakov, S. A. Glazkov, A. V. Lysenkov, S. V. Matyash, A. V. Semenov, and J. Quest. Slotted Wall Interference Investigation in ETW using the NASA CRM model. *AIAA Paper 2015-0621*, Jan. 2015.

[46] P. R. Grant, G. J. Moszczynski, and J. A. Schroeder. *Post-stall Flight Model Fidelity Effects on Full Stall Recovery Training*. 2018. doi: 10.2514/6.2018-2937.

[47] N. Hamilton, H. S. Kang, C. Meneveau, and R. B. Cal. Statistical analysis of kinetic energy entrainment in a model wind turbine array boundary layer. *Journal of Renewable and Sustainable Energy*, 4(063105):1–19, 2012. doi: 10.1063/1.4761921.

[48] C. W. Harper and R. L. Maki. A Review of the Stall Characteristics of Swept Wings. Technical Report TN D-2373, NASA, 1964.

[49] D. P. Hart. PIV error correction. *Experiments in Fluids*, 29(1):13–22, 2000.

[50] J. Havas and G. Jenaro Rabadan. Prediction of Horizontal Tail Plane Buffeting Loads.

International Forum on Aeroelasticity and Structural Dynamics, Seattle, WA, IFASD-2009-128, Jun 2009.

[51] G. Hefer. ETW — A Facility for High Reynolds Number Testing. In H. Sobieczky, editor, *IUTAM Symposium Transsonicum IV*, pages 157–164, Dordrecht, 2003. Springer Netherlands. ISBN 978-94-010-0017-8.

[52] E. H. Hirschel. Vortex Flows: Some General Properties, and Modelling, Configurational and Manipulation Aspects. doi: 10.2514/6.1996-2514, AIAA-96-2514-CP, 1996.

[53] E. H. Hirschel, J. Cousteix, and W. Kordulla. *Three-Dimensional Attached Viscous Flow*. Springer Verlag Berlin Heidelberg, 2014. ISBN 978-3-642-41377-3. doi: 10.1007/978-3-642-41378-0.

[54] C.-M. Ho and L.-S. Huang. Subharmonics and vortex merging in mixing layers. *Journal of Fluid Mechanics*, 119:443–473, 1982.

[55] C.-M. Ho and P. Huerre. Perturbed Free Shear Layers. *Annual Reviews in Fluid Mechanics*, 16:365–424, 1984.

[56] K. B. Howard, A. Singh, F. Sotiropoulos, and M. Guala. On the statistics of wind turbine wake meandering: An experimental investigation. *Physics of Fluids*, 27(075103): 1–19, 2015. doi: 10.1063/1.4923334.

[57] R. F. Huang and H. W. Lee. Turbulence Effect on Frequency Characteristics of Unsteady Motions in Wake of Wing. *AIAA Journal*, 38(1):87–94, Aug. 2000.

[58] R. F. Huang and C. L. Lin. Vortex Shedding and Shear-Layer Instability of Wing at Low-Reynolds Numbers. *AIAA Journal*, 33(8):1398–1403, Aug. 1995.

[59] W.-H. Hucho. *Aerodynamik der stumpfen Körper*. Springer Fachmedien Wiesbaden GmbH, 2nd edition, 2012. ISBN 978-3-8348-1462-3.

[60] P. Huerre and M. Rossi. *Hydrodynamic instabilities in open flows*, pages 81–294. Collection Alea-Saclay: Monographs and Texts in Statistical Physics. Cambridge University Press, 1998. doi: 10.1017/CBO9780511524608.004.

[61] S. Illi, C. Fingskes, T. Lutz, and E. Krämer. Transonic Tail Buffet Simulations for the Common Research Model. 31st AIAA Applied Aerodynamics Conference, San Diego, California. doi: https://doi.org/10.2514/6.2013-2510, AIAA 2013-2510, 2013.

[62] M. Iovnovich and D. E. Raveh. Numerical Study of Shock Buffet on Three-Dimensional Wings. *AIAA Journal*, 53(2):449–463, May 2014.

[63] R. Jain, A. Le Pape, A. Grubb, M. Costes, F. Richez, and M. Smith. High-resolution computational fluid dynamics predictions for the static and dynamic stall of a finite-span OA209 wing. *Journal of Fluids and Structures*, 78:126–145, 2018. doi: 10.2514/1.j056108.

[64] A. Jameson, W. Schmidt, and E. Turkel. Numerical solution of the Euler equations by finite volume methods using Runge Kutta time stepping schemes. 14th Fluid and Plasma Dynamics Conference, Palo Alto, California. doi: 10.2514/6.1981-1259, AIAA 1981-1259, 1981.

[65] W. K. G. Jr., P. D. Beuther, and J. L. Lumley. Processing of Random Signals. In B. W. Hansen, editor, *Proceedings of the Dynamic Flow Conference 1978 on Dynamic Measurements in Unsteady Flows*, pages 757–800, Dordrecht, 1978. Springer Netherlands.

[66] S. Keye, V. Togiti, B. Eisfeld, O. P. Brodersen, and M. B. Rivers. Investigation of Fluid-Structure-Coupling and Turbulence Model Effects on the DLR Results of the Fifth AIAA CFD Drag Prediction Workshop. 31st AIAA Applied Aerodynamics Conference, San Diego, California. doi: 10.2514/6.2013-2509, AIAA 2013-2509, Jan. 2013.

[67] S. Koike, M. Ueno, K. Nakakita, and A. Hashimoto. Unsteady pressure measurement of transonic buffet on NASA common research model. In *34th AIAA Applied Aerodynamics Conference*, page 4044, 2016.

[68] A. Kolmogorov. The local structure of turbulence in incompressible viscous fluid for very large Reynolds number. *Doklady Akademii Nauk*, 30:9–13, 1941. doi: 10.1007/978-94-011-3030-1_45.

[69] B. König and E. Fares. Validation of a Transonic Lattice-Boltzmann Method on the NASA Common Research Model. *AIAA Paper 2016-2023*, Jan. 2016.

[70] R. Konrath, R. Geisler, J. Agocs, D. Otter, H. Ehlers, F. Philipp, and J. Quest. High-speed PIV applied to wake of NASA CRM model at high Re-number sub- and transonic stall conditions. *CEAS Aeronautical Journal*, 9(2):339–346, June 2018.

[71] E. Krämer, T. Lutz, and S. A. Illi. LuFo-Verbundvorhaben ComFliTe, Teilvorhaben: Qualifizierung von CFD Methoden für Grenzbereiche der Flugenvelope. Final report 20A0801G, University of Stuttgart, Institute of Aerodynamics and Gas Dynamics, 2012.

[72] A. Le Pape, F. Richez, and S. Deck. Zonal Detached-Eddy Simulation of an Airfoil in Poststall Condition. *AIAA Journal*, 51(8):1919–1931, Aug. 2013. doi: 10.2514/1.J052235.

[73] B. Lee. Oscillatory shock motion caused by transonic shock boundary-layer interaction. *AIAA Journal*, 28(5):942–944, Oct. 1990.

[74] B. Lee. Vertical tail buffeting of fighter aircraft. *Progress in Aerospace Sciences*, pages 193–279, 2000.

[75] J. J. Lee, S. P. Lukachko, I. A. Waitz, and A. Schafer. Historical and Future Trends in Aircraft Performance, Cost and Emissions. *Annual Review of Energy and the Environment*, 26:167–200, 2001. doi: doi.org/10.1146/annurev.energy.26.1.167.

[76] J. Letzgus, P. Weihing, M. Keßler, and E. Krämer. Assessment of Delayed

Detached-Eddy Simulation of Dynamic Stall on a Rotor. In Y. Hoarau, S.-H. Peng, D. Schwamborn, A. Revell, and C. Mockett, editors, *Progress in Hybrid RANS-LES Modelling*, pages 311–321, Cham, 2020. Springer International Publishing.

[77] D. W. Levy, K. R. Laflin, E. N. Tinoco, J. C. Vassberg, M. Mani, B. Rider, C. L. Rumsey, R. A. Wahls, J. H. Morrison, and O. P. Summary of Data from the Fifth Computational Fluid Dynamics Drag Prediction Workshop. *Journal of Aircraft*, 51 (4):1194–1213, 2014. doi: 10.2514/1.C032389. URL `https://doi.org/10.2514/1.C032389`.

[78] A. Liberzon, R. Gurka, I. Tiselj, and G. Hetsroni. Spatial characterization of the numerically simulated vorticity fieldsof a flow in a flume. *Theoretical and Computational Fluid Dynamics*, 19:115–125, 2005.

[79] S. Longo, L. Chiapponi, and M. Clavero. Experimental analysis of the coherent structures and turbulence past a hydrofoil in stalling condition beneath a water-air interface. *European Journal of Mechanics B/Fluids*, 43:172–182, 2014. doi: 10.1016/j.euromechflu.2013.08.007.

[80] J. M. Luckring. A Survey of Factors Affecting Blunt Leading-Edge Separation for Swept and Semi-Slender Wings. 28th Applied Aerodynamics Conference, Chicago, IL, AIAA 2010-4820, 2010.

[81] J. L. Lumley. *Stochastic Tools in Turbulence*. Dover Publications, Inc., Mineola, NY, 1970.

[82] J. L. Lumley and G. R. Newman. The return to isotropy of homogeneous turbulence. *Journal of Fluid Mechanics*, 82(1):161–178, 1977. doi: 10.1017/S0022112077000585.

[83] T. Lutz, P. P. Gansel, J.-L. Godard, A. Gorbushin, R. Konrath, J. Quest, and S. M. B. Rivers. Going for Experimental and Numerical Unsteady Wake Analyses Combined with Wall Interference Assessment by Using the NASA CRM-model in ETW. Dallas, TX, number AIAA 2013-0871. doi: 10.2514/6.2013-871, Jan. 2013.

[84] T. Lutz, P. P. Gansel, A. Waldmann, D.-M. Zimmermann, and S. A. Schulte am Hülse. Time-Resolved Prediction and Measurement of the Wake Past the CRM at High Reynolds Number Stall Conditions. *Journal of Aircraft*, 53(2):501–514, 2016. doi: 10.2514/1.C033351.

[85] D. G. Mabey. Unsteady aerodynamics: retrospect and prospect. *The Aeronautical Journal*, 103(1019):1–18, 1999. doi: 10.1017/S0001924000065064.

[86] M. Mackay. A Review of Sting Support Interference and some Related Issues for the Marine Dynamic Test Facility (MDTF). *Defence Research Establishment Atlantic, DREA Report 93/107*, Oct. 1993.

[87] J. Mantik, H. Quix, and J. Quest. Enhancement of the Stereo Pattern Tracking Technique for Model Deformation Assessment at ETW. 51st AIAA Aerospace Sciences

Meeting including the New Horizons Forum and Aerospace Exposition, Grapevine, TX. doi: 10.2514/6.2013-0870, AIAA 2013-0870, Jan. 2013.

[88] J. Mathieu and J. Scott. *An Introduction to Turbulent Flow*. Cambridge University Press, Cambridge, UK, 2000. ISBN 9781316529850. doi: 10.1017/CBO9781316529850.

[89] G. B. McCullough and D. E. Gault. Examples of Three Representative Types of Airfoil-Section Stall at Low Speed. Technical Report TN 2502, NACA, 1951.

[90] M. A. McVeigh and E. Kisielowski. A Design Summary of Stall Characteristics of Straight Wing Aircraft. Technical Report TN CR-1646, NASA, 1971.

[91] F. R. Menter. Two-Equation Eddy-Viscosity Turbulence Models for Engineering Applications. *AIAA Journal*, 32(8):1598–1605, Aug. 1994.

[92] F. R. Menter and Y. Egorov. A Scale-Adaptive Simulation Model using Two-Equation Models. 43rd AIAA Aerospace Sciences Meeting and Exhibit, Reno, NV. doi: 10.2514/6.2005-1095, AIAA 2005-1095, Jan 2005.

[93] C. Mockett. *Efficiency Improvements of RANS-Based Analysis and Optimization Using Implicit and Adjoint Methods on Unstructured Grids*. PhD thesis, University of Manchester, Manchester, Aug. 2006.

[94] C. Mockett. *A comprehensive study of detached-eddy simulation*. PhD thesis, TU Berlin, Berlin, Aug. 2009.

[95] C. Mockett, W. Haase, and D. Schwamborn. *Go4Hybrid: Grey Area Mitigation for Hybrid RANS-LES Methods*. Springer International Publishing, 1 edition, 2018. ISBN 978-3-319-52995-0.

[96] M. Mokry. Evaluation of combined wall- and support-interference on wind tunnel models. *AGARD-CP-535, Paper 28*, Oct. 1993.

[97] P. A. Monkewitz and P. Huerre. Influence of the velocity ratio on the spatial instability of mixing layers. *Physics of Fluids*, 25:1137–1143, 1982. doi: 10.1063/1.863880.

[98] S. A. Morton, R. M. Cummings, and D. B. Kholodar. High Resolution Turbulence Treatment of F/A-18 Tail Buffet. *Journal of Aircraft*, (6):1769–1775, Nov. 2007. doi: 10.2514/1.29577.

[99] K. Mulleners and M. Rütten. Analysis of Intermittent Trailing-Edge Vortex Shedding Using Recurrence Plots. *AIAA Journal*, 56(2):571–580, Feb. 2018. doi: 10.2514/1.J056329.

[100] C. Norberg. Flow Around a Circular Cylinder: Aspects of Fluctuating Lift. *Journal of Fluids and Structures*, 15:459–469, Dec. 2001.

[101] Y. Ohmichi, T. Ishida, and A. Hashimoto. Modal Decomposition Analysis of Three-

Dimensional Transonic Buffet Phenomenon on a Swept Wing. *AIAA Journal 56(10)*, pages 3938–3950, 2018.

[102] R. Pain, P. E. Weiss, and S. Deck. Zonal Detached Eddy Simulation of the Flow Around a Simplified Launcher Afterbody. *AIAA Journal*, 52(9):1967–1979, Sept. 2014. doi: 10.2514/1.J052743.

[103] V. C. Patel and G. Scheuerer. Calculation of Two-Dimensional Near and Far Wakes. *AIAA Paper 82-4156*, 1982.

[104] R. Perrin, M. Braza, E. Cid, S. Cazin, A. Barthet, A. Sevrain, C. Mockett, and F. Thiele. Obtaining phase averaged turbulence properties in the near wake of a circular cylinder at high Reynolds number using POD. *Experiments in Fluids*, 43:341–355, Aug. 2007. doi: 10.1007/s00348-007-0347-6.

[105] E. C. Polhamus. A Survey of Reynolds Number and Wing Geometry Effects on Lift Characteristics in the Low Speed Stall Region. Technical Report CR-4745, NASA, 1996.

[106] D. I. A. Poll. On the generation and subsequent development of spiral vortex flow over a swept-back wing. *AGARD-CP-342, Paper 6*, pages 1–14, 1983.

[107] S. B. Pope. *Turbulent Flows*. Cambridge University Press, Cambridge, MA, 2000.

[108] L. Prandtl. Tragflügeltheorie. In *Nachrichten von der Gesellschaft der Wissenschaften zu Göttingen*, pages 451–477. 1912.

[109] A. Prasad and C. Williamson. The instability of the separated shear layer from a bluff body. *Physics of Fluids*, 8(6):1347–1349, May 1996. doi: 10.1063/1.868942.

[110] A. Probst, S. Schulze, C. J. Kähler, and R. Radespiel. Reynolds-Stress Modelling of Subsonic and Transonic Inlet Stall Compared to Measurements. Braunschweig, Germany, 2012.

[111] A. Probst, D. Schwamborn, A. Garbaruk, E. Guseva, M. Shur, M. Strelets, and A. Travin. Evaluation of grey area mitigation tools within zonal and non-zonal RANS-LES approaches in flows with pressure induced separation. *International Journal of Heat and Fluid Flow*, 68:237–247, 2017.

[112] D. R. Radenkovic, J. M. Burazer, and D. M. Novkovic. Anisotropy Analysis of Turbulent Swirl Flow. *FME Transactions*, 42(1):19–25, 2014. doi: 10.5937/fmet1401019R.

[113] M. R. Raupach. Conditional statistics of Reynolds stress in rough-wall and smooth-wall turbulent boundary layers. *Journal of Fluid Mechanics*, 108:363–382, 1981. doi: 10.1017/S0022112081002164.

[114] F. Richez, A. Le Pape, and M. Costes. Zonal Detached-Eddy Simulation of Separated

Flow Around a Finite-Span Wing. *AIAA Journal*, 53(11):3157–3166, Nov. 2015. doi: 10.2514/1.J053636.

[115] M. Rivers, C. Hunter, and R. Campbell. Further Investigation of the Support System Effects and Wing Twist on the NASA Common Research Model. 30th AIAA Applied Aerodynamics Conference, New Orleans. doi: 10.2514/6.2012-3209, AIAA 2012-3209, Jun 2012.

[116] P. J. Roache. Perspective: A Method for Uniform Reporting of Grid Refinement Studies. *Journal of Fluids Engineering*, 116:405–413, sep 1994.

[117] I. Rodriguez, O. Lehmkuhl, R. Borrell, and A. Oliva. Direct numerical simulation of a NACA0012 in full stall. *International Journal of Heat and Fluid Flow*, 43:194–203, 2013.

[118] P. Roe. Approximate Riemann Solvers, Parametric Vectors and Difference Schemes. *Journal of Computational Physics*, 43:357–372, Sept. 1981. doi: 10.1016/0021-9991(81)90128-5. URL `https://doi.org/10.1016/0021-9991(81)90128-5`.

[119] A. Roshko. On the Wake and Drag of Bluff Bodies. *Journal of the Aeronautical Sciences*, 22(2):124–132, Feb 1955. doi: 10.2514/8.3286. URL `https://doi.org/10.2514/8.3286`.

[120] C.-C. Rossow, J.-L. Godard, H. Hoheisel, and V. Schmitt. Investigations of propulsion integration interference effects on a transport aircraft configuration. *Journal of Aircraft*, 31(5):1022–1030, 1994. doi: 10.2514/3.46605. URL `https://doi.org/10.2514/3.46605`.

[121] R. Rudnik, D. Reckzeh, and J. Quest. HINVA - High lift INflight VAlidation - Project Overview and Status. 50th AIAA Aerospace Sciences Meeting, Nashville, TN. doi: 10.2514/6.2012-106, AIAA 2012-0106, Jan 2012.

[122] R. Rudnik, D. Melber-Wilkending, and P. Risley-Settle. TAU-SOLAR Contributions to the 3rd High Lift Prediction Workshop. AIAA Aerospace Sciences Meeting, Kissimmee, FL. doi: 10.2514/6.2018-1035, AIAA 2018-1035, Jan 2018.

[123] C. L. Rumsey, J. P. Slotnick, and A. J. Sclafani. Overview and Summary of the Third AIAA High Lift Prediction Workshop. *Journal of Aircraft*, 56(2):1–24, 2019. doi: 10.2514/1.C034940.

[124] N. D. Sandham, M. G. Mungal, J. E. Broadwell, and W. C. Reynolds. Scalar Entrainment in the Mixing Layer. In *Proceedings of the Summer Program 1988*, pages 69–76. Center for Turbulence Research, 1988.

[125] F. Sartor and S. Timme. Delayed Detached-Eddy Simulation of Shock Buffet on Half Wing-Body Configuration. *AIAA Journal*, 55(4):1230–1240, Apr. 2016.

[126] S. Scharnowski and C. J. Kähler. A combined direct numerical simulation-particle

image velocimetry study of the turbulent near wake. *Journal of Fluid Mechanics*, 569: 185–207, May 2006. doi: 10.1017/S0022112006002606.

[127] S. Scharnowski and C. J. Kähler. Investigation of a transonic separating/reattaching shear layer by means of PIV. *Theoretical and Applied Mechanics Letters*, 5:30–34, Feb. 2015. doi: 10.1016/j.taml.2014.12.002.

[128] S. A. Schulte am Hülse. *Simulation transsonischen Buffets an Transportflugzeugen mittels hybrider RANS-/LES Verfahren.* PhD thesis, University of Stuttgart, Dr. Hut Verlag, Munich, Aug. 2016.

[129] M. Schulz. ESWIRP Wind Tunnel Tests with NASA CRM Full Model in ETW. Technical Report Test Report E 9006 TR 153, ETW, 2015.

[130] A. Schütte. Numerical Investigations of Vortical Flow on Swept Wings with Round Leading Edges. *Journal of Aircraft*, (2):572–601, Mar. 2017. doi: 10.2514/1.C034057.

[131] D. Schwamborn, T. Gerhold, and R. Heinrich. The DLR TAU-Code, Recent Applications in Research and Industry. *European Conference on Computational Fluid Dynamics ECCOMAS CFD 2006*, Sept. 2006.

[132] A. Seifert and L. Pack. Characterization of the Flow over Periodic Hills with Advanced Measurement and Evaluation Techniques. International Symposium on Turbulence and Shear Flow Phenomena (TSFP-8), Paris, France, Aug. 2013.

[133] S. C. Shadden, F. Lekien, and J. E. Marsden. CDefinition and Properties of Lagrangian Coherent Structures from Finite-Time Lyapunov Exponents in Two-Dimensional Aperiodic Flows. *Physica D: Nonlinear Phenomena: Nonlinear Phenomena*, 212(3-4):271–304, 2005.

[134] J. Shin. The NASA Aviation Safety Program: Overview. Technical Report TM-2000-209810, NASA, 2000.

[135] M. Shur, P. R. Spalart, M. K. Strelets, and A. K. Travin. A hybrid RANS-LES model with delayed DES and wall-modeled LES capabilities. *International Journal of Heat and Fluid Flow*, 29:1638–1649, Sept. 2008. doi: 10.1016/j.ijheatfluidflow.2008.07.001.

[136] A. J. Simonsen and P. Å. Krogstad. Turbulent stress invariant analysis: Clarification of existing terminology. *Physics of Fluids*, 17(088103):1–4, 2005. doi: 10.1063/1.2009008.

[137] L. Sirovich. Turbulence and the Dynamics of Coherent Structures Part I: Coherent Structures. *Quarterly of Applied Mathematics*, XLV(3):561–571, 1987.

[138] J. Smagorinsky. General circulation experiments with the primitive equations, part I: the basic experiment. *Monthly Weather Rev.*, 91:99–164, 1963.

[139] A. M. O. Smith. High-Lift Aerodynamics. *Journal of Aircraft*, 12(6), June 1975. doi: 10.2514/3.59830.

[140] P. R. Spalart. Strategies for turbulence modelling and simulations. *Strategies for turbulence modelling and simulations*, 21:252–263, 2000.

[141] P. R. Spalart. Young-Person's Guide to Detached-Eddy Simulation Grids. Technical Report CR-2001-211032, NASA, 2001.

[142] P. R. Spalart and S. R. Allmaras. A One-equation Turbulence Model for Aerodynamic Flows. *AIAA-92-0439*, 1992.

[143] P. R. Spalart, W.-H. Jou, M. Strelets, and S. Allmaras. Comments on the Feasibility of LES for Wings, and on a Hybrid RANS/LES Approach. In C. Mockett, W. Haase, and D. Schwamborn, editors, *Advances in DNS/LES: proceedings of the First AFOSR International Conference on DNS/LES*, pages 137–148, Columbus, OH, 1997. Greyden Press. ISBN 1570743657.

[144] P. R. Spalart, S. Deck, M. L. Shur, K. D. Squires, M. K. Strelets, and A. Travin. A New Version of Detached-Eddy Simulation, Resistant to Ambiguous Grid Densities. *Theoretical and Computational Fluid Dynamics*, 20(3):181–195, 2006.

[145] B. Steinfurth and F. Haucke. Coherent Structures in the Actively Controlled Wake of a High-Lift Configuration. *AIAA Journal*, 56(10):3848–3856, 2018.

[146] M. Stojanowski and E. Germain. The FALCON 7x from ETW to flight. *46th AIAA Aerospace Sciences Meeting and Exhibit, Paper 2008-0835*, Jan. 2008.

[147] M. Strelets. Detached Eddy Simulation of Massively Separated Flows. 39th AIAA Aerospace Sciences Meeting and Exhibit, Reno, NV. doi: 10.2514/6.2001-0879, AIAA 2001-0879, Jun 2001.

[148] Y. Sugioka, S. Koike, K. Nakakita, D. Numata, T. Nonomura, and K. Asai. Experimental analysis of transonic buffet on a 3D swept wing using fast-response pressure-sensitive paint. *Experiments in Fluids*, 59(6):108, 2018. doi: 10.1007/s00348-018-2565-5.

[149] R. C. Swanson and E. Turkel. On central-difference and upwind schemes. *Journal of Computational Physics*, 101:292–306, 1992.

[150] T. T. Teng, T. S. Zhang, S. Liu, and P. R. Grant. Representative Post-Stall Modelling of T-tailed Regional Jets and Turboprops for Upset Recovery Training. AIAA Modeling and Simulation Technologies Conference, Kissimmee, FL, AIAA 2015-2032, Jan 2015.

[151] H. Tennekes and J. L. Lumley. *A first course in turbulence.* MIT Press, Cambridge, MA, 1972.

[152] F. O. Thomas and X. Liu. An experimental investigation of symmetric and asymmetric turbulent wake development in pressure gradient. *Physics of Fluids*, 16(5):1725–1745, May 2004.

[153] E. N. Tinoco, O. P. Brodersen, S. Keye, K. R. Laflin, E. Feltrop, J. Vassberg, M. Mani,

B. Rider, R. A. Wahls, J. H. Morrison, D. Hue, C. J.Roy, D. J. Mavriplis, and M. Murayama. Summary Data from the Sixth AIAA CFD Drag PredictionWorkshop: CRM Cases. *Journal of Aircraft*, 55(4):1352–1379, July 2017. doi: 10.2514/1.C034409.

[154] V. Togiti, B. Eisfeld, and O. Brodersen. Turbulence Model Stufy for the Flow Around the NASA Common Research Model. *Journal of Aircraft*, 51(4):1331–1343, July 2014.

[155] C. Torrence and G. P. Compo. A Practical Guide to Wavelet Analysis. *Bulletin of the American Meteorological Society*, 79(1):61–78, Jan. 1998.

[156] A. A. Townsend. *The Structure of Turbulent Shear Flow*. Cambridge University Press, Cambridge, UK, 2nd edition, 1976.

[157] A. K. Travin, M. L. Shur, P. R. Spalart, and M. K. Strelets. A hybrid RANS-LES model with delayed DES and wall-modeled LES capabilities. In J. P. P. Wesseling, E. Onate, editor, *Proceedings ECCOMAS CFD Conference 2006*, pages 1–23. Technische Universiteit Delft, 2006.

[158] M. van Dyke. *An Album of Fluid Motion*. Parabolic Press, Stanford, California, USA, 1982.

[159] B. W. van Oudsheusden, F. Scarano, N. van Hinsberg, and D. W. Watt. Phase-resolved characterization of vortex shedding in the near wake of a square-section cylinder at incidence. *Experiments in Fluids*, 39:86–98, May 2005. doi: 10.1007/s00348-005-0985-5.

[160] J. C. Vassberg, M. A. DeHaan, M. B. Rivers, and R. A. Wahls. Development of a Common Research Model for Applied CFD Validation Studies. 26th AIAA Applied Aerodynamics Conference, Guidance, Navigation, and Control and Co-located Conferences, Honolulu, Hawaii. doi: 10.2514/6.2008-6919, AIAA 2008-6919, Aug. 2008.

[161] J. C. Vassberg, E. N. Tinoco, M. Mani, B. Rider, T. Zickuhr, D. W. Levy, O. P. Brodersen, B. Eisfeld, S. Crippa, R. A. Wahls, J. H. Morrison, D. J. Mavriplis, and M. Murayama. Summary of the Fourth AIAA CFD Drag Prediction Workshop. 28th AIAA Applied Aerodynamics Conference, Chicago, Illinois. doi: 10.2514/6.2010-454, June 2010.

[162] J. Verriere, F. Gand, and S. Deck. Zonal Detached Eddy Simulations of a Dual-Stream Jet: Turbulence Rate Sensitivity. *AIAA Journal*, 55(8):2503–2521, Aug. 2017. doi: 10.2514/1.J055535.

[163] M. R. Visbal and D. J. Garmann. Analysis of Dynamic Stall on a Pitching Airfoil Using High-Fidelity Large-Eddy Simulations. *Journal of Aircraft*, 56(1):46–63, 2018. doi: 10.2514/1.j056108.

[164] T. von Kármán. Über den Mechanismus des Widerstandes, den ein bewegter Körper in einer Flüssigkeit erfährt. In *Nachrichten von der Gesellschaft der Wissenschaften zu Göttingen*, pages 547–556. Berlin, Weidmannsche Buchhandlung, 1912.

[165] R. Vos and S. Farokhi. *Introduction to Transonic Aerodynamics*. Springer Science+Business Media B.V., Dordrecht, Netherlands, 2015. doi: 10.1007/978-94-017-9747-4.

[166] A. Waldmann, P. P. Gansel, T. Lutz, and E. Krämer. Unsteady Wake of the NASA Common Research Model in Low-Speed Stall. *Journal of Aircraft*, 53(4):1073–1086, 2016. doi: 10.2514/1.C033413.

[167] A. Waldmann, T. Lutz, and E. Krämer. Wind Tunnel Support System Influence on NASA Common Research Model at Low-Speed Conditions. *Journal of Aircraft*, 55(5): 1762–1772, 2018. doi: 10.2514/1.C034440.

[168] A. Waldmann, T. Lutz, and E. Krämer. Unsteady Simulation of the Separated Wake of a Transport Aircraft by Detached Eddy Simulation. In A. Dillmann, G. Heller, E. Krämer, C. Wagner, S. Bansmer, R. Radespiel, and R. Semaan, editors, *New Results in Numerical and Experimental Fluid Mechanics XI*, pages 61–71. Springer, 2018. ISBN 978-3-319-64519-3.

[169] A. Waldmann, T. Lutz, and E. Krämer. Separated Wake Flow and Tail Loads of the Common Research Model in Low Speed Stall Conditions. San Diego, CA, number AIAA 2019-2315, Jan. 2019.

[170] A. Waldmann, T. Lutz, and E. Krämer. Unsteady Wake and Tailplane Loads of the Common Research Model in Low Speed Stall. In A. Dillmann, G. Heller, E. Krämer, C. Wagner, C. Tropea, and S. Jakirlic, editors, *New Results in Numerical and Experimental Fluid Mechanics XII*, pages 14–24. Springer, 2020. ISBN 978-3-030-25253-3.

[171] P. D. Welch. The use of the fast Fourier transform for the estimation of power spectra: A method based on time averaging over short, modified periodograms. *IEEE Transactions on Audio Electroacoustics*, 15(2):70–73, June 1967.

[172] M. J. Whitney, T. J. Seitz, and E. L. Blades. Low-Speed-Stall Tail Buffet Loads Estimation Using Unsteady CFD. *IFASD 2009-127*, Jun 2009.

[173] W. W. Willmarth and S. S. Lu. Structure of the Reynolds stress near the wall. *Journal of Fluid Mechanics*, 55(1):65–92, 1972. doi: 10.1017/S002211207200165X.

[174] C. C. Wolf. *The Subsonic Near-Wake of Bluff Bodies*. PhD thesis, RWTH Aachen, Aachen, Aug. 2014.

[175] S. H. Woodson, B. E. Green, J. J. Chung, D. V. Grove, P. C. Parikh, and J. R. Forsythe. Recommendations for Computational-Fluid-Dynamics Procedures for Predicting Abrupt Wing Stall. *Journal of Aircraft*, 42(3):627–633, May 2005.

[176] J.-Z. Wu, X.-Y. Lu, A. G. Denny, M. Fan, and J.-M. Wu. Post-stall flow control on an airfoil by local unsteady forcing. *Journal of Fluid Mechanics*, 371:21–58, Mar. 1998.

[177] Z. Yang, J. Li, J. Jin, H. Zhang, and Y. Jiang. Investigation and Improvement of

Stall Characteristic of High-LiftConfiguration without Slats. *International Journal of Aerospace Engineering*, 2019:1–14, 2019. doi: 10.1155/2019/7859482.

[178] S. Yarusevych and M. S. H. Boutilier. Vortex Shedding of an Airfoil at Low Reynolds Numbers. *AIAA Journal*, 49(10):2221–2227, Oct. 2011.

[179] S. Yarusevych, P. E. Sullivan, and J. G. Kawall. On vortex shedding from an airfoil in low-Reynolds-number flows. *Journal of Fluid Mechanics*, 632:245–271, 2009. doi: 10.1017/S0022112009007058.

[180] S. Zhang, A. J. Jaworski, S. C. McParlin, and J. T. Turner. Experimental investigation of the flow structures over a 40 swept wing. *The Aerodnautical Journal*, (1259):39–55, Jan. 2018. doi: 10.1017/aer.2018.118.

[181] N. H. Zimmerman, M. A. Ferman, R. N. Yurkovich, and G. Gerstenkorn. Prediction of Tail Buffet for Design Applications. Number AIAA 89-1378-CP, 1989.

[182] D.-M. Zimmermann, A. Waldmann, T. Lutz, and E. Krämer. Development of flow structures in the near-field wake region of the Common Research Model. *CEAS Aeronautical Journal*, Dec 2016. ISSN 1869-5590. doi: 10.1007/s13272-016-0222-3. URL `https://doi.org/10.1007/s13272-016-0222-3`.